



University of Zagreb

Faculty of Science

Neven Šantić

SYNTHETIC LORENTZ FORCE FOR NEUTRAL COLD ATOMS

DOCTORAL THESIS

Supervisor:
dr. sc. Ticijana Ban

Zagreb, 2018.



Sveučilište u Zagrebu

Prirodoslovno-matematički fakultet

Neven Šantić

SINTETIČKA LORENTZOVA SILA ZA NEUTRALNE HLADNE ATOME

DOKTORSKI RAD

Mentor:
dr. sc. Ticijana Ban

Zagreb, 2018.

Acknowledgments

First and foremost, I would like to thank my amazing advisor, Dr. Ticijana Ban. With her sheer will and undeterred drive she made my job and my research possible, inspired and motivated me and others around me. Always generous with her knowledge, advice and guidance, yet firm when needed, I am certain she is the best of all possible advisors and for this I am very grateful to her.

I would also like to thank Dr. Damir Aumiler who was many times a great substitute advisor, provided ingenious insights into problems and was often a welcomed deciding factor in the many enjoyable discussions within our small group.

A very big thank you to Prof. Hrvoje Buljan who open-handedly provided me with plentiful support throughout my doctorate, was often a great second advisor with his expertise and original ideas.

Many thanks to my colleagues and coworkers, to Tena Dubček who was always a pleasure working and traveling with, to Gordana Kregar who helped me with my first steps in the lab, to Nikolina Nekić and Ana Cipriš who after competently contributing in the lab during their master studies left us for greener pastures, to Danijel Buhin and Domagoj Kovačić who decided to stay on a little bit after their master's for their fresh enthusiasm, a last but not least Dr. Ivor Krešić, who was a great friend even before he joined us for a post-doc and became my quirky but delightful office-mate.

Thank you to Dr. Silvoje Vdović for being a very enjoyable lab co-inhabitant, to Dr. Nataša Vujičić and Dr. Mario Rakić for helpful advice and equipment sharing.

I am very grateful to the people whose hospitality I enjoyed in the recent years, to Dr. Daniel Comparat who very generously hosted me just after my master's, to Prof. Francesca Ferlino in whose lab I learned a lot, to Prof. Aleksandra Foltynowicz-Matyba for an extremely useful stay in Umeå, and especially to Dr. Robin Kaiser whose hospitality in Nice was wonderful, and from whom I learned a great deal.

Thank you to Damir Altus who always made electronics development interesting, and to Franjo and Čičko from the mechanical workshop for making the endless posts and detested clamps, as well as other parts for the setup.

Last but not least, I am immensely grateful to my family whose love and support mean the world to me, especially to Irena, the love of my life, you make all of this meaningful.

Contents

Abstract	i
Expanded abstract in Croatian	ii
1 Introduction	1
1.1. Cold atoms	1
1.2. Synthetic magnetism in cold atomic gases	2
1.3. Frequency comb cooling	5
2 Laser induced forces and the magneto-optical trap	8
2.1. The two-level atom	8
2.2. Laser cooling	14
2.3. The magneto-optical trap principle of operation	19
3 Experiment	24
3.1. The rubidium atom	24
3.2. The magneto-optical traps	27
3.3. External cavity diode lasers	35
4 Synthetic Lorentz force	44
4.1. The scheme	44
4.2. Synthetic Lorentz force for an atomic cloud with a center-of-mass velocity	49
4.3. Synthetic Lorentz force in an expanding cold atomic gas	57
5 Frequency comb cooling	65
5.1. Stabilizing the comb	66
5.2. Laser cooling using a frequency comb	73
6 Conclusion	80

Appendix A: Articles published during doctoral studies	82
<i>Synthetic Lorentz force in classical atomic gases via Doppler effect and radiation pressure, Phys. Rev. A</i> 89 , 063415 (2014)	83
<i>Experimental Demonstration of a Synthetic Lorentz Force by Using Radiation Pressure, Sci. Rep.</i> 5 , 13485 (2015)	88
<i>Synthetic Lorentz force in an expanding cold atomic gas, J. Opt. Soc. Am. B</i> 34 , 1264-1269 (2017)	97
Appendix B: Articles submitted or being prepared for submission	103
<i>Sub-Doppler cooling of atoms using an optical frequency comb</i>	104
<i>Frequency comb stabilization without self-referencing</i>	109
Appendix C: Technical drawings	113
Curriculum Vitae with a list of publications	115
Bibliography	117

Abstract

Presented in this thesis are results of research on two topics in the field of cold atoms. These topics are connected by the fact they both employ laser induced forces caused by momentum transfer from photons to atoms. In both cases the laser induced forces change the velocity distribution of the atomic ensemble.

In the first part of the thesis a new way to implement a synthetic Lorentz force into a cold atomic gas is presented. The synthetic Lorentz force (SLF) is based on radiation pressure and the Doppler effect, making it straightforward to implement in a large volume, for a broad range of velocities, and can be extended to different geometries. The force is perpendicular to the velocity of an atom, and zero for an atom at rest. This SFL is experimentally demonstrated in a system of cold rubidium atoms in two scenarios: first, by observing the center-of-mass motion of a cold atomic cloud and second, by observing the angular deflection of a rotationally asymmetrical cloud when released from a magneto-optical trap. The introduction of synthetic magnetism into the system of cold thermal atoms makes it an excellent candidate to emulate numerous complex classical systems, for example a tokamak fusion reactor or a star.

In the second part of the thesis, the possibility of laser cooling with a frequency comb (FC) is explored. For this purpose a scheme for full stabilization of a fiber based FC that does not require traditional self-referencing is developed and implemented; the repetition frequency is locked to a stable microwave reference while the offset frequency is indirectly stabilized by referencing the frequency comb to a continuous wave laser that is stabilized by polarization spectroscopy in rubidium vapor. The FC stabilized in this way is used to cool rubidium atoms on a dipole-allowed transition at 780 nm to sub-Doppler temperatures. Temperatures as low as $55 \mu\text{K}$ were measured in a one-dimensional FC cooling geometry using the time-of-flight method. Laser cooling with FCs could enable achieving sub-Doppler temperatures for atoms with dipole-allowed transitions in the vacuum ultraviolet. This can significantly improve the precision of optical frequency standards, enable measurements of fundamental constants with unprecedented accuracy, and open up the possibility to reach quantum degeneracy with atoms that have optical transitions unreachable by continuous wave lasers such as hydrogen, deuterium and antihydrogen.

Expanded abstract in Croatian

Prošireni sažetak na hrvatskome jeziku

U ovom doktorskom radu predstavljani su rezultati istraživanja dvije različite tematike u području hladnih atoma. Ove dvije tematike su povezane činjenicom da se u obje koriste laserski inducirane sile uzrokovane prijenosom impulsa s fotona na atome. U oba slučaja laserski inducirane sile mijenjaju brzinsku raspodjelu atomskog ansambla.

Rezultati predstavljeni u ovom radu su dobiveni radom u Laboratoriju za hladne atome na Institutu za fiziku u Zagrebu pod mentorstvom Ticijane Ban. Prve dvije i pol godine mojeg poslijediplomskoga studija istraživanja na kojima sam radio su bila dio projekta *Pseudo-magnetic forces and fields for atoms and photons* čiji voditelj je bio prof. Hrvoje Buljan s Fizičkog odsjeka Prirodoslovno-matematičkog fakulteta u Zagrebu. Preostalo vrijeme sam radio na projektu *Frequency-Comb-induced OptoMechanics* koji je u tijeku u trenutku pisanja ove radnje i čiji je voditelj Ticijana Ban sa Instituta za fiziku u Zagrebu. Spomenute dvije tematike istraživanja su se vezale na ova dva projekta.

Ovaj rad je organiziran na sljedeći način.

U uvodu, poglavlje 1, dan je kratki povijesni pregled istraživanja hladnih atoma i posljednjih dostignuća u području.

U poglavlju 2 se nalazi teorijski pregled interakcije lasera i atoma što je temelj za obje prethodno spomenute tematike. Sličan pregled se može naći u literaturi [1], u ovom radu je uključen zbog cjelovitosti rada.

Dva različita eksperimentalna postava, magneto-optičke stupice, su izrađena tokom izrade ovog rada. U poglavlju 3 je izložen njihov dizajn te su objašnjene specifičnosti oba postava.

U poglavlju 4 predstavljen je novi način implementacije sintetičke Lorentzove sile za hladni atomski plin. Ova sintetička Lorentzova sila se temelji na tlaku zračenja i Dopplerovom efektu, što ju čini jednostavnom za implementaciju u velikom volumenu, za veliki raspon brzina te se može primijeniti na različite geometrije. Sila je okomita na brzinu atoma te iznosi nula za atome koji miruju. Sintetičku Lorentzovu silu demonstriramo na dva načina: prvo, promatramo gibanje centra mase oblaka hladnih atoma i drugo, promatramo za koliki kut se rotacijski nesimetričan oblak otklonio od početnog položaja pri ispuštanju iz magneto-optičke stupice. Uvođenjem sin-

tetičkoga magnetizma u sistem hladnih termalnih atoma ovaj sistem postaje odličan kandidat za emulaciju brojnih kompleksnih klasičnih sistema, na primjer tokamak fuzijskog reaktora ili zvijezda.

U poglavlju 5 istraživana je mogućnost laserskog hlađenja frekventnim češljem. U tu svrhu bilo je potrebno osmisliti i implementirati tehniku za potpunu stabilizaciju frekventnog češlja koji se temeljeni na optičkim vlaknima, i to na način koji ne koristi uobičajeno samo-referenciranje; frekvencija repeticije je stabilizirana pomoću vrlo stabilne mikrovalne reference, dok je frekvencija odmaka indirektno stabilizirana referenciranjem frekventnog češlja pomoću kontinuiranog lasera koji je pak stabiliziran pomoću polarizacijske spektroskopije u rubidijevim parama. Frekventni češalj stabiliziran na ovaj način je korišten za hlađenje atoma rubidija na dipol dozvoljenom prijelazu na 780 nm do sub-Dopplerovskih temperatura. Izmjerene su temperature do $55 \mu\text{K}$ prilikom hlađenja u jednoj dimenziji pomoću tehnike vremena proleta. Ovime je pokazano da bi se lasersko hlađenje frekventnim češljem može koristiti za postizanje sub-Dopplerovskih temperatura s atomima koji imaju dipol dozvoljene prijelaze u vakuum ultraljubičastom području. Ovo bi značajno unaprijedilo preciznost optičkih frekventnih standarda, omogućilo bi mjerenje fundamentalnih konstanti s do sad ne postignutom preciznošću te bi se omogućilo dobivanje kvantno degeneriranih uzoraka atoma koji imaju optičke prijelaze u spektralnim područjima koja nisu pokrivena s kontinuiranim laserima, kao što su na primjer vodik, deuterij i antivodik.

1 Introduction

The work presented in this thesis was done in the Cold atoms lab at the Institute of Physics in Zagreb under the supervision of Ticijana Ban. For the first two and a half years of my doctoral studies my research was a part of the project *Pseudo-magnetic forces and fields for atoms and photons* whose PI was prof. Hrvoje Buljan from the Department of Physics, Faculty of Science at the University of Zagreb. The remaining time I was a part of the project *Frequency-Comb-induced OptoMechanics* which is ongoing at the time of writing this thesis, and whose PI is Ticijana Ban from the Institute of Physics in Zagreb. As mentioned in the abstract, two topics were explored during my studies and these were defined by the two projects mentioned above.

The thesis is organized as follows. Described in the introduction is some historical background and the current state of the art along with possible outlooks. Laser-atom interactions and laser cooling are the underpinning of both of these topics and the theory behind them will be briefly presented in chapter 2 for completeness. Two different rubidium magneto-optical traps (MOTs) were built during my studies and their specifics and design will be presented in chapter 3. Presented in chapter 4 are experimental results concerning our implementation of a synthetic Lorentz force along with a theoretical description. In chapter 5 results regarding frequency comb laser cooling are presented. Finally, we end with the [conclusion](#).

1.1 Cold atoms

Since its emergence in the 1980s laser cooling and trapping has revolutionized atomic physics and opened up new avenues of research such as quantum sensors based on atom interferometry, atomic clocks with unprecedented stability, ultracold chemistry, quantum many body simulation. Pioneers of the field, W. D. Phillips, C. Cohen-Tannoudji and S. Chu, won the Nobel prize in 1997 [2]. The prevalent implementation for cooling and trapping of neutral atoms, the MOT, became a common experiment in laboratories worldwide.

Further cooling techniques allowed cooling below the single photon recoil limit [3] and eventually low enough to reach quantum degeneracy, which in the case of bosons produces a Bose-Einstein condensate (BEC). This discovery earned C. Wieman,

W. Ketterle, E. A. Cornell the Nobel prize in 2001 [4], only 6 years after the original discoveries for which it was awarded were made, evidence to its immediate impact and importance.

Cold atom experiments provide a very controllable physical system. This is due to the atoms being confined and suspended in ultra-high vacuum, the lack of collisions due to the low temperature and the absence of forces acting on the atoms besides gravity and laser-induced ones. Additionally, these laser-induced forces provide the means to generate almost arbitrary potentials in real and velocity space. Furthermore, the dipole-dipole interaction between atoms can be modified by use of Feshbach resonances [5], and finally there is the choice of statistics by using either bosons or fermions. Due to this ease of control over experimental parameters cold atoms are used to explore problems that are found in areas of physics that do not offer this kind of flexibility, such as solid state systems, by mimicking potentials and interactions found in these systems. When used in this way, experiments with quantum degenerate gases are called quantum simulators or emulators [6]. Similarly, thermal atoms that scatter and rescatter photons can mimic systems of charged particles such as plasma.

1.2 Synthetic magnetism in cold atomic gases

In recent years there has been a lot of interest to introduce synthetic magnetism into cold atom systems by using specially tailored laser fields motivated by the quest to create a fully controllable quantum emulator. The ability to mimic and simulate other physical systems is improved by the addition of a synthetic magnetic field, where the neutral atoms in this synthetic magnetic field mimic charged particles in a real magnetic field.

In this thesis we explore a scheme to introduce synthetic magnetism into a system of thermal cold atoms based on the Doppler effect and radiation pressure. We prepare our samples of cold atoms in a MOT, far from quantum degeneracy. Since the atoms are classical particles we call the introduced synthetic magnetic field the synthetic Lorentz force.

Very soon after the first samples of BECs were obtained, the first implementation of synthetic magnetism was employed in which the condensate was made to rapidly rotate [7]. The Coriolis force plays the role of the (synthetic) magnetic field in these systems due to its analogy between it and the Lorentz force. These experiments led to the observation of quantized vortexes, similar in nature to vortexes in superconductors. However, this mechanism is limited to rotationally symmetrical systems. A review of research regarding rotating gases can be found in [8].

To overcome this symmetry restriction, methods based on laser-atom interaction have been developed and studied vehemently in recent years. These methods are

based on the analogy between the Aharonov-Bohm phase that a charged particle accumulates as it moves in a magnetic field and a geometric phase called the Berry phase that an atom accumulates as it moves in a specially tailored light field. The first implementation [9] was in bulk BECs utilizing spatially dependent Raman coupling between hyperfine states. In optical lattices the mechanisms are based on engineering the complex tunneling matrix elements between lattice sites. These include shaking the optical potential in a rotating fashion and laser assisted tunneling in lattices either tilted or non-tilted producing homogeneous or staggered fields, respectively. Experiments using these mechanisms have enabled the realization of the Hall effect [10], famous Hamiltonians found in solid state systems [11, 12], various topological effects [13] and realization of Dirac monopoles [14]. For recent reviews see [6, 15, 16].

1.2.1 Synthetic magnetism by using radiation pressure

Understandably, all of the mentioned mechanisms avoid spontaneous emission since it causes heating due to the random nature of the recoil momentum; heating is detrimental to the phase coherence of the atoms in question. This is part of the reason radiation pressure was not explored as a means to realize synthetic magnetism. However, when working with cold, but still thermal atoms that are comparatively hot to BECs, some additional heating is not a big problem. At the same time there are many physical systems that are analogous with atoms in a MOT thereby motivating us to explore synthetic magnetism for these, still classical, cold atoms.

Using radiation pressure in dense atomic gases is necessarily accompanied by radiation trapping. This effect arises because of the high probability of a scattered photon being re-absorbed in the dense cloud. The spontaneously emitted photon transfers momentum because of recoil to the initial atom scatterer in the opposite direction it was emitted in, and when re-absorbed again transfers momentum to the second atom, but now in the same direction it was emitted in. One can see that this will lead to a repulsive force between the atoms. The re-absorption probability is given by the ratio of the effective size of the atom and the total surface of the imaginary sphere the second atom is positioned on. This ratio, and thus the force, scales as $1/r^2$ which gives a force that is analogous to the Coulomb force between same species charges (since it is repulsive). Consequently, we can attribute to the atoms an effective, synthetic charge, whose value can be tuned by varying the intensity or the detuning of the scattered radiation. This gives the possibility of exploring regimes that are not accessible in electrodynamics with real charges, such as the realization of a time dependent charge [17].

The analogy between charges and atoms in a MOT has been studied very early after the realization of the MOT [18, 19], partly due to fact that radiation trapping sets a limit to the maximum obtainable density in a MOT. Additionally, a host of plasma-

like phenomena have been observed or predicted to occur in a cloud of trapped atoms, from a Coulomb-like explosion of expanding molasses [20] to plasma acoustic waves and photon bubbles [21, 22, 23]. A trapped cold cloud in a MOT also shows analogous behavior to stars, where gravity is replaced by the trapping potential and the internal pressure is replaced by radiation trapping. This analogy was demonstrated by showing that large trapped clouds exhibit self-sustained oscillations similar to those observed in stars [24]. Additionally, equations of equilibrium governing the atomic distribution in a dense atomic cloud have been shown to be similar to the equation of hydrostatic equilibrium in stars, the Lane-Emden equation, experimentally demonstrated in [25].

Considering this analogy between dense cold atomic clouds in a MOT and plasma it is intriguing to explore the possibility of using a system of cold atoms as an emulator of complex classical system, such as confined plasma, e.g. in a tokamak fusion reactor, or stars and hydrodynamic phenomena inside them. Since these systems constitute of charged particles magnetism plays a critical role. It would then be useful to further the analogy with these systems by introducing magnetism into the system of cold atoms in a MOT. Since the atoms are neutral, this magnetism needs to be synthetic. It could be assumed that introducing synthetic magnetism to these systems would enable research of new physical phenomena and open up new avenues of research, similar to what synthetic magnetism brought to the field of quantum simulators/emulators with quantum degenerate atomic gases.

Presented in this thesis is the work on a scheme to introduce synthetic magnetism into a system of cold atoms, prepared in a MOT. The scheme is based on the radiation pressure force and the Doppler effect. Since our scheme is based on radiation pressure, and radiation pressure is necessarily accompanied by spontaneous emission, it is not applicable to quantum degenerate gases. As stated before, this is not a problem for atoms prepared in a MOT. On the other hand, spontaneous emission in dense cloud leads to radiation trapping and the emergence of the repulsive Coulomb-like force. This means that using our scheme we introduce synthetic magnetism *and* a effective (synthetic) charge. Therefore, we can conclude that our scheme presents an extension of the ability of a cold atom system to emulate complex classical systems.

This research has been done by a collaboration of the theory (PI H. Buljan) and experimental (PI T. Ban) groups based in Zagreb. We proposed and theoretically analyzed the scheme in [26] and experimentally realized it in [27]. This was the first realization of synthetic magnetism that does not involve ultracold quantum degenerate gases. Finally, we used the scheme to observe an effect on a freely expanding cold atom cloud [28].

1.3 Frequency comb cooling

Regardless of the great importance laser cooling and trapping has today, laser cooling techniques are still limited to atoms with simple energy level structure and closed transitions [1] accessible by current continuous wave (CW) laser technology. The periodic table of elements with the elements that have been laser cooled marked in blue is presented in Fig. 1.1. Laser cooling of more complex atomic species and molecules, or even simple atoms with strong cycling transitions in the vacuum ultraviolet (VUV) where generation of CW laser light is demanding, most notably hydrogen and antihydrogen, still remains an experimental challenge.

1 H Hydrogen 1.008																	2 He Helium 4.003	
3 Li Lithium 6.94	4 Be Beryllium 9.012											5 B Boron 10.81	6 C Carbon 12.011	7 N Nitrogen 14.007	8 O Oxygen 15.999	9 F Fluorine 18.998	10 Ne Neon 20.180	
11 Na Sodium 22.990	12 Mg Magnesium 24.305											13 Al Aluminum 26.982	14 Si Silicon 28.085	15 P Phosphorus 30.974	16 S Sulfur 32.06	17 Cl Chlorine 35.45	18 Ar Argon 39.948	
19 K Potassium 39.098	20 Ca Calcium 40.078	21 Sc Scandium 44.956	22 Ti Titanium 47.867	23 V Vanadium 50.942	24 Cr Chromium 51.996	25 Mn Manganese 54.938	26 Fe Iron 55.845	27 Co Cobalt 58.933	28 Ni Nickel 58.693	29 Cu Copper 63.546	30 Zn Zinc 65.38	31 Ga Gallium 69.723	32 Ge Germanium 72.630	33 As Arsenic 74.922	34 Se Selenium 78.97	35 Br Bromine 79.904	36 Kr Krypton 83.798	
37 Rb Rubidium 85.468	38 Sr Strontium 87.62	39 Y Yttrium 88.906	40 Zr Zirconium 91.224	41 Nb Niobium 92.906	42 Mo Molybdenum 95.95	43 Tc Technetium [97]	44 Ru Ruthenium 101.07	45 Rh Rhodium 102.906	46 Pd Palladium 106.42	47 Ag Silver 107.868	48 Cd Cadmium 112.414	49 In Indium 114.818	50 Sn Tin 118.710	51 Sb Antimony 121.760	52 Te Tellurium 127.60	53 I Iodine 126.904	54 Xe Xenon 131.293	
55 Cs Cesium 132.905	56 Ba Barium 137.327	* 57 - 70	71 Lu Lutetium 174.967	72 Hf Hafnium 178.49	73 Ta Tantalum 180.948	74 W Tungsten 183.84	75 Re Rhenium 186.207	76 Os Osmium 190.23	77 Ir Iridium 192.227	78 Pt Platinum 195.084	79 Au Gold 196.967	80 Hg Mercury 200.592	81 Tl Thallium 204.38	82 Pb Lead 207.2	83 Bi Bismuth 208.980	84 Po Polonium [209]	85 At Astatine [210]	86 Rn Radon [222]
87 Fr Francium [223]	88 Ra Radium [226]	* 89 - 102	103 Lr Lawrencium [262]	104 Rf Rutherfordium [267]	105 Db Dubnium [270]	106 Sg Seaborgium [269]	107 Bh Bohrium [270]	108 Hs Hassium [270]	109 Mt Meitnerium [278]	110 Ds Darmstadtium [281]	111 Rg Roentgenium [281]	112 Cn Copernicium [285]	113 Nh Nihonium [286]	114 Fl Flerovium [289]	115 Mc Moscovium [289]	116 Lv Livermorium [293]	117 Ts Tennessine [293]	118 Og Oganesson [294]
*Lanthanide series		57 La Lanthanum 138.905	58 Ce Cerium 140.116	59 Pr Praseodymium 140.908	60 Nd Neodymium 144.242	61 Pm Promethium [145]	62 Sm Samarium 150.36	63 Eu Europium 151.964	64 Gd Gadolinium 157.25	65 Tb Terbium 158.925	66 Dy Dysprosium 162.500	67 Ho Holmium 164.930	68 Er Erbium 167.259	69 Tm Thulium 168.934	70 Yb Ytterbium 173.045			
**Actinide series		89 Ac Actinium [227]	90 Th Thorium 232.038	91 Pa Protactinium 231.036	92 U Uranium 238.029	93 Np Neptunium [237]	94 Pu Plutonium [244]	95 Am Americium [243]	96 Cm Curium [247]	97 Bk Berkelium [247]	98 Cf Californium [251]	99 Es Einsteinium [252]	100 Fm Fermium [257]	101 Md Mendelevium [258]	102 No Nobelium [259]			

Figure 1.1: Periodic table of elements with the elements that have been laser cooled marked in blue.

Due to the relative ease by which pulsed sources can produce higher harmonics that stretch to the UV and further, cooling with pulses has been explored very early on in the history of laser cooling [29, 30, 31]. However, short optical pulses necessarily have large bandwidth (a wide spectrum), meaning that when interacting with narrow atomic resonances or narrow velocity distributions, most of the power will be wasted or misplaced and the standard Doppler cooling scheme will be impossible to implement.

The aforementioned problems can be approached by using mode-locked femtosecond or picosecond lasers with high pulse repetition rates which produce stabilized optical frequency combs (FCs). Employing the highly precise and regular comb spectrum has been proposed for laser cooling of complex multilevel atoms and molecules

in an approach that essentially mimics the use of multiple phase-coherent CW lasers [32]. Following the same approach, simultaneous cooling of multiple atomic species by FC is proposed in [33]. FC cooling on the Rb two-photon transition at 778 nm has been demonstrated recently [34], where cooling is achieved through a coherent process in which multiple excitation pathways are excited by different combinations of comb modes.

Furthermore, as pulsed sources, FCs provide high peak powers needed for efficient frequency conversion via nonlinear crystals [35] or high harmonic generation in gas jets [36, 37], while simultaneously preserving long coherence times needed for efficient laser cooling. These benefits have recently been employed to open a new and promising route towards laser cooling of species with strong cycling transitions in the UV and VUV such as trapped magnesium ions that was demonstrated in [38].

The use of FCs has revolutionized high-resolution spectroscopy, where FC-based spectrometers of unprecedented accuracy, resolution and sensitivity now operate from the EUV [39] to the mid-IR [40] spectral range. A similar impact on the field of quantum optics can be envisaged as well, where the use of FCs for laser cooling could lead to significant advances in research focused toward quantum technologies such as optical clocks, quantum simulators, and quantum networks. Intriguing applications of FC cooling include:

- laser cooling of atoms with dipole allowed transitions in the VUV, e.g. hydrogen, deuterium and antihydrogen atoms for precision measurements of the Rydberg constant and the deuterium nuclear radius, as well as for testing charge, parity and time reversal symmetry and probing physics beyond the standard model [32]. Reaching quantum degeneracy with these light atoms would also be of interest for experiments in many body physics.
- optical atomic clocks, e.g. realization of FC cooling of trapped Al and He ions in the VUV [38].
- producing cold samples of most prevalent atoms in organic chemistry, e.g. hydrogen, carbon, oxygen and nitrogen to improve understanding of their long-range interactions and chemical bonding [32, 34].

For all the aforementioned FC cooling applications it is important to maximize the scattering rate to reduce cooling times and also reach temperatures as low as possible.

In this thesis results demonstrating sub-Doppler FC cooling of rubidium atoms are presented. We demonstrate sub-Doppler cooling of Rb atoms to 55 μK on a single-photon transition at 780 nm, a transition typically used in CW laser cooling experiments with an associated Doppler temperature of 146 μK . For experiments in FC cool-

ing one first needs a stabilized FC, this is somewhat technically challenging. We stabilized our FC in a atypical way, our scheme is also presented in this thesis.

2 Laser induced forces and the magneto-optical trap

This chapter will cover the theoretical treatment of phenomena that are relevant for the results presented in later chapters. This includes the basic quantum mechanical treatment of laser-atom interaction, principles of Doppler cooling and the mechanism that enable the working of the MOT. These topics are covered in more detail in several books, the best known being "Laser Cooling and Trapping" by H. J. Metcalf and P. van der Straten [1]. This chapter borrows from it and other sources [41]. Since the purpose of this chapter is to provide context things will be kept short and concise.

2.1 The two-level atom

We will first look at the two-level model and its interaction with an electric field of a laser. The two-level model is an approximation that holds in an monochromatic field and when the detuning, given by $\delta = \omega_L - \omega_0$, satisfies $|\delta| \ll \omega_0, \omega_L, |\omega_i - \omega_L|$ where ω_i are transition frequencies associated with all other levels. Although the schemes studied in this thesis often include light from two lasers, hence a bichromatic field, or even multifrequency light, it is nevertheless instructive to study the two-level model. The two levels are the ground state and the excited state.

The atom wave function satisfies the time dependent Schrödinger equation

$$\hat{H}\Psi(\mathbf{r}, t) = i\hbar\frac{\partial\Psi(\mathbf{r}, t)}{\partial t}. \quad (2.1)$$

The solution of $\Psi(\mathbf{r}, t)$ can be expanded in terms of the eigenfunctions $\phi_n(\mathbf{r})$ of the field-free Hamiltonian, \hat{H}_0

$$\psi(\mathbf{r}, t) = \sum_k c_k(t)\phi_n(\mathbf{r})e^{i\omega_{jk}t}. \quad (2.2)$$

We introduce laser radiation as an classical electromagnetic field, the total Hamiltonian is thus $\hat{H}(t) = \hat{H}_0 + \hat{H}'(t)$. From the Schrödinger equation after some manipulation we

find

$$i\hbar \frac{dc_j(t)}{dt} = \sum_k c_k(t) \hat{H}'_{jk}(t) e^{i\omega_{jk}t}, \quad (2.3)$$

where $H'_{jk}(t) = \langle \phi_j | H'(t) | \phi_k \rangle$ and $\omega_{jk} = \omega_j - \omega_k$. Here is where the two-level approximation comes in: if the conditions stated above are fulfilled then there will only be one nonzero off-diagonal element, $\hat{H}'_{ge}(t) = \hat{H}'_{eg}^*(t)$, where g and e denote the ground and the excited state, respectively. The Hamiltonian is evaluated to be

$$\hat{H}'(t) = -e\mathbf{E}(\mathbf{r}, t) \cdot \mathbf{r}. \quad (2.4)$$

By taking in the electric field operator for a traveling plane wave in the z direction $\mathbf{E}(\mathbf{r}, t) = E_0 \hat{\mathbf{e}} \cos(kz - \omega_l t)$, we find $\hat{H}'_{eg}(t) = \hbar\Omega \cos(kz - \omega_l t)$, where Ω is the Rabi frequency given by

$$\Omega = -\frac{eE_0}{\hbar} \langle e | r | g \rangle. \quad (2.5)$$

Here the dipole approximation was made, where we neglected the spatial variation of the electromagnetic field. This is justified due to the wavelength being large compared the atom size, $\lambda \gg r$. This means we only consider the *time* variation of the field. Introducing the Hamiltonian, $\hat{H}'_{ge}(t)$, to equation 2.3 we get two oscillating terms, one that oscillates with the laser detuning frequency $\delta = \omega_{ge} - \omega_l$ and the other that oscillates with the sum frequency, $\omega_{ge} + \omega_l$. Here we introduce another approximation, the rotating wave approximation (RWA), where we neglect the rapidly rotating terms and consider only the slowly rotating ones. This approximation is not appropriate for far-detuned fields, however we will not encounter this in this thesis.

After these approximations from equation 2.3 we find

$$\frac{dc_g}{dt} = -\frac{i}{2} c_e \Omega^* e^{i\delta t}, \quad (2.6a)$$

$$\frac{dc_e}{dt} = -\frac{i}{2} c_g \Omega e^{-i\delta t}. \quad (2.6b)$$

2.1.1 The optical Bloch equations

At this point we introduce the density matrix, $\rho = |\Psi\rangle \langle\Psi|$ whose elements are

$$\rho_{ij} = \langle \phi_i | \rho | \phi_j \rangle = \langle \phi_i | |\Psi\rangle \langle\Psi| | \phi_j \rangle = c_i c_j^*. \quad (2.7)$$

The density matrix approach is useful for numerical modeling of atom systems because it enables the incorporation of decoherence, by spontaneous emission for instance, and therefore the description of not just pure states, for which $\rho_{ij}\rho_{ji} = \rho_{ii}\rho_{jj}$, but also mixed states.

The density matrix also enables us to easily calculate the expectation value of arbi-

trary quantum mechanical operators:

$$\begin{aligned}\langle \hat{A} \rangle &= \langle \Psi | \hat{A} | \Psi \rangle = \left\langle \sum_i c_i \phi_i \left| \hat{A} \right| \sum_j c_j \phi_j \right\rangle = \sum_{i,j} c_i^* c_j \langle \phi_i | \hat{A} | \phi_j \rangle \\ &= \sum_{i,j} \rho_{j,i} \hat{A}_{i,j} = \sum_j (\rho \hat{A})_{jj} = \text{Tr}(\rho \hat{A})\end{aligned}\quad (2.8)$$

For our two-level model the density matrix will be a 2×2 matrix (easily extended to a $n \times n$ matrix for an n level atom) written as

$$\rho = \begin{pmatrix} \rho_{ee} & \rho_{eg} \\ \rho_{ge} & \rho_{gg} \end{pmatrix} = \begin{pmatrix} c_e c_e^* & c_e c_g^* \\ c_g c_e^* & c_g c_g^* \end{pmatrix}.\quad (2.9)$$

From equations 2.6 we find, for instance for ρ_{gg}

$$\frac{d\rho_{gg}}{dt} = \frac{dc_g}{dt} c_g^* + c_g \frac{dc_g^*}{dt} = i \frac{\Omega^*}{2} \rho_{eg} e^{i\delta t} - i \frac{\Omega}{2} \rho_{ge} e^{-i\delta t}.\quad (2.10)$$

Similarly, one can find equations for the other elements of the density matrix. It is also necessary to include spontaneous emission which is described by an additional term that introduces an exponential decay of the coherence, $(d\rho_{eg}/dt)_{spontaneous} = -(\Gamma/2)\rho_{eg}$. The ground and excited state populations also change due to spontaneous emission, namely the populations increases and decrease, respectively. The resulting equations are called the optical Bloch equations (OBE)¹:

$$\begin{aligned}\frac{d\rho_{gg}}{dt} &= +\Gamma \rho_{ee} + \frac{i}{2} (\Omega^* \tilde{\rho}_{eg} - \Omega \tilde{\rho}_{ge}) \\ \frac{d\rho_{ee}}{dt} &= -\Gamma \rho_{ee} + \frac{i}{2} (\Omega \tilde{\rho}_{ge} - \Omega^* \tilde{\rho}_{eg}) \\ \frac{d\tilde{\rho}_{ge}}{dt} &= -\left(\frac{\Gamma}{2} + i\delta\right) \tilde{\rho}_{ge} + \frac{i}{2} \Omega^* (\rho_{ee} - \rho_{gg}) \\ \frac{d\tilde{\rho}_{eg}}{dt} &= -\left(\frac{\Gamma}{2} - i\delta\right) \tilde{\rho}_{eg} + \frac{i}{2} \Omega^* (\rho_{gg} - \rho_{ee}).\end{aligned}\quad (2.11)$$

where $\tilde{\rho}_{ij} = \rho_{ij} e^{i\omega_{ij}t}$.

We can now look at the steady state solution of the OBE by setting time derivatives to zero and using the fact that the population is conserved, that is $\rho_{gg} + \rho_{ee} = 1$, and that $\rho_{eg} = \rho_{ge}^*$, we can solve for ρ_{ee} and ρ_{gg} :

$$\rho_{ee} = \frac{s}{2(1+s)} = \frac{s_0/2}{1+s_0+4(\delta/\Gamma)^2},\quad (2.12)$$

¹the number of equations for an n level atom will be n^2

and

$$\rho_{eg} = \frac{i\Omega}{2(\Gamma/2 - i\delta)(1 + s)}, \quad (2.13)$$

where s is the saturation parameter given by

$$s = \frac{s_0}{1 + 4(\delta/\Gamma)^2}, \quad (2.14)$$

and s_0 is the on-resonance saturation parameter

$$s_0 = 2|\Omega|^2/\Gamma^2 = I/I_s, \quad (2.15)$$

where I is the laser intensity and I_s is the saturation intensity. One can see that if we scan the laser frequency and measure the excited state population, equation 2.12, we will obtain a Lorentzian curve² with a full width at half-maximum (FWHM) of Γ for small s_0 . The width of this line profile will increase with increasing s_0 , that is with increasing intensity, to $\Gamma_P = \Gamma\sqrt{1 + s_0}$. This is the well known power broadening mechanism. Note that when measuring a line profile it is necessary to take into account other line-broadening effects and especially the spectral width of the laser used. While line-broadening mechanism like Doppler broadening and collision broadening will be negligible in our cold atom system, the laser width will be important in later chapters.

2.1.2 The light force

We can calculate the force acting on our two-level atom. The force is defined as the expectation value of its quantum mechanical operator:

$$\mathbf{F} = \langle \hat{F} \rangle = \frac{d}{dt} \langle \hat{p} \rangle = \frac{i}{\hbar} \langle [\hat{H}, \hat{p}] \rangle = -\langle \nabla \hat{H} \rangle. \quad (2.16)$$

The final expression is an example of the Ehrenfest theorem and is the quantum mechanical analogue of the classical expression $\mathbf{F} = -\nabla U$. We now introduce the Hamiltonian, where the only relevant part is \hat{H}' given by equation 2.4, and use the dipole approximation to interchange the gradient with the expectation value:

$$\mathbf{F} = e \langle \nabla (\mathbf{E}(\mathbf{r}, t) \cdot \mathbf{r}) \rangle = e \nabla \langle (\mathbf{E}(\mathbf{r}, t) \cdot \mathbf{r}) \rangle. \quad (2.17)$$

Using the definition of the Rabi frequency, equation 2.5, and the last expression from equation 2.11 to calculate the expectation value we find

$$\mathbf{F} = \hbar (\nabla \Omega \rho_{eg}^* + \nabla \Omega^* \rho_{eg}). \quad (2.18)$$

² ρ_{ee} will later be shown to be proportional to the force in some cases, see Fig. 2.1

Then, by evaluating the gradient we find

$$\mathbf{F} = \hbar \frac{\nabla \Omega}{\Omega} (\Omega \rho_{eg}^* + \Omega^* \rho_{eg}) + i \hbar \nabla \phi (\Omega \rho_{eg}^* - \Omega^* \rho_{eg}). \quad (2.19)$$

The obtained expression is a general one, and can be used to find the force in any situation. Also note that the first term is proportional to the real part of the coherence, while the second one is proportional to the imaginary part of the coherence. To find the force on a two level atom we use the solution for ρ_{eg} given by equation 2.13, finding

$$\mathbf{F} = -\frac{\hbar s}{1+s} \left(\delta \frac{\nabla \Omega}{\Omega} + \frac{\Gamma}{2} \nabla \phi \right). \quad (2.20)$$

The first term in equation 2.20 is proportional to the detuning and the gradient of the *amplitude*, and will give rise to a conservative force called the dipole force. Note that for a plane wave this force will be zero. The second term is proportional to the scattering rate and to the gradient of the *phase* and will give rise to a dissipative force called radiation pressure. In this thesis the laser fields used all have small detunings and can be approximated with a plane wave. This means that the radiation pressure force will be orders of magnitude greater than the dipole force, because of this we will not take it into account while analyzing the dynamics of atoms in later chapters.

2.1.3 Radiation pressure force

From equation 2.20 the radiation pressure force, which we label F_{pr} , is given by

$$\mathbf{F}_{pr} = -\frac{s}{1+s} \frac{\hbar \Gamma}{2} \nabla \phi. \quad (2.21)$$

For a plane wave the phase is given by $\phi = -\mathbf{k}_1 \cdot \mathbf{r}$, where \mathbf{k}_1 is the wave vector of the corresponding laser radiation. The gradient is therefore $\nabla \phi = -\mathbf{k}_1$. The force is then

$$\mathbf{F}_{pr} = \frac{s}{1+s} \frac{\hbar \Gamma}{2} \mathbf{k}_1 = \Gamma_{sp} \hbar \mathbf{k}_1, \quad (2.22)$$

where Γ_{sp} is the spontaneous scattering rate, also equal to the product of the natural linewidth and the excited state population, $\Gamma_{sp} = \Gamma \rho_{ee}$. We can see that the expression for the force takes on an intuitive form, the force is equal to the momentum of a single photon, $\hbar k$, multiplied by the rate at which the atom absorbs the photons, and is directed in the direction of propagation of the laser beam. Absorption is followed by spontaneous emission, which also causes photon recoil; however, for many cycles this averages out to zero due to the random propagation direction of the spontaneously emitted photon.

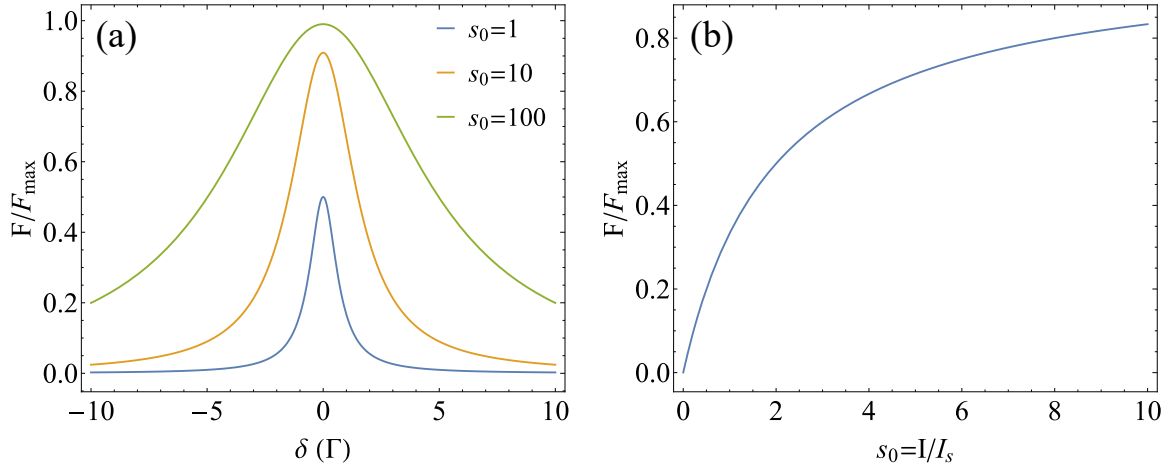


Figure 2.1: Radiation pressure force described by equation 2.23. The force is given in units of $F_{\max} = \hbar k \Gamma / 2$ which is the maximum value to which the force saturates for large intensities, $s_0 \gg 1$. In (a) dependence on detuning is shown for three different saturation parameters, in (b) dependence on intensity is shown for $\delta = -\Gamma/2$

Using equation 2.12, from equation 2.22 we find the force

$$F_{pr} = \frac{\hbar k \Gamma}{2} \frac{s_0/2}{1 + s_0 + 4(\delta/\Gamma)^2}, \quad (2.23)$$

and look at the dependence of the force on intensity and detuning, shown in Fig. 2.1(a) and (b), respectively. The force saturates at a value limited by the natural linewidth of the transition, $F_{\max} = \hbar k \Gamma / 2$. The wings of the Lorentzian shown in Fig. 2.1(a) saturate later than the center, leading to the well known effect of power broadening, where the observed linewidth increases to $\Gamma' = \Gamma \sqrt{1 + s_0}$.

2.2 Laser cooling

In this section we will look at how the radiation pressure force can be used to reduce the temperature of a atomic gas. It is important to note at this point that when talking about the "temperature" of a cold atom sample we are using it to describe the average kinetic energy of the atoms in one dimension

$$\frac{1}{2}k_bT = \langle E_k \rangle, \quad (2.24)$$

and not the "usual" thermodynamic temperature. That kind of description is not appropriate for a cold atom sample because it is not in thermal contact with a heat bath and also not in equilibrium.

2.2.1 Doppler cooling

First we will look at Doppler cooling, named such because it uses the Doppler shift to the laser frequency, $-\mathbf{k}_1\mathbf{v}$, where \mathbf{v} is the atomic velocity, to make the force velocity dependent. The first to suggest that atomic velocities could be manipulated with laser light was Ashkin in 1970 [42], while the Doppler cooling scheme was proposed by Hänsch and Schawlow in 1975 [43]. It was then first demonstrated on ions by Wineland and colleagues [44] and later on neutral atoms by Chu and colleagues [45].

For cooling in one dimension one needs two laser beams traveling in opposite directions. The laser light then needs to be red detuned in respect to the atomic resonance in order to achieve a force that is in an opposite direction to that of the atomic velocity. In that case the laser beam traveling in the opposite direction of the atomic velocity will be Doppler shifted toward the blue bringing it closer to resonance, at the same time the beam traveling in the same direction as the atom will be Doppler shifted toward the red taking it further away from resonance. This change in the effective detunings will mean that the atom preferably scatters photons from the beam that opposes its velocity thus leading to its reduction.

Shown in Fig. 2.2 is the radiation pressure force for a pair of beams with a detuning $\delta = -0.5\Gamma$. One can see that the total force is linear for small velocities and will thus lead to viscous damping, because of this the resulting effect is called "optical molasses". We find the force of the two beams by introducing the Doppler contribution to the detuning, from equation 2.23:

$$\mathbf{F}_{\pm} = \pm \frac{\hbar\mathbf{k}\Gamma}{2} \frac{s_0/2}{1 + s_0 + 4f[(\delta \mp \mathbf{k} \cdot \mathbf{v})/\Gamma]^2}. \quad (2.25)$$

The total force is then the sum of the contributions of the two counter-propagating

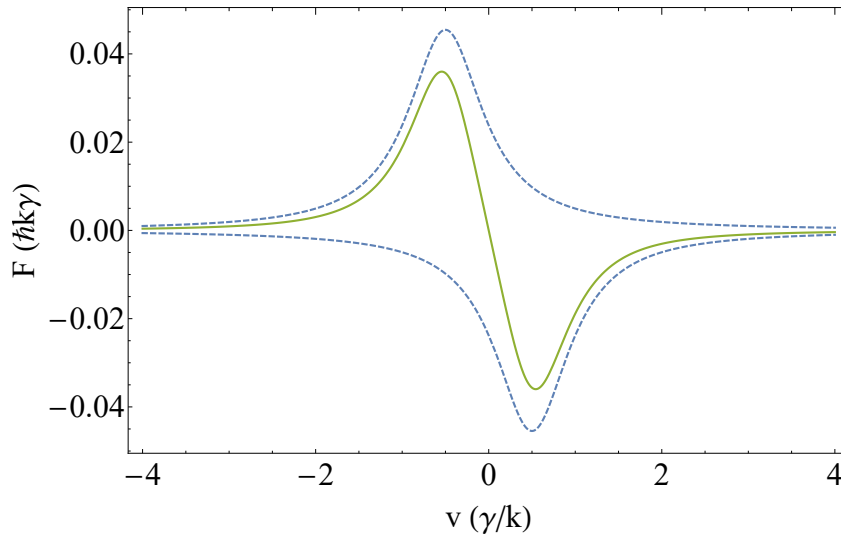


Figure 2.2: Force as a function of velocity for $s_0 = 0.1$ and $\delta = -0.5\Gamma$. The blue dashed lines are force contributions from each of the oppositely traveling beams, while the green curve is the total force.

beams

$$\mathbf{F}_{\text{OM}} = \mathbf{F}_+ + \mathbf{F}_- \cong \frac{8\hbar k^2 \delta s_0 \mathbf{v}}{\Gamma[1 + s_0 + 4(\delta/\Gamma)^2]^2} \equiv -\beta \mathbf{v}, \quad (2.26)$$

where we neglected terms of order $\propto v^4$ and higher, β is the damping rate. If this was the only influence on atomic motion the atom velocity would quickly be reduced to zero, along with the temperature. Of course, this will not happen due to heating caused by spontaneous emission i.e. the photon recoil imparted in a random direction with each cycle. Heating caused in this way will set a limit to the lowest achievable temperature by Doppler cooling, called accordingly, the Doppler temperature. One can find it by equating the heating and cooling rates, the maximum cooling rate is found for $\delta = \Gamma/2$, or by looking at diffusion in momentum space. One finds for the temperature:

$$k_B T_D = \frac{\hbar\Gamma}{2}. \quad (2.27)$$

We see that this temperature is a function of *solely* the linewidth of the transition used for cooling.

2.2.2 Sub-Doppler cooling

Soon after the first realization of optical molasses [45], where the authors measured temperatures similar to the (then) expected Doppler temperature, other groups began reproducing the result and measuring the temperature in a more precise way [46]. Temperatures lower than the Doppler temperature were measured, prompting a revisit of the theoretical description of the cooling process.

The different sub-Doppler cooling mechanisms all include population pumping be-

tween different ground-state magnetic sublevels while the atom is moving in a light field whose polarization is a function of position. Such a light field is for instance produced by two counter-propagating laser fields that have orthogonal polarizations and the resulting sub-Doppler mechanism is called polarization gradient cooling due to the spatially changing polarization. The first to describe this mechanism were Dalibard and Cohen-Tannoudji [47] for the simplest case, transition between a $J_g = 1/2$ to a $J_e = 3/2$. To look at the resulting polarization from the two fields we will look at the total field, given by

$$\begin{aligned} \mathbf{E} &= E_0 \hat{x} \cos(\omega_l t - kz) + E_0 \hat{y} \cos(\omega_l t + kz) \\ &= E_0 [(\hat{x} + \hat{y}) \cos(\omega_l t) \cos kz + (\hat{x} - \hat{y}) \sin(\omega_l t) \sin kz], \end{aligned} \quad (2.28)$$

which constitutes a constant polarization for a fixed z , for $z = 0$ the polarization is linear at an angle of $+\pi/4$ to the x-axis, for $z = \lambda/8$ the polarization is σ^- , for $z = \lambda/4$ it is again linearly polarized at an angle of $+\pi/4$, for $z = 3\lambda/8$ it is σ^- and so on, alternating from linearly polarized to circularly polarized, this is shown in Fig. 2.3. When the polarization is σ^- (σ^+) the whole population will be pumped to the $M_g = -1/2$ ($M_g = +1/2$) magnetic sublevel, the population fraction is schematically represented with the size of the black circles in Fig. 2.3.

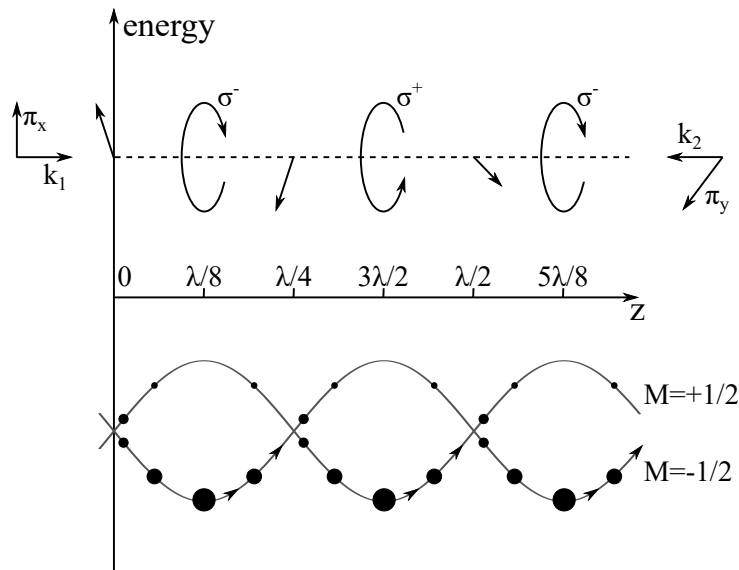


Figure 2.3: Polarization gradient cooling in the lin \perp lin case. The spatial dependence of the light shift is shown as is the polarization of the corresponding field, upper part of the image. The size of the black circles represents the population fraction in the two substates. We can see that the majority of the population will be in the substate with the lower energy due to optical pumping and that this population will have an upward climb toward the "node" of the potential where the populations are the same in the two sublevels. Adapted from [1, 47]

We also need to take into account the light shift (or the AC-Stark shift) caused by the electric field of the laser light. The light shifts the energy of the ground magnetic

substates by

$$\Delta E_g = \frac{\hbar \delta s_0 C_{ge}^2}{1 + (2\delta/\Gamma)^2}, \quad (2.29)$$

where C_{ge} are the corresponding Clebsch-Gordan coefficients that determine the coupling of the atom and the field, this depends on the polarization of the field. When the light is σ^- (σ^+) polarized the light shift will be three times larger for the $M_g = -1/2$ ($M_g = +1/2$) sublevel than that of the $M_g = 1/2$ ($M_g = -1/2$) sublevel, see Fig. 2.3.

We can now conclude on the origin of the damping force. It is a combined effect of the spatially dependent optical pumping and light shift. The majority of the population will always be optically pumped to the energetically lowest magnetic sublevel. This means that by moving through space the majority of the population is climbing uphill toward the "node" of the potential where the energy of the substates is the same. There the pumping process again shifts the population to the energetically lowest state meaning that the atoms will again be traveling uphill. Due to similarity, the Greek myth borrows its name to this cooling process also called "Sisyphus cooling".

Sub-Doppler cooling also works for the polarization configuration found in a MOT, with two counter-propagating beams being $\sigma^+ \sigma^-$ polarized. Here the total field is given by

$$\begin{aligned} \mathbf{E} &= E_0 [\hat{x} \cos(\omega t - kz) + \hat{y} \sin(\omega t - kz)] \\ &\quad + E_0 [\hat{x} \cos(\omega t + kz) - \hat{y} \sin(\omega t + kz)] \\ &= E_0 \cos \omega t [\hat{x} \cos kz + \hat{y} \sin kz], \end{aligned} \quad (2.30)$$

resulting in a field that is linearly polarized in all points in space, but the polarization vector rotates about the propagation axis for 2π over one wavelength. Here the light shift is constant in space so there is no "Sisyphus" effect, rather the cooling scheme relies on the quantization axis changing for an atom in motion. An atom with $J_g = 1$ and with zero velocity will have its population evenly distributed between the magnetic substates. On the other hand, an atom that is moving, for instance, toward the σ^+ beam will "see" the polarization as somewhat σ^+ circularly polarized and this will pump the population into the $M_g = +1$ state. Due to different Clebsch-Gordan coefficients this substate scatters σ^+ photons six times more efficiently than σ^- photons which will lead to a considerable damping force and consequently temperatures lower than the Doppler temperature.

Another sub-Doppler mechanism includes the presence of a magnetic field, and is termed magnetic-field-induced laser cooling, reported in [48]. Again, the force arises because of optical pumping between magnetic substates. Then, the magnetic field induces mixing of the magnetic substates in positions where they are degenerate. For a standing wave this happens at the nodes. This mechanism also enables sub-Doppler

cooling for polarization configurations that do not produce a polarization gradient, such as the $\sigma^+-\sigma^+$ and $\text{lin} \parallel \text{lin}$ polarization configurations, observed in [49]. Here, the magnetic-field-induces mixing of the magnetic substates at the nodes of the standing wave and the optical pumping in the anti-nodes again produce the familiar Sisyphus pattern for a moving atom.

2.3 The magneto-optical trap principle of operation

In the previous section we looked at laser cooling in one dimension with a pair of laser beams. Cooling in three dimensions is a simple extension of this scheme, requiring three pairs of beam, or six in total. However, even with six beams and atom velocities of ≈ 10 cm/s for typical alkali atoms, the atoms will diffuse from the beam intersection and will be lost. In order to really trap the atoms it is necessary to have a spatially dependent force, a restoring force that will force an atom from the edge of the trap to the center. The solution for this was found by adding a magnetic field along with the optical part of the trap, hence the name magneto-optical trap (MOT). First demonstrated in 1986 [50], the MOT is today a very common experiment with a wide range of applications.

2.3.1 Zeeman shift

By adding a magnetic field we introduce an interaction of the atom and the magnetic field, $\hat{V}_m = -\hat{\mathbf{J}} \cdot \mathbf{B}(\mathbf{r})$, where $\mathbf{J} = \mathbf{L} + \mathbf{S}$ is the total spin and $\mathbf{B}(\mathbf{r})$ is the strength of the magnetic field. This will result in the magnetic sublevel $|F, m_F\rangle$ being Zeeman shifted by $m_J g_J \mu_B B$, where g_J is the corresponding Landé factor and μ_B is the Bohr magneton.

We will consider a transition between $J = 0$ and $J' = 1$ for simplicity, but the same principles are easily extended to states with a larger number of magnetic substates. The transition frequency between $|J = 0, m = 0\rangle$ and $|J', m'\rangle$ will be Zeeman shifted to give $\omega_0 + m' g_J \mu_B B$. If we apply a linear magnetic gradient b' giving a magnetic field $B = b'x$ it will result in a detuning of the transition frequency from the driving frequency that is a function of the atoms position

$$\delta' = \delta - \frac{m' g_J \mu_B b' x}{\hbar}, \quad (2.31)$$

where $\delta = \omega_l - \omega_0$. This means that at positive x positions because of the increase of the frequency of the $\Delta M = +1$ transition the absolute value of the detuning will increase tuning it away from resonance. At the same time the frequency of the $\Delta M = -1$ transition will decrease, decreasing the detuning and thus tuning it closer to resonance. We can write for the transition frequency between $|J = 0, m = 0\rangle \rightarrow |J', m'\rangle$ as $\omega(m') = \omega_0 + m' \gamma' b' x$, where $\gamma' = g_J \mu_B / \hbar$ is the gyromagnetic ratio of the transition.

We want an atom that moves to positive x coordinates to preferentially absorb photons propagating in the $-x$ direction than those propagating in the $+x$ direction. The trick is to use a σ^- polarized beam propagating in the $-x$ direction and a σ^+ beam propagating in the $+x$ direction. The σ^- beam will drive only the $\Delta M = -1$ transition which is tuned closer to resonance for atoms at positive x positions, see right part of Fig. 2.4, while the σ^+ beam will drive only the $\Delta M = +1$ transition which is tuned

away from resonance at positive x positions. This means that our atom will preferably absorb photons from the σ^- polarized beam bringing it closer to the center of the trap at $x = 0$. Similarly, because of opposite Zeeman shifts atoms at negative x positions will preferably absorb photons from the σ^+ polarized beam, again forcing the atoms toward the center of the trap, see left part of Fig. 2.4.

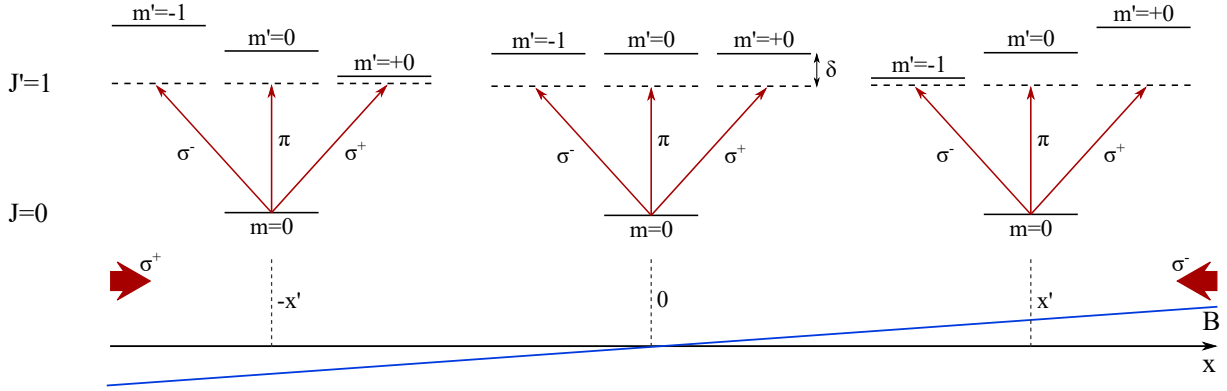


Figure 2.4: A schematic representation of the 1D MOT scheme for a $J = 0 \rightarrow J' = 1$ transition. Shown are positions of the magnetic sublevels for three different x coordinates and the associated laser beams that couple them. The position dependent detunings result in a position dependent force that forces the atoms toward the point in which $B = 0$, the center of the trap. Adapted from [1, 41]

A linear gradient for all three dimensions is achieved by using a quadrupole magnetic field, experimentally achieved by two coils that have the same current flowing through them but in opposite directions. Six beams are again required, with each pair having opposite circular polarizations chosen according to the sign of the magnetic field gradient.

2.3.2 Trapping force

We find the total force by again summing the contributions, given by equation 2.25, for the two counter-propagating beams. However, the detuning is now position dependent and is given, by

$$\delta_{pm} = \delta \mp \mathbf{k} \cdot \mathbf{v} \mp \gamma' b' x / \hbar, \quad (2.32)$$

Similar to 2.26, we can expand the force for small \mathbf{v} and small x that produce a small Doppler shift and a small Zeeman shift compared to δ . We find for the force in the x direction

$$F_x = -\beta v_x - \kappa x, \quad (2.33)$$

where β is the damping rate from equation 2.26, and where the spring constant κ is given by

$$\kappa = \frac{\gamma' b'}{\hbar k}. \quad (2.34)$$

Also worth noting is that since for three dimensional trapping we need a quadrupole magnetic field, the gradient in one dimension will unavoidably be twice as large as in the other two, due to $\nabla \cdot \mathbf{B} = 0$. Thus the force in three dimensions, if all trapping beams have the same intensity, will be in the form $\mathbf{F}(\mathbf{r}) = -\kappa x \hat{\mathbf{x}} - \kappa y \hat{\mathbf{y}} - 2\kappa z \hat{\mathbf{z}}$ where z will be the axis of the coils that produce the field. To obtain an isotropic spring constant one can reduce the power in the trapping beams that propagate along the direction of the highest field gradient, along z , by a factor of two.

We can see that the force, equation 2.33, is that of a damped harmonic oscillator. The solution for the motion of a damped oscillator is given by

$$x(t) = A \cos(\omega t + \phi) e^{-\frac{\Gamma}{2}t}, \quad (2.35)$$

where $\omega = \sqrt{\kappa/M}$ is the trap oscillation frequency and $\Gamma = \beta/M$ is the damping rate. In Fig. 2.5 we can see an example of such motion measured for a cold atom cloud dislocated from the center of the trap; one can see that the fit to the solution given by equation 2.35 is excellent. More details on these kind of measurements are given in later chapters.

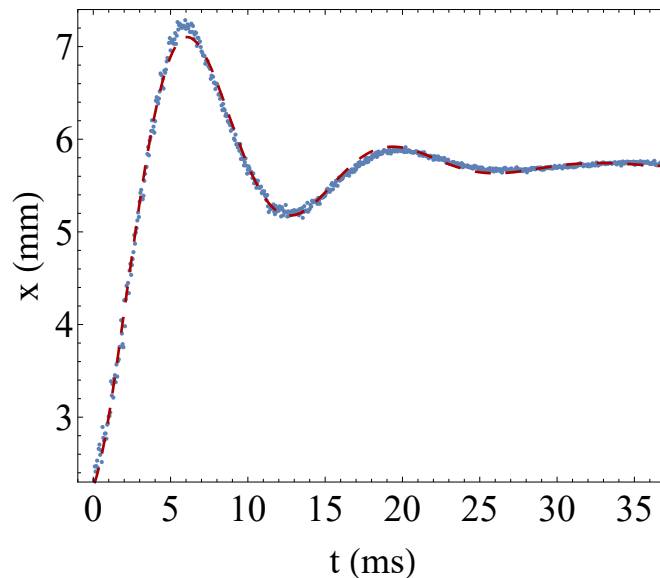


Figure 2.5: Damped oscillations of a cold atom cloud in a MOT after being displaced by a pushing beam. The x axis is the axis of the pushing beam propagation, while the time scale is from shutdown of the pushing beam. Points are experimental data while the red dashed curve is a fit to the solution for a damped harmonic oscillator. From the fit we obtain $\omega = (473 \pm 1)$ Hz and $\beta = (287 \pm 2)$. Trap parameters were $b' = 6.5$ G/cm, $\delta = -2.7\Gamma$, $s_0 = 0.48$.

From the restoring force, equation 2.33, we can find the corresponding harmonic potential $\kappa x^2/2$. Then, by using the equipartition theorem we can deduce the temper-

ature of the atomic cloud from its size:

$$\frac{1}{2}\kappa\langle x^2\rangle = \frac{1}{2}k_B T. \quad (2.36)$$

If we evaluate the size by using, e.g., the Doppler temperature we find a cloud size of a few tens of microns. However, this only holds true if the atoms are noninteracting. Typical MOT sizes are on the order of one millimeter and can go up to a centimeter.

2.3.3 Radiation trapping

The main effect limiting densities in a MOT is radiation trapping, this will also lead to increased MOT sizes compared to the one expected from the equipartition theorem. It is a known and well-studied effect that was identified early in the development of the MOT [18, 19]. In dense atom samples there is a chance that a scattered photon from one atom is reabsorbed by a second atom. The light induced interaction is repulsive due to the recoil being in opposite directions, see Fig. 2.6.

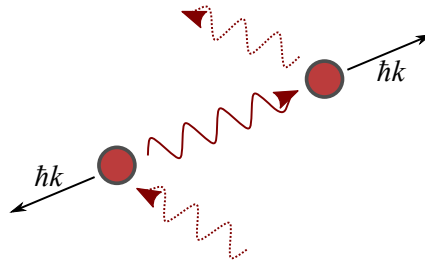


Figure 2.6: Schematic representation of radiation trapping. The rescattered photon that mediates the repulsive interaction is depicted with a full wiggly line. Notice that the momentum change of the atoms due to recoil is in opposite directions. Adapted from [41].

The probability of absorption by the second atom is given by $\sigma/(4r^2\pi)$ where σ is the absorption cross section and r is the inter-atomic distance. The scattering rate of the first atom, assuming all beam are of the same intensity, is six times the scattering rate from one beam:

$$\Gamma_{sc} = 6 \times \frac{\Gamma}{2} s_0 = 3\Gamma s_0. \quad (2.37)$$

The momentum change per photon is $\hbar k$ so the resulting force is given by

$$\mathbf{F}_{\text{reabs}} = 3\Gamma s_0 \frac{\sigma}{4r^2\pi} \hbar k \hat{\mathbf{r}}. \quad (2.38)$$

Since this force is repulsive and scales with $\propto 1/r^2$ it is analogous to the Coulomb force between same-species charges. The mapping is

$$\frac{q^2}{\epsilon_0} = 3\Gamma s_0 \sigma \hbar k. \quad (2.39)$$

For alkali atoms for the effective charge of the atoms one finds $q_{eff} \approx 10^{-4}e - 10^{-3}e$ depending on the intensity of the trapping laser. Thus the system of neutral cold atoms trapped in a MOT is analogous to a plasma confined in a harmonic potential. The dependence on the intensity of the scattered radiation also means that the effective charge is tunable opening up the possibility of a emulator of complex classical systems, this will be further discussed in chapter 4.

3 Experiment

In the course of my doctorate training two different MOT setups were built . Of course, MOT setups tend to be similar and these two are not an exception, however due to specifics in design they will be presented in this chapter. The first trap was built around a glass cell with rubidium dispensers incorporated in the glass. This made the cell expendable and motivated the introduction of a more sustainable setup. Another reason for building the second setup was to have more flexibility regarding future experiments, for this reason a stainless steel chamber was chosen. Accordingly, the second setup is centered around such a chamber.

3.1 The rubidium atom

First we will look at the properties of rubidium, the atom that we cool and trap, mostly those relevant for its interaction with light.

Rubidium is a member of the alkali metal group with an electron configuration $[\text{Kr}] 5s^1$. The single electron in the outer shell means it has a simple level structure, sometimes called hydrogen-like. The transition from the ground state to the first excited states of all alkalis is in the visible or near infra-red region of the spectrum, meaning that producing the light needed for laser cooling is relatively simple. This is especially true for rubidium, where we need 780 nm light. Incidentally, this is the same wavelength that the compact disc (CD) format uses meaning that laser diodes at this wavelength were and are mass-produced, meaning they are cheap to acquire. Additionally, rubidium has a melting point of 39.3 °C and it is easy to produce relatively high vapor pressures by heating it at moderate temperatures.

The physical advantages along with the affordability make the rubidium the most commonly used element in laser cooling experiments and are the reason why it was chosen in our lab.

The lowest electronic state is $5^2S_{1/2}$ where the first excited states are $5^2P_{1/2}$ and $5^2P_{3/2}$, the transitions to these states are called the D_1 and D_2 , respectively. The fine-structure splitting between these two states is 7123 GHz, the D_1 transition is at 795 nm while the D_2 that is used for cooling is at 780 nm. The total angular momentum $\mathbf{F} = \mathbf{I} + \mathbf{J}$, is found by including the nuclear spin, for the two isotopes of rubidium, ^{85}Rb and ^{87}Rb ,

it is $I=5/2$ and $I=3/2$, respectively. Different values of F will have different energies due to the interaction $I \cdot J$, the resulting splitting is called the hyperfine splitting. The natural abundances of ^{85}Rb and ^{87}Rb are 72% and 28%, respectively. However, we use ^{87}Rb due to a more user-friendly hyperfine structure. More details on rubidium properties can be found in [51].

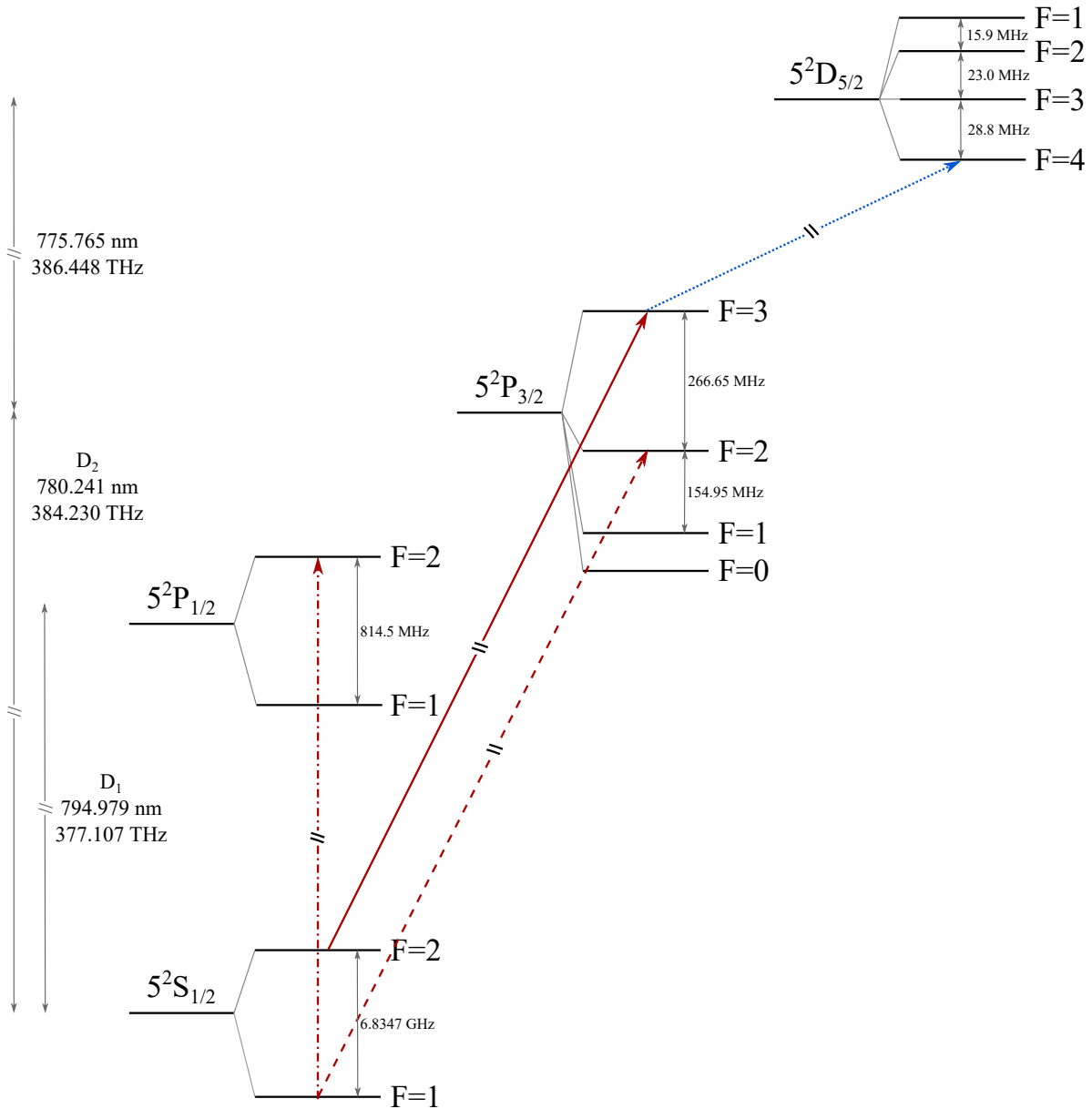


Figure 3.1: Level structure in ^{87}Rb relevant to further text. The cooling transition, ^{87}Rb the $|5^2S_{1/2}; F=2\rangle \rightarrow |5^2P_{3/2}; F'=3\rangle$, is marked with a full red line, two possible repumper transitions are also marked: with a dashed line the $|5^2S_{1/2}; F=1\rangle \rightarrow |5^2P_{3/2}; F'=2\rangle$ transition and with a dot-dashed line the $|5^2S_{1/2}; F=1\rangle \rightarrow |5^2P_{1/2}; F'=2\rangle$ transition. The transition $|5^2P_{3/2}; F=3\rangle \rightarrow |5^2D_{5/2}; F'=4\rangle$ is marked with a dotted blue line. A laser coupling an excited state with a second excited state is needed for our scheme to implement a synthetic magnetic field, more details in chapter 4. The relevant hyperfine splittings are noted. Adapted from [51] and [52].

In Fig. 3.1 the level structure relevant to laser cooling of ^{87}Rb is shown, also added

is the $5^2D_{5/2}$ state, relevant to our work in synthetic magnetism. To cool down atoms many absorption and emission cycles are necessary. This means that for a real atom the transition used for cooling needs to be a closed one. In ^{87}Rb the $|5S_{1/2}; F = 2\rangle \rightarrow |5P_{3/2}; F' = 3\rangle$ transition is used. For usual red detunings of a few Γ the cooling laser will be $\approx 40\Gamma$ blue detuned from the $|5S_{1/2}; F = 2\rangle \rightarrow |5P_{3/2}; F' = 2\rangle$ transition. Although this is considerable, there is small chance that the atom will be excited to the $|5P_{3/2}; F' = 2\rangle$ state. From there the atom can decay to the $|5S_{3/2}; F' = 1\rangle$ state, which is a dark state, and it will be lost from the cooling cycle. The chance of this happening is $\approx 1/1000$; since cycling happens at a rate of $\approx \Gamma$ this means that very quickly all atoms will be pumped into the dark state and will no longer be cooled or trapped. For this reason a second laser is needed, the so-called repumper laser. It couples the $|5S_{3/2}; F' = 1\rangle$ state with any excited state that has a chance of decaying into the $|5S_{3/2}; F' = 2\rangle$ state. Two different realizations for the repumper laser have been used in our experiment, one using the D_1 transition and the other the D_2 , shown in Fig. 3.1.

3.2 The magneto-optical traps

As previously mentioned, two separate MOT systems were built in the course of my studies and both will be detailed here.

3.2.1 First generation vacuum system

The first vacuum system, in which the work on synthetic magnetism was done, was centered around a glass cell made by *Technical Glass*, which in the mean time became part of *Precision Glassblowing*. It is a six-way cross with Rb sources built in, it is shown in Fig. 3.2. The Rb dispensers require around 4 A of current flowing through them to generate a Rb background pressure that is adequate for loading the MOT. Besides the large six windows, there are additional three small windows that allow beam inputs at an angle of 45° from the ones in the large windows. The windows were not anti-reflection coated and typical losses at transmission through them were 10%.

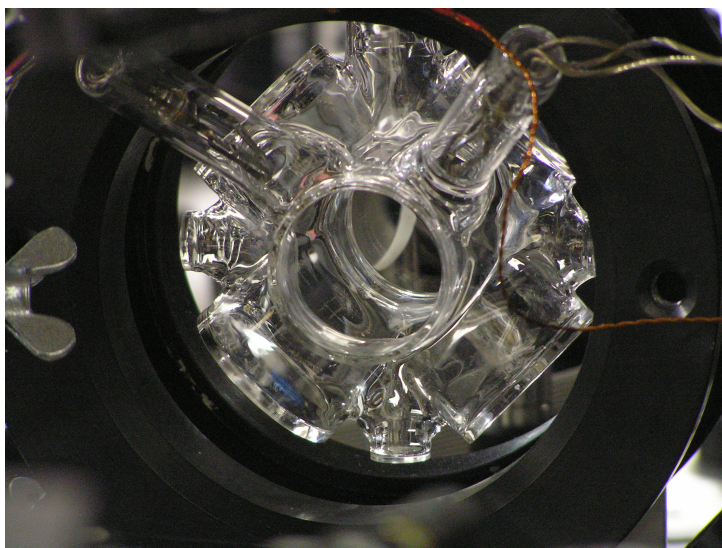


Figure 3.2: Glass cell used for the first generation Rb MOT. The rubidium dispensers can be seen in the longer glass tubes protruding towards the point of view. The connection to the vacuum pump is to the top, but out of the frame.

The glass chamber was directly connected via a reduction flange to the ion pump, *Varian Vaclon Plus StarCell 55*, a 50 L/s ion pump. The direct connection was needed to obtain the desired vacuum since any tubing reduces the pumping rate. The vacuum reached after baking at $\approx 200^\circ$ C for a few days was 3×10^{-8} mbar deduced from the ion pump current. For typical dispenser currents of 4 A no increase of the background pressure was noticed.

3.2.2 Second generation vacuum system

The second vacuum system was built around a stainless steel chamber from *Kimball Physics*, a spherical octagon 8" in diameter (MCF800-ExtOct-G2C8A16). This chamber was fitted with two 8" windows, eight 2.75" windows, and four 1.33" windows. Two 1.33" ports were fitted with extension nipples in which rubidium dispensers were mounted, four dispensers in each nipple. The remaining twelve 1.33" ports were closed with blanks for financial reasons. The windows were acquired from *Torr Scientific*, made from the same 316LN stainless steel as the chamber, with glass seals made from tantalum so as to be nonmagnetic, and with a broadband anti-reflection coating. Although, despite this coating we experience a 10% intensity loss on transmission, this is probably due to rubidium being deposited on the windows¹. Two of the 8" windows were not fitted directly on the chamber, rather on extension nipples and a four-way cross so as to provide a means to mount the chamber and to connect the ion pump (same pump as in the first generation). The pump axis is slightly misaligned from the chamber axis due to a particular reduction flange. The chamber assemble was mounted on an aluminum board that is elevated 15 cm from the optical table so as to provide space for optics. A 3D render of the setup along with a real life photograph can be seen in Fig. 3.3 while the technical drawings can be found in [appendix C](#).

3.2.3 Anti-Helmholtz coils

As mentioned in section 2.3.1, to create a quadrupole magnetic field needed to trap atoms we use a pair of coils with current flowing in opposite directions in either one. This coil configuration with the coil spacing equal to $d = \sqrt{3}r$, where r is the coil radius, produces a homogeneous gradient in a large volume, hence the name anti-Helmholtz (AH) coils in analogy to the Helmholtz coils that produce a homogeneous field in a large volume. For two different vacuum system two different coils needed to be wound.

In the first generation MOT a pair of air-cooled coils was wound. Their mounts can be seen in Fig. 3.2. Each coil has 423 windings for a total length of 314 m. The two coils were mounted with typical holders to the optical table, 9 cm apart, close to the optimal distance that produces a near-homogeneous gradient in the largest volume. The gradient produced is 13 G/cmA. As 13 G/cm is enough for a rubidium MOT, the coils were usually run at 1 A, producing up to 40 W of heat. With current flowing through them they heated up to $\approx 70^\circ\text{C}$. Since this is a reasonable temperature and the coils were not in direct contact with the glass cell, no active cooling was necessary. For time-of-flight measurements (TOF) turning off the trapping potential is necessary, this

¹This could be remedied with a "cold finger", a metal part of the chamber is cooled to have rubidium deposit on it. This will be applied in the future after baking the chamber again to remove current deposits.

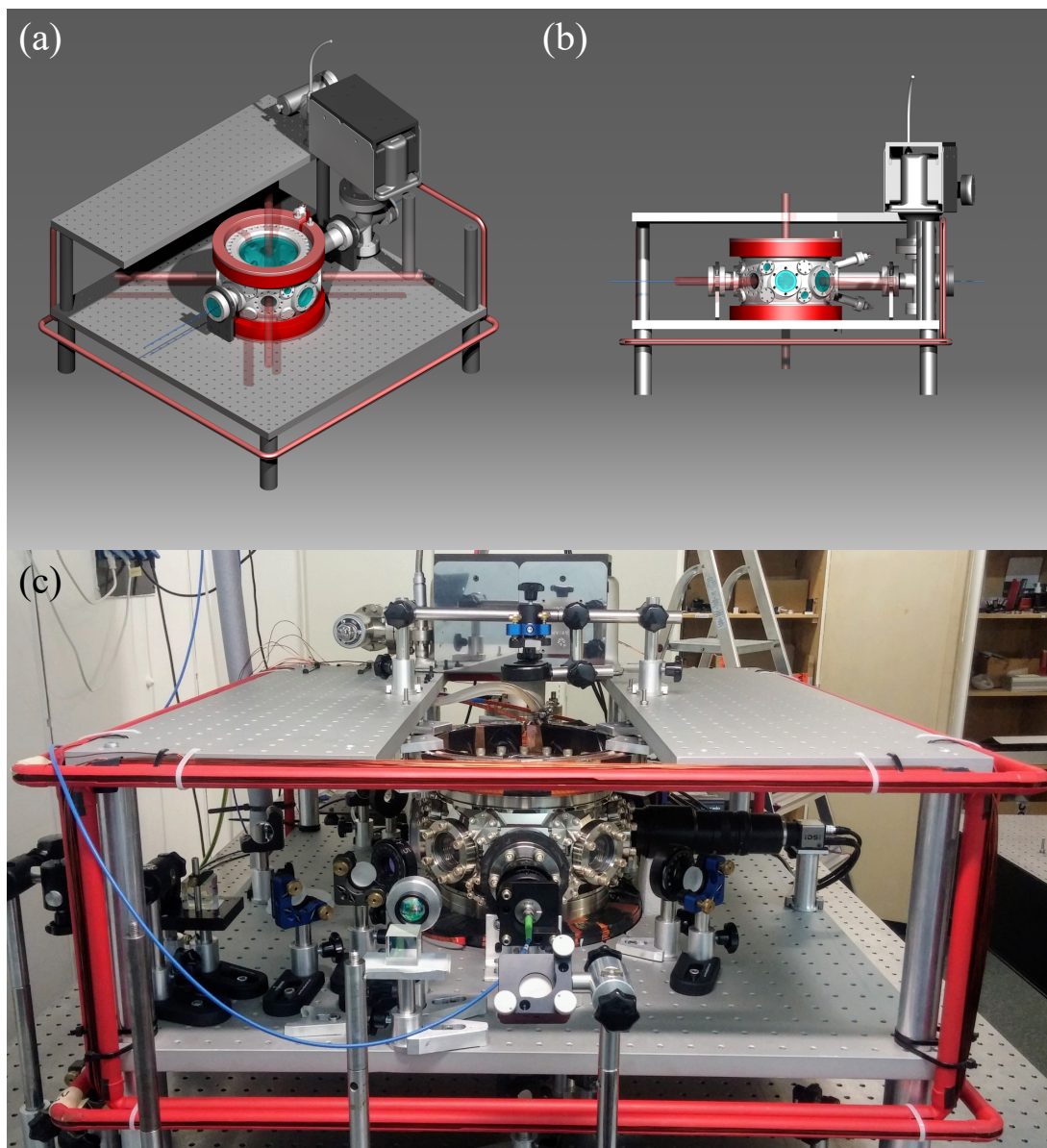


Figure 3.3: Stainless steel chamber for the second generation Rb MOT. (a) angled perspective with the upper breadboard removed, (b) side view. Red rectangular tubes are holders of the the bias coils. Cooling beams are shown in red, partially transparent, while a probe beam is shown in blue, partially transparent. Red cylindrical pieces under and on top of the chamber are the AH coils assembly. Renders provided by Damir Altus (c) A photograph of the chamber.

preferably includes turning off the magnetic field. The relatively low current meant that a simple solid state relay (SSR) could be used, namely model MPD3CD3 from *Crydom*. This SSR is optimized for digital control, meaning it requires very low control signal current, meaning that it could be controlled directly by an digital output from our data acquisition (DAQ) card. This was both a simple and a cost effective solution. Switching times were measured to be ≈ 1 ms. The on-or-off nature of SSRs means that linear control of the current, and therefore the magnetic field gradient, is not possible, however this was not needed in our experiment.

Table 3.1: Comparison of MOT coils

	r_{inner}	N turns	wire dimensions	resistance	P diss. @13G/cm
I generation	5.5 cm	423	$\varnothing = 0.5$ mm	17 Ω	34 W
II generation	10.5 cm	102	1 \times 5 mm	0.62 Ω	248 W

In the second generation experiment the larger volume of the stainless steel chamber required larger coils. A comparison between the two coil designs can be seen in table 3.1. A rectangular cross section was chosen for the coils so as to increase the filling factor² of the coil which in turn decreases the coil size. However a similar filling factor to the one achieved in the first generation coil of 0.7 was achieved due to the (unpredictably) larger thickness of the Kapton insulation compared to the enamel on the round wire used in the first generation coils. Since switching times are shorter for coils that have less windings³ we chose to work with 80% of the highest current that our DC power supply (Kepco ATE 15-25 M) can provide, 20 A, and then find the number of windings needed to achieve a magnetic field gradient suitable for a MOT. Each coil has 100 windings in four layers, 25 windings each layer. Between each layer a thermo-conducting epoxy glue was applied in an attempt to improve heat conduction, however it was found that the epoxy does not hold well to the Kapton insulation so the effect of the epoxy is uncertain. The high power dissipation of the coils means that they have to be water cooled. For this purpose the coils are mounted on copper mounts, visible as the pink part of the coil assembly in Fig. 3.3. The coil mounts were designed to have water flowing through them, however a water-tight seal could not be achieved by our machine shop. As an alternative, copper tubes were soldered directly to the mount which have water flowing through them, this proved to be robust regarding water leakage and adequate in terms of heat dissipation. The mounts also have a gap to avoid eddy currents flowing through them when switching off the field.

The second generation coils are placed as close as the vacuum chamber allows them to be to maximize the generated field gradient at a certain current, namely $d=14.8$ cm. This is less than the optimal $d=18.7$ cm that would give the most spatially homogeneous gradient. However, the larger, optimal spacing would require a $\approx 20\%$ increase in current to generate the same gradient. Since dissipated power scales as $\propto I^2$ and the MOT is very robust to this kind of gradient inhomogeneity, the smaller spacing was judged to be more suitable. With the spacing $d=14.8$ cm we achieve a magnetic field gradient of 0.665 G/cmA, for 20 A of current this gives 13.3 G/cm, enough for standard MOT operation.

²ratio of the conductor to non-conductor cross section area, increasing it reduces the coil dimensions and therefore reduces the needed current to achieve a desired field gradient

³The switching time is proportional to the inductance and current, $\tau \propto LI$, the inductance increases quadratically with the number of turns, $L \propto N^2$, while the needed current for a given field decreases with the number of turns, $I \propto 1/N$. Therefore the switching time is proportional to N, $\tau \propto N$, hence for

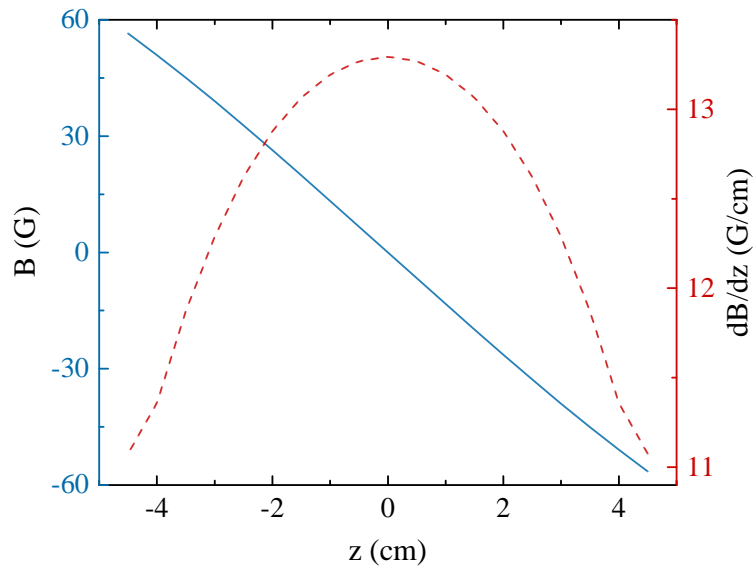


Figure 3.4: Numerically calculated magnetic field produced by the coils, full blue line, and the corresponding field gradient, dashed red line.

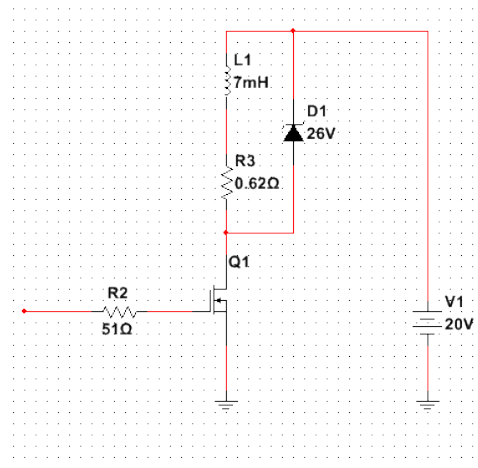


Figure 3.5: Equivalent scheme of the switching circuit. L1 and R3 are inductance and resistance of the coil pair, respectively, V1 is the power supply, the rest of the components comprise the switching circuit, Q1 is an array of two MOSFETs and D1 is an array of three MOSFETs acting as a Zener diode.

The power supply that we use with the second generation coil (Kepco ATE 15-25 M) has the option of analogue control which allows us to remotely change the current through the coils and hence the field. However, the bandwidth is low so this is unsuitable for switching off the current quickly and a separate switch had to be implemented. Since the current flowing through the second generation coils is considerably higher than in the first generation the use of a SSR was not possible. Instead, we utilized the design from [53]. It is schematically depicted in Fig. 3.5. An important component

shorter switching times a lower number of turns is better

in the design is the Zener diode, D1. Without it the coil current would decay exponentially, $\exp^{-t/(L/R)}$, the decay being driven solely by the ohmic resistance of the coils themselves, shown in Fig. 3.6(a). We can see that the switch-off time is ≈ 30 ms, impractically high for cold atom experiments. To reduce the switch-off time we added a Zener diode, marked as D1 in Fig. 3.5. By adding the Zener diode we introduce a constant voltage drop and therefore constant power dissipation. A consequence of this is almost a linear decay of the current, shown in 3.6(b).

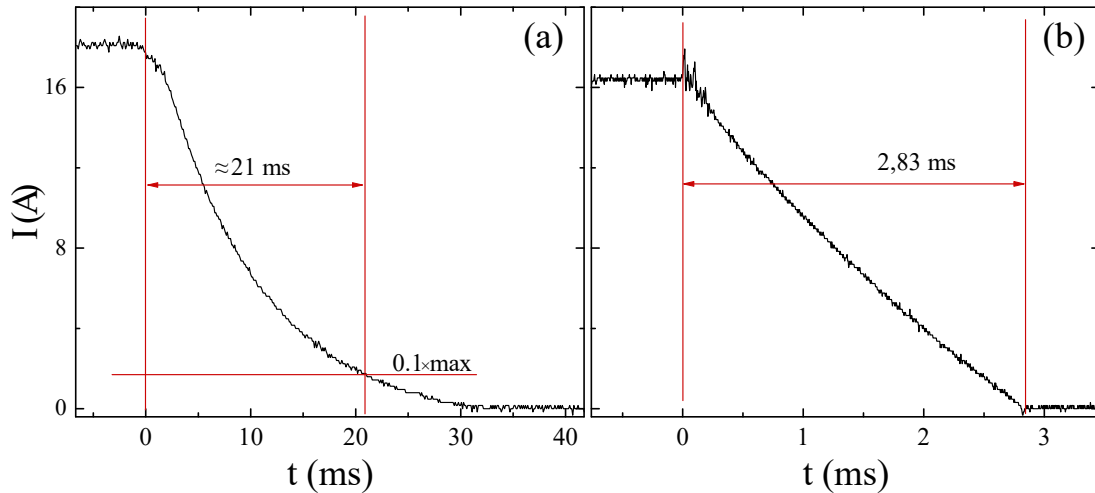


Figure 3.6: Current decay through the coils after disconnecting them from the power supply: (a) without the Zener diode D1, shown in Fig. 3.5 and (b) with the Zener diode incorporated into the circuit.

One can see that by introducing the Zener diode we reduce the switching time by a factor of ≈ 10 . However, the quickly decaying magnetic field can induce eddy currents in metal components of the setup, and therefore the magnetic field can decay significantly slower than the current through the coils.

To measure the time dependence of the magnetic field we perform a type of spectroscopy to measure the Zeeman splitting of the $|5S_{1/2}; F = 2\rangle \rightarrow |5P_{3/2}; F' = 3\rangle$ transition. Some time after we switch off the trap (both the trapping beams and the AH coils from the power supply) we turn on a CW laser probe beam propagating perpendicular to the AH coils axis, corresponding to the blue beam in Fig. 3.3; this beam then exerts radiation pressure force upon the cloud. We keep the interaction time short, 0.5 ms, to increase temporal resolution. After an additional 4 ms of free motion to increase sensitivity we image the cloud which is now displaced from its original position. The displacement is proportional to the force which is in turn proportional to absorption, i.e. the imaginary part of the coherence, see equation 2.19. We then perform the same TOF measurement for different frequencies of the probe laser to retrieve the line shape of the transition. The polarization vector of the probe beam is also perpendicular to the AH coils axis. We assume that the induced eddy currents generate a magnetic field that is parallel to the AH coils axis, the z axis. With the polarization and magnetic field

being perpendicular we have $\Delta m_F = \pm 1$ transitions allowed. By calculating the Zeeman shift of all m_F states, adding them together we find that the resulting splitting of the two peaks (corresponding to positive and negative m_F states) will be 2.4 MHz/G.

We see an example of the displacement as a function of detuning measurement in Fig. 3.7(a). By probing the cloud with the CW laser at different times after switching off the trap we can measure the magnetic field as a function of time, shown in Fig. 3.7(b).

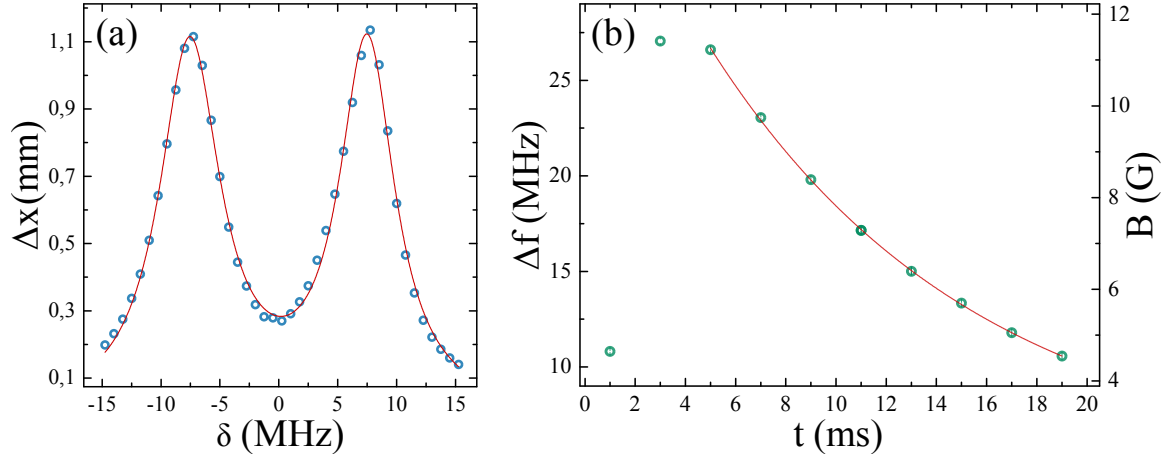


Figure 3.7: (a) An example of the measurement of the Zeeman splitting measured 13 ms after switching of the power supply from our AH coils. Propagation and polarization vectors of the probe beam are perpendicular to the AH coils axis. The red curve is the fitted sum of two Lorentzian peaks. (b) The measured splitting of the two peaks versus time. By assuming that $\Delta m_F = \pm 1$ transition are allowed we calculate the magnetic field, shown on the right axis. The red curve is a fit to an exponential decay.

It is clear from Fig. 3.7 that strong eddy currents are induced in the metal parts of our system. The increase of the magnetic field in the first ≈ 3 ms corresponds to the current decay time measured, Fig. 3.6(b). The subsequent decay is exponential with a decay constant $\tau = (10.6 \pm 0.3)$ ms. Similar results were obtained with the polarization vector parallel to the AH coil axis and with circular polarization. The magnitude of the induced field and its slow decay is a problem in almost any experimental scenario because of the resulting Zeeman splitting. Since the bias coils were designed to produce up to 3 G and their large size results in a large inductance it was concluded that the large induced field could not be compensated either statically in a certain point in time or dynamically following the decay pattern.

The largest and the most conductive metal part in our setup, the aluminum breadboard on which the vacuum system is mounted, is suspected to carry most of the eddy currents. The lower coil of the AH pair is mounted in the same plane as the breadboard and very close, suitable for large mutual inductance with the coil. This was an unfortunate oversight in the design. There is a plan to cut through the breadboard to have it not complete a closed loop, however this was not yet implemented in the moment of writing this thesis. In the meantime it was decided that the intermediate solution was

to work with the AH field left on during TOF measurements. The field in the center of the trap is zero and the spatial extent of the cloud is such that the field experienced by the atoms should be < 1 G, a preferable alternative to the large fields produced by the eddy currents.

3.2.4 Experimental control

Atom dynamics in a MOT happens on μs and ms time scales. This means that automation of the experiment is necessary. For this we utilize a DAQ card from *National Instruments*, USB-6259. The card has 4 analog outputs and 128 digital ones. The outputs can be refreshed in $10 \mu\text{s}$ intervals, this is adequately fast for our experiments. The scheduling of the outputs is done on the card using the first in, first out (FIFO) method from a buffer on the card itself assuring accurate timing for each TOF run.

The number of analog outputs is small, but proved sufficient so far. In the first generation experiment the four outputs were used for frequency modulation of the AOMs determining the detunings of the four beams implementing the SLF. The digital outputs were used for amplitude modulation of the cooling beams⁴, i.e. switching off and on, for switching of the magnetic field and for triggering the camera.

In the second generation experiment we use the analog outputs for control of the cooling beams detuning, the repumper detuning (also using a double-pass AOM), control of the voltage across the AH coils and the detuning of an additional CW probe beam. The detuning of the frequency comb is controlled by a DDS, see chapter 5.

The card and its outputs are controlled by a number of self-written *Labview* programs. The user interface can be seen in Fig. 3.8. Typically, the experimental procedure would be to initialize program (d), set the range of a frequency to be scanned, the number of points in this range and the number of repeats of the scan for later averaging. For each point program (d) would then initialize program (c) or (e), depending on which laser's detuning we wanted to scan, and then initialize program (b) that would perform TOF sequence⁵ a given number of times. The camera software captures an image for each TOF. The images are later analyzed by *Matlab* code to extract data, e.g. center of mass (CM), width, angle of the cloud or total fluorescence.

⁴Since the output of the digital outputs is the typical 5 V and amplitude modulation inputs of the AOMs have a range of 0 – 1 V we use a simple voltage divider to reduce the voltage from 5 V to 1 V

⁵Typically the AH field and the cooling laser would turn off at time $t = 0$, then a probe laser(s) would turn on for a given period and after further free motion of the cloud, the cooling laser would turn on causing fluorescence of the atoms in the cloud. At the same time as turning on the cooling laser we trigger the camera. The cooling laser is turned off after the exposure time to avoid additional light falling onto the pixels of the camera while they are being read. After few tens of ms the AH field and cooling laser are turned on for a set time to load the trap.

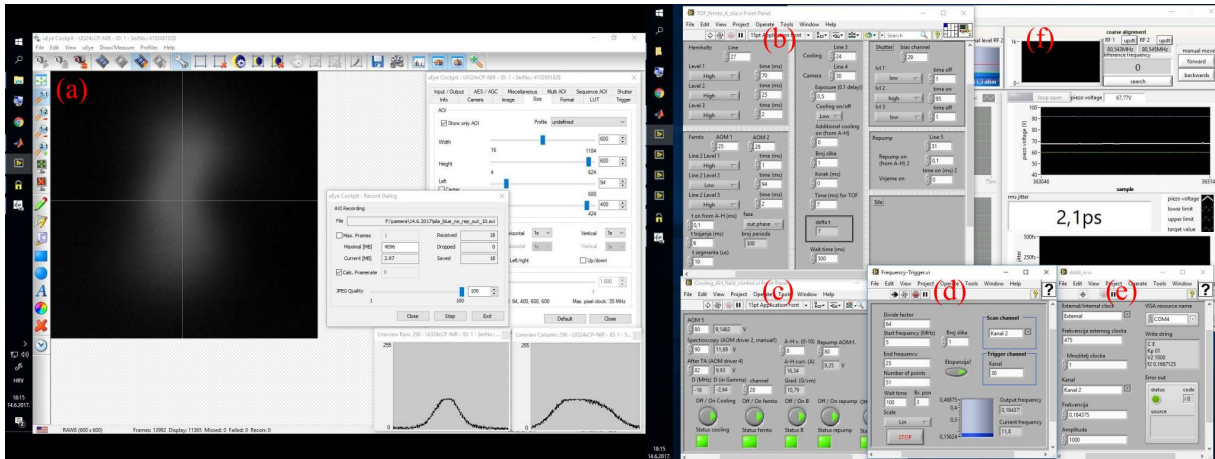


Figure 3.8: A snapshot of the computer screen that runs the experiment showing the software used. (a) Camera software used to capture images, typically working in continuous trigger mode i.e. the camera captures an image when triggered by the DAQ card (b) TOF sequence parameters and execution, controls for timing of the various on/off signals for control of the trapping light, repumper light, frequency comb light, CW light, magnetic field, duration of all sequences, MOT loading time, etc. (c) Monitoring software of the frequency comb f_{rep} lock, see chapter 5. (d) Control of AOM frequencies and AH current control, i.e. analog outputs. (e) A scan program that continuously changes either an AOM frequency or a DDS output frequency, and then executes program (b). It performs this for a given number of points between arbitrary values, i.e. different frequencies and repeats the scan a number of times. (e) Control of the DDS output frequencies, primarily used to change the detuning of the frequency comb, see chapter 5.

3.3 External cavity diode lasers

As mentioned before, rubidium is a popular choice element for laser cooling experiments, one of the reasons being the availability of semiconductor laser diodes at 780 nm, the wavelength of its cooling transition. All the lasers we use, with the notable exception of the Er:fiber pulsed laser which will be addressed in chapter 5, are external cavity laser diodes (ECDLs). The operating principle of ECDLs will not be addressed here since it is not a distinct feature of our experiment, there is ample literature available, for instance [54]. In the first generation experiment four ECDLs were used, all in the Littrow configuration, model DL 100 from *Toptica*. The purpose of extending the cavity is to reduce the linewidth of the laser, the DL 100s achieve 1-2 MHz linewidth while free-running measured by heterodyne beating with our frequency comb, more details on this can be found in chapter 5.

The frequency of a laser is typically detected by some version of Doppler-free spectroscopy, in the case of the DL 100 we used saturation spectroscopy. This is probably the most widely used spectroscopy technique in rubidium experiments as it provides narrow Doppler-free peaks at the position of the hyperfine levels in rubidium. The details of this technique will not be revisited here, since again, ample literature is avail-

able, for instance [55].

3.3.1 Laser stabilization

For achieving cooling a red detuning from a certain hyperfine transition is needed and the laser needs to maintain this frequency for a long time, on the order of a day. The same is true for lasers used for implementing our synthetic magnetism scheme, they need to have a particular detuning from a hyperfine level and be stable for long periods of time.

To stabilize the DL 100s used at the 780 nm transitions we use the simple dither lock. We modulate the current at 5-10 kHz, and then demodulate the signal detected on a photodiode with a phase sensitive detector to obtain an error signal. The error signal is then fed into a PID controller that provides the necessary feedback to the piezo voltage and the diode current to keep the laser frequency at the wanted peak. Both the modulation, demodulating electronics and the PID are part of a *Toptica* module, the LIR 110. A necessary drawback of this technique is that by modulating the laser frequency we effectively increase its linewidth. However, the free-running linewidth of the DL 100s is already larger than the modulation amplitude (1-2 MHz compared to ≈ 100 kHz) so the influence of the modulation is not significant.

We attempted to reduce the effective linewidth by using an AC magnetic field instead of the current modulation. We use a Maxwell coil to create a near-homogenous field in a large volume. This coil is similar to a Helmholtz coil but has a significantly smaller radius, thus requiring less space on the optical table. It's made up of three coils, two smaller ones, $d=46$ mm, at a distance of 53 mm from each other with 26 turns, and a larger central coil exactly in between the two smaller ones, $d=60$ mm, 33 turns. The wound coil can be seen in Fig. 3.9(b). This configuration produces a near-homogeneous field along the length of the rubidium cell used, ≈ 5 cm. The coil produces 100 G/A, so to modulate the magnetic field at an amplitude that produces a ≈ 200 kHz Zeeman frequency shift in rubidium we need a ≈ 20 mA and 1.5 V ($R = 7.6 \Omega$), this is higher than what the LIR 110 can give, because of this we use a commercial audio amplifier. By using a $\lambda/4$ plate to obtain circular polarization of the pump and probe the AC magnetic field produces a frequency modulation because of the Zeeman shift that can then be used to obtain the signal in the same way as with current modulation. A schematic representation of this setup is depicted in Fig. 3.9(a).

However, despite avoiding directly modulating the laser frequency the achieved linewidths of the DL 100s are above 1 MHz. This is somewhat expected considering the free-running linewidth is similar, and the bandwidth of the technique is low (few tens of Hz) and thus provides no linewidth narrowing.

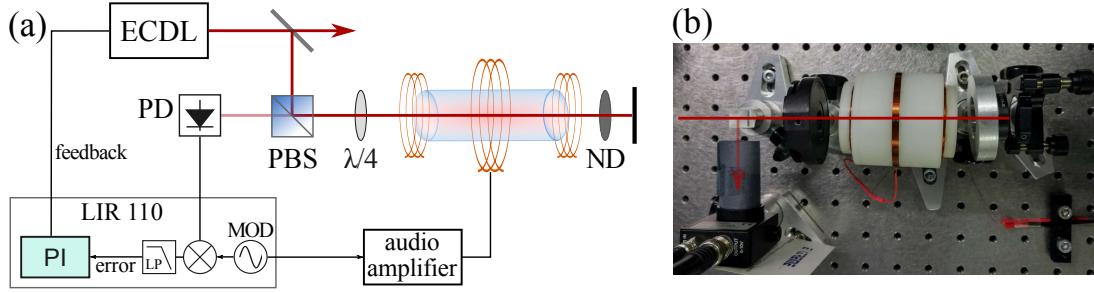


Figure 3.9: (a) Schematic representation of the setup that we use for the dither lock. (b) The real life optical part of the setup, the coil mount that also houses the rubidium cell is white and in the center of the image. Abbreviation used in the image: PD - photodiode, PBS - polarizing beam splitter, ND - neutral density filter, MOD - function generator used for modulating the signal, the same signal is used to demodulate the signal to obtain the error signal.

3.3.2 Stabilization of the $|5P_{3/2}\rangle \rightarrow |5D_{5/2}\rangle$ laser

As mentioned in section 3.1 in experiments in which we implement the synthetic Lorentz force (SLF) we drive the $|5P_{3/2}\rangle \rightarrow |5D_{5/2}\rangle$ transition. Since this transition involves two excited states one cannot use the standard saturation spectroscopy. To obtain an appropriate signal to which to lock to we counter-propagate picked off beams from the 776 nm ($P \approx 500\mu\text{W}$) laser and the 780 nm laser ($P \approx 6\text{mW}$) through a heated ^{87}Rb glass cell ($\approx 60^\circ\text{C}$), where the 780 nm laser populates the $|5P_{3/2}; F' = 3\rangle$ level. By monitoring the 776 laser intensity we observe an absorption signal resulting from the $|5P_{3/2}; F' = 3\rangle \rightarrow |5P_{5/2}; F'' = 4\rangle$ transition. This signal is mixed with the modulation signal from the 780 nm laser to obtain a frequency locking error signal. Therefore, there is no need to modulate the 776 nm laser frequency to stabilize it.

We can see the obtained absorption signal in Fig. 3.10. The obtained peaks are prominent enough to produce a good error signal to which to lock to. The lifetime of the $|5D_{5/2}\rangle$ state is $\tau_{5D_{5/2}} = 246$ ns giving a linewidth of $\Gamma_{5D_{5/2}} = 0.66$ MHz [56]. The fitted full width at half maximum (FWHM) of the $|5P_{3/2}; F' = 3\rangle \rightarrow |5P_{5/2}; F'' = 4\rangle$ transition to which we lock to is (15.6 ± 0.1) MHz, this is because of the natural linewidth of the intermediate state, $\Gamma_{5P_{3/2}} = 6.066\text{MHz}$, and also power broadening because of the considerable pump power (needed to have a considerable population in $|5P_{3/2}\rangle$).

Interesting to note is that the transitions that share the final excited state are overlapped when scanning the frequency of the 776 nm laser, i.e. there are no separate absorption dips for different intermediate states. To understand this consider for example the case shown in Fig. 3.10 when the 780 nm pump laser is locked to the $|5S_{3/2}; F = 2\rangle \rightarrow |5P_{5/2}; F' = 2\rangle$ transition. The $v = 0$ velocity group is excited to the $|5P_{5/2}; F' = 2\rangle$ state, the velocity group for which the Doppler effect compensates the -157 MHz hyperfine splitting is excited to the $|5P_{5/2}; F' = 1\rangle$ state and the velocity group for which the Doppler effect compensates the +267 MHz hyperfine splitting is excited

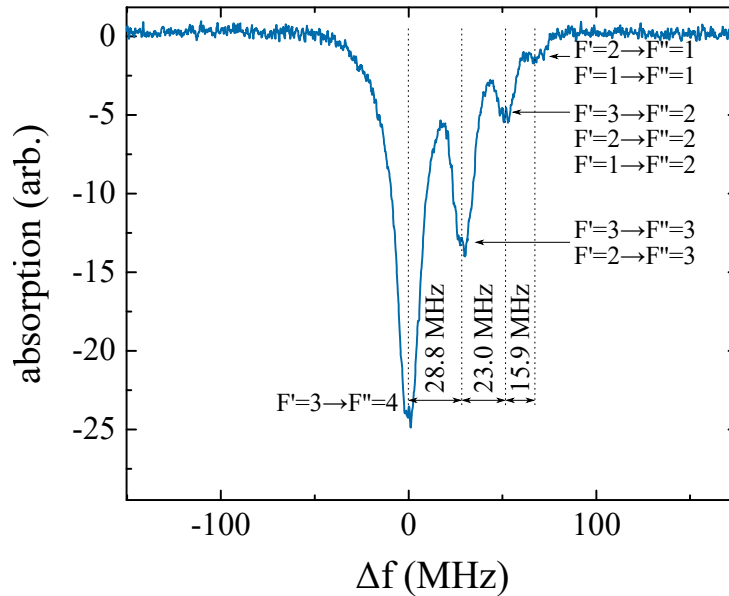


Figure 3.10: Measured absorption signal for the $|5P_{3/2}\rangle \rightarrow |5D_{5/2}\rangle$ transition. We lock to the largest peak, the $|5P_{3/2}; F' = 3\rangle \rightarrow |5P_{5/2}; F'' = 4\rangle$ transition. The 780 nm laser was locked to $|5S_{3/2}; F = 2\rangle \rightarrow |5P_{5/2}; F' = 2\rangle$ transition. Other peak have multiple transitions overlapped because they have the same two-photon energy, i.e. the final state is the same. More details in text. The frequency scale was calibrated using values of the hyperfine splittings found in [52].

to the $|5P_{5/2}; F' = 3\rangle$ state. Now, when the 776 nm probe laser, propagating in the opposite direction, is on resonance $|5P_{3/2}; F' = 2\rangle \rightarrow |5P_{5/2}; F'' = 2\rangle$ for velocity group $v = 0$ it is blue detuned by $\delta = 267$ MHz from $|5P_{3/2}; F' = 2\rangle \rightarrow |5P_{5/2}; F'' = 3\rangle$ and red detuned by $\delta = -157$ MHz from $|5P_{3/2}; F' = 2\rangle \rightarrow |5P_{5/2}; F'' = 3\rangle$. Since the 776 nm laser propagation vector is opposite of the 780 nm laser's the detuning for velocity groups excited to the $|5P_{5/2}; F' = 1\rangle$ and $|5P_{5/2}; F' = 3\rangle$ will directly cancel the hyperfine detuning, meaning that the probe laser will be in resonance with all three transitions/velocity groups at the same time.

3.3.3 Polarization spectroscopy

Presented in chapter 5 is the way in which we stabilize our frequency comb. For this purpose a very narrow CW laser was needed. As a simple solution was found in polarization spectroscopy with the (at that time) newly acquired *Moglabs* ECDL, model CEL002. Pioneered by Wieman and Hänsch [57], it is a sub-Doppler technique that give a far better signal-to-noise ration than typical saturation spectroscopy.

Polarization spectroscopy uses a circularly polarized pump beam to induce anisotropy in the medium, in this case rubidium vapor, that causes birefringence. A schematic representation of the optics layout used for the spectroscopy is shown in Fig. 3.11. As a consequence the polarization plane of the linearly polarized probe beam rotates. This is because the circularly polarized pump beam anisotropically saturates

the medium; for a σ^+ polarized pump the absorption of the σ^+ component of the probe beam is decreased while the absorption of the σ^- component of the probe beam is increased. A difference in absorption is necessarily accompanied by a difference in the refractive index for the two components, in accordance with the Kramers-Kronig relation.

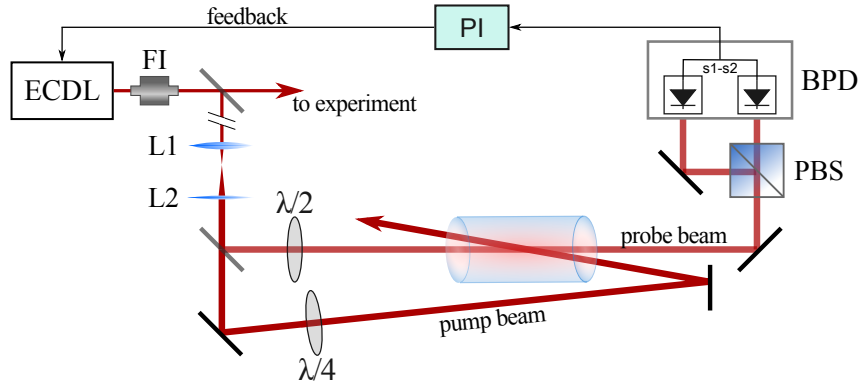


Figure 3.11: Schematic representation of the experimental layout for polarization spectroscopy. BPD - balanced photodiode, L1 and L2 - telescope to expand the beam to reduce power broadening.

To detect the rotation of the polarization of the probe beam we use a detection scheme that uses a polarizing beam splitter (PBS) cube and two detectors [58], conveniently provided as a balanced differential photodiode pair with the *Moglabs* controller, DLC502. By subtracting the signals laser intensity noise is removed, further increasing the signal-to-noise ratio. The probe beam polarization is chosen such that the two polarization components are of the same intensity, giving a zero signal if there is no anisotropy. The birefringence then creates a dispersion signal with the zero crossing at the transition frequency, shown in Fig. 3.12(c) for the $|5S_{1/2}; F = 2\rangle \rightarrow |5P_{3/2}; F' = 3\rangle$ transition. This signal is ideal for laser locking. It not only has the needed dispersive shape, it is steeper than the usual error signal obtained from saturated spectroscopy with the dither technique. Also, unlike saturation spectroscopy where the most prominent features are crossovers, here the largest signal obtained are for closed transitions which is practical for laser cooling.

Also convenient is the fact that no modulation of any kind is necessary to obtain the dispersive signal. In practice this means that the possible feedback bandwidth is limited by the bandwidth of the servo controller used. Achieving sub-kilohertz linewidths has recently been demonstrated using a servo controller with higher bandwidth than the one we use [59].

In our setup, we achieve linewidths of ≈ 60 kHz, based on heterodyne beating with our frequency comb. The achieved linewidth is critical to the way in which we stabilize our frequency comb. The same laser is used for laser cooling. After we amplify the power of this laser with a tapered amplifier (TA), which we then use for cooling in the

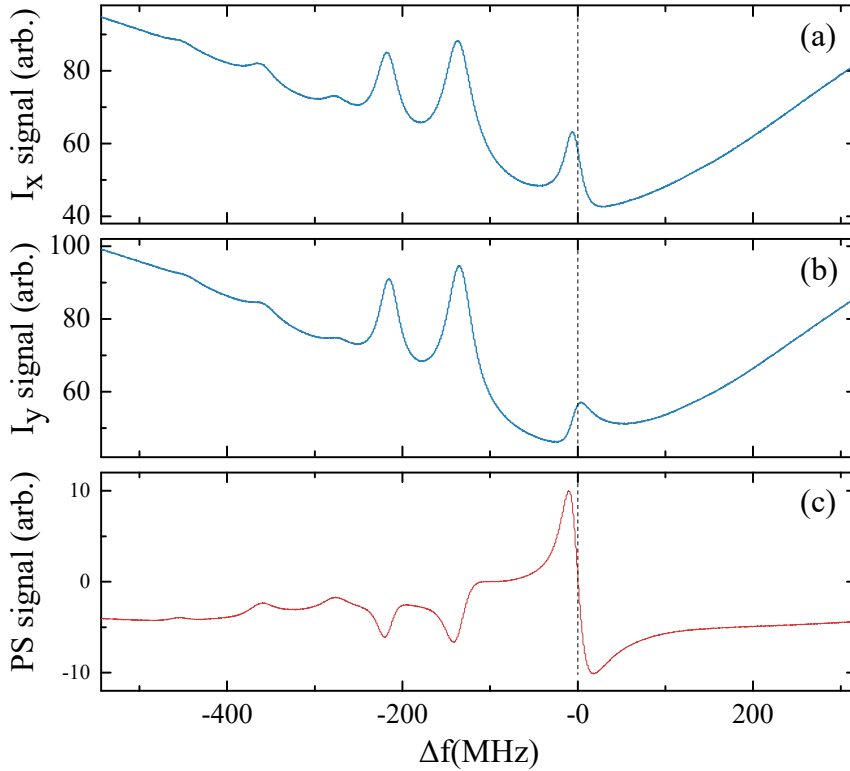


Figure 3.12: Polarization spectroscopy signals. (a) Photodiode signal of the x polarization component. (b) Photodiode signal of the y polarization component. (c) The balanced signal, difference of the signals (a) and (b) generating the dispersive signal suitable for laser locking. The x axis is the frequency difference from the $|5S_{3/2}; F = 2\rangle \rightarrow |5P_{3/2}; F' = 3\rangle$ transition. The spectra were calibrated using values of the hyperfine splittings found in [51]. The two prominent peaks left of the cooling transition peaks are the usual crossovers that also appear in saturation spectroscopy.

second generation experiment, the linewidth is increased to 200 kHz, still very much suitable for laser cooling.

3.3.4 Cooling and trapping optics, imaging

To cool and trap atoms in three dimension we need six circularly polarized beams crossing the center of the vacuum chamber, all red detuned. The red detuning in the first generation was determined by the difference in frequencies that were used to drive two acousto-optical modulators (AOMs). First, a double pass acousto-optical modulator provided light for the saturation spectroscopy setup that was used for stabilizing the cooling laser (*Toptica*, DL 100), the laser was then locked to the crossover of transitions $|5S_{1/2}; F = 2\rangle \rightarrow |5P_{3/2}; F' = 2, 3\rangle$, the most prominent peak in the saturation spectroscopy spectrum which is detuned 133.3 MHz from the $|5S_{1/2}; F = 2\rangle \rightarrow |5P_{3/2}; F' = 3\rangle$ transition. The second single pass AOM was used for quickly turning off and on the input to the fiber, i.e. the cooling beams. The detuning was then $\delta = -133.3 + 2f_{DP} - f_{SP}$ MHz, where f_{DP} and f_{SP} are the double pass and single pass

AOM driving frequencies, respectively. With typical AOM driving frequencies 80-100 MHz this provided a wide range of possible detunings.

In the second generation setup a double pass AOM was again used to provide light for the spectroscopy, now polarization spectroscopy, see section 3.3.3. Since here we lock to the $|5S_{1/2}; F = 2\rangle \rightarrow |5P_{3/2}; F' = 3\rangle$ transition we again need a double pass AOM for reaching adequate detuning, which is now used for fast switching of the cooling light, this setup is shown in Fig. 3.13.

In both generations of the experiment single mode, polarization maintaining (PM) fibers are used for obtaining a clean Gaussian mode for the cooling and repumper beams. From this point the setup in the two generations is the same, the second generation setup is shown in Fig. 3.13.

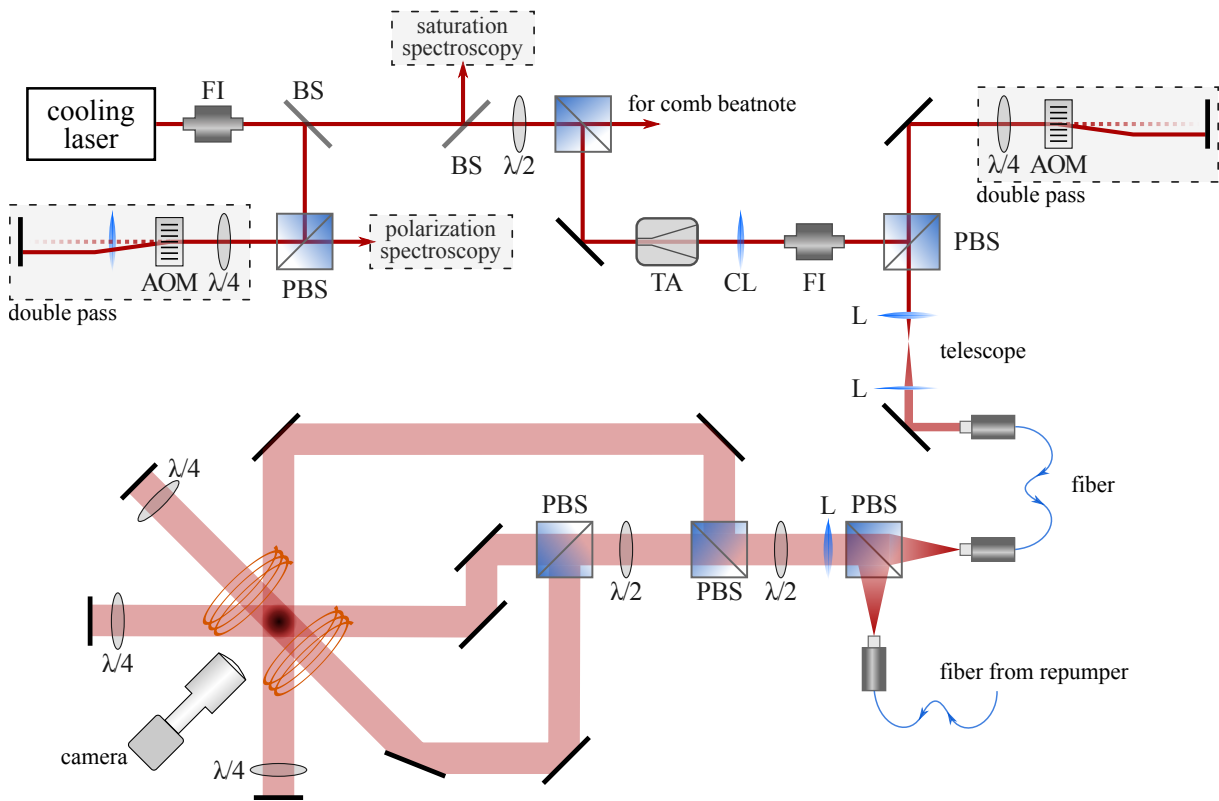


Figure 3.13: A simplified schematic of the experimental layout for cooling and trapping atoms in the second generation setup. The two perpendicular MOT beams propagate in the horizontal plane, the angled propagates vertically. Abbreviations used: FI - Faraday isolator, AOM - acousto-optical modulator, BS - beam splitter, PBS - polarizing beam splitter, $\lambda/2$ - half-wave plate, $\lambda/4$ - quarter-wave plate, TA - tapered amplifier, CL - cylindrical lens, L - lens.

The cooling laser light fiber output is joined with the repumper light by a polarizing beam splitter (PBS) cube. This PBS also serves the purpose of cleaning the polarizations of the repumper and cooling light, this is needed because there is always a small drift present in the polarization angle because of suboptimal coupling to the PM fiber. After the PBS a lens is used to collimate the beams. By using two additional PBS cubes a

total of three beams are obtained. These are directed through the center of the chamber, after exiting the chamber are passed through a quarter-wave plate (QWP), reflected off a mirror and again passed through the QWP before entering the chamber again. The two passes through the QWP change the polarization of the beam from σ^+ to σ^- or vice versa. The three retro-reflected beams provide, along with the original three, the total of six beams needed to cool and trap atoms. This setup is also sometimes called a retro-reflected MOT.

In the second generation setup we use a homebuilt tapered amplifier (TA) chip from *Eagleyard Photonics* to increase the available power, the design was based on [60]. The TA amplifies the input from $P_{IN} = 22.7\text{mW}$ to a maximum output of 1 W, however typically we use 100-200 mW as we do not need large atom numbers. After the TA there is an cylindrical lens to correct for the large astigmatism of the chip output followed by a tandem Faraday isolator (FI) providing 60 dB isolation. The tandem FI is needed because the chip is extremely sensitive to back-reflections. About 20% of the output from the TA reaches the atoms, this is because a lot of power is lost on the mentioned double pass AOM used for fast switching, and because of low coupling efficiency into the single mode fiber. Since the polarization spectroscopy we use to stabilize the laser used for cooling uses light from a double-pass AOM, and since the cooling light passes through another double-pass AOM, the detuning will be given by $\delta = 2f_{PS} - 2f_{TA}$, where f_{PS} is the driving frequency for the AOM feeding the polarization spectroscopy, and f_{TA} is the frequency driving the AOM providing the cooling light, see Fig. 3.13. As mentioned before, the laser we use for cooling (*Moglabs*, model CEL002) is also used as a reference for the frequency comb, see chapter 5. The TA was implemented in part to have ample power from the heterodyne beat with the comb, and to generally be flexible.

As explained before, atoms are efficient scatterers of near-detuned light - they fluoresce. The scatter photons can be captured by a camera to obtain an image of the cloud density since scattered photons are proportional to the atom number, this is called fluorescence imaging. We use a CMOS camera, *IDS UI-3240CP-NIR* which is optimized for near-infrared imaging; it has a quantum efficiency of 60% at 780 nm. A high quantum efficiency is important for fluorescence imaging. Typically CCD sensors have much lower sensitivities, however the drawback of the CMOS chip is the larger readout noise. The main advantage of the camera was its low price. The camera was equipped with a 18-108 mm macro objective MVL7000 from *Thorlabs*, usually we use a magnification of $M=0.33\times$.

In the first generation experiment the imaging was done through the bottom window, see Fig. 3.2. As the glass cell was too close to the surface of the optical table to fit a large objective, a mirror was placed underneath it. Imaging parallel to gravity and perpendicular to the horizontal plane was useful when implementing the syn-

thetic Lorentz force. The experiment could then be setup with beams propagating in the horizontal plane and thus we could neglect gravity as explained in chapter 4.

In the second generation experiment imaging is done through a 2.75" window whose axis is 90° to the one the probe beam enters through, the one that is en face in Fig. 3.3(b). This setup is optimal for measuring the forces on the cloud along the axis of propagation of the probe beam(s), more details on these measurements are found in chapter 5.

4 Synthetic Lorentz force

In this chapter results on the implementation of the synthetic Lorentz force (SLF) and its experimental demonstration are presented. Results on this topic have been published in [26, 27, 28].

4.1 The scheme

The scheme that we use is based on the Doppler effect and radiation pressure. The standard Doppler cooling force arises when a laser field is red detuned compared to the atomic resonance frequency as described in section 2.2.1. As described before, due to the Doppler effect, the atom has a greater probability for absorbing a photon when it moves towards the light source. Absorption changes the atom's momentum along the laser propagation axis, whereas spontaneously emitted photons yield random kicks. Cycles of absorption and emission result in a viscous damping force $\mathbf{F}_D \approx \alpha \mathbf{v}$ for small velocities [1]; this force is *collinear* with the velocity and is used to obtain optical molasses.

Now, let us look at how to construct a laser-atom system (in the xy plane) where the radiation pressure force is *perpendicular* to the velocity, e.g., where F_y depends on v_x . To achieve this via the Doppler effect we utilize the multilevel structure of atoms. The simplest scheme is sketched in Fig. 4.1(b), where a three-level atom interacts with two orthogonal laser beams linearly polarized along z . The laser driving the $|0\rangle \rightarrow |1\rangle$

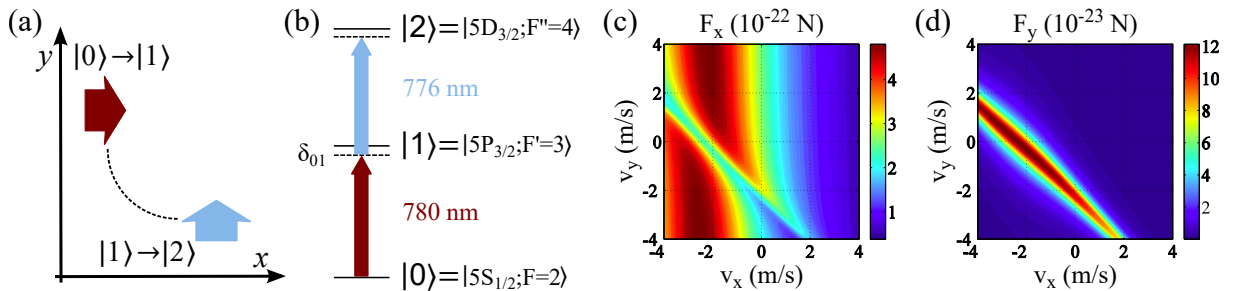


Figure 4.1: The main idea for constructing the synthetic Lorentz force. (a) Beam geometry for the SLF in the simplest three-level system. (b) The three levels in ^{87}Rb which can be used for the SLF. The force components (c) F_x and (d) F_y calculated as a function of the atomic velocity.

transition is red detuned, $\delta_{01} < 0$, whereas the laser driving the $|0\rangle \rightarrow |1\rangle$ transition is on resonance, $\delta_{12} = 0$. The absorption of photons $|1\rangle \rightarrow |2\rangle$, which results in F_y , is the second step in the two-step, two-photon absorption process: $|0\rangle \rightarrow |1\rangle \rightarrow |2\rangle$. The probability for the two-step absorption depends on the Doppler-shifted detuning values $\delta_{01} - k_{01}v_x$ and $\delta_{01} - k_{01}v_x$, which provides the desired dependence of F_y on v_x . The maximum in F_y is expected for atoms with velocity ($v_x = \delta_{01}/k_{01}$, $v_y = \delta_{12}/k_{12}$), i.e., when each of the two steps in the two photon process is resonant.

However, the force pattern shown in Fig. 4.1 is not symmetrical, i.e., an atom that has a positive velocity in the x direction will feel no force. The solution to this is to add a second pair of beams, symmetric in regards to the atom position to the first two beams. For the second pair we cannot use same configuration of levels and detunings, the atom has to somehow distinguish from which second-step beam to absorb photons from. Two solutions for this are possible and both were realized experimentally, they are shown in Figs. 4.2(a) and (b). These two realizations were used for different scenarios for the observation of the SLF, each characterized with a completely different initial velocity distribution of cold atoms and each suitable for emulation of different classical systems.

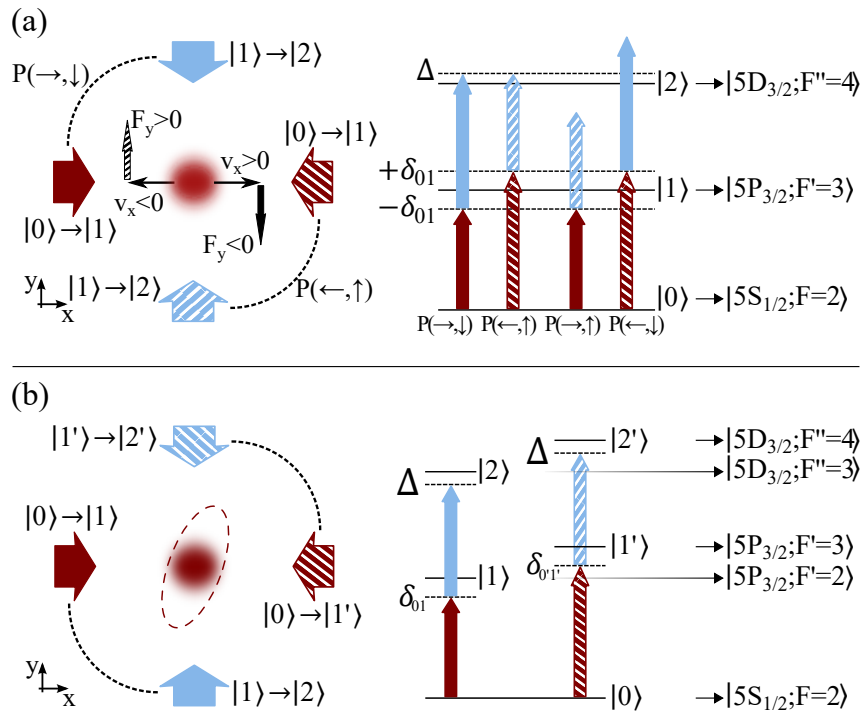


Figure 4.2: Two possible configurations of implementing synthetic magnetism to ^{87}Rb atoms with two pairs of laser beams. (a) A configuration that uses only two distinct excited states. (b) A configuration that uses four distinct excited states.

The first scenario uses the beam configuration shown in Fig. 4.2(a) and is suitable for the emulation of a single charged particle in a magnetic field, and its experimental realization is presented in section 4.2. We first prepared a cloud with a given center-of-

mass (CM) velocity, after which we measured trajectories of the CM of the atomic cloud in the presence of the SLF for various initial CM velocities. The observed trajectories of the CM of the atomic cloud can be interpreted as dynamics of a single charged particle under the influence of the Lorentz force, suggesting approximately equal SLF for all atoms in the cloud, due to the equal initial velocities.

The second scenario uses the beam configuration shown in Fig. 4.2(b) and is presented in section 4.3. The cold cloud is considered as an ensemble of particles with a Maxwell–Boltzmann velocity distribution. The signature of the SLF is observed in the shape of the expanding cloud, i.e., an asymmetric and tilted expanding cloud is observed. Our system in this case, a dense atomic cloud released from a MOT, is analogous to an expanding single species plasma in a magnetic field, and also to an expanding neutral gas in a rotating reference frame, i.e., under the influence of a Coriolis force, for instance, an anticyclone.

4.1.1 Numerical analysis

The force can be calculated by using density matrices and the Ehrenfest theorem as described in section 2.1.3. First we numerically solve the optical Bloch equations to find the stationary density matrix $\hat{\rho}$ for an atom with velocity \mathbf{v} ; the matrix elements are $\tilde{\rho}_{ij} = \rho_{ij}e^{i\omega_{ij}t}$ with $d\rho_{ij}/dt = 0$, ω_{ij} is the frequency of the laser driving the transition. In the calculation, the following parameters are used: the energies E_j of the levels participating in the interaction, ($j = 1, \dots, N$), the Rabi frequencies Ω_{ij} , detuning values δ_{ij} , the wave vectors \mathbf{k}_{ij} of the lasers, and the decay parameters of the excited states, Γ_{ij} is the decay rate via $|j\rangle \rightarrow |i\rangle$; the total width of the state $|j\rangle$ is $\Gamma_j = \sum_{i<j} \Gamma_{ij}$.

The force is given by equation 2.19, which generalized for multilevel atoms under the influence of more than one monochromatic fields reads

$$\mathbf{F} = - \sum_{i=1}^{N-1} \sum_{j=i+1}^N \hbar \mathbf{k}_{ij} \text{Im}(\rho_{ij} \Omega_{ij}^*). \quad (4.1)$$

The density matrix depends on the Doppler-shifted detuning values $\delta_{ij} - \mathbf{k}_{ij} \cdot \mathbf{v}$, this provides the velocity dependence of the force.

It should be emphasized that this scheme for constructing a SLF presented here is general and potentially applicable to various atomic species. Since we work with ^8Rb atoms in the calculations we use experimentally relevant atomic states and transitions. The three-level system that can be used to experimentally realize the simplest scheme is presented in Fig. 4.1(b). The transition wavelengths are $\lambda_{01} = 780 \text{ nm}$ [51] and $\lambda_{12} = 776 \text{ nm}$ [56]. The decay rate of the $|5P_{3/2}\rangle$ hyperfine states is $\gamma_P = 2\pi \times 6.1 \text{ MHz}$ [51], and $\Gamma_D = 2\pi \times 0.66 \text{ MHz}$ for the $|5D_{5/2}\rangle$ states [56]. The decay pattern is $\gamma_{21} = \Gamma_D$, $\Gamma_{20} = 0$, and $\Gamma_{21} = \Gamma_P$ [51, 56].

In Figs. 4.1(c) and 4.1(d) we show the calculated $\mathbf{F}(\mathbf{v})$ for detuning values $\delta_{01} = -0.5\Gamma_P$, $\delta_{12} = 0$, and Rabi frequencies $\Omega_{01} = 0.12\Gamma_P$, and $\Omega_{23} = 0.34\Gamma_P$. As expected, the maximum of the force F_y occurs when $v_x = \delta_{01}/k_{01}$ and $v_y = \delta_{12}/k_{12} = 0$. Interestingly, $F_y(v_x, v_y)$ has the shape of a mountain ridge peaked at $\delta_{01} + \delta_{12} - k_{01}v_x - k_{12}v_y = 0$. This is a consequence of the fact that the intermediate state $|1\rangle$ is much broader than state $|2\rangle$. For the two-step absorption to be effective, the Doppler-shifted detuning of the first photon should roughly be $|\delta_{01} - k_{01}v_x| < \Gamma_1$, and the total detuning $|\delta_{01} + \delta_{12} - k_{01}v_x - k_{12}v_y| < \Gamma_2$. Since $\Gamma_2 \ll \Gamma_1$, the velocities satisfying these inequalities are close to the ridge line. The ridge can be shifted in the $v_x v_y$ plane by changing the detuning values. The scheme above illustrates the main idea towards constructing the synthetic Lorentz force via the Doppler effect.

Note that the force in the x direction is also altered for atoms with velocities at the ridge. The presence of the second-step transition $|1\rangle \rightarrow |2\rangle$ changes the populations of all three levels, which affects the rate of the first-step transition $|0\rangle \rightarrow |1\rangle$ and hence F_x . It should be noted that deformations of the ridge can arise for larger Rabi frequencies due to the Autler-Townes effect [61].

4.1.2 The Fokker-Planck equation

The calculated force is sufficient to analyze single-particle-like dynamics. However, for experiments observing the expansion of the cloud the experimental results are in the form of TOF images so for a direct comparison with numerics we need a prediction of the shape of the cloud after a particular time under the influence of the SLF. Also, further analysis will provide a deeper insight to our scheme. For sufficiently small velocities the force is linear around zero, therefore a good approximation is to neglect higher order terms considering the low atom velocities in a MOT. We Taylor expand the force in velocity up to the linear term:

$$\begin{bmatrix} F_x \\ F_y \end{bmatrix} = \begin{bmatrix} F_{x0} \\ F_{y0} \end{bmatrix} + \begin{bmatrix} \alpha_{xx} & \alpha_{xy} \\ \alpha_{yx} & \alpha_{yy} \end{bmatrix} \begin{bmatrix} v_x \\ v_y \end{bmatrix} \quad (4.2a)$$

$$= \begin{bmatrix} F_{x0} \\ F_{y0} \end{bmatrix} + \begin{bmatrix} \alpha_{xx} & 0 \\ 0 & \alpha_{yy} \end{bmatrix} \begin{bmatrix} v_x \\ v_y \end{bmatrix} + \begin{bmatrix} 0 & \alpha_{xy} \\ \alpha_{yx} & 0 \end{bmatrix} \begin{bmatrix} v_x \\ v_y \end{bmatrix} \quad (4.2b)$$

$$= \mathbf{F}_0 + \mathbf{F}_D(\mathbf{v}) + \mathbf{F}_{SL}(\mathbf{v}). \quad (4.2c)$$

Here $\alpha_{ij} = \partial F_i / \partial v_j$ evaluated at $\mathbf{v} = 0$ ($i, j \in \{x, y\}$). The third term $\mathbf{F}_{SL}(\mathbf{v})$ is a general form of the synthetic Lorentz force with components perpendicular to the velocity components: $\mathbf{F}_{SL,x} = \alpha_{xy}v_y$, $\mathbf{F}_{SL,y} = \alpha_{yx}v_x$. The force on a standing atom is \mathbf{F}_0 , while the components of the standard Doppler force are $\mathbf{F}_{D,x} = \alpha_{xx}v_x$, and $\mathbf{F}_{D,y} =$

$\alpha_{yy}v_y$. When $\alpha_{xy} = -\alpha_{yx}$, \mathbf{F}_{SL} takes the form of the standard Lorentz force, $\mathbf{F}_{SL} = \mathbf{v} \times \mathbf{B}^*$, where $\mathbf{B}^* = \alpha_{xy}\hat{z}$.

One can alternatively divide the second term in equation 4.2a into two terms, one that has zero curl in velocity space, while the other is of the form of the standard Lorentz force, and thus rotates:

$$\begin{aligned} \begin{bmatrix} \alpha_{xx} & \alpha_{xy} \\ \alpha_{yx} & \alpha_{yy} \end{bmatrix} \begin{bmatrix} v_x \\ v_y \end{bmatrix} &= \left(\begin{bmatrix} \alpha_{xx} & \alpha_D \\ \alpha_D & \alpha_{yy} \end{bmatrix} + \begin{bmatrix} 0 & \alpha_R \\ -\alpha_R & 0 \end{bmatrix} \right) \begin{bmatrix} v_x \\ v_y \end{bmatrix} \\ &= \mathbf{F}_{pot}(\mathbf{v}) + \mathbf{F}_{SL}(\mathbf{v}), \end{aligned} \quad (4.3)$$

where $\alpha_{xy} = \alpha_D + \alpha_R$ and $\alpha_{yx} = \alpha_D - \alpha_R$. We again identify the second term $\mathbf{F}_{SL}(\mathbf{v})$ as the one responsible for the SLF. The first term $\mathbf{F}_{pot}(\mathbf{v})$ depends on both components of the atom velocity, and includes the usual Doppler force through the α_{xx} and α_{yy} diagonal terms. However, by dividing the second term in equation 4.2a in this way we get $\nabla_v \times \mathbf{F}_{pot}(\mathbf{v}) = 0$, this means we can calculate the corresponding potential in velocity space from $\mathbf{F}_{pot} = -\nabla_v U(v_x, v_y)$, where $\nabla_v = \hat{\mathbf{v}}_x \partial / \partial v_x + \hat{\mathbf{v}}_y \partial / \partial v_y$. By having a term that produces a potential in velocity space and one that rotates interpretations of results can be clearer.

The expansion of the cloud in the presence of the SLF laser beams is calculated by employing the Fokker-Planck equation [1]:

$$\frac{\partial P(\mathbf{x}, \mathbf{v}, t)}{\partial t} + \mathbf{v} \cdot \nabla_r P = \frac{-1}{m} \nabla_v \cdot [(\mathbf{F}_D + \mathbf{F}_{SL})P] + \frac{D}{m^2} \nabla_v^2 P, \quad (4.4)$$

where $P(\mathbf{x}, \mathbf{v}, t)$ is the distribution of particles in the phase space, D is the diffusion constant, approximately given by $D \approx (\hbar k)^2 \sum_j \rho_{jj} \Gamma_j$ [1], where $k \approx 2\pi/780 \text{ nm}^{-1}$, $\nabla_v = \hat{\mathbf{x}} \partial / \partial v_x + \hat{\mathbf{y}} \partial / \partial v_y$. For forces $\mathbf{F}_D + \mathbf{F}_{SL}$ (or $\mathbf{F}_{pot} + \mathbf{F}_{SL}$) linearized in velocity, equation 4.2a, the Fokker-Planck equation is solved by the ansatz

$$P(x, y, v_x, v_y, t) = P_0 \exp \left(- \sum_{i,j=1}^4 \frac{1}{2} a_{ij}(t) \eta_i \eta_j \right) \quad (4.5)$$

where $(\eta_1, \eta_2, \eta_3, \eta_4) = (x, y, v_x, v_y)$. After inserting equation 4.5 in 4.4, one obtains ten coupled ordinary differential equations (ODEs) for the functions $a_{ij}(t)$, ten because $a_{ij} = a_{ji}$ by construction. These coupled ODEs can be solved numerically and the cloud density in space can be found by integrating $P(x, y, v_x, v_y, t)$ over velocity space.

4.2 Synthetic Lorentz force for an atomic cloud with a center-of-mass velocity

In this section we show measurements of the dependence of the transverse radiation pressure force (analogous to the transverse Hall deflection) on the velocity of a cold atomic cloud by observing the centre-of-mass (CM) motion. The results in this section were obtained with the configuration shown in Fig. 4.2(a). As explained in section 4.1, due to the Doppler effect and the perpendicular configuration of the laser beams, both components of the radiation pressure force depend on both components of the atomic velocity: $F_x = F_x(v_x, v_y)$ and $F_y = F_y(v_x, v_y)$. This gives us the opportunity to design the detuning values of our lasers such that F_y is positive/negative for atoms with negative/positive velocity component v_x , and that the total force is zero for an atom at rest: $\mathbf{F}(\mathbf{v} = 0) = 0$. These are the characteristics of the synthetic Lorentz force that we experimentally demonstrated.

The design of the detuning values of the lasers is crucial in obtaining the desired result. The beams driving the first step of the transition $|0\rangle \rightarrow |1\rangle$ are detuned by the same magnitude, but with the opposite sign. The one towards the positive x -direction is red-detuned $\delta_{\rightarrow} = -\delta_{01} < 0$, while the other is blue-detuned by $\delta_{\leftarrow} = \delta_{01} > 0$. Their intensities are equal. Thus, if just these two lasers were present, the net force on atoms (of any velocity) would be zero. However, the population of level $|1\rangle$ would depend on the velocity v_x , which implies that the rate of transitions $|1\rangle \rightarrow |2\rangle$ giving the transverse force will depend on v_x . The detuning values of the beams driving the second step of the transition, $|1\rangle \rightarrow |2\rangle$ are denoted by δ_{\uparrow} and δ_{\downarrow} , for the beam propagating in the positive and negative y direction, respectively. For now, let us set these values such that $\delta_{\rightarrow} + \delta_{\downarrow} = \delta_{\leftarrow} + \delta_{\uparrow} = \Delta > 0$, as indicated in Fig. 4.2(a).

The two-step two-photon transitions, where absorption of a $|1\rangle \rightarrow |2\rangle$ photon follows absorption of a $|0\rangle \rightarrow |1\rangle$ photon with perpendicular momentum, yield the synthetic Lorentz force via momentum transfer from photons to atoms. Given the fact that we have two counterpropagating beams for each transition, we have four excitation pathways for the two-step two-photon transition denoted by $P(\rightarrow, \uparrow)$, $P(\leftarrow, \uparrow)$, $P(\rightarrow, \downarrow)$, and $P(\leftarrow, \downarrow)$, see Fig. 4.2(a). The arrows correspond to the direction of the photon's momentum, for example, $P(\rightarrow, \downarrow)$ denotes the pathway where absorption of a photon traveling in the $+x$ direction is followed by absorption of a photon in the $-y$ direction and so on. Since the detuning magnitudes of the first step are identical for all pathways ($|\delta_{\rightarrow}| = \delta_{\leftarrow}$), the relevant quantity is the total detuning for the two-step two-photon transitions. It is important to note that the total detuning Δ for pathways $P(\rightarrow, \downarrow)$ and $P(\leftarrow, \uparrow)$, is much smaller in magnitude from detuning values of $P(\rightarrow, \uparrow)$ and $P(\leftarrow, \downarrow)$. The last two are thus negligible in the setup of Fig. 4.2(a).

To understand the origin of the synthetic Lorentz force, we take into account the

Doppler shift. For an atom moving along the x -axis with velocity v_x ($v_y = 0$), the $P(\leftarrow, \uparrow)$ pathway is detuned by $\Delta + k_x v_x$, i.e., it is on resonance when $v_x = -\Delta/k_x < 0$. Because photons from the second step of $P(\leftarrow, \uparrow)$ impart momentum towards the positive y -direction, there will be a positive force F_y for atoms with negative v_x . In the same fashion, the $P(\rightarrow, \downarrow)$ pathway will be on resonance when $v_x = +\Delta/k_x > 0$ yielding negative F_y for positive v_x .

4.2.1 The experimental protocol

The ^{87}Rb atoms were cooled and trapped in the first generation MOT setup, described in chapter 3. The typical experimental starting point condition is a cloud 0.4 mm in diameter, which contains about 10^8 atoms of ^{87}Rb , at a temperature of $\approx 50\mu\text{K}$. The four beams implementing the synthetic Lorentz force, arranged as in Fig. 4.2, are of much smaller intensity than the MOT beams. Therefore, they are negligible when the MOT beams are ON. For the experimental detection of the synthetic Lorentz force, we turn the MOT beams OFF, as described in detail below.

We need to measure the transverse force F_y in dependence of the velocity v_x of the atomic cloud. Thus, we must prepare a cloud with a given center of mass (CM) velocity. For this purpose we use an additional pair of current coils¹ that produce a bias magnetic field along the symmetry axis of the anti-Helmholtz coils, x in our notation here. The bias field moves the center of the trap (the point where $\mathbf{B} = 0$), which displaces the cloud approximately 1 mm along the x -axis.

The measurement protocol is depicted in Fig. 4.3 and is as follows:

- i We load the trap with the bias magnetic field on.
- ii At $t = -2$ ms we reverse the bias magnetic field by reversing the current², which suddenly shifts the center of the trap. This introduces a force on the cloud due to the MOT beams. During the next 2 ms the cloud accelerates along the x -axis towards the new trap centre.
- iii Next we turn off the MOT cooling laser and all real magnetic fields. This moment corresponds to $t = 0$ in our presentation. The system is now simplified because Zeeman splitting of hyperfine levels is absent and the radiation force left, arising solely from the lasers implementing the synthetic Lorentz force, is not spatially dependent, it is only velocity-dependent.

¹Each coil has 4 turns.

²This is done with two DC voltage outputs of different polarity and two solid state relays, same model as used for switching the AH current, MPDCD3. The one that is initially on is switched off, and after $10\mu\text{s}$ the second one is turned on, reversing the voltage and hence the current

- iv The cloud starts to expand because the trapping is absent, but it also moves in the xy plane due to both the initial velocity, $v_x(t = 0)$, and the radiation pressure force.
- v After some delay time t , the cooling laser is suddenly turned on and the cloud is imaged with the camera.

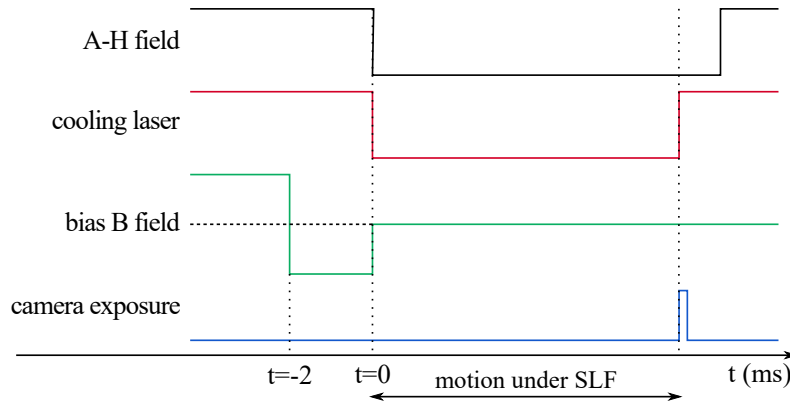


Figure 4.3: The measurement protocol for measuring the SLF.

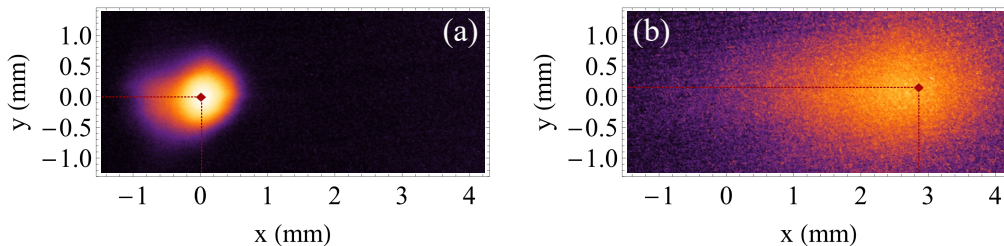


Figure 4.4: Cloud images with the position of the CM marked with a red diamond, at (a) $t = 0$ and at (b) $t = 4$ ms. The cloud is moving in the positive x direction because of the prior acceleration caused by the bias field, see text for details. It is also expanding because of the thermal distribution of the atoms.

From each frame we calculate the clouds CM by assuming that the fluorescence is proportional to the density. Examples of the images with the calculated CM indicated are shown in Fig. 4.4. From the trajectory traversed by the CM of the cloud $(x(t), y(t))$, we can find the force acting on the atoms. If we wish to image a cloud initially at rest we skip steps (i) and (ii). For a given delay time t , we repeat the measurement protocol a number of times (20 times in identical conditions), and subsequently average to obtain $x(t)$ and $y(t)$. As previously mentioned, gravity is along the z -axis in our system; free fall of atoms due to gravity does not affect the motion in the xy plane. It should be stated that we perform these measurements first with $|1\rangle \rightarrow |2\rangle$ lasers OFF, and then with these lasers ON, keeping all other parameters identical. The difference in the path $y(t)$, with lasers $|1\rangle \rightarrow |2\rangle$ ON and OFF, gives us the transverse motion due to the synthetic Lorentz force.

4.2.2 Results demonstrating the synthetic Lorentz force

The results of the experiment are illustrated in Fig. 4.5. We show the trajectory of the cloud $(x(t), y(t))$, in the presence of the synthetic Lorentz force, for three initial velocities: $v_x = -0.3$ m/s (squares), $v_x = 0$ m/s (diamonds), and $v_x = 0.6$ m/s (circles); $v_y = 0$ at $t = 0$ in each run of the experiment. There is a difference in the magnitude of the initial v_x for the positive and negative velocity [circles and squares in Fig. 4.5(a)], which is a result of our MOT retro-reflected geometry (see section 3.3.4), and the way we accelerate the cloud in step (ii) of the protocol. In order to prepare a cloud with positive v_x , the cloud is accelerated with the incoming MOT beam (coming from the laser side of the setup), whereas acceleration in the opposite direction is performed with the reflected beam which has smaller intensity. The reflected beam intensity is smaller due to the losses, which are a result of the passage of the incoming beam through the dense cloud (absorption), and partially due to reflection. Consequently, the negative initial velocity is smaller than the positive velocity.

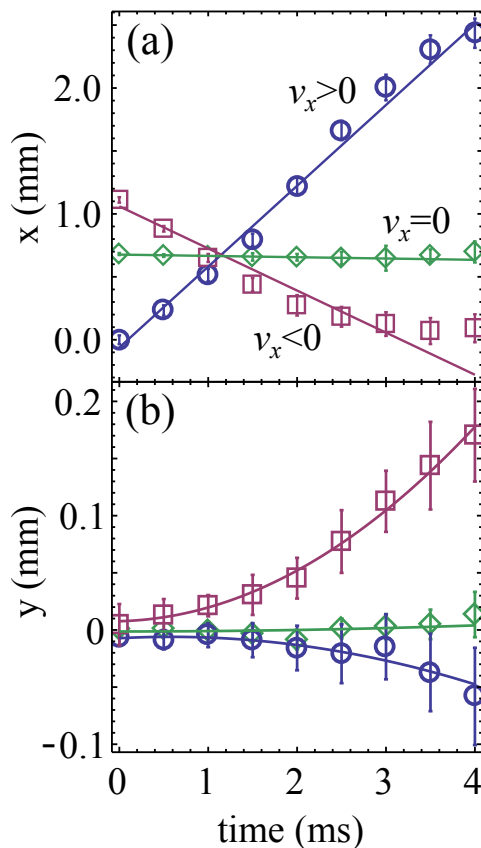


Figure 4.5: The trajectories of the CM of the atomic cloud in the presence of the synthetic Lorentz force. (a) $x(t)$, and (b) $y(t)$ for three different initial velocities, $v_x = 0.6$ m/s > 0 (circles), $v_x = -0.3$ m/s < 0 (squares), and $v_x = 0$ m/s (diamonds); initial component of $v_y = 0$ in all measurements. Accelerating motion along y is the signature of the transverse force F_y , which depends on v_x . The lines are fitted to the experimental data, linear fits for $v_x(t)$, and quadratic for $v_y(t)$.

For the lasers implementing the synthetic Lorentz force, we use the following detuning values: for the first step at 780 nm $\delta_{\leftarrow} = -\delta_{\rightarrow} = 2\pi \times 6$ MHz, and for the second step at 776 nm $\delta_{\uparrow} = -2\pi \times 3.5$ MHz and $\delta_{\downarrow} = 2\pi \times 7.1$ MHz. The two operational two-step pathways are $P(\leftarrow, \uparrow)$ and $P(\rightarrow, \downarrow)$, whereas the other two are far from resonance. The intensities of the beams used for Fig. 4.5 are $I_{780} = 0.060$ mW/cm² and $I_{776} = 2.9$ mW/cm², giving Rabi frequencies $\Omega_{780} = 2\pi \times 1.2$ MHz and $\Omega_{776} = 2\pi \times 0.94$ MHz.

By inspection of Fig. 4.5, we see that the cloud travels along the x -axis by inertia, whereas it accelerates along the y -axis due to the synthetic Lorentz force. The direction of the force depends on the sign of the velocity v_x (negative/positive v_x gives positive/negative F_y), and the force is zero for a cloud at rest. We observe an asymmetry in the force F_y , for the positive and negative velocity. In order to justify the exact choice of the detuning values δ_{\uparrow} and δ_{\downarrow} , and further investigate the observed asymmetry in the measured synthetic Lorentz force, we perform measurements in a slightly simplified configuration.

4.2.3 Further insight into the scheme

In order to inspect the force along the y direction arising from the two-step two-photon resonances in more detail, we perform measurements in a slightly simplified configuration, illustrated in Fig. 4.6.

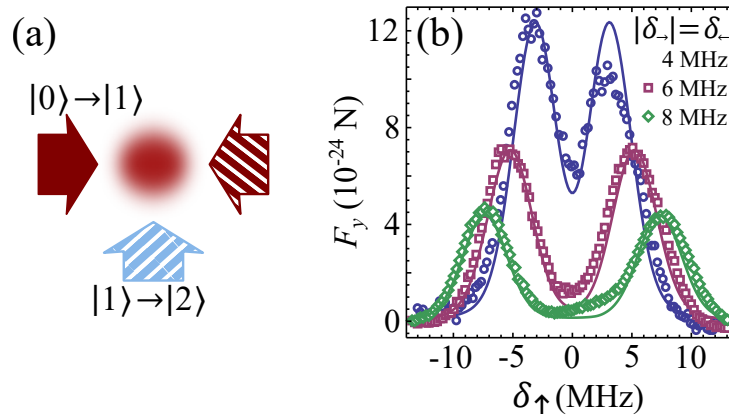


Figure 4.6: (a) The auxiliary configuration. Three beams are used, one of the second-step beams is omitted. (b) Frequency scan of the two-step two-photon resonance in the auxiliary configuration. The calculated (solid lines) and measured force F_y as a function of δ_{\uparrow} for the excitation with just three beams as shown in (a). Measurements are performed for the cloud with initial velocity zero. The plots show resonances for three values of the detuning $\delta_{\leftarrow} = -\delta_{\rightarrow} = 2\pi \times 4$ MHz (circles), 6 MHz (squares) and 8 MHz (diamonds).

We block the beam pointing towards the negative y -direction, and measure F_y arising from the remaining beam (propagating in the positive y -direction), which drives the $|1\rangle \rightarrow |2\rangle$ transition. The force is measured for an atomic cloud with velocity zero, as a function of the detuning δ_{\uparrow} , see Fig. 4.6. Measurements are done for three different

detuning values of the first-step beams $\delta_{\leftarrow} = -\delta_{\rightarrow} = 2\pi \times 4, 6, 8$ MHz. The intensities of the lasers driving the transitions are now $I_{780} = 0.043$ mW/cm² and $I_{776} = 4.8$ mW/cm², giving Rabi frequencies $\Omega_{780} = 2\pi \times 1.1$ MHz and $\Omega_{776} = 2\pi \times 1.2$ MHz. The two maxima in Fig. 4.6 are profiles of the two-step two-photon resonances: the peak in the vicinity of $\delta_{\uparrow} = -\delta_{\rightarrow} > 0$ corresponds to the excitation pathway $P(\rightarrow, \uparrow)$, and the peak close to $\delta_{\uparrow} = -\delta_{\leftarrow} < 0$ corresponds to $P(\leftarrow, \uparrow)$.

Solid lines in Fig. 4.6 show the theoretically calculated profiles of F_y as described in section 4.1.1 while taking into account the laser linewidth that increases due to the dithering of the laser frequency needed for the lock. The frequency at which we dither the laser is 14 kHz, this means that the laser will complete many cycles during the relevant interaction with the cloud and that the force can be calculated as a time average. The linewidth was determined to be $2\pi \times 1.5$ MHz by fitting to the experimental profiles. All parameters are identical as in the experiment, except that the Rabi frequencies are reduced by 20%. This partially arises from absorption which reduces the intensity of the lasers across a dense atomic cloud [62].

It should be pointed out that the peaks in $F_y(\delta_{\uparrow})$ are slightly displaced from the values $\delta_{\uparrow} = \pm|\delta_{\rightarrow}|$ towards $\delta_{\uparrow} = 0$; for example, for $|\delta_{\rightarrow}|$ at 6 MHz, the maxima are at 5.3 MHz. Moreover, the FWHM of the peaks is larger than the linewidth of the state $|2\rangle$, which is expected from the theory, see Fig. 4.1(d)³. This is explained by the fact that laser linewidth is finite, as mentioned previously. The finite laser linewidth of $|0\rangle \rightarrow |1\rangle$ lasers at 780 nm distorts the resonances as follows: the side of the peak closer to $\delta_{\uparrow} = 0$ is lifted up in comparison the opposite side of the peak. This follows from the fact that the two-step two-photon resonance is stronger when $|\delta_{\rightarrow}|$ is closer to zero, which is evident from Fig. 4.6. The exact positions of the peaks at ± 5.3 MHz, explain the chosen detuning values for the second step at 776 nm, which were used to obtain Fig. 4.5: $\delta_{\uparrow} = -2\pi \times 3.5$ MHz and $\delta_{\downarrow} = 2\pi \times 7.1$ MHz. They are chosen such that the operational pathways are effectively equally detuned from the two-step two-photon resonance: $P(\rightarrow, \downarrow)$ is detuned by $2\pi \times (-5.3 + 7.1)$ MHz = $2\pi \times 1.8$ MHz, and $P(\leftarrow, \uparrow)$ is detuned by $2\pi \times (+5.3 - 3.5)$ MHz = $2\pi \times 1.8$ MHz.

4.2.4 Discussion

Suppose that we repeat measurements corresponding to Fig. 4.6, but for an atomic cloud with mean velocity v_x different from zero. The results of such measurements would be identical as for $v_x = 0$, but the positions of the peaks would correspond to the Doppler shifted detuning values $\delta_{\rightarrow} - kv_x$ and $\delta_{\leftarrow} + kv_x$. Thus, because detuning can be mapped to velocity space, Fig. 4.6 can be reinterpreted as measurements for a

³Fig. 4.6(b) corresponds to a vertical cut in velocity space for $\delta_{\downarrow} = \delta_{\uparrow} = 0$, the two pairs of beams would form two perpendicular ridges in velocity space. The width of the cut through each ridge would be the width of the second excited state, $\Gamma_D = 2\pi \times 0.66$ MHz

fixed value of $\delta_{\leftarrow} = -\delta_{\rightarrow}$, and for three different velocities $v_x < 0$ (4 MHz), $v_x = 0$ (6 MHz), and $v_x > 0$ (8 MHz). This is sketched in Fig. 4.7, where we see that the two peaks separate (approach) each other for $v_x > 0$ ($v_x < 0$, respectively).

We use Fig. 4.7 for a detailed explanation of the synthetic Lorentz force measured in Fig. 4.5. In measurements shown in Fig. 4.5, we have $\delta_{\uparrow} < 0$, which means that the positive force $F_y > 0$ in Fig. 4.5 results from the left resonance peak in Fig. 4.7. Likewise, because $\delta_{\downarrow} > 0$ was used for Fig. 4.5, the negative force $F_y < 0$ results from the right resonance peak in Fig. 4.7. The transverse force F_y measured in Fig. 4.5, can be approximately identified with $[F_y(\delta_{\uparrow}) - F_y(\delta_{\downarrow})]v_x$, as illustrated in Fig. 4.7.

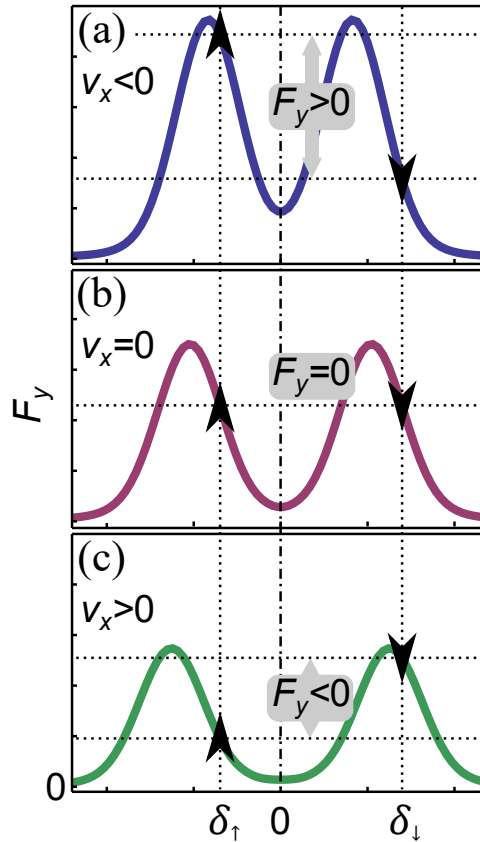


Figure 4.7: Interpretation of the synthetic Lorentz force from Figs. 4.2(a) and 4.5, via two-step two-photon resonances presented in Fig. 4.6. Sketch of the resonant peaks that would be obtained in the setup shown in Fig. 4.6 for three atomic velocities: (a) $v_x < 0$, (b) $v_x = 0$, and (c) $v_x > 0$. Vertical dotted lines illustrate the values of the detuning used for the lasers aligned on the y -axis in Fig. 4.1(a). Arrows denote the direction of the force exerted by those lasers, and illustrate the way F_y observed in Fig. 4.5 arises as a function of velocity v_x .

The choice of δ_{\uparrow} and δ_{\downarrow} in Fig. 4.5 is such that the strength of the forces arising from the two peaks balance each other, giving $F_y = 0$ for $v_x = 0$ [Fig. 4.7(b)]. Moreover, δ_{\uparrow} and δ_{\downarrow} are on the slopes of the two peaks in Fig. 4.7(b) for an atom with $v_x = 0$, where the maximal magnitude of $\Delta F_y / \Delta v_x$ is expected (detuning translates into velocity space via Doppler effect). For an atom with $v_x < 0$ [see Fig. 4.7(a)], the two

peaks approach each other, yielding greater force from the left peak, which results in $F_y > 0$ for $v_x < 0$, and the opposite for $v_x > 0$ which yields $F_y < 0$ as shown in Fig. 4.7(c).

It should be noted that while doing the experiment an opposite chronological order was used to the order in which the figures are presented here. First scans such as the one shown in Fig. 4.6 were performed from which we chose the detunings based on criteria mentioned. This was also performed each day we ran the experiment due to the small drifts of the lock point of the lasers and other systematic effects.

It should be pointed out that this scheme is inherently asymmetric. The intensity of the resonance peaks shown in Fig. 4.7 decreases when they separate (for $v_x > 0$), in contrast to when they approach each other (for $v_x < 0$). Thus, the net force along y is larger for negative v_x , than for the velocity of the same magnitude but with a positive sign. By using a scheme from Fig. 4.2(b), one can remedy the asymmetry in the force, present in the three-level scheme, this will be presented in section 4.3. In addition, the initial density of the atomic cloud is not identical prior to acceleration in the positive/negative direction due to the slight asymmetry of the displaced trapping potential. This also affects the transverse force due to absorption and multiple scattering [62]. The inherent asymmetry in the force $F_y(v_x)$ and in the initial density of the cloud, is reflected in the asymmetry of the observed motion in Fig. 4.5 for $v_x < 0$ and $v_x > 0$. Importantly, all of these details only quantitatively affect the results, but not qualitatively.

4.3 Synthetic Lorentz force in an expanding cold atomic gas

In this chapter we present results obtained with the configuration shown in 4.2(b). In this configuration each pair again drives two-step two-photon transitions between three levels, from the same ground state but to *different* excited states. One pair of perpendicular laser beams, depicted with arrows with solid color filling, drives the $|0\rangle \rightarrow |1\rangle \rightarrow |2\rangle$ transition, while the other pair, marked with pattern filling, drives the $|0\rangle \rightarrow |1'\rangle \rightarrow |2'\rangle$ transition. Again, due to the Doppler effect and the geometry of the laser beams, both components of the radiation pressure force depend on both components of the atom velocity: $F_x = F_x(v_x, v_y)$ and $F_y = F_y(v_x, v_y)$. This gives us the opportunity to choose the detuning values of our lasers such that the radiation pressure force again mimics the Lorentz force.

In Fig. 4.8(a,b) we show the calculated force components F_x and F_y as a function of atom velocities for the system and laser detunings used in the experiment. This force pattern in velocity space can be separated into two components, equation 4.3. The resulting scalar potential, along with the rotating part of the force, is shown in Fig. 4.8(c). These two components will both influence the observed shape of the cloud. A detailed explanation of the numerical calculations can be found in section 4.1.1 and contributions of the two force components in velocity space are discussed later in this section. In contrast to the previous experimental realization detailed in section 4.2 where three different levels were used, in this work we use five different levels. As mentioned, using three different levels results in a similar force pattern in velocity space, however the force is not symmetric, i.e., F_y has different magnitudes for positive and negative v_x of same magnitude. Using five levels avoids this problem resulting in a better analogy with the Lorentz force and is adequate for experiments in which a symmetrical initial velocity distribution is used. Additionally, the cloud can be made rotationally asymmetric (elongated) enabling the observation of its rotation; this was not possible with the previous scheme

4.3.1 Analysis of the shape of the cloud in the presence of the SLF

The starting point in the experiment is again a cold atom cloud of ^{87}Rb atoms, as detailed in chapter 3.

For the SLF we use the geometry sketched out in Fig. 4.2(b) where the xy plane is the horizontal one. Beams propagating along the x direction drive the first step of our two-step scheme, where for $|0\rangle \rightarrow |1\rangle$ we now use the $|5S_{1/2}; F = 2\rangle \rightarrow |5P_{3/2}; F' = 2\rangle$ transition and for $|0\rangle \rightarrow |1'\rangle$ we use the $|5S_{1/2}; F = 2\rangle \rightarrow |5P_{3/2}; F' = 3\rangle$ transition. Beams propagating along the y direction drive the second step of the two-step exci-

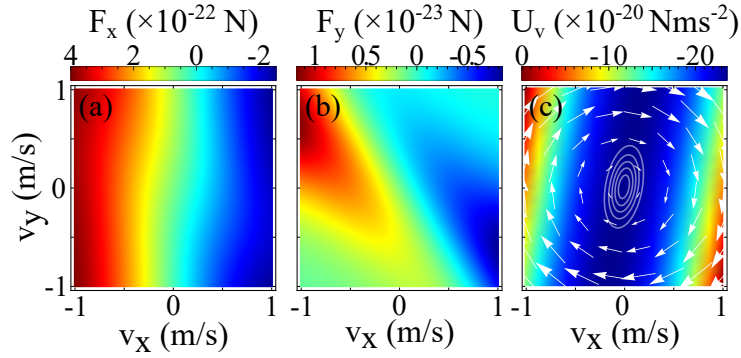


Figure 4.8: (a) The calculated force in the x and (b) y direction as a function of velocity. (c) Resulting potential in velocity space when the rotating part of the force (shown with white arrows) is excluded. The white contours show the calculated velocity distribution after 1 ms of expansion.

tation, for $|1\rangle \rightarrow |2\rangle$ we use the $|5P_{3/2}; F' = 2\rangle \rightarrow |5D_{5/2}; F'' = 3\rangle$ transition and for $|1'\rangle \rightarrow |2'\rangle$ we use the $|5P_{3/2}; F' = 3\rangle \rightarrow |5D_{5/2}; F'' = 4\rangle$ transition.

As before, the four SLF beams are provided from the output of the two frequency stabilized external cavity diode lasers (ECDLs) with nominal emission at 780 nm for the first step and 776 nm for the second step, as explained in section 3.3. Using heterodyne spectroscopy with an optical frequency comb, similar to the one shown in section 5.1, a laser linewidth of 1 MHz is measured. All beams are passed through acousto-optic modulators to obtain the desired frequencies.

Since one of the two-step two-photon pathways drives an open transition the presence of a repumper is necessary, for this we drive the $|5S_{1/2}; F = 1\rangle \rightarrow |5P_{3/2}; F' = 1\rangle$ transition. Compared to normal MOT conditions the population in the $|5S_{1/2}; F = 1\rangle$ state will be substantial leading to an appreciable radiation pressure force from the repumper beam. To avoid masking the observation of the SLF by introducing unaccounted forces into the system we copropagate the repumper beam with the $|5S_{1/2}; F = 2\rangle \rightarrow |5P_{3/2}; F' = 2\rangle$ beam.

The same experimental protocol is used as in section 4.2 for a cloud with zero velocity, i.e., no bias magnetic field is used to accelerate the cloud prior to the trap shutdown. Again, the SLF beams have no effect on the initial spatial and velocity distributions of the cloud while the trapping beams are present since the force arising from their absorption is small compared to forces due to the trapping beams. We repeat the measurement protocol 20 times in identical conditions, and subsequently average the TOF images to obtain the density distribution of the cloud for a given τ .

Following detuning values are chosen in the experiment: the first step beams, propagating along the x direction, are red detuned by $\delta_{01} = \delta_{01'} = -\Gamma_P/2$, where $\Gamma_P = 2\pi \times 6.1$ MHz is the decay rate of the ^{87}Rb $5P_{3/2}$ state [51]. The second step beams, propagating along the y direction, are blue detuned. Their detuning values, δ_{12} and $\delta_{1'2'}$ are chosen in such a way that the total two-photon detuning, Δ , for both two-

photon two-step pathways is equal to $\Delta = -\Gamma_D/2$, where $\Gamma_D = 2\pi \times 0.66$ MHz is the decay rate of the $^{87}\text{Rb } 5D_{5/2}$ state [56]. Following this condition, $\delta_{12} = \delta_{1'2'} = 2\pi \times 2.7$ MHz. The repumper laser is on resonance.

The choice of those detuning values follows from a similar experimental protocol used in section 4.2.3 in the same three beam configuration as in Fig. 4.6(a). Now, however, instead of two prominent peaks only one is present since we use different intermediate excited states. In this configuration not only does the CM move, there is also a tilting of the cloud present that was not visible in the previous configuration due to the rotationally symmetric shape of the cloud. In contrast, in this configuration the cloud has an ellipsoid shape; it is elongated along the y axis due to the Doppler friction force in the x direction that is a consequence of the red detuning of both the first step beams. We perform a frequency scan with each of the second step beams; we find the detuning at which the tilting angle is maximum, set the detuning in this way for both second step beams and finally measure the angle with both beams interacting with the cloud.

Intensities of the SLF beams are: $I_{01} = 0.039$ mW/cm², $I_{01'} = 0.063$ mW/cm², $I_{12} = 3.18$ mW/cm², and $I_{1'2'} = 0.063$ mW/cm². The intensity of the repumper beam is $I_{\text{repumper}} = 3.2$ mW/cm². Again, all beams are fiber coupled to PM fibers and polarized in the z direction. For the reasons discussed earlier, the repumper beam is coupled to the same fiber as the $|0\rangle \rightarrow |1\rangle$ beam. The offset in the force in the x direction, coming from the repumper radiative force, is compensated with a lower intensity of the $|0\rangle \rightarrow |1\rangle$ beam relative to a case in which the repumper would not be present. In such a way we achieved that the total force on atoms with zero velocity is zero, i.e., $F_x(v=0) = 0$. As a consequence the SLF will be of lower magnitude but will have the same characteristics.

To be able to analyze the TOF experimental results, first we turn to numerical simulations of our system.

The force in velocity space is calculated as detailed in section 4.1.1. Again, the procedure assumes that the lasers are perfectly monochromatic. However, as mentioned previously, there is a finite laser linewidth in the experiment that should be taken into account. Considering that the spectral profile of diode lasers can be described by a Gaussian in the frequency domain, we now introduce the laser linewidth in the simulations in a somewhat simpler fashion, although equivalent to the way in which it was introduced in section 4.2; we now convolve the force in velocity space with a Gaussian whose FWHM corresponds to the measured laser linewidth, i.e., to 1 MHz. Calculated resulting forces F_x and F_y as a function of atom velocities for relevant rubidium atomic levels and laser parameters used in the experiment are shown in Fig. 4.8(a,b). The repumper laser is also included in the calculations. It is obvious that the features in velocity space are not as prominent as those shown in Figs. 4.1(c) and (d), this is a

consequence of the laser linewidth being included in the calculations as mentioned.

One can see from Fig. 4.8(b) that the obtained force pattern has the wanted properties: F_y is positive/negative for atoms with a negative/positive velocity component v_x . Positive F_y arises as a result of driving the $|0\rangle \rightarrow |1\rangle \rightarrow |2\rangle$ transition, by the laser beam pair marked with solid filling in Fig. 4.2(b). Due to the red detuned first step laser driving the $|0\rangle \rightarrow |1\rangle$ transition, this two-step two-photon pathway is resonant only for atoms with negative v_x . The positive force in the $+y$ direction is then a consequence of the second step laser beam driving the $|1\rangle \rightarrow |2\rangle$ transition. In a completely analogous way, a negative F_y arises as a result of driving $|0\rangle \rightarrow |1'\rangle \rightarrow |2'\rangle$ transition which is resonant only for atoms with positive v_x .

In Fig. 4.8(c) we present the calculated potential in velocity space; a consequence of the first term on the right hand side in equation 4.3 as described in section 4.1.1. Direction and magnitude of the $\mathbf{F}_{SL}(\mathbf{v})$ force is also shown, given by the white arrows. Consider now how these two terms effect the atomic velocity distribution. We start with a symmetric velocity distribution at $t = 0$, which is a common initial condition in a MOT. Shortly after $t = 0$ the cloud will be reshaped in velocity space to a tilted ellipsoid by the potential shown in Fig. 4.8(c). Simultaneously, the rotating part of the force, $\mathbf{F}_{SL}(\mathbf{v})$ increases the distribution's deflection angle while preserving its ellipsoidal shape. This reshaped velocity distribution will give rise to a reshaped spatial distribution of the cloud, which can be detected in TOF measurements.

The expansion of the cloud in the presence of the SLF laser beams is calculated by employing the Fokker-Planck equation, again, see section 4.1.1. The initial phase space distribution of atoms $P(x, y, v_x, v_y, t = 0)$, which is the input distribution for the Fokker-Planck equation, is defined using measured experimental values. These were determined by measuring the time evolution of the cloud's thermal expansion in a standard TOF measurement with no SLF beams present. The Fokker-Planck equation is solved numerically for different expansion times, providing the phase space distribution of atoms in the cloud for a given time. The calculated atomic density distribution is then subsequently compared to the TOF measurements.

In Fig. 4.9 we present measured (b,e,h) and calculated (c,f,i) atom density distributions after $\tau = 4$ ms of expansion time for three experimental configurations (a,d,g), respectively.

The atomic system and laser parameters used in the calculations are identical to the experimental ones, given above. The cooling laser detuning is -3.6Γ , providing a symmetrical Gaussian shaped density distribution of the cloud at $t=0$ ms whose standard deviation (SD) is $\sigma_x = 0.25$ mm and a velocity distribution whose SD is $\sigma_v = 0.1$ m/s.

In the configuration presented in Fig. 4.9(a) only the first step SLF beams, $|0\rangle \rightarrow |1\rangle$ and $|0\rangle \rightarrow |1'\rangle$, are present. An ellipsoid shape of the cloud is measured elongated along the y axis, Fig. 4.9(b). The simulated atom density distribution corresponding

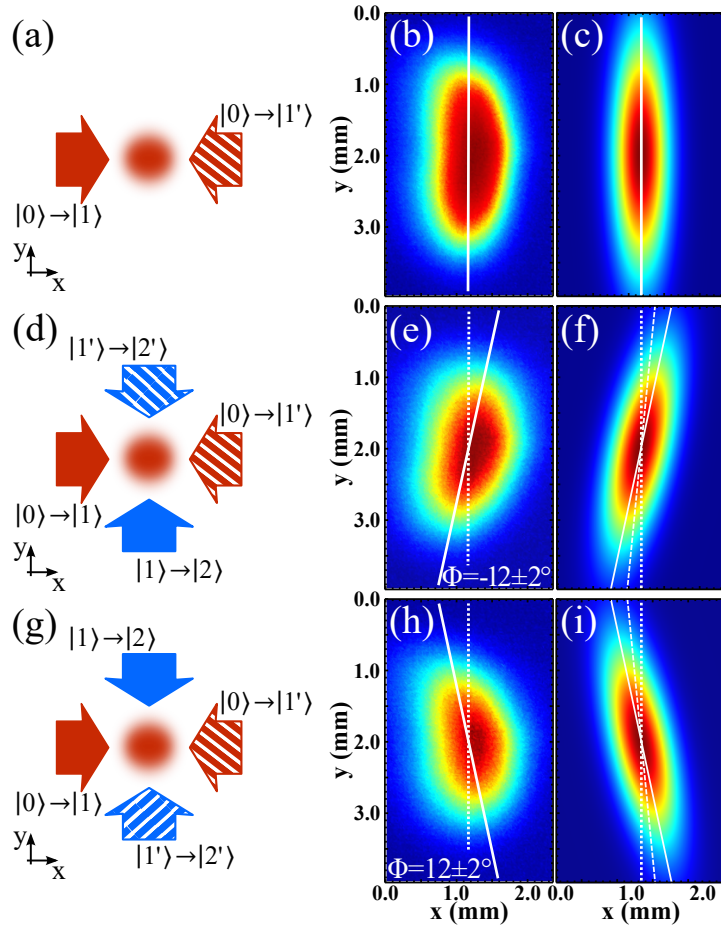


Figure 4.9: Atom density distributions after TOF of 4 ms for three different configurations, (a,d,g). Corresponding experimental, (b,e,h), and numerical results, (c,f,i), are shown in the same row. (b,c) Density distribution with only the first step beams present. (e,f,h,i) Density distributions with all four beams present, hence under the influence of the SLF. Note that the two second step beams have switched places from (d) to (g). The deflection angles of the major axes are indicated with full white lines. In panels (f,i) a dashed line indicates what the deflection angle would be without the SLF term in equation ???. See text for details

to this experimental geometry is shown in Fig. 4.9(c). As mentioned, the ellipsoid shape is a result of a friction force in the x direction resulting from the red detuned first step SLF beams. This measurement serves as a control, not only to make sure that the ellipsoid shape of the cloud is due to the first step beams, but also to gauge the reference angle of the ellipsoid. We find the deflection angle of the major axis by fitting a 2D Gaussian to the density distribution.

By adding the second step SLF beams, $|1\rangle \rightarrow |2\rangle$ and $|1'\rangle \rightarrow |2'\rangle$, our scheme of two pairs of two-step two-photon transitions is fully realized, Fig. 4.9(d). The measured atom density distribution is still ellipsoidal, but tilted by an angle $\Phi = (-12 \pm 2)^\circ$ relative to the y axis, Fig. 4.9(e). This angle is a unique signature of our scheme of atoms interacting with the field of two pairs of perpendicular laser beams that drive two-step two-photon transitions. The corresponding simulation of the atom density distribu-

tion, is shown in Fig. 4.9(f). Good agreement between measured and calculated atom density distribution is observed. The calculated angle, $\Phi_{num} = -11.6^\circ$, is within the uncertainty of the measured angle. For the density distribution in Fig. 4.9(f), the α_{ij} coefficients are calculated to be $(\alpha_{xx}, \alpha_{xy}, \alpha_{yx}, \alpha_{yy}) = (-3.4, 0.79, -0.20, -0.10) \times 10^{-22} \text{ Ns/m}$, giving $\alpha_R = 0.50 \times 10^{-22} \text{ Ns/m}$. In order to distinguish between the two contributions that produce the Φ_{num} angle, i.e., the trapping potential and the SLF, arising from the first and second term in equation 4.3, we calculate the density distribution without the SLF contribution ($\alpha_R = 0$). The obtained deflection angle $\Phi_{num}(\alpha_R = 0) = -5.0^\circ$ is significantly smaller than the angle $\Phi_{num} = -11.6^\circ$ and is indicated with a dashed line in Fig. 4.9(f). This is expected based on the discussion presented in Section III, which confirms the observation of the synthetic Lorentz force in a measured cold cloud density distribution shown in Fig. 4.9(e).

To recheck our experimental findings we switch the two second step SLF beams, obtaining the configuration shown in Fig. 4.9(g). To ensure the same alignment only the output of the fibers for the two beams are exchanged, whereas all holders, optics and experimental parameters are left unchanged. The atom density distribution remains ellipsoidal, but it is now tilted at an angle $\Phi = (12 \pm 2)^\circ$ relative to the y axis. The corresponding calculated distribution shown in 4.9(i) confirms the experimental result and conclusions analogous to the conclusions from the previous configuration can be made.

Another thing to note is that the tilt angle of the cloud does not increase for larger expansion times. This is due to the scalar potential, which would decrease the tilt angle if the rotating part of the force was not present. The tilt angle therefore stops increasing when the influences of these two terms on the tilt angle cancel each other. The expansion of $\tau = 4 \text{ ms}$ was therefore chosen because of optimal signal quality, since for smaller times the cloud is similar to the initial symmetric shape, while for larger times the signal deteriorates due to heating and diffusion.

Considering that the cyclotron frequency does not depend on the velocity of the charged particle, by analogy we expect that the deflection angle Φ in our system does not depend on the initial width of the Maxwell-Boltzmann velocity distribution of the cold cloud, i.e., on the cloud temperature. In Fig. 4.10 we show the measured and calculated deflection angle Φ as a function of the SD of the velocity distribution, points and line, respectively. As mentioned in section III, the SD of the initial velocity distribution, σ_v , is obtained from TOF measurements without the SLF beams. In the experiment σ_v , i.e., the temperature of the cold atoms in the MOT is easily tuned by changing the detuning of the cooling laser. The deflection angle is measured using the experimental configuration shown in Fig. 4.9(d), with all other experimental parameters identical to the ones used before. We can see that the measured and calculated angles agree well with the expected behavior, i.e., the deflection angle does not depend on the width of

the velocity distribution almost in the entire range. Deviation of the measured angle from the calculated constant value at wider velocity distributions arises because there is a considerable number of atoms with velocities that are beyond the velocity range in which the approximation used in equation (1) is valid, and therefore the effect of the SLF is less pronounced. For reference, see inset of Fig. 4.10 which shows the force in the y direction, $F_y(v_x, v_y = 0)$. Within the shaded area, which is from $v_x = -0.15$ m/s to $v_x = 0.15$ m/s the difference between the calculated force (green curve) and the linear approximation from equation (1) is below 4 %. However, for a cloud with $\sigma_v = 0.15$ m/s, already 32 % of the atoms have a velocity that is outside of the shaded area. For increasing σ_v this fraction will be even larger which illustrates why the model and the experimental results differ increasingly past $\sigma_v \approx 0.15$ m/s. The values of v_x for which $F_y(v_x, v_y = 0)$ has maximum absolute values are defined by the two-photon detuning via the Doppler shift. For a larger two-photon detuning the maximum force values would be further apart and so the velocity range in which the force is linear, and thus the effective observation of the SLF is possible, could be made larger. A more complicated model could be implemented that would take into account atoms with larger velocities, as well as other effects present in the MOT such as radiation trapping.

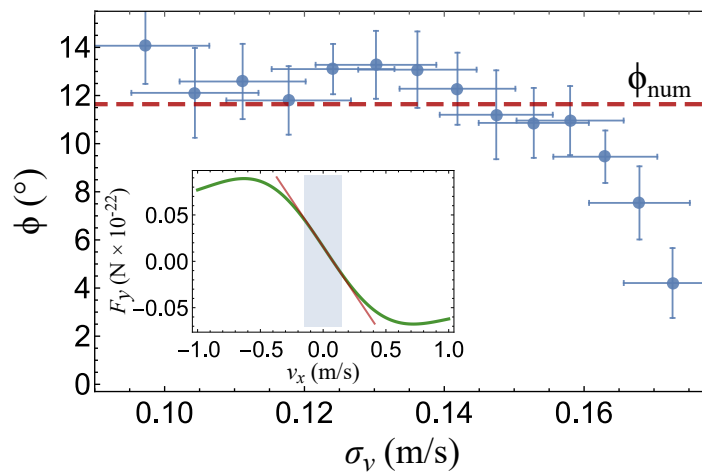


Figure 4.10: The deflection angle as a function of the SD of the velocity distribution, measured (circles) and calculated (line). The inset shows the force in the y direction as a function of the velocity in the x direction, $F_y(v_x, v_y = 0)$, the region $|v_x| < 0.15$ m/s is shaded while the line shows the slope at $v_x = 0$.

A visible difference between the experimental TOF distribution and the numerically predicted ones in Fig. 4.9 is the larger width of the experimentally observed distributions along the x axis, along which we effectively have optical molasses due to the red detuning of the first step beams. This faster expansion is possibly a consequence of radiation trapping and very similar to the effect observed in [20]. There the authors also observed a much faster expansion of their cloud in the molasses stage than what was predicted by the Fokker-Planck equation, and this was attributed to Coulomb-like

forces caused by radiation trapping. There is also additional heating not accounted for in the model, mostly due to the linewidths of the lasers which can also increase the observed width of the cloud. However, these potential additions to our model are out of scope for this thesis. The model presented here is simple yet powerful in the sense that it explains and fully predicts the behavior of our system for sufficiently low atomic temperatures that are typically achieved in MOT.

5 Frequency comb cooling

In this chapter results on our experiments in which we study the interaction of an optical frequency comb with a cloud of cold rubidium atoms are presented. Manuscripts based on these results are either submitted for review or being prepared for submission at the time of writing this thesis. The corresponding manuscripts can be found in [appendix B](#).

Mode-locked lasers have been proposed [63] and developed [64, 65] in the early days of laser physics. However, most of the focus in the later part of the 20th century was on the time domain; mode locked lasers produce very short pulses that are created as a sum of the of the longitudinal modes which have a fixed phase relationship, i.e., are "locked". At the turn of the century a paradigm shift happened¹ and the focus was shifted to the frequency domain in which the pulse train of a mode-locked laser generates a frequency comb: discrete, sharp lines that are regularly spaced [66].

A depiction of the time- and frequency-domain relationship is shown in Fig. 5.1, the two are connected by the Fourier transform.

The optical frequency of the n th comb mode is given by:

$$f_n = n f_{rep} + f_{ceo}, \quad (5.1)$$

where n is the comb mode number, f_{rep} is the repetition frequency of the laser, f_{ceo} is the carrier-to-envelope phase offset frequency. Since f_{rep} and f_{ceo} are measurable radio frequencies (RF), it follows that the FC provides a direct link between measurable radio frequencies to optical frequencies; by measuring these two frequencies we can determine the *absolute* frequency of all the comb modes (in terms of the primary cesium frequency standard). This has enabled absolute measurements of optical frequency standards [68, 69] and the unprecedented fractional accuracy and stability of optical clocks [70] down to the 10^{-18} level [71] will certainly lead to a redefinition of the second in terms of an *optical* frequency in the near future.

¹mostly enabled by the advent of the titanium-doped sapphire laser in the early 1990s

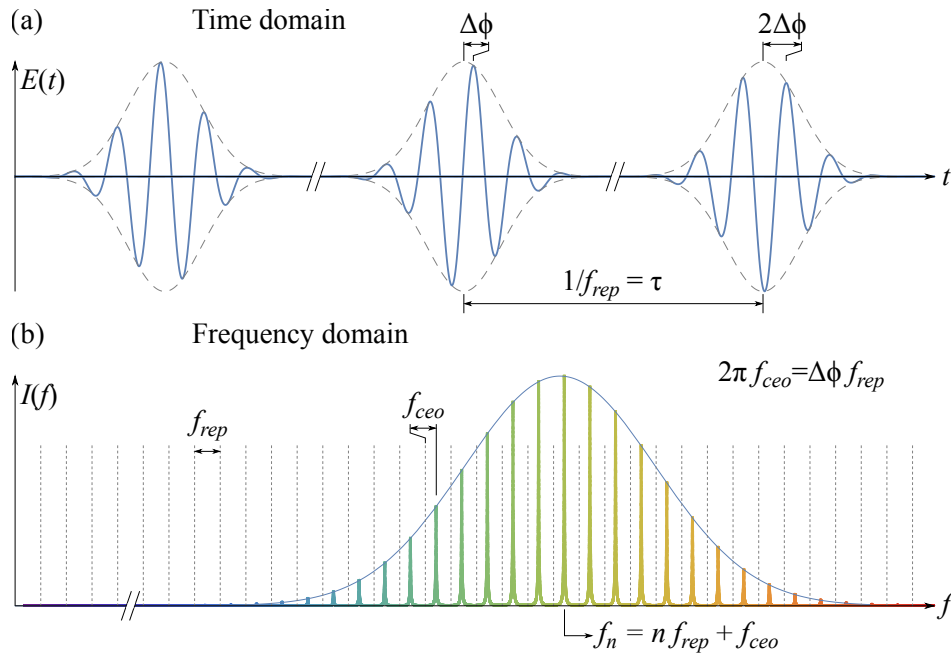


Figure 5.1: In the time domain (a) a mode-locked laser produces a train of ultra-short pulses (ps or fs) while in the frequency domain (b) it generates a frequency comb. The phase between the carrier (solid, blue) and the envelope (dashed, gray) changes from pulse to pulse by a fixed quantity, $\Delta\phi$, the relationship of this phase to the f_{ceo} is indicated. Adapted from [67].

5.1 Stabilizing the comb

Generally, f_{rep} and f_{ceo} depend on cavity length and dispersion in the cavity, which in turn depends on pump power. In practice this means that both frequencies will change over time due to temperature drifts and acoustic and current noise. For a FC to be an useful experimental tool these frequencies need to be stabilized.

The most common use of the FC today is in absolute optical frequency measurements. As mentioned, this stems from the fact that by stabilizing f_{rep} and f_{ceo} we stabilize the *absolute* frequencies of all the comb modes. This is usually achieved by measuring these two frequencies, and phase locking them to stable frequency references. While measuring f_{rep} is straight forward and just requires a photodiode, measuring f_{ceo} is experimentally complex and typically highly power consuming, requiring the well established f-2f interferometry [67]. This interferometry technique includes generating an octave-spanning spectrum by nonlinear pulse propagation through a highly nonlinear photonic crystal fiber and subsequent frequency doubling of the low frequency part of the spectrum; both processes are power consuming. To achieve the detection of f_{ceo} the n th mode is frequency doubled and interfered with its harmonic, the $2n$ th mode, on the far side of the octave spanning spectrum: $2(n f_{rep} + f_{ceo}) - (2n f_{rep} + f_{ceo}) = f_{ceo}$. Similar interferometric techniques can be used but all include nonlinear, power consuming processes (2f-3f, 3f-4f or other combinations [72, 73, 74]).

However, as stated in the introduction, we want to use the comb for laser cooling. As described in section 2.2.1, Doppler cooling requires knowledge of the absolute position of the laser/comb mode interacting with the atomic transition only to the same order as the width of the transition in question, that is, most important is the *relative* position with respect to the atomic transition used for cooling [1].

In this section we detail how we stabilize a fiber based frequency comb to an external cavity diode laser (ECDL) which is stabilized to the cooling transition in ^{87}Rb , $|5S_{1/2}; F = 2\rangle \rightarrow |5P_{3/2}; F' = 3\rangle$. This enables us to determine and stabilize the detuning of a specific comb tooth relative to this transition which is needed for Doppler cooling, as mentioned above. By stabilizing the relative position of a single comb tooth, f_n , in respect to the stabilized ECDL and simultaneously stabilizing f_{rep} we indirectly stabilize f_{ceo} , i.e., the whole comb, evident from equation 5.1. However, the absolute stability of the comb is then determined by the stability of the ECDL. We analyze and discuss the absolute stability of the comb later in the text.

The femtosecond fiber laser used to produce the comb is an erbium doped fiber laser² [75] (Toptica FemtoFiber) whose primary emission is a 50 nm (FWHM) broad spectrum centered around 1580 nm, with a repetition frequency $f_{rep} \approx 80.5$ MHz, an average power of $P_{avg} \approx 230$ mW, and a pulse length of 200 fs. This output is frequency doubled on a PPLN crystal to obtain a spectrum centered around 780 nm (FWHM = 10 nm), the wavelength of the rubidium transition of interest with an average total power of $P_{avg} \approx 75$ mW. Approximately 100 000 comb lines are contained under the FC spectral envelope. The ECDL used (Moglabs CEL002) is stabilized to the wanted rubidium line by polarization spectroscopy, as described in section 3.3.3. This locking technique allows high bandwidth feedback and also avoids directly modulating the laser frequency reducing the achievable linewidth. It is important to note that cold atom experiments require the use of a stabilized laser relative to the cooling transition which means that in laboratories performing these kinds of experiments a stabilized CW laser is necessarily already set up. This makes our stabilizing scheme straightforward to implement in these setups.

We achieve the fixing of the optical frequency of a single comb mode by phase locking the frequency comb to the stabilized ECDL, see right part of Fig. 5.2. A fraction of the ECDL light (≈ 10 mW) and a fraction of the FC light (≈ 1 mW) are copropagated and directed first onto a grating (Thorlabs GR13-1208) to spatially filter the unwanted comb modes to reduce background noise, and then onto a fast photodiode (Thorlabs PDA10A-EC). The signal, f_{beat} , is then fed through a series of filters (Mini Circuits BLP-30+ and BLP-50+) and amplifiers (Mini Circuits ZFL-1000LN+), shown in Fig. 5.2. Despite spatial filtering the beat signal contains beats with multiple comb modes, for this reason the cut-off frequency of the filters is chosen to be $f_{cut-off} < f_{rep}/2$, this way

²Mode-locking is achieved by nonlinear polarization rotation, see reference for more details.

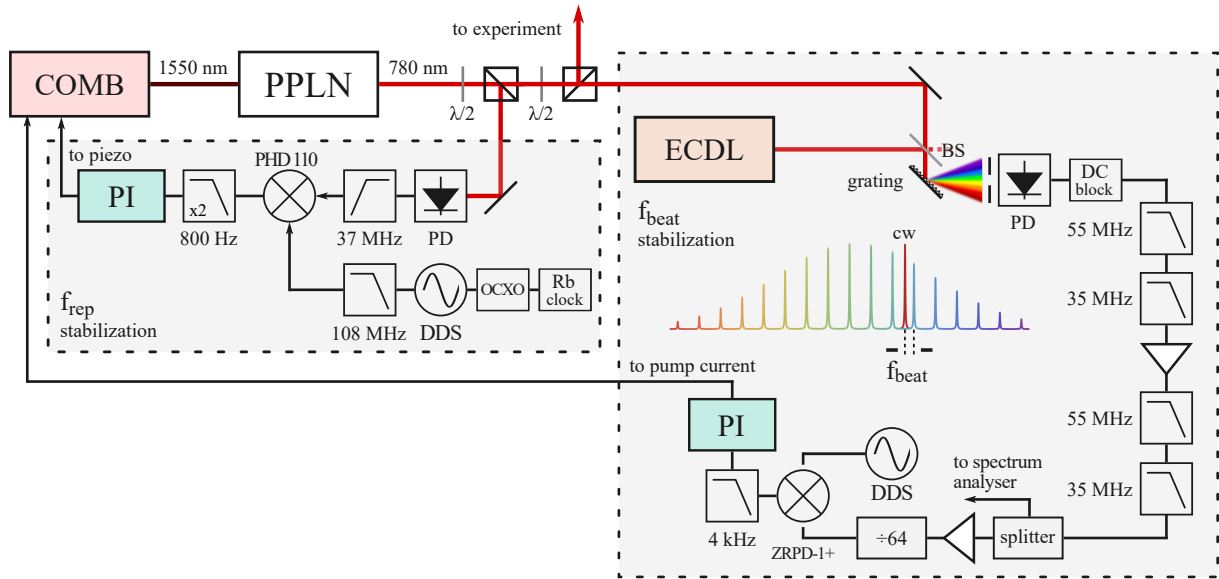


Figure 5.2: Sketch of the experimental setup for fully stabilizing the comb using an ECDL reference. The left and right section of the image shows the scheme for stabilizing f_{rep} and f_{beat} , respectively. The DDS's in the left and right part of the figure are the same unit. The spectrum after the grating is an illustration, in reality it does not stretch to the visible part of the spectrum. The setup does not require an iris, the spatial filtering is achieved due to the photodiode active area being small. PPLN: periodically poled lithium niobate crystal, PD - photodiode, $\lambda/2$ - half-wave plate, DDS - direct digital synthesizer, OCXO - oven controlled crystal oscillator, ECDL - external cavity diode laser, BS - beam splitter.

the beat with a single mode gets filtered through. This amplified signal is then split, with one part being used for monitoring the beat frequency. The beat signal is shown in Fig. 5.3. The cutoff of the low pass filters is clearly visible in Fig. 5.3(a). For the beat signal we achieve a 40 dB signal-to-noise ratio with a measured FWHM of 60 kHz (1 kHz bandwidth), this width sets an upper limit on the width of both the comb and the ECDL.

The other part of the filtered and amplified signal is sent to a 64-fold divider (RF bay, FAS-64). The divider serves to increase the capture range of the lock which is necessary due to limits on the feedback bandwidth characteristic to lasers based on Er-doped fibers. The output signal from the divider is fed into an analog phase detector (Mini Circuits ZRPD-1+) together with a reference signal supplied by a direct digital synthesizer board (DDS, Novatech instruments, DDS9m). The output from the phase detector is and passed through low pass filter (4 kHz cutoff) to obtain an error signal. We then use a PI controller (Newport LB1005) to generate the feedback signal which modulates the pump power in the cavity in order to keep the selected comb mode fixed relative to the ECDL frequency, at a frequency difference f_{beat} .

To stabilize the repetition frequency we mix the detected and filtered (to reduce low frequency noise, Mini Circuits BHP-50+) repetition rate with a reference signal from

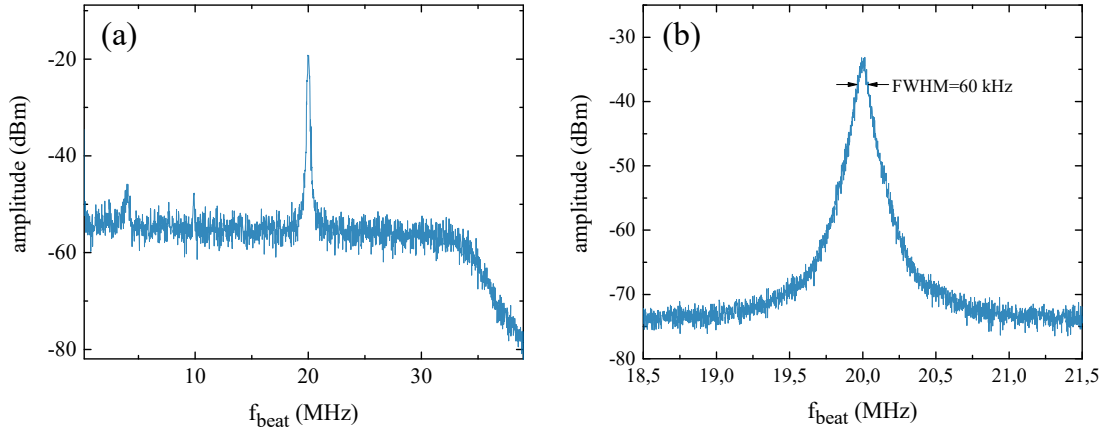


Figure 5.3: The beat signal of the FC and the CW reference laser. (a) A larger range showing approximately the available scanning range, bandwidth was 30 kHz, sweep time 1 s. At very low frequencies the divider stop functioning normally, while at frequencies > 30 MHz the roll-off because of the low-pass filters begins. (b) The beat signal recorded with a 3 MHz range, the -3 dB width is indicated. Bandwidth was 1 kHz, sweep time 10 s.

the same DDS generating the reference signal for the stabilization of the optical beat frequency, see left part of Fig. 5.2. The error signal is generated with a phase detector module that is installed into the laser controller (Toptica PHD 110), passed through a second order low pass filter with a 800 Hz cutoff to filter out high frequency noise, and then fed into a built-in PID controller (Toptica PID 110) which then controls the piezo which changes the length of the cavity. This enables the stabilization of the repetition frequency, f_{rep} , which together with stabilizing the position of a single comb tooth as described earlier, stabilizes the whole comb.

5.1.1 Evaluation of the stability

The measured repetition frequency and optical beat frequency, f_{rep} and f_{beat} , are shown in Fig. 5.4(a) and (b) with the corresponding Allan deviations shown in panel (c). One can see from the Allan deviations that the lock functions very well, going below the mHz level at 10 s integration time for both f_{rep} and f_{beat} . From this we can conclude that the stability of the comb is limited not by the noise introduced by the locking procedure, but rather by the stability of the ECDL reference laser, expected to be orders of magnitude lower [59, 76].

The PI corners of the f_{rep} and f_{beat} loops are set to 14 Hz and 300 Hz, respectively. These values are deliberately chosen to be low, especially for the f_{rep} loop, in order to avoid transferring high frequency noise from the reference frequency onto the optical spectrum. Any noise on the reference frequency for the loop that controls the repetition frequency transfers to the optical spectrum, multiplied by the mode number, n , evident from equation 5.1. Since n is of the order of $n \approx 5 \times 10^6$ the influence on optical

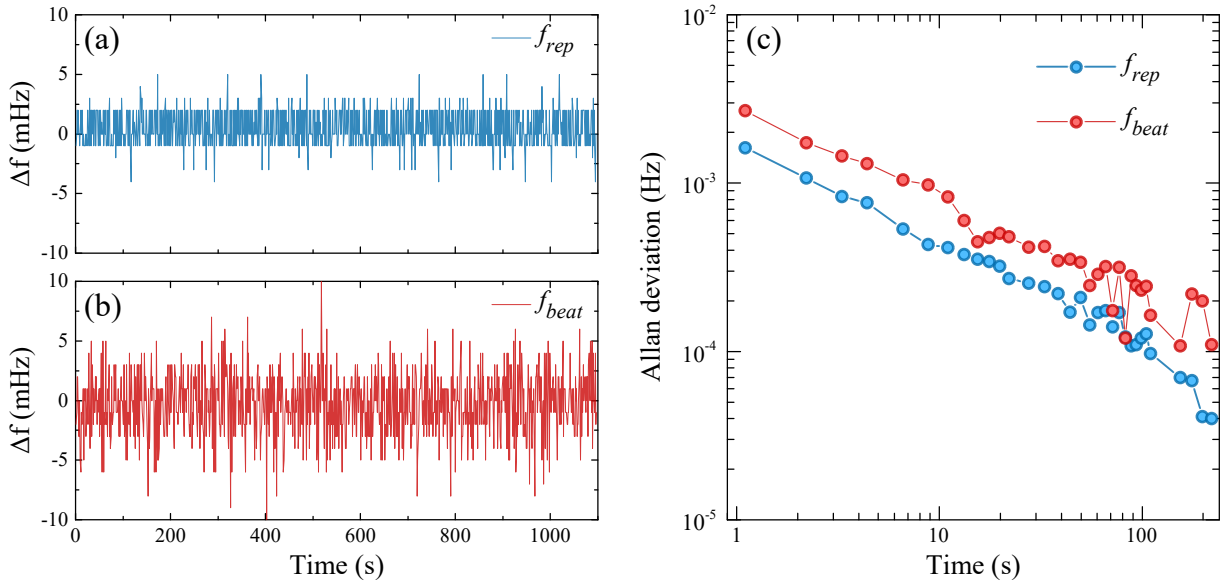


Figure 5.4: Measurement of the lock performance, frequency offset Δf from the starting measured value of (a) f_{rep} and (b) f_{beat} frequencies while both feedback loops are enabled. (c) the corresponding Allan deviations.

frequencies is considerable. For this reason it is necessary to use a frequency reference with very low phase noise. The DDS that we use to synthesize the reference frequency is self-referenced to an oven-controlled crystal oscillator (OCXO, Miteq PLD-1C-10-475-15P), which is in turn phase-locked to a rubidium frequency standard (Stanford Research Systems FS725) with a 10 MHz output. The OCXO has a 475 MHz output and acts here as a frequency multiplier that introduces very little phase noise. The DDS then divides this clock frequency to the wanted $\approx 80.5\text{ MHz}$, which is further filtered (Mini Circuits BLP-100+) to remove remainders of the clock frequency and aliasing frequencies. An alternative way would be to use the 10 MHz output of the Rb standard to reference the DDS, which would then multiply this to the wanted $\approx 80.5\text{ MHz}$, however, this was found to unexpectedly introduce far more phase noise. Although the resulting signal is very clean (stated phase noise of $< -120\text{ dBc}$ at 10 kHz offset) the intrinsic short-term stability of the frequency comb is better. For this reason we set the PI corner of the f_{rep} loop low in order not to interfere with this intrinsic short-term stability, rather only correct for long-term drifts which occur mostly because of temperature variations. Since the two control loops are not orthogonal the PI corner of the f_{beat} loop is also set low so as to not transfer high-frequency noise to the other loop.

As mentioned previously, the absolute stability of the FC is expected to be limited by the absolute stability of the ECDL reference laser. To evaluate this stability and to demonstrate the abilities of our locking scheme we perform a heterodyne beat of the stabilized FC with a separate ECDL laser. This laser is locked to a two-photon transition, ^{87}Rb , $|5S_{1/2}; F=2\rangle \rightarrow |5D_{5/2}; F'=4\rangle$ by a dither lock. To observe a peak to which to lock to we detect 420 nm fluorescence with a photomultiplier tube in a rubidium

cell heated and to $\approx 110^\circ\text{C}$. The temperature of the cell is stabilized with a temperature controller (MPT-5000, *Wavelength Electronics*) controlling the current through the heating wire. For the purpose of this measurement, the polarization spectroscopy cell was also temperature stabilized to reduce the drift in frequency. This was done by placing the cell in a acrylic glass case and heating it to $\approx 60^\circ\text{C}$ with a Peltier module controlled with a temperature controller (MPT-2500, *Wavelength Electronics*). The fluorescence spectra are shown in Fig. 5.5. Somewhat expectedly, the spectra of the $|5S_{1/2}; F = 2\rangle \rightarrow |5D_{5/2}; F' = 4\rangle$ fluorescence, shown in Fig. 5.5(b), and the one photon transition absorption to the same states, shown in Fig. 3.10, are almost identical, the only difference being the observed width and a factor of two in the frequency scale due to the number of photons in the process. A laser stabilized to this transition can be used as a primary standard for length measurements due to the inherent absolute stability of the transition, reported to be on the 10^{-11} level [77]. The measured beat frequency is shown in Fig. 5.6(a) with the corresponding Allan deviation in Fig. 5.6(b).

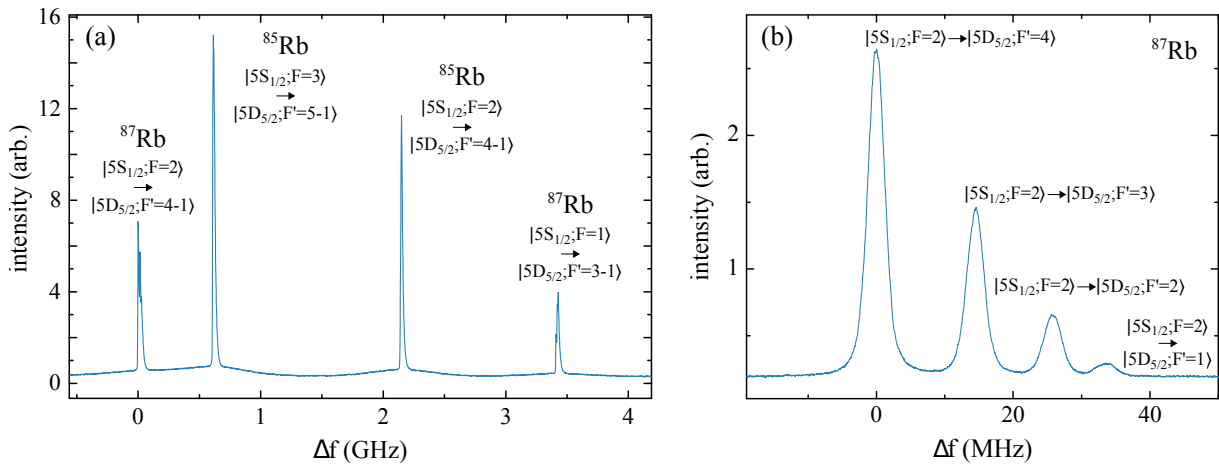


Figure 5.5: Fluorescence spectra of the two-photon transition in rubidium from the $|5S_{1/2}\rangle$ state to the $|5D_{5/2}$ state. (a) A scan across all possible transitions for ^{85}Rb and ^{87}Rb . Notice that a Doppler broadened background is visible. (b) A scan across the $|5S_{1/2}; F = 2\rangle \rightarrow |5D_{5/2}; F' = 4$ to 1 transitions. Notice that a Doppler broadened background is visible. Also notice that the frequency scale is a factor of two less than what they would be for a single photon transition. The level splitting used for calibrating the spectra are found in [51, 78].

The measured Allan deviation determines the upper limit on the absolute stability of our locking scheme which is on the order of tens of kilohertz. The measured stability is expected from a DC locking technique such as the one used, polarization spectroscopy. The fractional stability at 10 s integration time is below $\Delta f/f \approx 10^{-11}$ which is excellent considering the simplicity of our setup, and more importantly more than satisfactory for laser cooling. Further enhancement of the absolute stability could be achieved by stabilizing the temperature of the AOM crystal that provides the light for the polarization spectroscopy, see Fig. 3.13. The efficiency of an AOM varies signif-

icantly with regards to temperature, hence any drift in the temperature of the crystal would change the total power in the pump and probe beams in the polarization spectroscopy setup, changing the position of the zero crossing and thus the frequency of the reference laser.

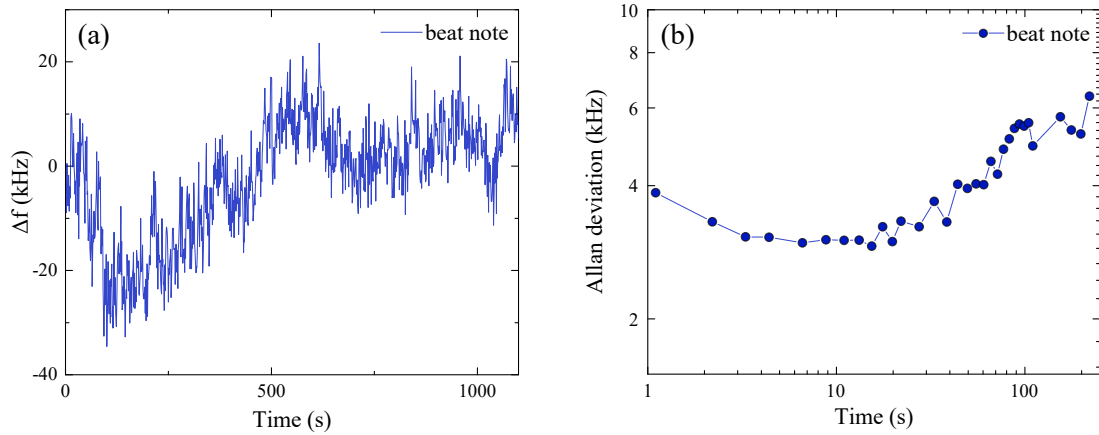


Figure 5.6: Measurement of the absolute stability of our locking scheme by heterodyne beating our FC with a ECDL locked to a two-photon transition, ^{85}Rb , $|5S_{1/2}; F = 2\rangle \rightarrow |5D_{5/2}; F' = 4\rangle$. (a) The measured frequency drift of the beat note. (b) The corresponding Allan deviation.

5.2 Laser cooling using a frequency comb

In this section we show results demonstrating sub-Doppler FC cooling of rubidium atoms. As stated in the introduction, up until now only the two previously mentioned recent experiments have reported FC cooling, and both of them achieve cooling to near the Doppler temperature [34, 38]. We also demonstrate FC cooling and additionally show that temperatures below the Doppler limit, i.e. sub-Doppler temperatures, can be achieved by FC cooling. We demonstrate sub-Doppler cooling of Rb atoms to $55 \mu\text{K}$ on a single-photon transition at 780 nm, a transition typically used in CW laser cooling experiments with an associated Doppler temperature of $146 \mu\text{K}$ [51]. Also, as stated in chapter 3, the results shown here were performed with the 2nd generation setup MOT.

5.2.1 Frequency comb radiation pressure force

Laser cooling relies on the radiation pressure force. Hence, in order to understand the physical mechanisms that drive the FC cooling, one has to first understand the force exerted on atoms when they are resonantly excited by the FC. We therefore start our study by measuring the FC radiation pressure force on cold Rb atoms. The comb centered at 780 nm drives the standard ^{87}Rb $|5S_{1/2}\rangle \rightarrow |5P_{3/2}\rangle$ cooling transition. A single linearly polarized beam is collimated and sent through an acousto-optic modulator (AOM) for fast on/off switching, and then directed to the center of the trap. A total power of 18 mW was used with a beam FWHM of 2.7 mm, which gives translates to $\approx 0.5 \mu\text{W}$ per comb mode. The measurement sequence starts with preparation of a cold ^{87}Rb cloud using the CW MOT setup (FC beam off). At $t=0$ we turn off the MOT cooling beams, and switch on the FC beam. The weak repumper light is left on continuously to optically pump the atoms out of the $|5S_{1/2}; F = 1\rangle$ ground state. It propagates perpendicular to the FC, is arranged in a counter-propagating configuration, and has no measurable mechanical effect. We let the FC to interact with the cold cloud for 1 ms, and during this time the cloud center of mass (CM) accelerates along the FC beam propagation axis ($+x$ -direction) due to the FC radiation pressure force. At $t = 1$ ms FC and repumper beams are switched off, and the cloud is left to freely move and expand for 5 ms. At $t = 6$ ms the CW cooling beams are turned on and the cloud fluorescence is imaged with the camera to determine the cloud CM displacement in the x direction, Δx_{CM} . We then use Δx_{CM} to calculate the acceleration of the cloud, which, using the mass of a single Rb atom, finally gives the FC force. Averaging of 4 consecutive measurements is performed and shown in Fig. 2.23(b).

The FC force depends on the relative detuning of the comb lines with respect to the hyperfine transitions. As the FC spectrum consists of identical, regularly spaced comb lines, we describe the FC spectrum by the detuning δ of the n -th comb mode from the $|5S_{1/2}; F = 2\rangle \rightarrow |5P_{3/2}; F' = 3\rangle$ transition. Accordingly, the $F(\delta)$ scan in

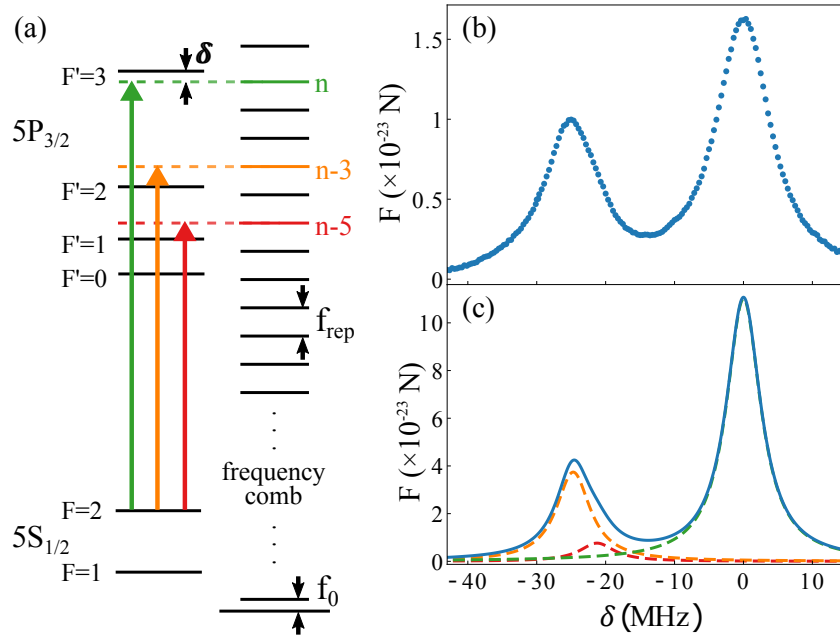


Figure 5.7: (a) Scheme of relevant ^{87}Rb energy levels and FC modes; (b) measured and (c) calculated FC force as a function of detuning. The total force in (c), blue line, reflects the interaction with three comb modes: n -th comb mode with the $|5S_{1/2}; F = 2\rangle \rightarrow |5P_{3/2}; F' = 3\rangle$ transition - green dashed line; $(n - 3)$ -rd mode resonance with the $|5S_{1/2}; F = 2\rangle \rightarrow |5P_{3/2}; F' = 2\rangle$ transition - orange dashed line; and $(n - 5)$ -th mode resonance with the $|5S_{1/2}; F = 2\rangle \rightarrow |5P_{3/2}; F' = 1\rangle$ transition - red dashed line.

Fig. 2.23(b,c) repeats every $f_{\text{rep}} = 80.5$ MHz. Two distinct peaks appear in one f_{rep} scan reflecting the interaction with three comb modes, as shown schematically in Fig. 5.7(a). The peak at $\delta = 0$ is due to n -th comb mode in resonance with the $|5S_{1/2}; F = 2\rangle \rightarrow |5P_{3/2}; F' = 3\rangle$ transition, whereas the peak at $\delta \approx -25.5$ MHz is due to $(n - 3)$ -rd mode in resonance with the $|5S_{1/2}; F = 2\rangle \rightarrow |5P_{3/2}; F' = 2\rangle$ transition, and $(n - 5)$ -th mode in resonance with the $|5S_{1/2}; F = 2\rangle \rightarrow |5P_{3/2}; F' = 1\rangle$ transition. The contributions to the FC force coming from resonances with different comb modes are expressed more clearly in the results of calculations of the FC force shown in Fig. 2.23(c), where contributions of relevant transitions are explicitly given. The calculated FC force is obtained by numerically solving the Optical Bloch Equations describing the excitation of six-level ^{87}Rb atoms by the FC [79], and subsequently using the Ehrenfest theorem.

The agreement between measured and calculated FC force in Fig. 5.7(b,c) is reasonable, considering there are no free parameters in the model. Relative positions of the two peaks are well reproduced, though there is a small but noticeable broadening of the measured peaks, which we attribute to systematic effects such as stability of the RF reference used to stabilize FC, Zeeman splitting due to the stray magnetic fields, and Doppler broadening due to the photon-momentum transfer. It is worth noting

that similar line broadening has also been observed in [34], whereas a detailed analysis of all possible systematic sources of errors which affect line broadening and shifts in FC spectroscopy can be found in [80]. The discrepancies in the magnitude of the measured and calculated force can be attributed to the approximations used in our model, namely the neglecting of spatial variation of the beam profile. The largest force is measured when the n -th comb mode is resonant with the standard cooling transition for ^{87}Rb , i.e. the right peak in Fig. 2.23(b), for which Δx_{CM} of 0.6 mm is obtained. During 1 ms of FC cooling time the atoms are accelerated with a constant acceleration of 110 m/s^2 and acquire velocity of 0.11 m/s. From the measured force, we calculate an on resonance scattering rate of $\gamma_{scat} = 18600 \text{ s}^{-1}$, which is comparable to the scattering rate calculated in the case of excitation by CW laser of intensity comparable to the intensity of n -th comb mode. Measured FC scattering rate is nearly three times larger than the value reported in Ref. [34] for a two-photon FC excitation, despite having the intensity an order of magnitude smaller than in [34]. This clearly suggests that FC cooling via one-photon excitation is viable, and could therefore be a preferable choice when pursuing cooling of atoms and ions with a dipole allowed transitions in VUV spectral region.

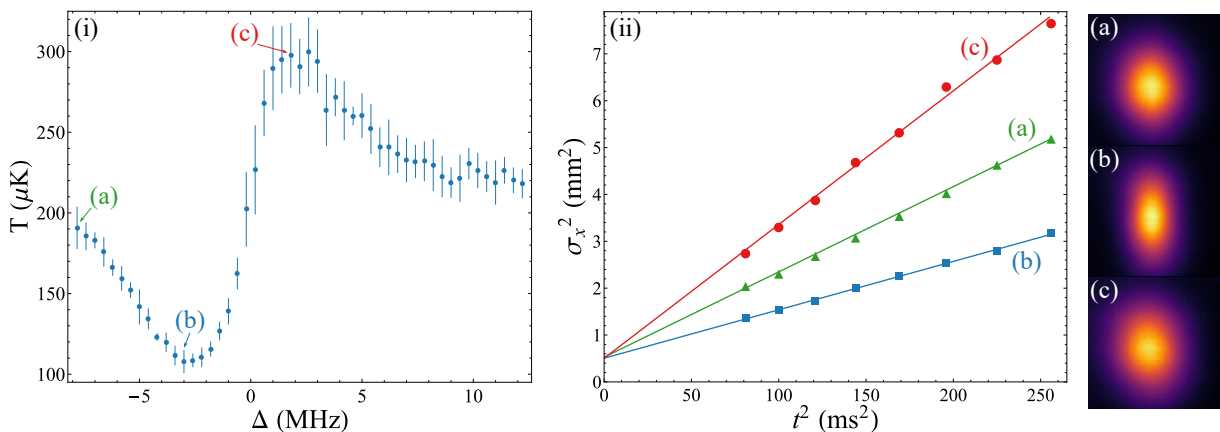


Figure 5.8: (i) Temperature obtained by TOF spectroscopy after 1D FC cooling for lin \perp lin configuration of the FC beams as a function of FC detuning. (ii) Corresponding TOF data for 8-16 ms expansion times. The right most panel shows three TOF images taken after 8 ms expansion time for a FC detuning that corresponds to the cloud's temperature that is (a), approximately equal to the initial temperature, (b), lowest obtained, and (c), highest.

In order to employ the measured FC force to achieve FC cooling in one dimension, we split the FC beam into two beams and send them counter-propagating to the center of the trap where they are carefully overlapped. $\lambda/2$ or $\lambda/4$ waveplates are put in the beam path prior to entering the MOT chamber, depending on the beam polarization configuration to be studied: lin \perp lin, lin \parallel lin or $\sigma^+\sigma^-$. The measurement sequence for studying FC cooling starts by preparing a cold rubidium cloud in the MOT. At $t = 0$ ms the cooling beams are switched off. The weak CW repumper laser is again

left on. A quadrupole magnetic field with a gradient of 13 G/cm remains on during the measurements as mentioned in section 3.2.3. Since the cloud is in the center of the quadrupole field, the magnetic field is $B \approx 0$. At $t = 100 \mu\text{s}$ the FC beams are turned on. The FC beams are on for a time t_c (typically 3 ms), which we call the FC cooling time, after which the FC beams are switched off, and the cloud is left to expand freely for several ms before it is imaged with the camera. A series of time-of-flight (TOF) images are taken in this way at different expansion times of up to 16 ms. We then determine the cloud radius (which increases with expansion time) by fitting the spatial distributions of the atoms in the cloud to a Gaussian function. The obtained spatial width of the cloud as a function of the expansion time gives an accurate measure of the cloud temperature by fitting to the expression $\sigma_t^2 = \sigma_0^2 + \frac{kT}{m}t^2$, where $t = 0$ is the time when the MOT CW cooling laser is switched off. Long expansion times are used in order to reduce any systematic effects related to FC action on the cloud during the interaction time, as $t_{TOF}^2 \gg t_c^2$, where t_{TOF} is the TOF time. A similar experimental procedure for measuring Doppler and sub-Doppler temperatures was used in [34, 81]. We repeat the measurement protocol 7 times for a given expansion time, and subsequently average the results to obtain the temperature. Temperatures obtained by TOF measurements as a function of δ are shown in Fig. 5.8(a). Lin \perp lin polarization of the FC beams was used. The intensity per comb mode in the FC beams was 0.02 mW/cm^2 , initial cloud temperature $\approx 200 \mu\text{K}$, and $t_c = 3 \text{ ms}$.

The measured temperatures approach the initial cloud temperature for large δ . Fig. 5.8(a) shows a TOF image at 8 ms for $\delta = -8 \text{ MHz}$ where the measured width along the x -axis is $2\sigma_x = 2.88 \text{ mm}$. The lowest temperature is observed for $\delta \approx -3 \text{ MHz}$, i.e. when there is a comb (n -th comb) detuned by $\approx -3 \text{ MHz}$ from the ^{87}Rb $|5S_{1/2}; F = 2\rangle \rightarrow |5P_{3/2}; F' = 3\rangle$ transition. The corresponding TOF image shown in Fig. 5.8(b) shows $2\sigma_x = 2.34 \text{ mm}$, and the temperature given by the slope in the inset is $(108 \pm 7) \mu\text{K}$. The highest temperature is obtained for $\delta \approx 2 \text{ MHz}$, i.e. for a blue-detuned comb, when the force induced by the counter-propagating FC beams accelerates the atoms and causes additional heating. The corresponding TOF image shown in Fig. 5.8(c) shows $2\sigma_x = 3.32 \text{ mm}$. One can clearly draw analogy here between FC and CW laser cooling as a comb line red-detuned from the cooling transition is needed to obtain cooling. The changes in the cloud temperature (along the x -axis) with the FC detuning are accompanied with the increase of the temperature in the y -axis, i.e. perpendicular to the FC cooling beams, due to the heating caused by spontaneous emission. The signature of this heating along the y -axis is evident in larger σ_y in Figs. 5.8(b,c) than in Fig. 5.8(a), since more efficient excitation (and consequently more spontaneous emission) is obtained for these detunings.

We investigated FC cooling for different polarization configurations of the FC beams, lin \perp lin, lin \parallel lin and $\sigma^+\sigma^-$. For all three configurations we measure similar temper-

ature dependencies on the FC detuning with comparable sub-Doppler temperatures obtained. We verify these findings by performing the same measurements with two counter-propagating CW beams (instead of FC beams), keeping all experimental parameters identical, with the two CW laser beams having a comparable intensity with the intensity of the relevant comb mode. Particularly interesting are measurements for the $\text{lin} \parallel \text{lin}$ polarization configuration, shown in Fig. 5.9, for which no sub-Doppler cooling is expected, yet we observe it. The minimum temperatures reached are very similar from which we can conclude that the same sub-Doppler mechanism is at play for both FC and CW cooling.

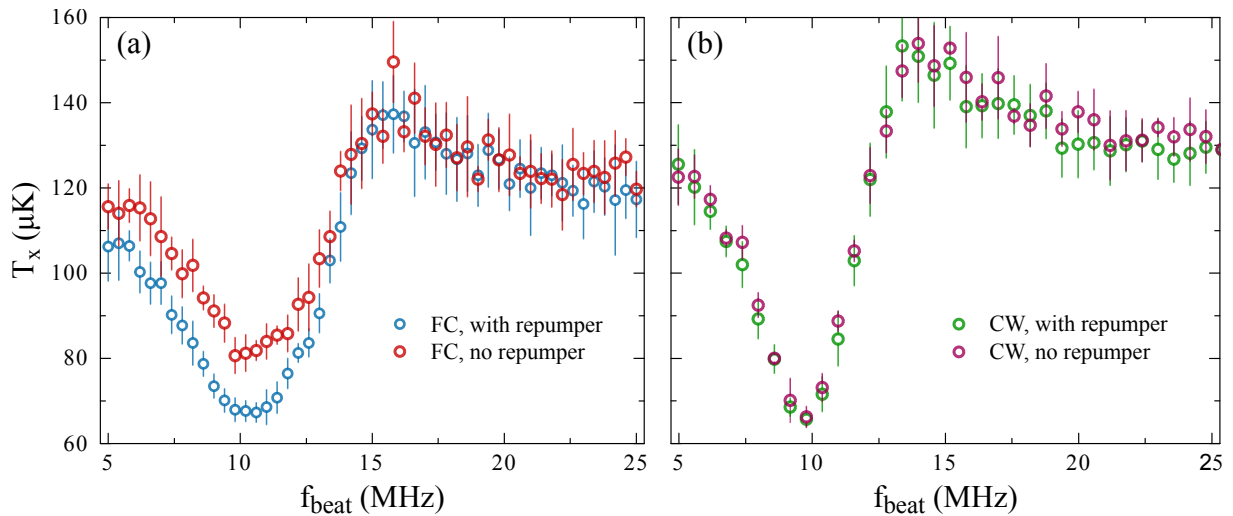


Figure 5.9: A comparison of cooling efficiency between (a) the FC with and without the repumper on during the cooling stage and (b) a CW laser with and without the repumper on. All measurements were performed for the $\text{lin} \parallel \text{lin}$ polarization configuration.

With respect to this, we attribute the sub-Doppler temperatures observed in FC cooling to the same mechanisms that produce sub-Doppler temperatures when cooling with CW lasers, described in section 2.2.2, in line with the interpretation that each comb mode can be considered as a CW laser of appropriate intensity. These sub-Doppler mechanisms arise from the multilevel structure of the atomic ground state in combination with the polarization gradient of the FC field and optical pumping. For the case of the $\text{lin} \perp \text{lin}$ FC beam polarizations, we conclude that the cooling mechanism is analogous to the well known CW Sisyphus cooling [47]. Sub-Doppler cooling with CW lasers for the $\text{lin} \parallel \text{lin}$ configuration can be found in early experimental [82] and theoretical works [83] for the case of low CW laser intensities and small initial atomic velocities. Also, since we leave the AH quadrupole field on, it is possible we observe magnetically assisted sub-Doppler cooling, previously mentioned in section 2.2.2. As mentioned, this was experimentally observed for the $\text{lin} \parallel \text{lin}$ configuration in [49], however this mechanism should yield different sub-Doppler cooling efficiencies for different polarization configurations, which is not the case in our experiment. Another

possibility is that the polarization of the beams changes due to the presence of the AH magnetic field due to Faraday rotation [84]. This could change the angle between the two incoming cooling beams to a non-zero value, where then we would have the same sub-Doppler mechanism as in the $\text{lin} \perp \text{lin}$ case. Both of these possibilities are being explored at the time of writing this thesis.

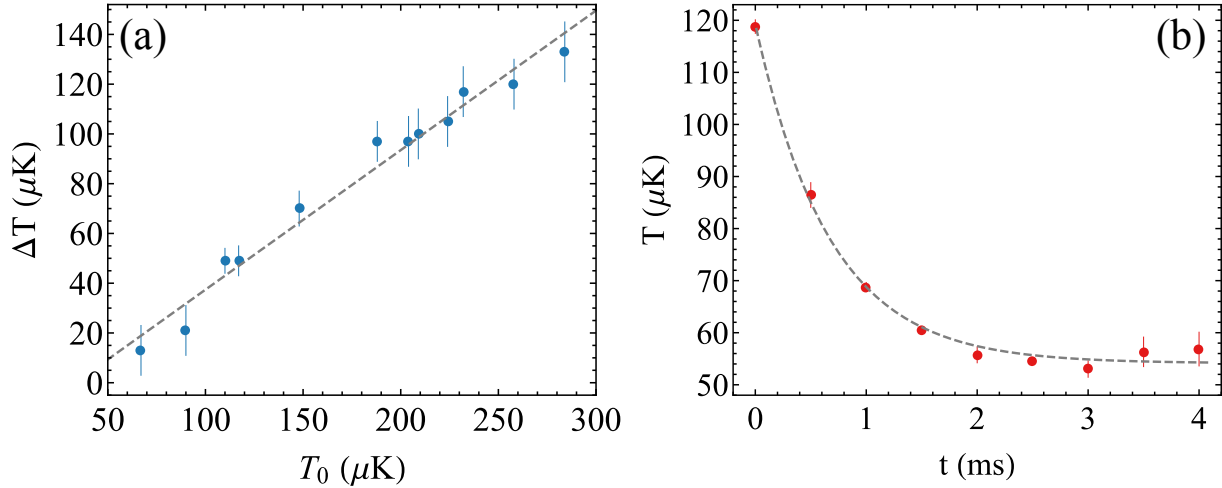


Figure 5.10: (a) The decrease in cloud temperature due to FC cooling as a function of the cloud initial temperature. Gray dashed line is a linear fit to the data. (b) The dependence of the measured sub-Doppler temperature on the FC cooling time for cloud initial temperature $T_0 = 120 \mu\text{K}$ and $\delta = -3 \text{ MHz}$. The gray dashed line is an exponential decay fitted to the data.

It is important to note that cooling down to sub-Doppler temperatures is obtained despite the fact that when n -th comb mode is red-detuned by 3 MHz from $^{87}\text{Rb} |5S_{1/2}; F = 2\rangle \rightarrow |5P_{3/2}; F' = 3\rangle$ transition the $(n-3)$ -th comb it is simultaneously blue-detuned by $\approx 22 \text{ MHz}$ from $^{87}\text{Rb} |5S_{1/2}; F = 2\rangle \rightarrow |5P_{3/2}; F' = 1, 2\rangle$ transitions, see Fig. 5.7. Similar sub-Doppler temperatures are observed in the analogous experiments performed with CW beams, see Fig. 5.9. We observe a slight difference in the case where there is no repumper present in the cooling stage of the experiment, this is due to the increased pumping to the $|5S_{1/2}; F = 1\rangle$ state caused by the mentioned $(n-3)$ -th comb, however this is mitigated by the presence of the repumper. We conclude that blue-detuned comb lines do not have a detrimental effect on the observed FC cooling, a fact that was not immediately clear beforehand and that can rule out additional heating coming from other blue-detuned comb lines.

Finally, let's look at the change of the cloud temperature due to FC cooling, ΔT , as a function of the cloud initial temperature, T_0 , shown in Fig. 5.10(a). The trend is linear, i.e., the temperature difference increases as the initial temperature increases. To understand this we look at the difference in kinetic energy which is proportional to

temperature

$$\Delta T \propto \Delta E_k = \frac{m(\sigma_v - \Delta\sigma_v)^2}{2} - \frac{m\sigma_v^2}{2} \quad (5.2a)$$

$$= \frac{m(\Delta\sigma_v)^2}{2} - m\sigma_v\Delta\sigma_v. \quad (5.2b)$$

If we assume that, due to the Doppler effect bringing more atoms closer to resonance, the reduction in the width of the velocity distribution is proportional to the initial width, $\Delta\sigma_v \propto \sigma_v$ we find that $\Delta T \propto \sigma_v \propto T_0$, in accordance with our measurements. This also leads to the observed exponential decrease of the cloud temperature from the initial value (obtained in the MOT phase) as FC cooling time is increased, as seen in Fig. 5.10(b). The steady state temperature at which the cooling rate is equal to the heating rate is reached (at $t_c \approx 3$ ms) at $\approx 55\mu\text{K}$. This is in agreement with the measurements shown in Fig. 5.10(a), where ΔT approaches zero at $T_0 \approx 50\mu\text{K}$. The lowest temperature obtained in our FC cooling experiment is limited by the low intensity per comb mode, and by the existence of stray magnetic fields in the center of the experimental chamber.

6 Conclusion

In conclusion, in this thesis we presented details of two different MOT setups that were implemented in the Cold atom laboratory in the Institute of Physics in Zagreb. Results obtained with these setups were presented in further chapters.

We have presented a scheme for creating synthetic Lorentz forces in cold classical atomic clouds, based on the Doppler effect and radiation pressure. The force is a result of the interaction of atoms with the field of two pairs of perpendicular laser beams which drive two-step two-photon transitions. We have demonstrated the synthetic Lorentz force by observing the center-of-mass motion of a cold atomic cloud. By comparing the results with numerical calculations we confirm the results and further our understanding of the underlying principles. The experiment was performed in a classical cold atomic gas of rubidium, prepared in a MOT, where the heating due to spontaneous emission does not prevent the observations.

Additionally, we observed a second signature of the SLF produced by our scheme. This signature is imprinted in an tilted ellipsoidal shape atomic cloud, measured after a given expansion time of the cloud. The experimental results show excellent agreement with the simulations of the atom density distributions. Indeed, by simulating the atom density distributions with and without the synthetic Lorentz force contribution, we can determine the contribution of the synthetic Lorentz force in the measured deflection angle. The observed SLF has the form of the standard Lorentz force $\mathbf{F}_{SL}(\mathbf{v}) = \mathbf{v} \times \mathbf{B}^*$, where $\mathbf{B}^* = \alpha_R \hat{\mathbf{z}}$ is the effective magnetic field. Our measurement gives $\alpha_R = 0.50 \times 10^{-22} \text{ N s/m}$ which for an ^{87}Rb ion would give an effective field $\mathbf{B}^*/e \approx 0.3 \text{ mT}$, or a cyclotron frequency of $\alpha_R/m = 0.35 \text{ kHz}$. As stated previously, our scheme for introducing the SLF is necessarily accompanied by spontaneous emission. This will lead to radiation trapping in dense atomic clouds and therefore to an effective Coulomb force between atoms. This means that by introducing the SLF we, at the same time, introduce an effective Coulomb force in to the system. Since the effective charge as a result of radiation trapping is typically $q_{eff} \approx 10^{-4} e$ (see section 2.3.3) the effective synthetic field scales to $B_{eff} \approx 3 \text{ T}$. In addition, we showed that our relatively simple model can be readily used for future experiments with synthetic fields in classical cold atom systems. Our work reinforces the analogy between a cloud of cold atoms and plasma-like systems, thus potentially opening a new direction of research based on the

use of cold atoms as classical emulator of complex classical systems in which magnetic fields play a significant role, such as a tokamak fusion reactor or a star.

Furthermore, we presented a scheme for fully stabilizing an Er-fiber laser frequency comb without self-referencing by referencing it to a stabilized ECDL laser. We also measured the performance of the scheme and evaluated the attained absolute stability. The ECDL used is referenced to a rubidium transition at 780 nm so the same scheme could be easily used to stabilize a Ti-Sapphire laser FC. The scheme is simple, cost effective and power efficient. We emphasize that our scheme requires two orders of magnitude less power (≈ 1 mW) than f-2f interferometry (≈ 100 -200 mW) and achieves an absolute fractional frequency stability on the order of $\Delta f/f \approx 10^{-10}$. Due to the availability of CW lasers stabilized in this way in laboratories worldwide we expect it can be used widely in experiments exploring FC Doppler cooling or other physical phenomena involving FC-atom interaction.

Finally, we have studied FC cooling on a standard Rb MOT transition. By using TOF spectroscopy, we have demonstrated that sub-Doppler temperatures can be obtained in a 1D FC cooling geometry, for both linear and circular polarizations of the FC beams. Sub-Doppler temperatures as low as $55 \mu\text{K}$ have been obtained, primarily limited by the low intensity per comb mode in the FC spectrum. The analogy between FC (single comb line) and CW sub-Doppler laser cooling is verified by performing the same measurements using a CW laser of appropriate intensity. We believe that in future experiments the power per comb line can easily be increased by at least a few orders of magnitude by reducing the spectral width of the comb used and increasing the total power. Using high-intensity FCs could therefore lead to achieving temperatures down to the recoil limit, thus opening the VUV spectral region to quantum optics experiments and their applications.

Appendix A

Articles published during doctoral studies

Synthetic Lorentz force in classical atomic gases via Doppler effect and radiation pressureT. Dubček,¹ N. Šantić,¹ D. Jukić,^{1,2} D. Aumiler,³ T. Ban,³ and H. Buljan^{1,*}¹*Department of Physics, University of Zagreb, Bijenička cesta 32, HR-10000 Zagreb, Croatia*²*Max Planck Institute for the Physics of Complex Systems, Nöthnitzer Straße 38, D-01187 Dresden, Germany*³*Institute of Physics, Bijenička cesta 46, HR-10000 Zagreb, Croatia*

(Received 28 February 2014; published 18 June 2014)

We theoretically predict synthetic Lorentz force for classical (cold) atomic gases, which is based on the Doppler effect and radiation pressure. A fairly spatially uniform and strong force can be constructed for gases in macroscopic volumes of several cubic millimeters and more. This opens the possibility to mimic classical charged gases in magnetic fields in cold-atom experiments.

DOI: [10.1103/PhysRevA.89.063415](https://doi.org/10.1103/PhysRevA.89.063415)

PACS number(s): 37.10.Vz

The quest for synthetic magnetism in quantum degenerate atomic gases is motivated by producing controllable quantum emulators, which could mimic complex quantum systems such as interacting electrons in magnetic fields [1]. An appealing idea is to place the atomic gas in a specially tailored laser field which, due to laser-atom interactions, acts as a synthetic magnetic field for neutral atoms [2]. The mechanism is based on the analogy between the Aharonov-Bohm phase accumulated when a charged quantum particle undergoes a closed loop in a magnetic field, and the Berry phase accumulated when an atom adiabatically traverses a closed loop in the tailored laser field [2,3].

Recent experiments in bulk Bose-Einstein condensates (BECs) have produced synthetic magnetic fields by spatially dependent optical coupling between the internal states of the atoms [4,5]. Superfluid vortices [4] and the Hall effect [5] were observed as signatures of synthetic magnetism in those BECs. Synthetic magnetism in optical lattices is achieved by engineering the complex tunneling parameter between the lattice sites, which is experimentally accomplished by different means [6,7]. Interestingly, even Dirac monopoles were observed in a synthetic magnetic field produced by a spinor BEC [8]. Synthetic magnetic fields for light (e.g., see Ref. [9]) are also attractive. Recently they were observed in deformed honeycomb photonic lattices [10]. Noninertial effects were studied in rotating waveguide arrays [11].

However, *classical* (rather than quantum degenerate) cold atomic gases have been circumvented in the quest for synthetic magnetism, even though they could emulate in a controllable fashion, and in tabletop experiments, versatile complex classical systems (e.g., see Refs. [12,13]); one desirable system for tabletop emulation is the tokamak plasma. We emphasize that here we consider classical atomic gases. This differs from using quantum degenerate gases to mimic frustrated classical magnetism in Ref. [12]. Laser forces on atoms in classical gases can generally depend on atomic velocity [14] and position [15]. A typical example is the Doppler cooling force—a viscous damping force that cools a classical gas to μK temperatures [14,15]. Here we demonstrate a scheme for creating a synthetic Lorentz force via the Doppler effect and radiation pressure, which is applicable for classical cold atomic gases. The experimental realization of the scheme is proposed

with ^{87}Rb atoms cooled in a magneto-optical trap (MOT). The signature of the Lorentz force can be observed in the motion of the center of mass (CM) and/or the shape of the atomic cloud.

Numerous schemes have been proposed to create synthetic magnetic fields with ultracold atoms (see Refs. [1,2,16] for reviews). In the approach based on the Berry phase [3], when atoms move in space, they adiabatically follow the ground state of the light-atom coupling (dressed state), which depends on the spatial coordinates [2,3]. Their CM wave function acquires a geometric (Berry) phase, which corresponds to the gauge potentials [2]. The synthetic magnetic (and electric [17]) fields are derived from these gauge potentials [2]. In these schemes spontaneous emission must be minimized to prevent heating of the ultracold gas. For this reason, the dressed (ground) state is often a superposition of quasidegenerate ground states [3,18,19], i.e., the population of excited states is negligible [18,19]. A semiclassical interpretation of geometric gauge potentials, i.e., the connection with the Lorentz force, was reported in Ref. [20].

Another avenue for creating artificial magnetic fields in ultracold atomic gases is to rotate the system at some angular frequency, which provides the synthetic Lorentz force in the rotating frame [16]; the role of the Lorentz force is played by the Coriolis force. This scheme is suitable for rotationally invariant trapping potentials. However, the laser-atom interaction avenue is more appealing since it does not impose symmetries and produces synthetic magnetic fields in the laboratory frame [2].

In classical atomic gases, any scheme for synthetic magnetism must be operational on atoms moving with fairly large velocities (at least up to ~ 0.5 m/s). The Berry phase method demanding adiabatic dynamics is therefore limited [2]. On the other hand, schemes for classical gases do not need to be limited by avoiding spontaneous emission. Next, classical gases in a standard MOT are typically of millimeter size [15] and the synthetic Lorentz force should therefore be large in volumes of at least a few cubic millimeters. With these guidelines in mind, it seems prosperous to seek for a scheme using laser-atom interactions for creating synthetic Lorentz forces, which would be specially designed for classical atomic gases.

The scheme proposed here is based on the Doppler effect and radiation pressure. The standard Doppler cooling force arises when a laser field is red detuned compared to the atomic resonance frequency as sketched in Fig. 1(a) [14,15].

*hbuljan@phy.hr

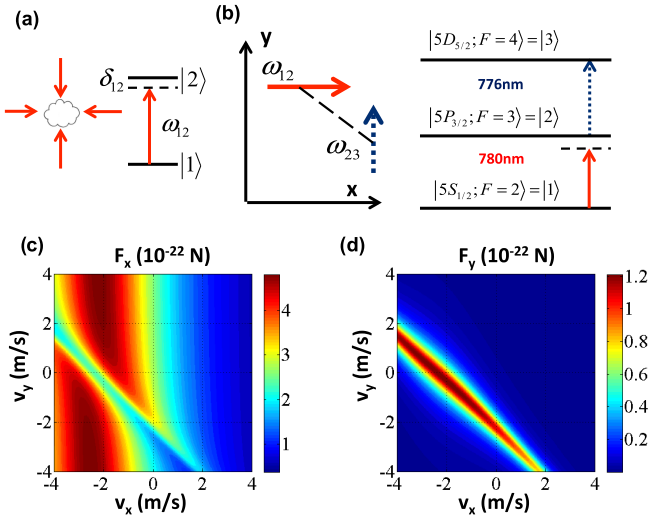


FIG. 1. (Color online) Sketch of the main idea for constructing the synthetic Lorentz force. (a) Illustration of the setup for the standard Doppler cooling force (using two-level atoms). (b) The idea for the synthetic Lorentz force in the simplest three-level system that can be realized with ^{87}Rb atoms. The dashed line indicates that two-step absorption of $\omega_{12} + \omega_{23}$ yields F_y . The force components (c) F_x and (d) F_y calculated as a function of the atomic velocity. See text for details.

Due to the Doppler effect, the atom has a greater probability for absorbing a photon when it moves towards the light source. Absorption changes the atom's momentum along the laser propagation axis, whereas spontaneously emitted photons yield random kicks. Cycles of absorption and emission result in a viscous damping force $\mathbf{F}_D(\mathbf{v}) \approx -\alpha\mathbf{v}$ for small velocities [15]; this force is collinear with the velocity and is used to obtain optical molasses [15].

Our first objective is to construct a laser-atom system (in the xy plane) where F_y depends on v_x . To achieve this via Doppler effect we utilize the multilevel structure of atoms. The simplest scheme is sketched in Fig. 1(b), where a three-level atom interacts with two orthogonal laser beams (linearly polarized along z). The laser ω_{12} is red detuned, $\delta_{12} = \omega_{12} - (E_2 - E_1)\hbar^{-1} < 0$, whereas ω_{23} is on resonance, $\delta_{23} = 0$. The absorption of ω_{23} photons, which results in F_y , is the second step in the two-step, two-photon absorption process: $|1\rangle \rightarrow |2\rangle \rightarrow |3\rangle$. The probability for the two-step absorption depends on the Doppler-shifted detuning values $\delta_{12} - k_{12}v_x$ and $\delta_{23} - k_{23}v_y$, which provides the desired dependence of F_y on v_x . The maximum in F_y is expected for atoms with velocity ($v_x = \delta_{12}/k_{12}, v_y = \delta_{23}/k_{23}$), i.e., when each of the two steps is resonant.

The force can be calculated by using density matrices and the Ehrenfest theorem as described in detail in Ref. [15]. First we (numerically) solve the optical Bloch equations to find the stationary density matrix $\hat{\rho}$ for an atom with velocity \mathbf{v} ; the matrix elements are $\rho_{ij} = \sigma_{ij}e^{i\omega_{ij}t} = \rho_{ji}^*$, and $d\sigma_{ij}/dt = 0$; ω_{ij} is the frequency of the laser driving the transition $|i\rangle \rightarrow |j\rangle$. In the calculation, the following parameters are used [15]: the energies E_j of the levels participating in the interaction ($j = 1, \dots, N$), the Rabi frequencies Ω_{ij} , detuning values δ_{ij} ,

the wave vectors \mathbf{k}_{ij} of the lasers, and the decay parameters of the excited states (Γ_{ji} is the decay rate via $|j\rangle \rightarrow |i\rangle$); the total width of state $|j\rangle$ is $\Gamma_j = \sum_{i < j} \Gamma_{ji}$. The force is given by $\mathbf{F} = \langle -\nabla_r \hat{H} \rangle = -\text{Tr}(\hat{\rho} \nabla_r \hat{H})$, where \hat{H} is the Hamiltonian associated with the dipole interaction, and $\nabla_r = \hat{\mathbf{x}}\partial/\partial x + \hat{\mathbf{y}}\partial/\partial y$ [15]. For plane (traveling) waves used here, $\mathbf{F} = -\sum_{i=1}^{N-1} \sum_{j=i+1}^N \hbar \mathbf{k}_{ij} \text{Im}(\sigma_{ij} \Omega_{ij}^*)$. The density matrix depends on the Doppler-shifted detuning values $\delta_{ij} - \mathbf{k}_{ij} \cdot \mathbf{v}$, which provides the velocity dependence of the force [15].

It should be emphasized that the ideas for constructing synthetic Lorentz forces presented here are general and potentially applicable to various atomic species. For concreteness, the ideas are presented for ^{87}Rb atoms using experimentally relevant atomic states and transitions. The three-level system that can be used to experimentally realize the simplest scheme is presented in Fig. 1(b). The transition wavelengths are $\lambda_{12} = 780 \text{ nm}$ [21] and $\lambda_{23} = 776 \text{ nm}$ [22]. The decay rate of the $|5P_{3/2}\rangle$ hyperfine states is $\Gamma_P = 2\pi \times 6.1 \text{ MHz}$ [21], and $\Gamma_D = 2\pi \times 0.66 \text{ MHz}$ for $|5D_{5/2}\rangle$ states [22]; the decay pattern is $\Gamma_{32} = \Gamma_D$, $\Gamma_{31} = 0$, and $\Gamma_{21} = \Gamma_P$ [21,22]. In Figs. 1(c) and 1(d) we illustrate $\mathbf{F}(\mathbf{v})$ for detuning values $\delta_{12} = -0.5\Gamma_P$, $\delta_{23} = 0$, and Rabi frequencies $\Omega_{12} = 0.12\Gamma_P$, and $\Omega_{13} = 0.34\Gamma_P$. As expected, the maximum of the force F_y occurs when $v_x = \delta_{12}/k_{12}$ and $v_y = \delta_{23}/k_{23}$. Interestingly, $F_y(v_x, v_y)$ has the shape of a mountain ridge peaked at $\delta_{12} + \delta_{23} - k_{12}v_x - k_{23}v_y = 0$. This is a consequence of the fact that the intermediate state $|2\rangle$ is much broader than state $|3\rangle$. For the two-step absorption to be effective, the Doppler-shifted detuning of the first photon should roughly be $|\delta_{12} - k_{12}v_x| < \Gamma_2$, and the total detuning $|\delta_{12} + \delta_{23} - k_{12}v_x - k_{23}v_y| < \Gamma_3$; since $\Gamma_3 \ll \Gamma_2$, the velocities satisfying these inequalities are close to the ridge line. The ridge can be shifted in the v_x, v_y plane by changing the detuning values. The scheme above illustrates the main idea towards constructing the synthetic Lorentz force via the Doppler effect.

Note that the force in the x direction is also altered for atoms with velocities at the ridge. The presence of the second-step transition $|2\rangle \rightarrow |3\rangle$ changes the populations of all three levels, which affects the rate of the first-step transition $|1\rangle \rightarrow |2\rangle$ and hence F_x . It should be noted that deformations of the ridge can arise for larger Rabi frequencies due to the Autler-Townes effect [23].

In order to provide a general framework for our scheme we Taylor expand the force in velocity up to the linear term:

$$\begin{aligned} \begin{bmatrix} F_x \\ F_y \end{bmatrix} &= \begin{bmatrix} F_{x0} \\ F_{y0} \end{bmatrix} + \begin{bmatrix} \alpha_{xx} & 0 \\ 0 & \alpha_{yy} \end{bmatrix} \begin{bmatrix} v_x \\ v_y \end{bmatrix} + \begin{bmatrix} 0 & \alpha_{xy} \\ \alpha_{yx} & 0 \end{bmatrix} \begin{bmatrix} v_x \\ v_y \end{bmatrix} \\ &= \mathbf{F}_0 + \mathbf{F}_D(\mathbf{v}) + \mathbf{F}_{\text{SL}}(\mathbf{v}). \end{aligned} \quad (1)$$

Here $\alpha_{ij} = \partial F_i / \partial v_j$ evaluated at $\mathbf{v} = 0$ ($i, j \in \{x, y\}$). This form is often an excellent approximation for $\mathbf{F}(\mathbf{v})$ because of the small velocities of cold atoms. The third term $\mathbf{F}_{\text{SL}}(\mathbf{v})$ is a general form of the synthetic Lorentz force with components perpendicular to the velocity components: $F_{\text{SL},x} = \alpha_{xy}v_y$, $F_{\text{SL},y} = \alpha_{yx}v_x$ [24]. The force on a standing atom is \mathbf{F}_0 ; the components of the standard Doppler force are $F_{D,x} = \alpha_{xx}v_x$, and $F_{D,y} = \alpha_{yy}v_y$. When $\alpha_{xy} = -\alpha_{yx}$, \mathbf{F}_{SL} takes the form of the standard Lorentz force, $\mathbf{F}_{\text{SL}} = \mathbf{v} \times \mathbf{B}^*$, where $\mathbf{B}^* = \alpha_{xy}\hat{\mathbf{z}}$ [24].

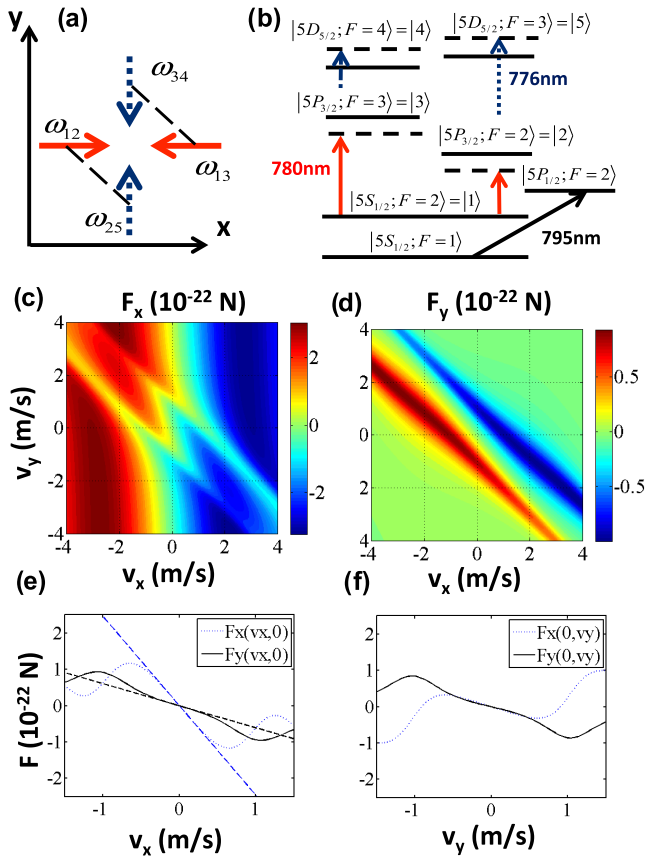


FIG. 2. (Color online) The five-level scheme. (a) The symmetric configuration of lasers for creating the synthetic Lorentz force, and (b) its realization with hyperfine ^{87}Rb levels. Density plots of (c) F_x and (d) F_y , as a function of velocity. Cross sections (e) $F_x(v_x, 0)$ and $F_y(v_x, 0)$ and (f) $F_x(0, v_y)$ and $F_y(0, v_y)$. See text for details.

Let us illustrate a few force patterns $\mathbf{F}(\mathbf{v})$ that can be achieved with our scheme. Consider a system of five-level atoms and two orthogonal pairs of counterpropagating beams depicted in Fig. 2(a). This is simply a generalization of the idea presented in Fig. 1 with a symmetric pair of two-step arms such that $\mathbf{F}_0 = \mathbf{0}$. It can be experimentally realized by using hyperfine levels of ^{87}Rb depicted in Fig. 2(b); the use of a repumper laser is mandatory since the chosen five-level system is not closed: $|5P_{3/2}; F=2\rangle \xrightarrow{50\%} |5S_{1/2}; F=1\rangle = |0\rangle \xrightarrow{795\text{ nm}} |5P_{1/2}; F=2\rangle = |6\rangle \xrightarrow{50\%} |5S_{1/2}; F=2\rangle$ (this is included in our calculations). The Rabi frequencies and detuning values for the transitions are $\Omega_{12} = \Omega_{13} = 0.11\Gamma_P$, and $\delta_{12} = \delta_{13} = -0.5\Gamma_P$. The pairs of beams along x are red detuned, while the pairs along y are blue detuned (by a smaller magnitude): $\delta_{25} = \delta_{34} = 0.25\Gamma_P$; $\Omega_{25} = \Omega_{34} = 0.38\Gamma_P$. The repumper is on resonance with high intensity $\Omega_{06} = 1.77\Gamma_P$, in a standing-wave configuration (it does not produce net force on atoms). The decay pattern is given by $\Gamma_{21} = \Gamma_{20} = 0.5\Gamma_P$, $\Gamma_{31} = \Gamma_P$, $\Gamma_{43} = \Gamma_D$, $\Gamma_{53} = 0.2\Gamma_D$, $\Gamma_{52} = 0.8\Gamma_D$, and $\Gamma_{60} = \Gamma_{61} = 0.5\Gamma_P$; the rest of $\Gamma_{ji} = 0$. In Figs. 2(c) and 2(d) we show the force $\mathbf{F}(\mathbf{v})$. Atoms moving towards the left (right) will experience $F_y > 0$ ($F_y < 0$, respectively). From Figs. 2(e) and 2(f) we see that the force depends linearly on the velocity v_x

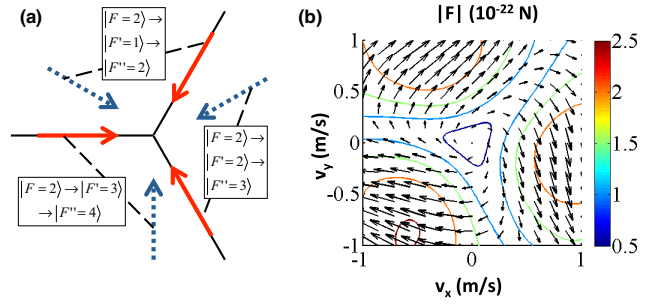


FIG. 3. (Color online) The tripod configuration of the three two-step excitations arms, and the obtained force. (a) Red solid arrows depict first-step excitations (red detuned), and blue dotted arrows depict second steps (blue detuned). Black dashed lines connect beams that correspond to one arm; $|F=2\rangle$ denotes the $5S_{1/2}$ hyperfine state, $|F'=1,2,3\rangle$ denote three $5P_{3/2}$ hyperfine states, and $|F''=2,3,4\rangle$ denote three $5D_{5/2}$ hyperfine states. (b) Contour lines and length of the arrows correspond to the magnitude of the force $|\mathbf{F}(\mathbf{v})|$.

for velocities below ~ 0.7 m/s (which includes essentially all atoms in a standard ^{87}Rb MOT [15]). The two ridges in F_y correspond to the pair of arms of the two-step absorption; their position and shape was explained in Fig. 1(d). By changing the detuning values, the ridges can be shifted in the $v_x v_y$ plane, which changes the parameters α_{ij} and therefore the strength of the synthetic Lorentz force.

It should be noted that because our approach is based on the Doppler effect, it usually also yields the Doppler (cooling) force \mathbf{F}_D . If for some reason this is not wanted, dissipation can be diminished (for example, by using one blue-detuned and one red-detuned laser in the counterpropagating configuration for the first-step excitation). Moreover, the synthetic force can be made of the form $\mathbf{v} \times \mathbf{B}^*$: By using three arms of the two-step scheme at 120° [Fig. 3(a)], one can obtain the force plotted in Fig. 3(b). Two arms are identical as in Fig. 2(b), and the third arm is $|5S_{1/2}; F=2\rangle \rightarrow |5P_{3/2}; F=1\rangle \rightarrow |5D_{5/2}; F=2\rangle$. The Rabi frequency of the first (second) step in all arms is $0.11\Gamma_P$ ($0.77\Gamma_P$); the detuning values are $-0.5\Gamma_P$ ($0.25\Gamma_P$) for the first (second) step. Clearly, the force rotates around zero in the $v_x v_y$ plane. Strictly, the force field is invariant under rotation by 120° , however, for small velocities it is effectively rotationally invariant. By fitting $\mathbf{F}(\mathbf{v})$ to Eq. (1) we obtain $\alpha_{xy} = -\alpha_{yx} = 0.23 \times 10^{-21}$ N s/m, i.e., $\mathbf{B}^* = \alpha_{xy} \hat{\mathbf{z}}$. The cyclotron frequency for ^{87}Rb atoms corresponding to our forces is $\alpha_{xy}/m \approx 1.6$ kHz. It should be emphasized that, because we are using hyperfine levels of ^{87}Rb , the scheme can be achieved with two cw lasers at 780 and 776 nm by using acoustic optical modulators (AOMs), i.e., it is experimentally viable.

The prediction of the synthetic Lorentz force is made for individual atoms, however, we should propose its signature in the CM motion and/or shape of a cold atomic cloud containing a huge number (say, $\sim 10^9$ [15]) of atoms. To this end we propose a quench-type scenario(s). First, we assume that an atomic cloud is present in the MOT, and cooled to mK- μ K temperatures. The laser fields driving the MOT have much larger Rabi frequencies than lasers producing a synthetic Lorentz force. The latter will slightly heat up the cloud, but will not change its shape. Then, at $t = 0$, the MOT lasers

and the magnetic field are suddenly turned off (it can be done within less than $1 \mu\text{s}$, which is essentially instantaneous for this system). After $t = 0$, the cloud starts moving in the presence of the synthetic Lorentz and Doppler forces. We focus on dynamics in the xy plane. Moreover, we assume that gravity is in the z direction and does not influence observations. The typical experimental observation time for the measurements proposed here is $5\text{--}10$ ms; an initially standing atom will fall for $0.12\text{--}0.49$ mm. The laser fields creating the synthetic Lorentz forces can be made of a much larger diameter (on the order of several cm). Since the dynamics in the xy plane is independent of the dynamics in the z plane, we do not expect a significant influence of gravity on our predictions below.

We will discuss two scenarios for the force plotted in Fig. 2. First, if the cloud is given an initial velocity ($v_x = 0.15$ m/s, $v_y = 0$), it will move along x due to inertia, but its CM will also move in the negative y direction due to the synthetic Lorentz force. After 10 ms the shift in y is ~ 0.2 mm, which is observable in MOT experiments. The initial velocity can be achieved by inducing oscillations of the cloud in the MOT trap for $t < 0$ (e.g., see Ref. [25]).

Second, we discuss expansion of the cloud by employing the Fokker-Planck equation [15]

$$\frac{\partial P(\mathbf{x}, \mathbf{v}, t)}{\partial t} + \mathbf{v} \cdot \nabla_{\mathbf{r}} P = \frac{-1}{m} \nabla_{\mathbf{v}} \cdot [(\mathbf{F}_D + \mathbf{F}_{\text{SL}})P] + \frac{D}{m^2} \nabla_{\mathbf{v}}^2 P. \quad (2)$$

Here, $P(\mathbf{x}, \mathbf{v}, t)$ is the distribution of particles in the phase space; D is the diffusion constant, approximately given by $D \approx (\hbar k)^2 \sum_j \rho_{jj} \Gamma_j$ [15], where $k \approx 2\pi/780 \text{ nm}^{-1}$; $\nabla_{\mathbf{v}} = \hat{\mathbf{x}} \partial / \partial v_x + \hat{\mathbf{y}} \partial / \partial v_y$. For forces $\mathbf{F}_D + \mathbf{F}_{\text{SL}}$ linearized in velocity (1), the Fokker-Planck equation is solved by the ansatz

$$P(x, y, v_x, v_y, t) = P_0 \exp \left\{ - \sum_{ij=1}^4 \frac{1}{2} a_{ij}(t) \eta_i \eta_j \right\}, \quad (3)$$

where $(\eta_1, \eta_2, \eta_3, \eta_4) = (x, y, v_x, v_y)$; after inserting (3) in Eq. (2), one obtains ten coupled ordinary differential equations (ODEs) for the functions $a_{ij}(t)$, ten because $a_{ij} = a_{ji}$ by construction. These coupled ODEs are solved numerically and the results are plotted in Fig. 4 for the following parameters: $(\alpha_{xx}, \alpha_{xy}, \alpha_{yx}, \alpha_{yy}) = -(2.4, 0.60, 0.69, 0.58) \times 10^{-22} \text{ N s/m}$, and $D/m_{\text{Rb}}^2 = 31 \text{ m}^2 \text{ s}^{-3}$; the initial state is $P = P_0 \exp\{-(\mathbf{x}/x_0)^2 - (\mathbf{v}/v_0)^2\}$, where $x_0 = 1 \text{ mm}$, and $v_0 = 0.25 \text{ m/s}$.

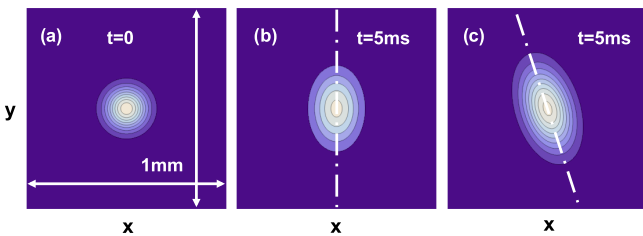


FIG. 4. (Color online) Dynamics of the shape of the cloud during expansion in the presence of a synthetic Lorentz force $\mathbf{F}_{\text{SL}}(\mathbf{v})$ and/or Doppler force $\mathbf{F}_D(\mathbf{v})$. The force corresponds to that from Fig. 2. (a) Density of the cloud at $t = 0$, (b) after 5 ms of expansion under the action of $\mathbf{F}_D(\mathbf{v})$, and (c) after 5 ms expansion in the presence of $\mathbf{F}_D(\mathbf{v}) + \mathbf{F}_{\text{SL}}(\mathbf{v})$. See text for details.

Starting from a centrosymmetric cloud plotted in Fig. 4(a), in the presence of solely the Doppler force, the cloud expands asymmetrically [Fig. 4(b)] because $|\alpha_{xx}| > |\alpha_{yy}|$. The signature of the synthetic Lorentz force is the rotation of the asymmetric cloud in the xy plane during expansion [see Fig. 4(c)]. The interpretation is simple: Particles moving to the left (right) are pushed up (down), as can be inferred from Fig. 2(d). There is another effect: The change in F_y for a given atomic velocity group also changes F_x for that group, as discussed above. For the parameters corresponding to Figs. 2 and 4, besides the targeted $\alpha_{yx} < 0$, we incidentally also obtained $\alpha_{xy} < 0$ (for small velocities) which also contributes to rotation. Note that expansion in the rotationally symmetric force field presented in Fig. 3 would cause the rotation of atoms around the center, but this would not be visible in the density (in the proposed scenario it is essential to have $|\alpha_{xx}| \neq |\alpha_{yy}|$). By shining a red-detuned laser beam in the plane of such a rotationally invariant but rotating cloud, one would have different absorption in the part of the cloud moving towards (away) from the laser beam due to the Doppler effect; this seems to be one viable scheme to observe rotation of the cloud.

Before closing, let us discuss specific approximations that we used here to simplify the calculation. First, we neglected the absorption of the lasers in the cold atomic cloud. Absorption changes the intensity of beams across the cloud, and therefore introduces spatial dependence of the synthetic Lorentz force (and not only the velocity dependence). This effect can be reduced by using clouds with a lower density (say, 10^9 atoms per cm^3), or by using lasers with a higher intensity (closer to saturation). The latter approach will also increase the diffusion coefficient. Second, in our proposal we neglected the Zeeman structure of the atomic levels. This simplification is acceptable when the dynamics of the cloud does not occur in a magnetic field (i.e., Zeeman splitting is absent), as in the two scenarios described above. Next, the dipole moments of different transitions used in the scheme will be generally different (they also depend on the polarization of the light used). The key goal one has to achieve is to have the same Rabi frequencies for all first (second) steps in each arm, as in our examples above. In experiments, this can be realized by using light of different intensities in steps that have different transition dipole moments. This could in principle be achieved by balancing the forces arising from different arms. Finally, let us note that the internal dynamics occurs on a much faster time scale than CM motion; the bottleneck for internal dynamics is the lifetime of the $5D_{5/2}$ state of 240 ns, whereas the typical time scale for CM motion is 1 ms.

In conclusion, we have demonstrated a scheme for creating synthetic Lorentz forces in cold classical atomic clouds, based on the Doppler effect and radiation pressure. We envision that following these ideas, one could design cold-gas experiments to mimic classical charged gases in magnetic fields. One desired classical system for emulation is the tokamak plasma. A necessary (but not sufficient) step towards this goal is to have a scheme for producing synthetic magnetic fields for classical gases. The next step towards mimicking the tokamak plasma would be to construct a toroidal synthetic magnetic field, which is beyond the scope of this paper. Here we have predicted synthetic Lorentz forces of magnitude $F/v \approx 0.23 \times 10^{-21} \text{ N s/m}$ in macroscopic volumes of a few mm^3 and more. The maximal

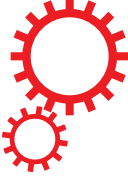
volume depends on the intensities of lasers; with standard diode lasers one could achieve the synthetic Lorentz force in at least 1 cm^3 . As a reference point we note that the obtained force on a unit charge particle (of any mass) is produced by a magnetic field of 1.5 mT . The cyclotron frequency (which includes the particle mass) for ^{87}Rb atoms corresponding to our forces is $F/(mv) \approx 1.6 \text{ kHz}$, which is large enough to see the phenomena associated with the synthetic Lorentz force on the time scale of the envisioned experiments. Even stronger forces can be achieved for larger intensities of the lasers at the expense of more heating and diffusion. We envision that our concept

involving two-photon absorption could be applicable in other systems, e.g., for suspended nanoparticles with a nonlinear index of refraction where one laser beam would induce an index change, and thus influence the force of another (say, perpendicular) beam on the particle. The concept holds the potential to be used for velocity selection in atomic beams.

This work was supported by the Unity through Knowledge Fund (UKF Grant No. 5/13). We are grateful to A. Eckardt, J. Radić, Th. Gasenzer, and A. Vardi for a critical reading of the manuscript.

-
- [1] I. Bloch, J. Dalibard, and S. Nascimbene, *Nat. Phys.* **8**, 267 (2012).
- [2] J. Dalibard, F. Gerbier, G. Juzeliunas, and P. Öhberg, *Rev. Mod. Phys.* **83**, 1523 (2011).
- [3] R. Dum and M. Olshanii, *Phys. Rev. Lett.* **76**, 1788 (1996).
- [4] Y.-J. Lin, R. L. Compton, K. Jiménez-García, J. V. Porto, and I. B. Spielman, *Nature (London)* **462**, 628 (2009).
- [5] L. J. Le Blanc, K. Jiménez-García, R. A. Williams, M. C. Beeler, A. R. Perry, W. D. Phillips, and I. B. Spielman, *Proc. Natl. Acad. Sci. USA* **109**, 10811 (2012).
- [6] M. Aidelsburger, M. Atala, S. Nascimbene, S. Trotzky, Y.-A. Chen, and I. Bloch, *Phys. Rev. Lett.* **107**, 255301 (2011).
- [7] J. Struck, C. Ölschläger, M. Weinberg, P. Hauke, J. Simonet, A. Eckardt, M. Lewenstein, K. Sengstock, and P. Windpassinger, *Phys. Rev. Lett.* **108**, 225304 (2012).
- [8] M. W. Ray, E. Ruokokoski, S. Kandel, M. Mottonen, and D. S. Hall, *Nature (London)* **505**, 657 (2014).
- [9] I. Carusotto and C. Ciuti, *Rev. Mod. Phys.* **85**, 299 (2013).
- [10] M. C. Rechtsman, J. M. Zeuner, A. Tünnermann, S. Nolte, M. Segev, and A. Szameit, *Nat. Photon.* **7**, 153 (2012).
- [11] S. Jia and J. W. Fleischer, *Phys. Rev. A* **79**, 041804(R) (2009).
- [12] J. Struck, Ölschläger, R. Le Targat, P. Soltan-Panahi, A. Eckardt, M. Lewenstein, P. Windpassinger, and K. Sengstock, *Science* **333**, 996 (2011).
- [13] Q. Baudouin, W. Guerin, and R. Kaiser, in *Annual Review of Cold Atoms and Molecules*, edited by K. Madison, Y. Wang, A. M. Rey, and K. Bongs (World Scientific, Singapore, 2014), Vol. 2.
- [14] S. Chu, L. Hollberg, J. E. Bjorkholm, A. Cable, and A. Ashkin, *Phys. Rev. Lett.* **55**, 48 (1985).
- [15] H. J. Metcalf and P. Van Der Straten, *Laser Cooling and Trapping* (Springer, New York, 1999).
- [16] N. R. Cooper, *Adv. Phys.* **57**, 539 (2008).
- [17] Y. J. Lin, R. L. Compton, K. Jiménez-García, W. D. Phillips, J. V. Porto, and I. B. Spielman, *Nat. Phys.* **7**, 531 (2011).
- [18] G. Juzeliunas and P. Öhberg, *Phys. Rev. Lett.* **93**, 033602 (2004).
- [19] G. Juzeliunas, J. Ruseckas, P. Öhberg, and M. Fleischhauer, *Phys. Rev. A* **73**, 025602 (2006).
- [20] M. Cheneau, S. P. Rath, T. Yefsah, K. J. Günter, G. Juzeliunas, and J. Dalibard, *Europhys. Lett.* **83**, 60001 (2008).
- [21] D. A. Steck, <http://steck.us/alkalidata/rubidium87numbers.pdf>
- [22] D. Sheng, A. Perez Galvan, and L. A. Orozco, *Phys. Rev. A* **78**, 062506 (2008).
- [23] S. H. Autler and C. H. Townes, *Phys. Rev.* **100**, 703 (1955).
- [24] The definition of the synthetic Lorentz force in Eq. (1) is broader than the form $\mathbf{v} \times \mathbf{B}^*$, but includes that standard form.
- [25] X. Xu, Th. H. Loftus, M. J. Smith, J. L. Hall, A. Gallagher, and J. Ye, *Phys. Rev. A* **66**, 011401(R) (2002).

SCIENTIFIC REPORTS



OPEN

Experimental Demonstration of a Synthetic Lorentz Force by Using Radiation Pressure

N. Šantić^{1,2}, T. Dubček¹, D. Aumiler², H. Buljan¹ & T. Ban²

Received: 13 April 2015

Accepted: 24 July 2015

Published: 02 September 2015

Synthetic magnetism in cold atomic gases opened the doors to many exciting novel physical systems and phenomena. Ubiquitous are the methods used for the creation of synthetic magnetic fields. They include rapidly rotating Bose-Einstein condensates employing the analogy between the Coriolis and the Lorentz force, and laser-atom interactions employing the analogy between the Berry phase and the Aharonov-Bohm phase. Interestingly, radiation pressure - being one of the most common forces induced by light - has not yet been used for synthetic magnetism. We experimentally demonstrate a synthetic Lorentz force, based on the radiation pressure and the Doppler effect, by observing the centre-of-mass motion of a cold atomic cloud. The force is perpendicular to the velocity of the cold atomic cloud, and zero for the cloud at rest. Our novel concept is straightforward to implement in a large volume, for a broad range of velocities, and can be extended to different geometries.

Experiments on synthetic magnetic/gauge fields for neutral atoms¹⁻¹¹ have enabled realizations of the Hall effect⁴, famous Hamiltonians such as the Harper^{7,8} and the Haldane Hamiltonian¹⁰, intriguing topological effects^{9,10}, and the observation of synthetic Dirac monopoles¹¹. There are a few recent reviews on this promising theoretical and experimental progress in synthetic magnetic/gauge fields¹²⁻¹⁵. The first implementation of synthetic magnetism was in rapidly rotating Bose-Einstein condensates (BECs), employing the analogy between the Lorentz force and the Coriolis force^{1,2}. The methods based on laser-atom interaction employ the analogy between the Berry phase in atomic systems¹⁶, and the Aharonov-Bohm phase for charged particles¹³. The first of them was realized in the NIST group with spatially dependent Raman optical coupling between internal hyperfine atomic states in bulk BECs³. Methods generating synthetic magnetic fields in optical lattices engineer the complex tunnelling matrix elements between lattice sites⁵⁻⁹. They include shaking of the optical lattice⁶, laser assisted tunnelling in optical superlattices realizing staggered synthetic magnetic fields⁵, in tilted lattices realizing homogeneous fields^{7,8}, and an all-optical scheme which enables flux rectification in optical superlattices⁹. Interestingly, radiation pressure has not yet been used among the methods for synthetic magnetism, that is, to create the analogue of the Lorentz force. Here we experimentally demonstrate the synthetic Lorentz force based on radiation pressure in cold atomic gases. We measure the dependence of the transverse radiation pressure force (analogous to the transverse Hall deflection) on the velocity of a cold atomic cloud by observing the centre-of-mass (CM) motion. The observed force is perpendicular to the velocity, and zero for the atomic cloud at rest. This concept based on radiation pressure, theoretically proposed in Ref. [17], is straightforward to implement in a large volume (e.g., volumes 1 mm³-1 cm³ are easily accessible)¹⁸, is applicable for a broad range of velocities, and can be extended to different geometries. The main reason for the absence of radiation pressure from the previously used methods of synthetic magnetism is the associated heating due to spontaneous emission. However, this is not an obstacle for atomic gases cooled and trapped in a Magneto-Optical Trap (MOT), where our experiments are performed.

¹Department of Physics, University of Zagreb, Bijenička c. 32, 10000 Zagreb, Croatia. ²Institute of Physics, Bijenička c. 46, 10000 Zagreb, Croatia. Correspondence and requests for materials should be addressed to H.B. (email: hbuljan@phy.hr) or T.B. (email: ticijana@ifs.hr)

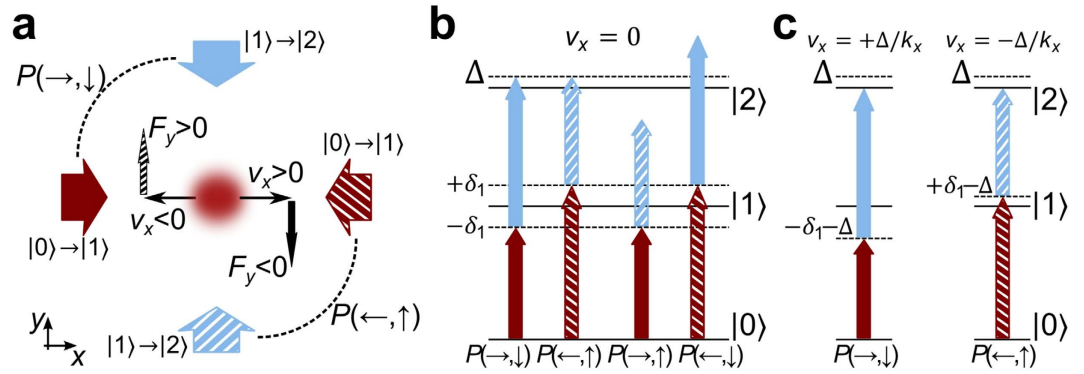


Figure 1. The scheme used to obtain the synthetic Lorentz force via radiation pressure. It is based on two-step two-photon transitions involving three atomic levels. (a) Two counter-propagating laser beams on the x -axis (red arrows) drive the $|0\rangle \rightarrow |1\rangle$ transition, while the $|1\rangle \rightarrow |2\rangle$ transition is driven by two counter-propagating beams on the y -axis (blue arrows). The transverse radiation pressure force arising from the $|1\rangle \rightarrow |2\rangle$ transition F_y , depends on the velocity v_x as indicated. (b) Four possible excitation pathways and a sketch of the detuning values: $P(\rightarrow, \downarrow)$ denotes absorption of a $|0\rangle \rightarrow |1\rangle$ photon going towards the positive x -direction, followed by absorption of a $|1\rangle \rightarrow |2\rangle$ photon travelling towards the negative y -direction, and so on. The total detuning value for $P(\rightarrow, \downarrow)$ and $P(\leftarrow, \uparrow)$ is Δ , whereas it is much larger in magnitude for $P(\rightarrow, \uparrow)$ and $P(\leftarrow, \downarrow)$; the two latter pathways are thus negligible in this configuration. (c) The Doppler shift provides F_y as a function of v_x as sketched in (a): pathway $P(\rightarrow, \downarrow)$ for an atom with positive velocity $v_x = +\Delta/k_x$ ($v_y = 0$) is on resonance, providing negative F_y . Likewise, $P(\leftarrow, \uparrow)$ is on resonance for an atom with negative velocity $v_x = -\Delta/k_x$, providing positive F_y . See text for details.

Results

The basic idea. The idea behind our experiment is to drive two-step two-photon transitions between three atomic levels, $|0\rangle \rightarrow |1\rangle \rightarrow |2\rangle$, with mutually perpendicular laser beams as illustrated in Fig. 1. Two counterpropagating laser beams aligned with the x -axis drive the $|0\rangle \rightarrow |1\rangle$ transition, whereas the $|1\rangle \rightarrow |2\rangle$ transition is driven by counterpropagating beams aligned on the y -axis. Due to the Doppler effect and the perpendicular configuration of the laser beams, both components of the radiation pressure force depend on both components of the atomic velocity: $F_x = F_x(v_x, v_y)$ and $F_y = F_y(v_x, v_y)$. This gives us the opportunity to design the detuning values of our lasers such that F_y is positive/negative for atoms with negative/positive velocity component v_x , and that the total force is zero for an atom at rest: $\mathbf{F}(\mathbf{v} = \mathbf{0}) = \mathbf{0}$. These are the characteristics of the synthetic Lorentz force that we experimentally demonstrate.

The design of the detuning values of the lasers is crucial in obtaining the desired result. The beams driving the first step of the transition $|0\rangle \rightarrow |1\rangle$ are detuned by the same magnitude, but with the opposite sign. The one towards the positive x -direction is red-detuned by $\delta_- = -\delta_1 < 0$, while the other is blue-detuned by $\delta_- = \delta_1 > 0$. Their intensities are equal. Thus, if just these two lasers were present, the net force on atoms (of any velocity) would be zero. However, the population of level $|1\rangle$ would depend on the velocity v_x , which implies that the rate of transitions $|1\rangle \rightarrow |2\rangle$ giving the transverse force will depend on v_x . The detuning values of the beams driving the second step of the transition, $|1\rangle \rightarrow |2\rangle$ are denoted by δ_+ and δ_1 , for the beam propagating in the positive and negative y direction, respectively. For now, let us set these values such that $\delta_- + \delta_1 = \delta_- + \delta_1 = \Delta > 0$, as indicated in Fig. 1(b).

The two-step two-photon transitions, where absorption of a $|1\rangle \rightarrow |2\rangle$ photon follows absorption of a $|0\rangle \rightarrow |1\rangle$ photon with perpendicular momentum, yield the synthetic Lorentz force via momentum transfer from photons to atoms. Given the fact that we have two counterpropagating beams for each transition, we have four excitation pathways for the two-step two-photon transition, denoted by $P(\rightarrow, \uparrow)$, $P(\leftarrow, \uparrow)$, $P(\rightarrow, \downarrow)$, and $P(\leftarrow, \downarrow)$, see Fig. 1. The arrows correspond to the direction of the photon's momentum, for example, $P(\rightarrow, \downarrow)$ denotes the pathway where absorption of a photon travelling in the $+x$ direction is followed by absorption of a photon in the $-y$ direction and so on. Since the detuning magnitudes of the first step are identical for all pathways ($|\delta_-| = \delta_-$), the relevant quantity is the total detuning for the two-step two-photon transitions. It is important to note that the total detuning Δ for pathways $P(\rightarrow, \downarrow)$ and $P(\leftarrow, \uparrow)$, is much smaller in magnitude than the detuning values of $P(\rightarrow, \uparrow)$ and $P(\leftarrow, \downarrow)$. The last two are thus negligible in the setup of Fig. 1.

To understand the origin of the synthetic Lorentz force, we take into account the Doppler shift. For an atom moving along the x -axis with velocity v_x ($v_y = 0$), the $P(\leftarrow, \uparrow)$ pathway is detuned by $\Delta + k_x v_x$, i.e., it is on resonance when $v_x = -\Delta/k_x < 0$. Because photons from the second step of $P(\leftarrow, \uparrow)$ impart

momentum towards the positive y -direction, there will be a positive force F_y for atoms with negative v_x . In the same fashion, the $P(\rightarrow, \downarrow)$ pathway will be on resonance when $v_x = +\Delta/k_x > 0$ yielding negative F_y for positive v_x .

The experiment. In the experiment, we use cold ^{87}Rb atoms. For the $|0\rangle \rightarrow |1\rangle$ transition we use the D2 transition in ^{87}Rb : $|5S_{1/2}; F = 2\rangle \rightarrow |5P_{3/2}; F' = 3\rangle$ at 780 nm¹⁹. The easily accessible transition, $|5P_{3/2}; F' = 3\rangle \rightarrow |5D_{5/2}; F'' = 4\rangle$ at 776 nm²⁰, is used for the second step $|1\rangle \rightarrow |2\rangle$. The linewidths of the states are $2\pi \times 6.1$ MHz for the $|5P_{3/2}; F' = 3\rangle$ state¹⁹, and $2\pi \times 0.66$ MHz for the $|5D_{5/2}; F'' = 4\rangle$ state²⁰.

The ^{87}Rb atoms are cooled and trapped in a standard glass vapour cell magneto-optical trap (MOT), arranged in a retro-reflected configuration. In this configuration, three orthogonal retro-reflected beams are used to create the total of six beams needed for the MOT. A pair of anti-Helmholtz coils provides a quadrupole magnetic field, which together with the laser beams creates a trapping potential (for example, see Ref. [18]). Fluorescence imaging of the cloud is performed with a camera aligned along the z -axis. In typical experimental conditions we obtain a cloud of 0.4 mm in diameter, which contains about 10^8 atoms of ^{87}Rb , at a temperature of 50 μK (for details of the experimental setup see Methods). The four beams implementing the synthetic Lorentz force, arranged as in Fig. 1, are of much smaller intensity than the MOT beams. Therefore, they are negligible when the MOT beams are ON. For the experimental detection of the synthetic Lorentz force, we turn the MOT beams OFF, as described in detail below.

We need to measure the transverse force F_y in dependence of the velocity v_x of the atomic cloud. Thus, we must prepare a cloud with a given centre of mass (CM) velocity. For this purpose we use an additional pair of current coils that produce a bias magnetic field along the symmetry axis of the anti-Helmholtz coils, x in our notation here. The bias field moves the centre of the trap (the point where $\mathbf{B} = 0$), which displaces the cloud approximately 1 mm along the x -axis.

The measurement protocol is as follows. (i) We load the trap with the bias magnetic field on. (ii) At $t = -2$ ms we reverse the bias magnetic field by reversing the current, which suddenly shifts the centre of the trap. This introduces a force on the cloud due to the MOT beams. During the next 2 ms the cloud accelerates along the x -axis towards the new trap centre. (iii) Next we turn off the MOT cooling laser and all real magnetic fields. This moment corresponds to $t = 0$ in our presentation. The system is now simplified because Zeeman splitting of hyperfine levels is absent and the radiation force left, arising solely from the lasers implementing the synthetic Lorentz force, is not spatially dependent (it is only velocity-dependent). (iv) The cloud starts to expand because the trapping is absent, but it also moves in the xy plane due to both the initial velocity, $v_x(t=0)$, and the radiation pressure force. (v) After some delay time t , the cooling laser is suddenly turned on and the cloud is imaged with the camera. From the trajectory traversed by the CM of the cloud ($x(t)$, $y(t)$), we can find the force acting on the atoms. If we wish to image a cloud initially at rest we skip steps (i) and (ii). For a given delay time t , we repeat the measurement protocol 20 times in identical conditions, and subsequently average to obtain $x(t)$ and $y(t)$. The gravity is along the z -axis in our system; free fall of atoms due to gravity does not affect the motion in the xy plane. It should be stated that we perform these measurements first with $|1\rangle \rightarrow |2\rangle$ lasers OFF, and then with these lasers ON, keeping all other parameters identical. The difference in the path $y(t)$, with lasers $|1\rangle \rightarrow |2\rangle$ ON and OFF, gives us the transverse motion due to the synthetic Lorentz force.

The experimental proof of the synthetic Lorentz force by radiation pressure. The results of the experiment are illustrated in Fig. 2. We show the trajectory of the cloud ($x(t)$, $y(t)$), in the presence of the synthetic Lorentz force, for three initial velocities: $v_x = -0.3$ m/s (squares), $v_x = 0$ m/s (diamonds), and $v_x = 0.6$ m/s (circles); $v_y = 0$ at $t = 0$ in each run of the experiment. There is a difference in the magnitude of the initial v_x for the positive and negative velocity [circles and squares in Fig. 2(a)], which is a result of our MOT retro-reflected geometry, and the way we accelerate the cloud in step (ii) of the protocol. In order to prepare a cloud with positive v_x , the cloud is accelerated with the incoming MOT beam (coming from the laser side of the setup), whereas acceleration in the opposite direction is performed with the reflected beam which has smaller intensity. The reflected beam intensity is smaller due to the losses, which are a result of the passage of the incoming beam through the dense cloud (absorption), and partially due to reflection. Consequently, the negative initial velocity is smaller than the positive velocity.

For the lasers implementing the synthetic Lorentz force, we use the following detuning values: for the first step at 780 nm $\delta_- = -\delta_+ = 2\pi \times 6$ MHz, and for the second step at 776 nm $\delta_1 = -2\pi \times 3.5$ MHz and $\delta_2 = 2\pi \times 7.1$ MHz. The two operational two-step pathways are $P(\leftarrow, \uparrow)$ and $P(\rightarrow, \downarrow)$, whereas the other two are far from resonance. The intensities of the beams used are $I_{780} = 0.060$ mW/cm² and $I_{776} = 2.9$ mW/cm², giving Rabi frequencies $\Omega_{780} = 2\pi \times 1.2$ MHz and $\Omega_{776} = 2\pi \times 0.94$ MHz.

By inspection of Fig. 2, we see that the cloud travels along the x -axis by inertia, whereas it accelerates along the y -axis due to the synthetic Lorentz force. The direction of the force depends on the sign of the velocity v_x (negative/positive v_x gives positive/negative F_y), and the force is zero for a cloud at rest. We observe an asymmetry in the force F_y , for the positive and negative velocity. In order to justify the exact

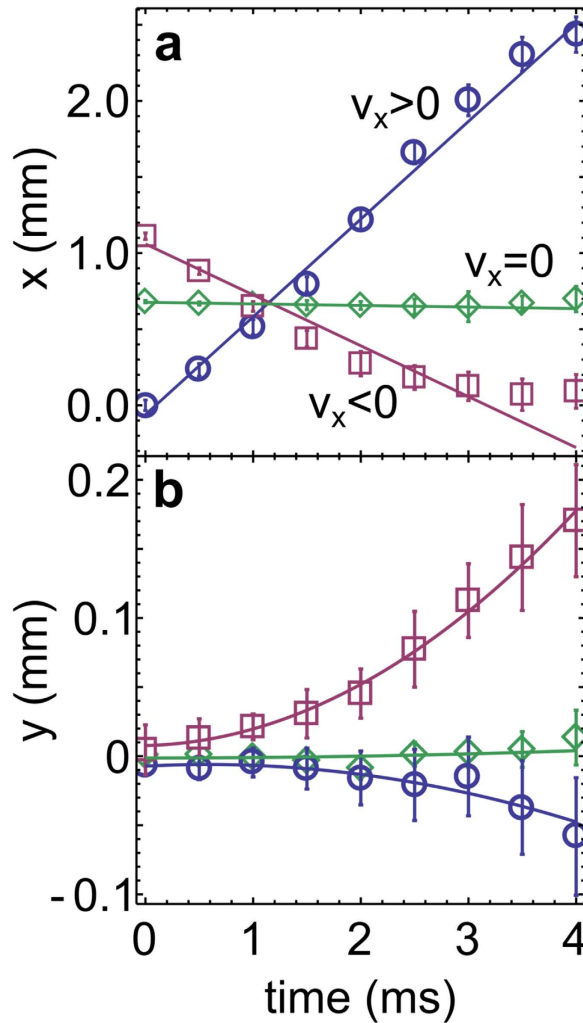


Figure 2. The trajectories of the CM of the atomic cloud in the presence of the synthetic Lorentz force. (a) $x(t)$, and (b) $y(t)$ for three different initial velocities, $v_x = 0.6 \text{ m/s} > 0$ (circles), $v_x = -0.3 \text{ m/s} < 0$ (squares), and $v_x = 0 \text{ m/s}$ (diamonds); initial component of $v_y = 0$ in all measurements. Accelerating motion along y is the signature of the transverse force F_y , which depends on v_x . The lines are fitted to the experimental data, linear fits for $v_x(t)$, and quadratic for $v_y(t)$.

choice of the detuning values δ_{\uparrow} and δ_{\downarrow} , and further investigate the observed asymmetry in the measured synthetic Lorentz force, we perform measurements in a slightly simplified configuration.

Measurements in an auxiliary configuration. We inspect the force along the y direction arising from the two-step two-photon resonances, by using a configuration with three laser beams illustrated in Fig. 3. We block the beam pointing towards the negative y -direction, and measure F_y arising from the remaining beam (the positive y -direction), which drives the $|1\rangle \rightarrow |2\rangle$ transition. The force is measured for an atomic cloud with velocity zero, as a function of the detuning δ_{\uparrow} , see Fig. 3. Measurements are done for three different detuning values of the first-step 780 nm beams $\delta_{\downarrow} = -\delta_{\uparrow} = 2\pi \times 4, 6, 8 \text{ MHz}$. The intensities of the lasers driving the transitions are now $I_{780} = 0.043 \text{ mW/cm}^2$ and $I_{776} = 4.8 \text{ mW/cm}^2$, giving Rabi frequencies $\Omega_{780} = 2\pi \times 1.1 \text{ MHz}$ and $\Omega_{776} = 2\pi \times 1.2 \text{ MHz}$. The two maxima in Fig. 3 are profiles of the two-step two-photon resonances: the peak in the vicinity of $\delta_{\uparrow} = -\delta_{\downarrow} > 0$ corresponds to the excitation pathway $P(\rightarrow, \uparrow)$, and the peak close to $\delta_{\uparrow} = -\delta_{\downarrow} < 0$ corresponds to $P(\leftarrow, \uparrow)$.

Solid lines in Fig. 3 show the theoretically calculated profiles of F_y (see Methods for details of the theoretical calculation). The agreement between theory and experiment is evident. All parameter values used in the theoretical calculation are taken from the experiment, except that the Rabi frequencies are reduced by 20%. This is reasonable because in the experiment, the absorption of laser beams across a dense atomic cloud reduces their intensity²¹.

It should be pointed out that the peaks in $F_y(\delta_{\uparrow})$ are slightly displaced from the values $\delta_{\uparrow} = \pm|\delta_{\downarrow}|$, towards $\delta_{\uparrow} = 0$. For example, for $|\delta_{\downarrow}|$ at 6 MHz, the maxima are at $\pm 5.3 \text{ MHz}$. Moreover, the FWHM of

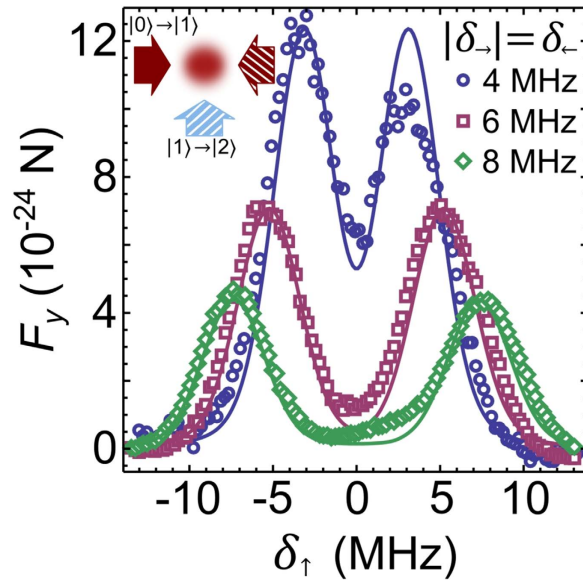


Figure 3. Frequency scan of the two-step two-photon resonance in the auxiliary configuration. The calculated (solid lines) and measured force F_y as a function of δ_1 for the excitation with just three beams as shown. Measurements are performed for the cloud with initial velocity zero. The plots show resonances for three values of the detuning $\delta_- = -\delta_+ = 2\pi \times 4$ MHz (circles), 6 MHz (squares) and 8 MHz (diamonds).

the peaks is larger than the linewidth of the state $|2\rangle$. These two observations are a consequence of the laser linewidth, which is larger than the linewidth of the state $|2\rangle = |5D_{5/2}; F'' = 4\rangle$ (see Methods). The finite linewidth of $|0\rangle \rightarrow |1\rangle$ lasers at 780 nm distorts the peaks as follows: the side of the peak closer to $\delta_1 = 0$ is lifted up in comparison the opposite side of the peak. This follows from the fact that the two-step two-photon resonance is stronger when $|\delta_-|$ is closer to zero, which is evident from Fig. 3. The exact positions of the peaks at ± 5.3 MHz, explain the chosen detuning values for the second step at 776 nm, which were used to obtain Fig. 2: $\delta_1 = -2\pi \times 3.5$ MHz and $\delta_1 = 2\pi \times 7.1$ MHz. They are chosen such that the operational pathways are effectively equally detuned from the two-step two-photon resonance: $P(\rightarrow, \downarrow)$ is detuned by $2\pi \times (-5.3 + 7.1)$ MHz = $2\pi \times 1.8$ MHz, and $P(\leftarrow, \uparrow)$ is detuned by $2\pi \times (+5.3 - 3.5)$ MHz = $2\pi \times 1.8$ MHz.

Discussion

Suppose that we repeat measurements corresponding to Fig. 3, but for an atomic cloud with mean velocity v_x different from zero. The results of such measurements would be identical as for $v_x = 0$, but the positions of the peaks would correspond to the Doppler shifted detuning values $\delta_- - kv_x$ and $\delta_+ + kv_x$. Thus, because detuning can be mapped to velocity space, Fig. 3 can be reinterpreted as measurements for a fixed value of $\delta_- = -\delta_+$, and for three different velocities $v_x < 0$ (4 MHz), $v_x = 0$ (6 MHz), and $v_x > 0$ (8 MHz). This is sketched in Fig. 4, where we see that the two peaks separate (approach) each other for $v_x > 0$ ($v_x < 0$, respectively).

We use Fig. 4 for a detailed explanation of the synthetic Lorentz force measured in Fig. 2. In measurements shown in Fig. 2, we have $\delta_1 < 0$, which means that the positive force $F_y > 0$ in Fig. 2 results from the left resonance peak in Fig. 4. Likewise, because $\delta_1 > 0$ was used for Fig. 2, the negative force $F_y < 0$ results from the right resonance peak in Fig. 4. The transverse force F_y measured in Fig. 2, can be approximately identified with $[F_y(\delta_1) - F_y(\delta_1)]_{v_x}$, as illustrated in Fig. 4.

The choice of δ_1 and δ_1 in Fig. 2 is such that the strength of the forces arising from the two peaks balance each other, giving $F_y = 0$ for $v_x = 0$ [Fig. 4(b)]. Moreover, δ_1 and δ_1 are on the slopes of the two peaks in Fig. 4(b) for an atom with $v_x = 0$, where the maximal magnitude of $\Delta F_y / \Delta v_x$ is expected (detuning translates into velocity space via Doppler effect). For an atom with $v_x < 0$ [see Fig. 4(a)], the two peaks approach each other, yielding greater force from the left peak, which results in $F_y > 0$ for $v_x < 0$, and the opposite for $v_x > 0$ which yields $F_y < 0$ as shown in Fig. 4(c).

It should be pointed out that our scheme is inherently asymmetric. The intensity of the resonance peaks shown in Fig. 4 decreases when they separate (for $v_x > 0$), in contrast to when they approach each other (for $v_x < 0$). Thus, the net force along y is larger for negative v_x , than for the velocity of the same magnitude but with a positive sign. By using a scheme with four atomic levels¹⁷, one could remedy the asymmetry in the force, present in the three-level scheme. In addition, the initial density of the atomic

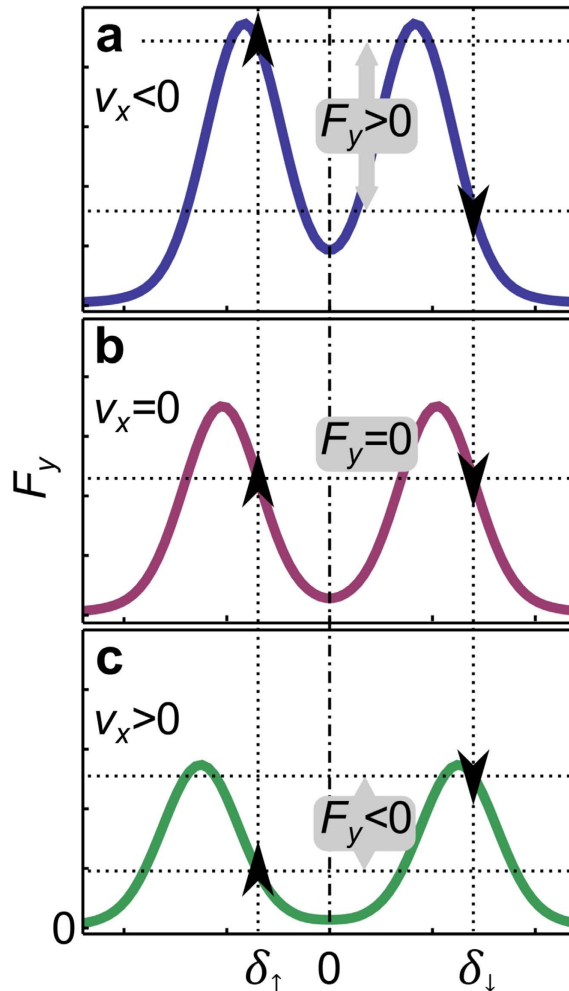


Figure 4. Interpretation of the synthetic Lorentz force from Figs 1 and 2, via two-step two-photon resonances presented in Fig. 3. Sketch of the resonant peaks that would be obtained in the setup shown in Fig. 3 for three atomic velocities: (a) $v_x < 0$, (b) $v_x = 0$, and (c) $v_x > 0$. Vertical dotted lines illustrate the values of the detuning used for the lasers aligned on the y -axis in Fig. 1. Arrows denote the direction of the force exerted by those lasers, and illustrate the way F_y observed in Fig. 2 arises as a function of velocity v_x . See text for details.

cloud is not identical prior to acceleration in the positive/negative direction due to the slight asymmetry of the displaced trapping potential. This also affects the transverse force due to absorption and multiple scattering²¹. The inherent asymmetry in the force $F_y(v_x)$ and in the initial density of the cloud, is reflected in the asymmetry of the observed motion in Fig. 2 for $v_x < 0$ and $v_x > 0$. Importantly, all of these details only quantitatively affect the results, but not qualitatively.

Conclusion

The presented experiment, which demonstrates the synthetic Lorentz force by using radiation pressure, is performed in a classical cold atomic gas, prepared in a MOT, where the heating due to spontaneous emission does not prevent the observations. The concept of a force is natural in our classical laser cooled system¹⁸. We would like to emphasize that our method is entirely different from the Berry phase approach, where the connection with the Lorentz force can be made in a semiclassical approximation²².

In the outlook, we foresee many intriguing novel experiments based on the presented method. First, one could develop experiments using more sophisticated schemes, involving more atomic levels (see Ref. [17]), to create a uniform synthetic magnetic field. Next, we plan to adjust our system for the observation of the predicted rotation of the cloud during expansion¹⁷. One of the goals of this research is to build up a toroidal trap for cold atoms with a toroidal synthetic magnetic field, which holds potential to emulate the plasma in a tokamak. The proposed concept could be used for velocity selection of atomic beams, or for developing a novel kind of mass spectrometer for neutral atoms. We believe that our concept or an analogous scheme could be applicable in other systems, such as suspended nanoparticles.

Methods

Experimental setup. The ^{87}Rb MOT is set up in the standard $\sigma^+ \sigma^-$ retro-reflected configuration, with beam diameters of 2 cm. The trap is vapour loaded in a glass cell which facilitates fast switching of the magnetic field. Cooling and repumper lasers are external cavity diode lasers (ECDL) delivering total powers of 80 mW and 20 mW, respectively. The cooling laser is typically $2\pi \times 24\text{ MHz}$ (4Γ) red-detuned from the $|5S_{1/2}; F=2\rangle \rightarrow |5P_{3/2}; F'=3\rangle$ hyperfine transition. The repumper laser is in resonance with the $|5S_{1/2}; F=1\rangle \rightarrow |5P_{1/2}; F'=2\rangle$ hyperfine transition, thus keeping most of population in the $|5S_{1/2}; F=2\rangle$ ground level. The quadrupole magnetic field gradient is 13 G/cm. The number of atoms in the trap is deduced by measuring the cloud fluorescence with a calibrated photodiode.

For the implementation of the synthetic Lorentz force two additional ECDL lasers were introduced in the experiment: one at 780 nm driving $|5S_{1/2}; F=2\rangle \rightarrow |5P_{3/2}; F'=3\rangle$ transition, and other at 776 nm driving $|5P_{3/2}; F'=3\rangle \rightarrow |5D_{5/2}; F''=4\rangle$ transition. Each laser beam is split into two beams which are sent on the rubidium cloud in counter-propagating configurations as shown in Fig. 1. Frequency and intensity control is done separately for each of the four laser beams with acoustic-optical modulators (AOM). After being frequency shifted, we couple the beams to single mode polarization maintaining fibres, which ensures linear polarization (in the z -direction) and uniform intensity.

All lasers used in the experiment are frequency stabilized by using modulation transfer spectroscopy. We modulate the laser diode current to modulate the laser frequency, which effectively increases the laser linewidth. This additional broadening is taken into account in theoretical calculations. The linewidths were checked by heterodyne beating of two stabilized lasers with similar locking parameters. For locking the laser tuned at 776 nm, we counter-propagate picked off beams from the 776 nm laser and the 780 nm laser through a heated ^{87}Rb glass cell, where the 780 nm laser populates the $|5P_{3/2}; F'=3\rangle$ level. We observe an absorption signal resulting from the $|5P_{3/2}; F'=3\rangle \rightarrow |5D_{5/2}; F''=4\rangle$ transition. This signal is mixed with the modulation signal from the 780 nm laser to obtain a frequency locking error signal. Therefore, there is no need to modulate the 776 nm laser frequency to stabilize it.

Theoretical calculation of the radiation pressure force. To calculate the force plotted in Fig. 3, we first solve the optical Bloch equations (OBEs) to find the density matrix $\hat{\rho}^{18}$:

$$\begin{aligned} \frac{d\rho_{nm}}{dt} &= -\frac{i}{\hbar} [\hat{H}, \hat{\rho}]_{nm} - \gamma_{nm}\rho_{nm}, \quad n \neq m, \\ \frac{d\rho_{nn}}{dt} &= -\frac{i}{\hbar} [\hat{H}, \hat{\rho}]_{nn} + \sum_{E_m > E_n} \Gamma_{nm}\rho_{mm} - \sum_{E_m < E_n} \Gamma_{mn}\rho_{nn}, \end{aligned} \quad (1)$$

where $n, m=0, 1, 2$. The Hamiltonian $\hat{H} = \hat{H}^{(0)} + \hat{H}^{(1)}$ describes a three-level system interacting with laser fields. $\hat{H}^{(0)}$ is represented by a diagonal matrix with elements $H_{00}^{(0)} = 0$, $H_{11}^{(0)} = \hbar\omega_{01}$, and $H_{22}^{(0)} = \hbar(\omega_{01} + \omega_{12})$, whereas the interaction Hamiltonian is, in the dipole and the rotating wave approximation¹⁸,

$$\begin{aligned} \hat{H}_{12}^* &= \hat{H}_{21} = -\frac{\hbar\Omega_{12}}{2} (e^{i(k_x x - \omega_{01}t - \delta_- t)} + e^{i(-k_x x - \omega_{01}t - \delta_- t)}), \\ \hat{H}_{23}^* &= \hat{H}_{32} = -\frac{\hbar\Omega_{23}}{2} e^{i(k_y y - \omega_{12}t - \delta_1 t)}, \end{aligned} \quad (2)$$

and zero otherwise. The linewidths, $\Gamma_{12} = 2\pi \times 6.1\text{ MHz}$, $\Gamma_{23} = 2\pi \times 0.66\text{ MHz}$, and the transition frequencies, $\omega_{01} = k_x c$ and $\omega_{12} = k_y c$, where $k_x = 2\pi/780\text{ nm}^{-1}$ and $k_y = 2\pi/776\text{ nm}^{-1}$, correspond to the experiment; $\Gamma_{13} = 0$; the coherences are $\gamma_{ij} = \frac{1}{2}(\Gamma_{ii} + \Gamma_{jj})$, where $\Gamma_{ii} = \sum_{j < i} \Gamma_{ji}$. Because transition $|0\rangle \rightarrow |1\rangle$ is driven with two lasers of different detuning values $\delta_{\pm} = -\delta_{\mp}$, there is no stationary solution, and the level populations oscillate with the frequency $|\delta_{\pm}| \sim 6\text{ MHz}$ (the phase of these oscillations depends on x , but this is not reflected in the force). The force on an atom is calculated by employing the Ehrenfest theorem¹⁸, and averaging over the oscillations: $F'_y(\delta_{\pm}, \delta_{\mp}, \delta_1) = \langle -\text{Tr} [\hat{\rho} \partial \hat{H} / \partial y] \rangle_t$. The average over time $\langle \dots \rangle_t$ is justified because the oscillations at frequency $|\delta_{\pm}| \sim 6\text{ MHz}$ are much faster than the characteristic scale for measuring the force, τ_F , which is on the order of a few milliseconds.

The outlined procedure for calculating the force assumes that the lasers are perfectly monochromatic. However, there is finite laser linewidth that should be taken into account to quantitatively describe the two-step two-photon resonances in Fig. 3, i.e., $F_y(\delta_1)$. The spectral profile of the diode laser can be described by a Gaussian in the frequency domain, $\propto \exp((\omega - \omega_0)^2 / 2\sigma^2)$. In the experiment, the modulation transfer spectroscopy for laser locking is used, and the central laser frequency is modulated with the amplitude $d \approx 2\pi \times 1\text{ MHz}$ and frequency $\eta = 2\pi \times 14\text{ kHz}$: $\tilde{\omega}_0(t) = \omega_0 + d \sin \eta t$. Thus, the laser spectral profile, over time-scales larger than $1/\eta$, is given by

$$\begin{aligned}
 p(\omega; \omega_0) &= \frac{p_0 \eta d}{\sigma \sqrt{2\pi^3}} \int_{\omega_0-d}^{\omega_0+d} \frac{\exp(-(\omega - \tilde{\omega}_0)^2/2\sigma^2)}{\left| \frac{d\tilde{\omega}_0}{dt} \right|_{t(\tilde{\omega}_0)}} d\tilde{\omega}_0 \\
 &= \frac{p_0}{\sigma \sqrt{2\pi^3}} \int_{\omega_0-d}^{\omega_0+d} \frac{\exp(-(\omega - \tilde{\omega}_0)^2/2\sigma^2)}{\sqrt{1 - \left(\frac{\tilde{\omega}_0 - \omega_0}{d}\right)^2}} d\tilde{\omega}_0,
 \end{aligned} \tag{3}$$

where p_0 is the normalization factor.

The detuning values of 780 nm lasers oscillate as follows: $\tilde{\delta}_- = \delta_- + d \sin \eta t$ and $\tilde{\delta}_+ = \delta_+ + d \sin \eta t$. Note that $\eta \ll |\delta|$, and at the same time $1/\eta$ is sufficiently smaller than τ_F . This means that we can employ the separation of scales to take into account finite laser linewidth. We calculate the resulting force $F_y(\delta_\uparrow)$ on the cloud by averaging $F'_y(\delta_-, \delta_+, \delta_\uparrow)$ with the appropriate laser profile distribution in the frequency domain:

$$F_y(\delta_\uparrow) = \int_{-\infty}^{\infty} p(\omega; \omega_{01} + \delta_-) F'_y(\omega - \omega_{01}, \omega - \omega_{01} + 2|\delta_-|, \delta_\uparrow) d\omega. \tag{4}$$

The width σ was determined to be $2\pi \times 1.5$ MHz by fitting to the experimental profiles. The Rabi frequencies used in the calculation are discussed in the Results Section.

References

- Madison, K. W., Chevy, F., Wohlleben, W. & Dalibard, J. Vortex Formation in a Stirred Bose-Einstein Condensate, *Phys. Rev. Lett.* **84**, 806–809 (2000).
- Abo-Shaeer, J. R., Raman, C., Vogels, J. M. & Ketterle, W. Observation of Vortex Lattices in Bose-Einstein Condensates, *Science* **292**, 476–479 (2001).
- Lin, Y.-J., Compton, R. L., Jimenez-Garcia, K., Porto, J. V. & Spielman, I. B. Synthetic magnetic fields for ultracold neutral atoms, *Nature* **462**, 628–632 (2009).
- Le Blanc, L. J. *et al.* Observation of a superfluid Hall effect, *PNAS* **109**, 10811–10814 (2012).
- Aidelsburger, M. *et al.* Experimental Realization of Strong Effective Magnetic Fields in an Optical Lattice, *Phys. Rev. Lett.* **107**, 255301 (2011).
- Struck, J. *et al.* Tunable Gauge Potential for Neutral and Spinless Particles in Driven Optical Lattices, *Phys. Rev. Lett.* **108** 225304 (2012).
- Miyake, H., Siviloglou, G. A., Kennedy, C. J., Burton, W. C. & Ketterle, W. Realizing the Harper Hamiltonian with Laser-Assisted Tunneling in Optical Lattices, *Phys. Rev. Lett.* **111**, 185302 (2013).
- Aidelsburger, M. *et al.* Realization of the Hofstadter Hamiltonian with Ultracold Atoms in Optical Lattices, *Phys. Rev. Lett.* **111**, 185301 (2013).
- Aidelsburger, M. *et al.* Measuring the Chern number of Hofstadter bands with ultracold bosonic atoms, *Nature Physics* **11**, 162–166 (2015).
- Jotzu, G. *et al.* Experimental realization of the topological Haldane model with ultracold fermions, *Nature* **515**, 237–240 (2014).
- Ray, M. W., Ruokokoski, E., Kandel, S., Mottonen, M. & Hall, D. S. Observation of Dirac monopoles in a synthetic magnetic field, *Nature* **505**, 657–660 (2014).
- Bloch, I., Dalibard, J. & Nascimbene, S. Quantum simulations with ultracold quantum gases, *Nature Physics* **8**, 267–276 (2012).
- Dalibard, J., Gerbier, F., Juzeliunas, G. & Öhberg, P. Colloquium: Artificial gauge potentials for neutral atoms, *Rev. Mod. Phys.* **83**, 1523–1543 (2011).
- Goldman, N., Juzeliunas, G., Öhberg, P. & Spielman, I. B. Light-induced gauge fields for ultracold atoms, *Rep. Prog. Phys.* **77**, 126401 (2014).
- Cooper, N. R. Rapidly rotating atomic gases, *Adv. Phys.* **57**, 539–616 (2008).
- Dum, R. & Olshanii, M. Gauge Structures in Atom-Laser Interaction: Bloch Oscillations in a Dark Lattice, *Phys. Rev. Lett.* **76**, 1788–1891 (1996).
- Dubček, T. *et al.* Synthetic Lorentz force in classical atomic gases via Doppler effect and radiation pressure, *Phys. Rev. A* **89**, 063415 (2014).
- Metcalf, H. J. & Van Der Straten, P. *Laser Cooling and Trapping*, (Springer, New York, 1999).
- Steck, D. A. Rubidium 87 D Line Data. Available online at: <http://steck.us/alkalidata/rubidium87numbers.pdf> (2010) Date of access: 1st June 2015.
- Sheng, D., Perez Galvan, A., and Orozco, L. A. Lifetime measurements of the 5d states of rubidium, *Phys. Rev. A* **78**, 062506 (2008).
- Chabe, J. *et al.* Coherent and incoherent multiple scattering, *Phys. Rev. A* **89**, 043833 (2014).
- Cheneau, M. *et al.* Geometric potentials in quantum optics: A semi-classical interpretation, *Europhys. Lett.* **83**, 60 001 (2008).

Acknowledgments

This work was supported by the Unity through Knowledge Fund (UKF Grant No. 5/13).

Author Contributions

All authors contributed in designing experiments, interpretation of the results, and writing the manuscript. N.Š. and T.B. performed all experiments. T.D., D.A. and H.B. performed all calculations.

Additional Information

Competing financial interests: The authors declare no competing financial interests.

How to cite this article: Šantić, N. *et al.* Experimental Demonstration of a Synthetic Lorentz Force by Using Radiation Pressure. *Sci. Rep.* **5**, 13485; doi: 10.1038/srep13485 (2015).



This work is licensed under a Creative Commons Attribution 4.0 International License. The images or other third party material in this article are included in the article's Creative Commons license, unless indicated otherwise in the credit line; if the material is not included under the Creative Commons license, users will need to obtain permission from the license holder to reproduce the material. To view a copy of this license, visit <http://creativecommons.org/licenses/by/4.0/>



Synthetic Lorentz force in an expanding cold atomic gas

N. ŠANTIĆ,^{1,2,*} T. DUBČEK,² D. AUMILER,¹ H. BULJAN,² AND T. BAN¹

¹Institute of Physics, Bijenička c. 46, 10000 Zagreb, Croatia

²Department of Physics, University of Zagreb, Bijenička c. 32, 10000 Zagreb, Croatia

*Corresponding author: nsantic@ifs.hr

Received 15 February 2017; revised 27 April 2017; accepted 29 April 2017; posted 3 May 2017 (Doc. ID 286769); published 26 May 2017

We implement a synthetic Lorentz force in a cold atomic gas released from a magneto-optical trap. The signature of this is an angular deflection of a rotationally asymmetrical cloud. The effect is a consequence of thermal expansion of the cold atomic cloud under the influence of the applied synthetic Lorentz force. The synthetic Lorentz force is based on radiation pressure and the Doppler effect, making it straightforward to implement. The introduction of synthetic magnetism into our system, together with the fact that it is readily described by the Fokker-Planck equation, makes it an excellent candidate to emulate numerous complex classical systems. © 2017 Optical Society of America

OCIS codes: (020.3320) Laser cooling; (020.0020) Atomic and molecular physics.

<https://doi.org/10.1364/JOSAB.34.001264>

1. INTRODUCTION

Radiation trapping in cold atomic gases is a known and well-studied effect [1] which sets an upper limit on achievable atom densities in a magneto-optical trap (MOT). The re-absorption of scattered photons in dense atomic clouds gives rise to an effective long-range repulsive force between atoms that scales as $1/r^2$, analogous to the Coulomb force between charges. Consequently, it is possible to assign an effective (synthetic) charge to the atoms [2], and tune its value by changing the intensity and detuning of the scattered radiation. This also offers the possibility of realizing a time-dependent synthetic charge, a regime not accessible with real charges in electrodynamics.

The analogy between clouds of cold atoms and plasmas has led to the observation of Coulomb explosion in expanding molasses [3], to the prediction of plasma-acoustic waves [4], and many other plasma-like phenomena [5–9]. In addition, equations of equilibrium governing the atomic distribution in a dense atomic cloud are similar to the equation of hydrostatic equilibrium in stars, experimentally demonstrated in [10], with the trapping force having replaced gravity. This led to the observation of self-sustained oscillations in a MOT [11], analogous to oscillations in stars. Consequently, it is reasonable to consider a dense cloud of cold atoms in a MOT as an ideal classical emulator that could simulate complex classical systems, for example a tokamak fusion reactor or astrophysical objects, such as stars and globular clusters. However, since magnetism plays a key role in the aforementioned systems, in order to achieve this goal it is necessary to introduce synthetic magnetism in the classical system of cold atoms in a MOT.

Apart from our recent work [12], all up-to-date realizations of synthetic magnetism involved ultra-cold, quantum degenerate atomic gases: Bose–Einstein condensates (BECs) and Fermi degenerated gases. Experiments implementing such systems hold potential to be used as quantum emulators of strongly correlated many-body systems. The introduction of synthetic magnetism to these experiments has enabled realization of many interesting phenomena, ranging from the Hall effect [13] to the experimental realization of the Hofstadter Hamiltonian [14], and has initiated a new and attractive research direction. For recent reviews see [15,16]. Early realizations of synthetic magnetism in ultra-cold atomic systems employed the analogy between the Coriolis force and the Lorentz force by rotating the BEC [17,18]. More recent experiments, both in bulk BECs [19] and optical lattices [20], use laser–atom interactions and employ the analogy between the Berry phase and the Aharonov–Bohm phase. However, methods relying on the Berry phase analogy used in BECs are not applicable for high atom velocities and large cloud volumes found in a MOT.

We use a different method to introduce a synthetic Lorentz force (SLF) to a classical system of cold atoms. It is based on radiation pressure and the Doppler effect, and was introduced theoretically in our recent paper [21]. Using radiation pressure is necessarily accompanied by spontaneous emission and radiation trapping, which makes our method non-applicable to quantum degenerate systems. However, atomic samples prepared in a MOT, still classical and relatively hot to those in BECs, are not significantly affected by the additional heating introduced by spontaneous emission. Moreover, the radiation

trapping which accompanies spontaneous emission is, as discussed above, the basis for the analogy between clouds of cold atoms and classical systems of charged particles such as plasmas.

Two scenarios for the observation of the SLF were proposed in [21], each characterized with a completely different initial velocity distribution of cold atoms and each suitable for emulation of different classical systems.

The first scenario is suitable for the emulation of a single charged particle in a magnetic field, and was experimentally demonstrated in our recent work [12]. We first prepared a cloud with a given center-of-mass (CM) velocity, after which we measured trajectories of the CM of the atomic cloud in the presence of the SLF for various initial CM velocities. The observed trajectories of the CM of the atomic cloud can be interpreted as dynamics of a single charged particle under the influence of the Lorentz force, suggesting approximately equal SLF for all atoms in the cloud, due to the equal initial velocities.

The second scenario is experimentally demonstrated in this work. The cold cloud is considered as an ensemble of particles with a Maxwell–Boltzmann velocity distribution. The signature of the SLF is observed in the shape of the expanding cloud, i.e., an asymmetric and tilted expanding cloud is observed. Our system, a dense atomic cloud in a MOT, is analogous to an expanding single species plasma in a magnetic field, also to an expanding neutral gas in a rotating frame under the influence of a Coriolis force, for instance, an anticyclone. Just as experiments with quantum degenerate gases benefited from the introduction of synthetic magnetism, experiments mimicking classical systems with electrical charges would benefit from the introduction of a SLF in a dense cloud of cold atoms in a MOT. Therefore, our work provides the final missing ingredient needed for the realization of an emulator of complex classical systems whose behavior cannot yet be understood by use of computer simulations [22].

For the purpose of this work, we have upgraded the basic idea presented in [12] and developed a modified experimental setup. A SLF is implemented in the experiment by introducing two pairs of perpendicular laser beams into a system of five-level atoms. Each pair drives two-step two-photon transitions between three levels, from the same ground state but to different excited states, see Figs. 1(a) and 1(b). One pair of perpendicular laser beams, depicted with arrows with solid color filling, drives the $|0\rangle \rightarrow |1\rangle \rightarrow |2\rangle$ transition, while the other pair, marked with pattern filling, drives the $|0\rangle \rightarrow |1'\rangle \rightarrow |2'\rangle$ transition. Due to the Doppler effect and the geometry of the laser beams, both components of the radiation pressure force depend on both components of the atom velocity: $F_x = F_x(v_x, v_y)$ and $F_y = F_y(v_x, v_y)$. This gives us the opportunity to choose the detuning values of our lasers such that the radiation pressure force mimics the Lorentz force, e.g., F_y is positive/negative for atoms with a negative/positive velocity component v_x and the total force is zero for an atom at rest $F(\mathbf{v} = 0) = 0$. In Figs. 1(c) and 1(d) we show the calculated force components F_x and F_y as a function of atom velocities for the system and laser detunings used in the experiment. This force pattern in velocity space can be separated in to two components, one that results in a scalar potential in velocity space and the other that

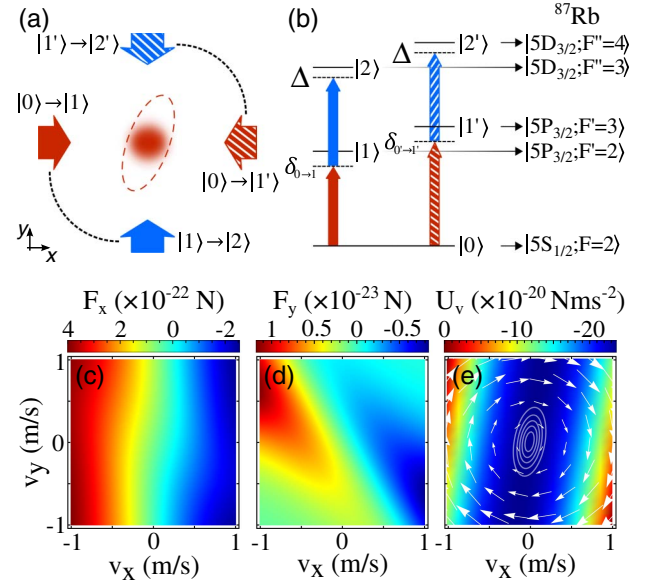


Fig. 1. Scheme for obtaining the synthetic Lorentz force and the resulting force patterns in velocity space. (a) The four beams responsible for the SLF. They propagate in the xy plane (horizontal). The red beams counterpropagating along the x -axis couple states $|0\rangle \rightarrow |1\rangle/|1'\rangle$ (solid/dashed) while the two blue beams counterpropagating along the y -axis couple states $|1\rangle/|1'\rangle \rightarrow |2\rangle/|2'\rangle$ (solid/dashed). (b) The hyperfine levels used for the realization of the SLF. (c) The calculated force in the x and (d) y direction as a function of velocity. (e) Resulting potential in velocity space when the rotating part of the force (shown with white arrows) is excluded. The white contours show the calculated velocity distribution after 1 ms of expansion.

rotates and is responsible for the SLF. The resulting scalar potential, along with the rotating part of the force, is shown in Fig. 1(e). These two components will both influence the observed shape of the cloud. A detailed explanation of the numerical calculations and of the contributions of the two force components in velocity space is given in Section 3. In contrast to the previous experimental realization [12] where three different levels were used, in this work we use five different levels. Using three different levels results in a similar force pattern in velocity space; however, the force is not symmetric, i.e., F_y has different magnitudes for positive and negative v_x of the same magnitude. Using five levels avoids this problem resulting in a better analogy with the Lorentz force and is adequate for experiments in which a symmetrical initial velocity distribution is used.

2. EXPERIMENT

The experiment is based on a ^{87}Rb MOT. The cold cloud of approximately 10^8 atoms is loaded from background vapor in a glass cell. The MOT is arranged in a standard three-beam retroreflected configuration which together with the anti-Helmholtz produced quadrupole magnetic field create the trapping potential.

For the SLF we use the geometry sketched out in Fig. 1(a) where the xy plane is the horizontal one. Beams propagating along the x direction drive the first step of our two-step scheme, where for $|0\rangle \rightarrow |1\rangle$ we use the $|5S_{1/2}; F=2\rangle$

$\rightarrow |5P_{3/2}; F' = 2\rangle$ transition and for $|0\rangle \rightarrow |1'\rangle$ we use the $|5S_{1/2}; F = 2\rangle \rightarrow |5P_{3/2}; F' = 3\rangle$ transition. Beams propagating along the y direction drive the second step of the two-step excitation, where for $|1\rangle \rightarrow |2\rangle$ we use the $|5P_{3/2}; F' = 2\rangle \rightarrow |5D_{5/2}; F'' = 3\rangle$ transition and for $|1'\rangle \rightarrow |2'\rangle$ we use the $|5P_{3/2}; F' = 3\rangle \rightarrow |5D_{5/2}; F'' = 4\rangle$ transition.

The four SLF beams are provided from the output of two frequency stabilized external cavity diode lasers (ECDLs) with nominal emission at 780 nm for the first step and 776 nm for the second step. The ECDL at 780 nm is stabilized using a dither technique to a saturation spectroscopy signal obtained from room temperature rubidium vapor. The ECDL at 776 nm is also stabilized using the dither technique to a Doppler-free two-photon signal obtained from heated rubidium vapor. Using heterodyne spectroscopy with an optical frequency comb, a laser linewidth of 1 MHz is measured. All beams are passed through acousto-optic modulators to obtain the desired frequencies.

Since one of the two-step two-photon pathways drives an open transition, the presence of a repumper is necessary. For this we drive the $|5S_{1/2}; F = 1\rangle \rightarrow |5P_{3/2}; F' = 1\rangle$ transition. Compared to normal MOT conditions the population in the $|5S_{1/2}; F = 1\rangle$ will be substantial leading to an appreciable radiation pressure force from the repumper beam. To avoid masking the observation of the SLF by introducing unaccounted forces into the system we copropagate the repumper beam with the $|5S_{1/2}; F = 2\rangle \rightarrow |5P_{3/2}; F' = 2\rangle$ beam.

Fluorescent imaging is performed along the z -axis, perpendicular to the xy plane in which the four beams driving two two-step two-photon transitions propagate. Gravitational force acts along the z -axis and therefore has no effect on atomic motion in the xy plane. An experimental protocol that is typical for time-of-flight measurements (TOF) is used, with the difference that all four SLF beams are present in the system throughout the experiment cycle. It is important to note here that the SLF beams have no effect on the initial spatial and velocity distributions of the cloud while the trapping beams are present since the force arising from their absorption is small compared to forces due to the trapping beams. The experiment cycle is as follows: (i) we load the cloud, (ii) at $t = 0$ we switch off the trapping beams and the quadrupole magnetic field and the cloud evolves in the presence of the synthetic Lorentz and Doppler forces induced by the SLF beams, (iii) after given expansion time τ we turn on the trapping beams and image the cloud fluorescence. We repeat the measurement protocol 20 times in identical conditions, and subsequently average to obtain the density distribution of the cloud for a given τ .

The following detuning values are chosen in the experiment: the first-step beams, propagating along the x direction, are red detuned by $\delta_{0\rightarrow 1} = \delta_{0\rightarrow 1'} = -\Gamma_p/2$, where $\Gamma_p = 2\pi \times 6.1$ MHz is the decay rate of the $^{87}\text{Rb}5P_{3/2}$ state [23]. The second-step beams, propagating along the y direction, are blue detuned. Their detuning values, $\delta_{1\rightarrow 2}$ and $\delta_{1'\rightarrow 2'}$, are chosen in such a way that the total two-photon detuning, Δ , for both two-photon two-step pathways is equal to $\Delta = -\Gamma_D/2$, where $\Gamma_D = 2\pi \times 0.66$ MHz is the decay rate of the $^{87}\text{Rb}5D_{5/2}$ state [24]. Following this condition, $\delta_{1\rightarrow 2} = \delta_{1'\rightarrow 2'} = 2\pi \times 2.7$ MHz. The repumper laser is on

resonance. The choice of those detuning values follows from our recent theoretical paper [21], and is such that we achieve the maximum deflection angle.

Intensities of the SLF beams are: $I_{0\rightarrow 1} = 0.039$ mW/cm², $I_{0\rightarrow 1'} = 0.063$ mW/cm², $I_{1\rightarrow 2} = 3.18$ mW/cm², and $I_{1'\rightarrow 2'} = 0.063$ mW/cm². The intensity of the repumper beam is $I_{\text{repumper}} = 3.2$ mW/cm². All beams are fiber coupled and polarized in the z direction. For the reasons discussed earlier, the repumper beam is coupled to the same fiber as the $|0\rangle \rightarrow |1\rangle$ beam. The offset in the force in the x direction, coming from the repumper radiative force, is compensated with a lower intensity of the $|0\rangle \rightarrow |1\rangle$ beam relative to a case in which the repumper would not be present. In such a way we achieved that the total force on atoms with zero velocity is zero, i.e., $F_x(v = 0) = 0$. As a consequence the SLF will be of lower magnitude but will have the same characteristics.

3. NUMERICAL SIMULATIONS

To be able to analyze the TOF experimental results, first we turn to numerical simulations of our system.

The force in velocity space is calculated by using the density matrix formalism and applying the Ehrenfest theorem [25]. The procedure assumes that the lasers are perfectly monochromatic. However, there is a finite laser linewidth in the experiment that should be taken into account. Considering that the spectral profile of diode lasers can be described by a Gaussian in the frequency domain, we introduce the laser linewidth in the simulations by convolving the force in velocity space with a Gaussian whose FWHM corresponds to the measured laser linewidth, i.e., to 1 MHz. Calculated resulting forces F_x and F_y as a function of atom velocities for relevant rubidium atomic levels and laser parameters used in the experiment are shown in Figs. 1(c) and 1(d). The repumper laser is also included in the calculations.

One can see from Fig. 1(d) that the obtained force pattern has the wanted properties: F_y is positive/negative for atoms with a negative/positive velocity component v_x . Positive F_y arises as a result of driving the $|0\rangle \rightarrow |1\rangle \rightarrow |2\rangle$ transition, by the laser beam pair marked with solid filling in Fig. 1(a). Due to the red-detuned first-step laser driving the $|0\rangle \rightarrow |1\rangle$ transition, this two-step two-photon pathway is resonant only for atoms with negative v_x . The positive force in the $+y$ direction is then a consequence of the second-step laser beam driving the $|1\rangle \rightarrow |2\rangle$ transition. In a completely analogous way, a negative F_y arises as a result of driving $|0\rangle \rightarrow |1'\rangle \rightarrow |2'\rangle$ transition, which is resonant only for atoms with positive v_x .

For sufficiently small velocities the force is linear around zero; therefore, a good approximation is to neglect higher-order terms considering the low atom velocities in a MOT. We Taylor expand the force in velocity up to the linear term:

$$\begin{bmatrix} F_x \\ F_y \end{bmatrix} = \begin{bmatrix} F_{x0} \\ F_{y0} \end{bmatrix} + \begin{bmatrix} \alpha_{xx} & \alpha_{xy} \\ \alpha_{yx} & \alpha_{yy} \end{bmatrix} \begin{bmatrix} v_x \\ v_y \end{bmatrix}. \quad (1)$$

The second term on the right-hand side can be divided into two terms, one that has zero curl in velocity space, while the other rotates:

$$\begin{bmatrix} \alpha_{xx} & \alpha_{xy} \\ \alpha_{yx} & \alpha_{yy} \end{bmatrix} \begin{bmatrix} v_x \\ v_y \end{bmatrix} = \left(\begin{bmatrix} \alpha_{xx} & \alpha_D \\ \alpha_D & \alpha_{yy} \end{bmatrix} + \begin{bmatrix} 0 & \alpha_R \\ -\alpha_R & 0 \end{bmatrix} \right) \begin{bmatrix} v_x \\ v_y \end{bmatrix} \\ = \mathbf{F}_{\text{pot}}(\mathbf{v}) + \mathbf{F}_{SL}(\mathbf{v}), \quad (2)$$

where $\alpha_{xy} = \alpha_D + \alpha_R$ and $\alpha_{yx} = \alpha_D - \alpha_R$. We identify the second term $\mathbf{F}_{SL}(\mathbf{v})$ as the one responsible for the SLF. The first term $\mathbf{F}_{\text{pot}}(\mathbf{v})$ depends on both components of the atom velocity, and includes the usual Doppler force through the α_{xx} and α_{yy} diagonal terms. Since $\nabla_{\mathbf{v}} \times \mathbf{F}_{\text{pot}}(\mathbf{v}) = 0$ we can calculate the corresponding potential in velocity space from $\mathbf{F}_{\text{pot}} = -\nabla_{\mathbf{v}} U(v_x, v_y)$, where $\nabla_{\mathbf{v}} = \hat{\mathbf{v}}_x \partial / \partial v_x + \hat{\mathbf{v}}_y \partial / \partial v_y$. It is a two-dimensional angled valley-like potential of the form $U(v_x, v_y) = \alpha_{xx} v_x^2 / 2 + \alpha_D v_x v_y + \alpha_{yy} v_y^2 / 2$. In Fig. 1(e), we present the calculated potential, together with the direction and magnitude of the $\mathbf{F}_{SL}(\mathbf{v})$ force, given by the white arrows. Consider now how these two terms affect the atomic velocity distribution. We start with a symmetric velocity distribution at $t = 0$, which is a common initial condition in a MOT. Shortly after $t = 0$ the cloud will be reshaped in velocity space to a tilted ellipsoid by the potential shown in Fig. 1(e). Simultaneously, the rotating part of the force, $\mathbf{F}_{SL}(\mathbf{v})$ increases the distribution's deflection angle while preserving its ellipsoidal shape. This reshaped velocity distribution will give rise to a reshaped spatial distribution of the cloud, which can be detected in TOF measurements.

The expansion of the cloud in the presence of the SLF laser beams is calculated by employing the Fokker–Planck equation [25]. We take the linearized form of $F(v)$ from Eq. (1), this enables us to solve the Fokker–Planck equation by using the ansatz from [21]. The coefficients α_{ij} are evaluated from the calculated force at $v = 0$. The initial phase space distribution of atoms $P(x, y, v_x, v_y, t = 0)$, which is the input distribution for the Fokker–Planck equation, is defined using measured experimental values. These were determined by measuring the time evolution of the cloud's thermal expansion in a standard TOF measurement. The Fokker–Planck equation is solved numerically for different expansion times, providing the phase space distribution of atoms in the cloud for a given time. The calculated atomic density distribution is then subsequently compared to the TOF measurements.

4. SHAPE OF THE CLOUD IN THE PRESENCE OF THE SLF

In Fig. 2 we present measured [Figs. 2(b), 2(e), and 2(h)] and calculated [Figs. 2(c), 2(f), and 2(i)] atom density distributions after $\tau = 4$ ms of expansion time for three experimental configurations [Figs. 2(a), 2(d), and 2(g), respectively].

The atomic system and laser parameters used in the calculations are identical to the experimental ones, given in Section 2. The cooling laser detuning is -3.6Γ , providing a symmetrical Gaussian-shaped density distribution of the cloud at $t = 0$ ms whose standard deviation (SD) is $\sigma_x = 0.25$ mm and a velocity distribution whose SD is $\sigma_v = 0.1$ m/s.

In the configuration presented in Fig. 2(a) only the first-step SLF beams, $|0\rangle \rightarrow |1\rangle$ and $|0\rangle \rightarrow |1'\rangle$, are present. An ellipsoid shape of the cloud is measured elongated along the y -axis, Fig. 2(b). The simulated atom density distribution corresponding to this experimental geometry is shown in Fig. 2(c). The ellipsoid

shape is a result of a friction force in the x direction resulting from the red-detuned first-step SLF beams. This measurement serves as a control, not only to make sure that the ellipsoid shape of the cloud is due to the first-step beams, but also to gauge the reference angle of the ellipsoid. We find the deflection angle of the major axis by fitting a 2D Gaussian to the density distribution.

By adding the second-step SLF beams, $|1\rangle \rightarrow |2\rangle$ and $|1'\rangle \rightarrow |2'\rangle$, our scheme of two pairs of two-step two-photon transitions is fully realized, Fig. 2(d). The measured atom density distribution is still ellipsoidal, but tilted by an angle $\Phi = (-12 \pm 2)^\circ$ relative to the y -axis, Fig. 2(e). This angle is a unique signature of our scheme of atoms interacting with the field of two pairs of perpendicular laser beams that drive two-step two-photon transitions. The corresponding simulation of the atom density distribution is shown in Fig. 2(f). Good agreement between measured and calculated atom density distribution is observed. The calculated angle, $\Phi_{\text{num}} = -11.6^\circ$, is within the uncertainty of the measured angle. For the density distribution in Fig. 2(f), the α_{ij} coefficients are calculated to be $(\alpha_{xx}, \alpha_{xy}, \alpha_{yx}, \alpha_{yy}) = (-3.4, 0.79, -0.20, -0.10) \times 10^{-22}$ Ns/m, giving $\alpha_R = 0.50 \times 10^{-22}$ Ns/m. In order to distinguish between the two

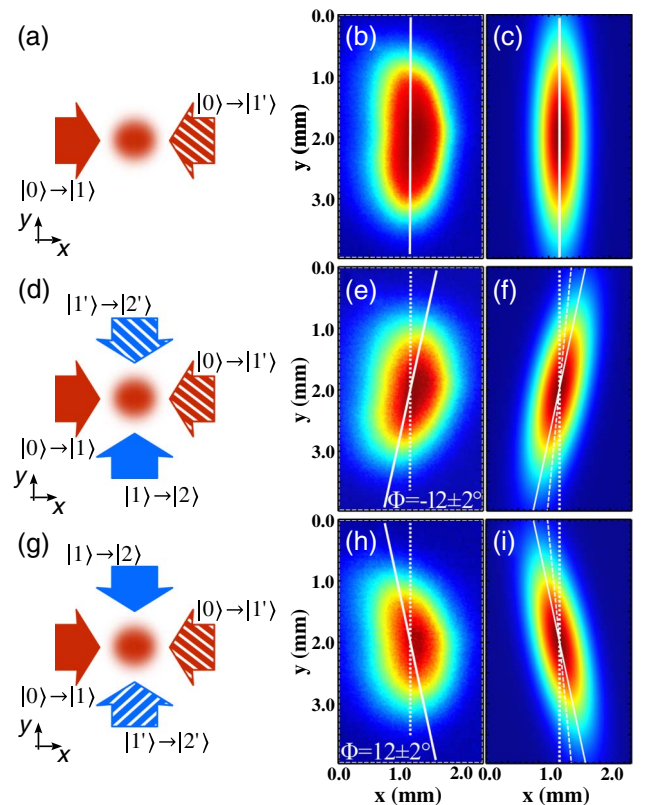


Fig. 2. Atom density distributions after TOF of 4 ms for three different configurations, (a, d, g). Corresponding experimental, (b, e, h), and numerical results, (c, f, i), are shown in the same row. (b, c) Density distribution with only the first-step beams present. (e, f, h, i) Density distributions with all four beams present, hence under the influence of the SLF. Note that the two second-step beams have switched places from (d) to (g). The deflection angles of the major axes are indicated with full white lines. In panels (f) and (i) a dashed line indicates what the deflection angle would be without the SLF term in Eq. (2). See text for details.

contributions that produce the Φ_{num} angle, i.e., the trapping potential and the SLF, arising from the first and second term in Eq. (2), we calculate the density distribution without the SLF contribution ($\alpha_R = 0$). The obtained deflection angle $\Phi_{\text{num}}(\alpha_R = 0) = -5.0^\circ$ is significantly smaller than the angle $\Phi_{\text{num}} = -11.6^\circ$ and is indicated with a dashed line in Fig. 2(f). This is expected based on the discussion presented in Section 3, which confirms the observation of the synthetic Lorentz force in a measured cold cloud density distribution shown in Fig. 2(e).

To recheck our experimental findings we switch the two second-step SLF beams, obtaining the configuration shown in Fig. 2(g). To ensure the same alignment only the output of the fibers for the two beams are exchanged, whereas all holders, optics, and experimental parameters are left unchanged. The atom density distribution remains ellipsoidal, but it is now tilted at an angle $\Phi = (12 \pm 2)^\circ$ relative to the y -axis. The corresponding calculated distribution shown in Fig. 2(i) confirms the experimental result and conclusions analogous to the conclusions from the previous configuration can be made.

Another thing to note is that the tilt angle of the cloud does not increase for larger expansion times. This is due to the scalar potential, which would decrease the tilt angle if the rotating part of the force was not present. The tilt angle therefore stops increasing when the influences of these two terms on the tilt angle cancel each other. The expansion of $\tau = 4$ ms was therefore chosen because of optimal signal quality, since for smaller times the cloud is similar to the initial symmetric shape, while for larger times the signal deteriorates due to heating and diffusion.

Considering that the cyclotron frequency does not depend on the velocity of the charged particle, by analogy we expect that the deflection angle Φ in our system does not depend on the initial width of the Maxwell–Boltzmann velocity distribution of the cold cloud, i.e., on the cloud temperature. In Fig. 3 we show the measured and calculated deflection angle Φ as a function of the SD of the velocity distribution, points, and line, respectively. As mentioned in Section 3, the SD of the initial velocity distribution, σ_v , is obtained from TOF measurements without the SLF beams. In the experiment σ_v , i.e., the temperature of the cold atoms in the MOT, is easily tuned by changing the detuning of the cooling laser. The deflection angle is measured using the experimental configuration shown in

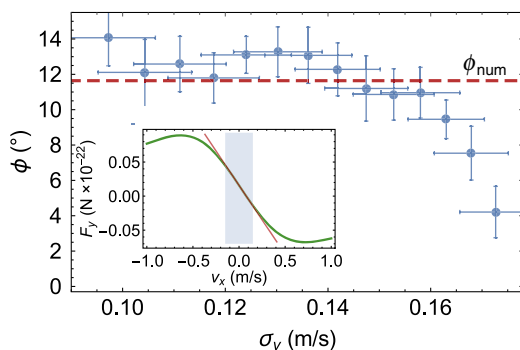


Fig. 3. Deflection angle as a function of the SD of the velocity distribution, measured (circles) and calculated (line). The inset shows the force in the y direction as a function of the velocity in the x direction, $F_y(v_x, v_y = 0)$, the region $|v_x| < 0.15$ m/s is shaded while the line shows the slope at $v_x = 0$.

Fig. 2(d), with all other experimental parameters identical to the ones used before. We can see that the measured and calculated angles agree well with the expected behavior, i.e., the deflection angle does not depend on the width of the velocity distribution almost in the entire range. Deviation of the measured angle from the calculated constant value at wider velocity distributions arises because there is a considerable number of atoms with velocities that are beyond the velocity range in which the approximation used in Eq. (1) is valid, and therefore the effect of the SLF is less pronounced. For reference, see the inset of Fig. 3 which shows the force in the y direction, $F_y(v_x, v_y = 0)$. Within the shaded area, which is from $v_x = -0.15$ m/s to $v_x = 0.15$ m/s the difference between the calculated force (green curve) and the linear approximation from Eq. (1) is below 4%. However, for a cloud with $\sigma_v = 0.15$ m/s, already 32% of the atoms have a velocity that is outside of the shaded area. For increasing σ_v this fraction will be even larger, which illustrates why the model and the experimental results differ increasingly past $\sigma_v \approx 0.15$ m/s. The values of v_x for which $F_y(v_x, v_y = 0)$ has maximum absolute values are defined by the two-photon detuning via the Doppler shift. For a larger two-photon detuning the maximum force values would be further apart and so the velocity range in which the force is linear, and thus the effective observation of the SLF is possible, could be made larger. A more complicated model could be implemented that would take into account atoms with larger velocities, as well as other effects present in the MOT, such as radiation trapping. A visible difference between the experimental TOF distribution and the numerically predicted ones in Fig. 2 is the larger width of the experimentally observed distributions along the x -axis, along which we effectively have optical molasses due to the red detuning of the first-step beams. This faster expansion is possibly a consequence of radiation trapping and very similar to the effect observed in [3]. There the authors also observed a much faster expansion of their cloud in the molasses stage than what was predicted by the Fokker–Planck equation, and this was attributed to Coulomb-like forces caused by radiation trapping. There is also additional heating not accounted for in the model, mostly due to the linewidths of the lasers which can also increase the observed width of the cloud. However, these potential additions to our model are out of scope for this paper. The model presented here is simple yet powerful in the sense that it explains and fully predicts the behavior of our system for sufficiently low atomic temperatures that are typically achieved in a MOT.

5. CONCLUSION

In conclusion, we have measured the synthetic Lorentz force in an expanding cloud of cold rubidium atoms. The force is a result of the interaction of atoms with the field of two pairs of perpendicular laser beams which drive two-step two-photon transitions. The signature of the force given by our scheme is imprinted in a tilted ellipsoidal-shaped atomic cloud, measured after a given expansion time of the cloud. The experimental results show excellent agreement with the simulations of the atom density distributions. Indeed, by simulating the atom density distributions with and without the synthetic Lorentz force contribution, we can determine the contribution of

the synthetic Lorentz force in the measured deflection angle. The observed SLF has the form of the standard Lorentz force $\mathbf{F}_{SL}(\mathbf{v}) = \mathbf{v} \times \mathbf{B}^*$, where $\mathbf{B}^* = \alpha_R \hat{\mathbf{z}}$ is the effective magnetic field. Our measurement gives $\alpha_R = 0.50 \times 10^{-22}$ Ns/m, which for an ^{87}Rb ion would give an effective field $\mathbf{B}^*/e \approx 0.3$ mT, or a cyclotron frequency of $\alpha_R/m = 0.35$ kHz. As stated previously, our scheme for introducing the SLF is necessarily accompanied by spontaneous emission. This will lead to radiation trapping in dense atomic clouds and therefore to an effective Coulomb force between atoms. This means that by introducing the SLF we, at the same time, introduce an effective Coulomb force in to the system. Since the effective charge as a result of radiation trapping is typically $q_{\text{eff}} \approx 10^{-4}e$ [2], the effective synthetic field scales to $B_{\text{eff}} \approx 3T$. In addition, we showed that our relatively simple model can be readily used for future experiments with synthetic fields in classical cold atom systems. Our work reinforces the analogy between a cloud of cold atoms and plasma-like systems, thus potentially opening a new direction of research based on the use of cold atoms as a classical emulator of complex classical systems in which magnetic fields play a significant role, such as a tokamak fusion reactor or a star.

Funding. Project Frequency-Comb-induced OptoMechanics; Hrvatska Zaklada za Znanost (HRZZ) (IP-2014-09-7342); QuantiXLie Center of Excellence.

Acknowledgment. We are grateful to R. Kaiser for advice and fruitful discussions.

REFERENCES

1. T. Walker, D. Sesko, and C. Wieman, "Collective behavior of optically trapped neutral atoms," *Phys. Rev. Lett.* **64**, 408–411 (1990).
2. D. W. Sesko, T. G. Walker, and C. E. Wieman, "Behavior of neutral atoms in a spontaneous force trap," *J. Opt. Soc. Am. B* **8**, 946–958 (1991).
3. L. Pruvost, I. Serre, H. T. Duong, and J. Jortner, "Expansion and cooling of a bright rubidium three-dimensional optical molasses," *Phys. Rev. A* **61**, 053408 (2000).
4. J. T. Mendonça, R. Kaiser, H. Terças, and J. Loureiro, "Collective oscillations in ultracold atomic gas," *Phys. Rev. A* **78**, 013408 (2008).
5. H. Terças, J. T. Mendonça, and R. Kaiser, "Driven collective instabilities in magneto-optical traps: a fluid-dynamical approach," *Europhys. Lett.* **89**, 53001 (2010).
6. J. T. Mendonça, H. Terças, G. Brodin, and M. Marklund, "A phonon laser in ultra-cold matter," *Europhys. Lett.* **91**, 33001 (2010).
7. J. T. Mendonça and R. Kaiser, "Photon bubbles in ultracold matter," *Phys. Rev. Lett.* **108**, 033001 (2012).
8. H. Terças, J. T. Mendonça, and V. Guerra, "Classical rotons in cold atomic traps," *Phys. Rev. A* **86**, 053630 (2012).
9. H. Terças and J. T. Mendonça, "Polytropic equilibrium and normal modes in cold atomic traps," *Phys. Rev. A* **88**, 023412 (2013).
10. J. D. Rodrigues, J. A. Rodrigues, O. L. Moreira, H. Terças, and J. T. Mendonça, "Equation of state of a laser-cooled gas," *Phys. Rev. A* **93**, 023404 (2016).
11. G. Labeyrie, F. Michaud, and R. Kaiser, "Self-sustained oscillations in a large magneto-optical trap," *Phys. Rev. Lett.* **96**, 023003 (2006).
12. N. Šantić, T. Dubček, D. Aumiler, H. Buljan, and T. Ban, "Experimental demonstration of a synthetic Lorentz force by using radiation pressure," *Sci. Rep.* **5**, 13485 (2015).
13. L. J. LeBlanc, K. Jiménez-García, R. A. Williams, M. C. Beeler, A. R. Perry, W. D. Phillips, and I. B. Spielman, "Observation of a superfluid Hall effect," *Proc. Natl. Acad. Sci. USA* **109**, 10811–10814 (2012).
14. M. Aidelsburger, M. Atala, M. Lohse, J. T. Barreiro, B. Paredes, and I. Bloch, "Realization of the Hofstadter Hamiltonian with ultracold atoms in optical lattices," *Phys. Rev. Lett.* **111**, 185301 (2013).
15. I. Bloch, J. Dalibard, and S. Nascimbene, "Quantum simulations with ultracold quantum gases," *Nat. Phys.* **8**, 267–276 (2012).
16. J. Dalibard, F. Gerbier, G. Juzeliunas, and P. Öhberg, "Colloquium: artificial gauge potentials for neutral atoms," *Rev. Mod. Phys.* **83**, 1523–1543 (2011).
17. K. W. Madison, F. Chevy, W. Wohlleben, and J. Dalibard, "Vortex formation in a stirred Bose-Einstein condensate," *Phys. Rev. Lett.* **84**, 806–809 (2000).
18. J. R. Abo-Shaeer, C. Raman, J. M. Vogels, and W. Ketterle, "Observation of vortex lattices in Bose-Einstein condensates," *Science* **292**, 476–479 (2001).
19. Y.-J. Lin, R. L. Compton, K. Jiménez-García, J. V. Porto, and I. B. Spielman, "Synthetic magnetic fields for ultracold neutral atoms," *Nature* **462**, 628–632 (2009).
20. M. Aidelsburger, M. Atala, S. Nascimbène, S. Trotzky, Y.-A. Chen, and I. Bloch, "Experimental realization of strong effective magnetic fields in an optical lattice," *Phys. Rev. Lett.* **107**, 255301 (2011).
21. T. Dubček, N. Šantić, D. Jukić, D. Aumiler, T. Ban, and H. Buljan, "Synthetic Lorentz force in classical atomic gases via Doppler effect and radiation pressure," *Phys. Rev. A* **89**, 063415 (2014).
22. A. Fasoli, S. Brunner, W. A. Cooper, J. P. Graves, P. Ricci, O. Sauter, and L. Villard, "Computational challenges in magnetic-confinement fusion physics," *Nat. Phys.* **12**, 411–423 (2016).
23. D. A. Steck, Rubidium 87 D line data, <http://steck.us/alkalidata/rubidium87numbers.pdf>.
24. D. Sheng, A. Perez Galvan, and L. A. Orozco, "Lifetime measurements of the 5d states of rubidium," *Phys. Rev. A* **78**, 062506 (2008).
25. H. J. Metcalf and P. Van Der Straten, *Laser Cooling and Trapping* (Springer, 1999).

Appendix B

**Articles submitted or being prepared for
submission**

Sub-Doppler cooling of atoms using an optical frequency comb

N. Šantić,¹ A. Cipriš,¹ I. Krešić,¹ D. Aumiler,¹ and T. Ban¹

¹*Institute of Physics, Bijenička c. 46, 10000 Zagreb, Croatia*

(Dated: July 31, 2017)

We report on sub-Doppler cooling of rubidium atoms on a dipole-allowed transition at 780 nm by using a frequency comb (FC). Temperatures as low as 55 μK were measured in a one-dimensional FC cooling geometry using time-of-flight spectroscopy. We attribute the sub-Doppler temperatures observed in FC cooling to the same mechanisms that produce sub-Doppler temperatures when cooling with continuous-wave lasers. Laser cooling with FCs could enable achieving sub-Doppler temperatures for the atoms with dipole-allowed transitions in the vacuum ultraviolet. This can significantly improve the precision of optical frequency standards, enable measurements of fundamental constants with unprecedented accuracy, and open up the possibility to reach quantum degeneracy with atoms that have optical transitions unreachable by continuous wave lasers such as hydrogen, deuterium and antihydrogen.

PACS numbers: 37.10.De, 37.10.Vz, 32.30.Jc

Laser cooling and trapping brings atomic and molecular physics to one of the most exciting frontiers in science, with applications ranging from atom interferometry [1] and optical frequency standards [2] to high precision spectroscopy and ultracold chemistry [3, 4]. Regardless of such a great importance, laser cooling techniques are still limited to atoms with simple energy level structure and closed transitions [5] accessible by current continuous wave (CW) laser technology. Laser cooling of more complex atomic species and molecules, or even simple atoms with strong cycling transitions in the vacuum ultraviolet (VUV) where generation of CW laser light is demanding, still remains an experimental challenge.

The aforementioned problems can be approached by using mode-locked femtosecond (fs) or picosecond (ps) lasers with high pulse repetition rates which produce stabilized optical frequency combs (FCs). Employing the highly precise and regular comb spectrum has been proposed for laser cooling of complex multilevel atoms and molecules in an approach that essentially mimics the use of multiple phase-coherent CW lasers [6]. Following the same approach, simultaneous cooling of multiple atomic species by FC is proposed in [7]. FC cooling on the Rb two-photon transition at 778 nm has been demonstrated recently [8], where cooling is achieved through a coherent process in which multiple excitation pathways are excited by different combinations of comb modes.

On the other hand, FCs provide high peak powers needed for efficient frequency conversion via nonlinear crystals [9] or high harmonic generation [10, 11], while simultaneously preserving long coherence times needed for efficient laser cooling. These benefits have recently been employed to open a new and promising route towards laser cooling of species with strong cycling transitions in the UV and VUV such as trapped magnesium ions [12].

The use of FCs has revolutionized high-resolution spectroscopy, where FC-based spectrometers of unprecedented accuracy, resolution and sensitivity now operate

from the EUV [13] to the mid-IR [14] spectral range. A similar impact on the field of quantum optics can be envisaged as well, where the use of FCs for laser cooling could lead to significant advances in research focused toward quantum technologies such as optical clocks, quantum simulators, and quantum networks. Intriguing applications of FC cooling include: a) optical atomic clocks, e.g. realization of FC cooling of trapped Al and He ions in the VUV [12], or FC cooling of the radioisotope thorium-229 ion (via multiple NIR sidebands) needed for the realization of a nuclear transition based optical clock [15]; b) achieving quantum degeneracy for atoms with dipole-allowed transitions in the VUV, e.g. hydrogen, deuterium and antihydrogen atoms for precision tests of many-body theory and of ultracold collisions, as well as for testing charge, parity and time reversal symmetry and probing physics beyond the standard model [6]; c) producing cold samples of most prevalent atoms in organic chemistry, e.g. hydrogen, carbon, oxygen and nitrogen to improve understanding of their long-range interactions and chemical bonding [6, 8]. For all the aforementioned FC cooling applications, achieving sub-Doppler temperatures is a great benefit, if not a necessity.

In this Letter we demonstrate sub-Doppler FC cooling of rubidium atoms. Up to now only the two previously mentioned recent experiments have reported FC cooling, and both of them achieve cooling to near the Doppler temperature [8, 12]. Here we show that temperatures below the Doppler limit, i.e. sub-Doppler temperatures, can be achieved by FC cooling. We demonstrate sub-Doppler cooling of Rb atoms to 55 μK on a single-photon transition at 780 nm, a transition typically used in CW laser cooling experiments with an associated Doppler temperature of 146 μK [16]. Achieving sub-Doppler FC cooling presented in this work is an important step towards storing FC cooled atoms in shallow optical potentials such as dipole traps, optical lattices, and finally towards achieving quantum degenerate gases

using FC light.

Our apparatus consists of a standard magneto-optical trap (MOT) for ^{87}Rb atoms. A cold rubidium cloud is loaded from background vapor in a stainless steel chamber. The MOT is arranged in a standard three-beam retro-reflected configuration based on CW lasers, which together with the anti-Helmholtz produced quadrupole magnetic field create the trapping potential. Fluorescence imaging of the cloud is performed with a camera aligned along a horizontal axis. In typical experimental conditions we obtain a cloud 1.4 mm in diameter, which contains about 10^8 atoms of ^{87}Rb . By changing the detuning of the CW MOT beams we are able to prepare a cloud with temperatures in the range of 50-300 μK . Such a cold cloud represents the initial sample for all our measurements presented in this work.

The FC is generated by frequency doubling an Er:fiber mode-locked laser (TOPTICA FFS) operating at a repetition rate $f_{rep}=80.5$ MHz with an output power of about 230 mW, a central wavelength at 1580 nm. The FC spectrum used in the experiment is centered at 780 nm with a bandwidth of about 10 nm and a total power of 65 mW after frequency doubling. Approximately 100 000 comb lines are contained under the FC spectral envelope. The FC is stabilized to a CW reference laser (ECDL, Moglabs CEL002) locked to the ^{87}Rb $|5S_{1/2}; F = 2\rangle \rightarrow |5P_{3/2}; F' = 3\rangle$ transition. The technical description of the FC stabilization is outlined in the online supplemental information [17]. More details about the used stabilization scheme can be found in [18].

Laser cooling relies on the radiation pressure force. Hence, in order to understand the physical mechanisms that drive the FC cooling, one has to first understand the force exerted on atoms when they are resonantly excited by the FC. We therefore start our study by measuring the FC radiation pressure force on cold Rb atoms. The comb centered at 780 nm drives the standard ^{87}Rb $|5S_{1/2}\rangle \rightarrow |5P_{3/2}\rangle$ cooling transition. A single linearly polarized beam is collimated and sent through an acousto-optic modulator (AOM) for fast on/off switching, and then directed to the center of the trap. Total power of 18 mW was used with the beam FWHM of 2.7 mm, which gives the FC power of about $0.5 \mu\text{W}$ per comb mode. The measurement sequence starts with preparation of a cold ^{87}Rb cloud using the CW MOT setup (FC beam off). At $t=0$ we turn off the MOT cooling beams, and switch on the FC beam. The weak repumper light is left on continuously to optically pump the atoms out of the $|5S_{1/2}; F = 1\rangle$ ground state. It propagates perpendicular to the FC, is arranged in a counter-propagating configuration, and has no measurable mechanical effect. We let the FC to interact with the cold cloud for 1 ms, and during this time the cloud center of mass (CM) accelerates along the FC beam propagation axis ($+x$ -direction) due to the FC radiation pressure force. At $t = 1$ ms FC beam and repumper are

switched off, and the cloud is left to freely expand for 5 ms. At $t = 6$ ms the CW cooling beams are turned on and the cloud fluorescence is imaged with the camera to determine the cloud CM displacement in the x direction, Δx_{CM} . We then use Δx_{CM} to calculate the acceleration of the cloud, which, using the mass of a single Rb atom, finally gives the FC force. Averaging of 4 consecutive measurements is performed and shown in Fig. 1(b).

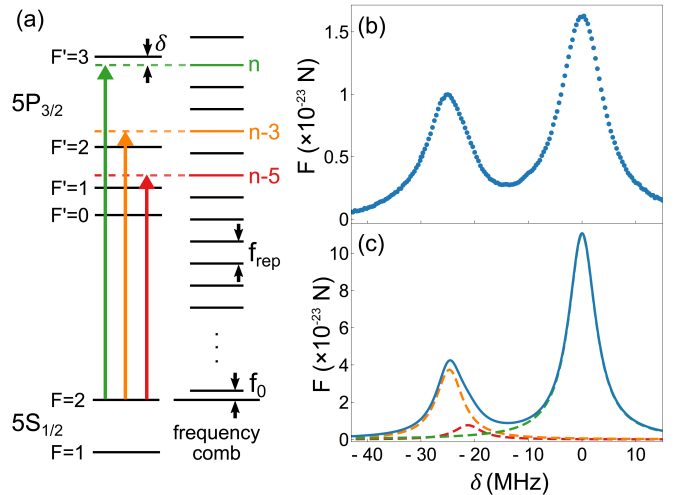


FIG. 1: (Color online) (a) Scheme of relevant ^{87}Rb energy levels and FC modes; (b) measured and (c) calculated FC force as a function of detuning. The total force in (c), blue line, reflects the interaction with three comb modes: n -th comb mode with the $|5S_{1/2}; F = 2\rangle \rightarrow |5P_{3/2}; F' = 3\rangle$ transition - green dashed line; $(n - 3)$ -rd mode resonance with the $|5S_{1/2}; F = 2\rangle \rightarrow |5P_{3/2}; F' = 2\rangle$ transition - orange dashed line; and $(n - 5)$ -th mode resonance with the $|5S_{1/2}; F = 2\rangle \rightarrow |5P_{3/2}; F' = 1\rangle$ transition - red dashed line.

The FC force depends on the relative detuning of the comb lines with respect to the hyperfine transitions. As the FC spectrum consists of identical, regularly spaced comb lines, we describe the FC spectrum by the detuning δ of the n -th comb mode from the $|5S_{1/2}; F = 2\rangle \rightarrow |5P_{3/2}; F' = 3\rangle$ transition. Accordingly, the $F(\delta)$ scan in Fig. 1(b,c) repeats every $f_{rep}=80.5$ MHz. Two distinct peaks appear in one f_{rep} scan reflecting the interaction with three comb modes, as shown schematically in Fig. 1(a). The peak at $\delta = 0$ is due to n -th comb mode in resonance with the $|5S_{1/2}; F = 2\rangle \rightarrow |5P_{3/2}; F' = 3\rangle$ transition, whereas the peak at $\delta \approx -25.5$ MHz is due to $(n - 3)$ -rd mode in resonance with the $|5S_{1/2}; F = 2\rangle \rightarrow |5P_{3/2}; F' = 2\rangle$ transition, and $(n - 5)$ -th mode in resonance with the $|5S_{1/2}; F = 2\rangle \rightarrow |5P_{3/2}; F' = 1\rangle$ transition. The contributions to the FC force coming from resonances with different comb modes are expressed more clearly in the results of calculations of the FC force shown in Fig. 1(c), where contributions of relevant transitions are explicitly given. The calculated FC force is obtained by numerically solving the Optical Bloch Equa-

tions describing the excitation of six-level ^{87}Rb atoms by the FC [19], and subsequently using the Ehrenfest theorem. More details on the FC force calculation are given in the online supplemental information [17].

The agreement between measured and calculated FC force in Fig. 1(b,c) is reasonable, considering there are no free parameters in the model. Relative positions of the two peaks are well reproduced, though there is a small but noticeable broadening of the measured peaks, which we attribute to systematic effects such as stability of the rf reference used to stabilize FC, Zeeman splitting due to the stray magnetic fields, and Doppler broadening due to the photon-momentum transfer. It is worth noting that similar line broadening has also been observed in [8], whereas a detailed analysis of all possible systematic source of errors which affect line broadening and shifts in FC spectroscopy can be found in [20]. The discrepancies in the magnitude of the measured and calculated force can be attributed to the approximations used in our model, namely the neglecting of spatial variation of the beam profile, see [17]. The largest force is measured when the n -th comb mode is resonant with the standard cooling transition for ^{87}Rb , i.e. the right peak in Fig. 1(b), for which Δx_{CM} of 0.6 mm is obtained. During 1 ms of FC cooling time the atoms are accelerated with constant acceleration of 110 m/s^2 and acquire velocity of 0.11 m/s . From the measured force, we calculate an on resonance scattering rate of $\gamma_{scat} = 18600 \text{ s}^{-1}$, which is comparable to the scattering rate calculated in the case of excitation by CW laser of intensity comparable to the intensity of n -th comb mode. Measured FC scattering rate is nearly three times larger than the value reported in Ref. [8] for a two-photon FC excitation, despite having the intensity an order of magnitude smaller than in [8]. This clearly suggests that FC cooling via one-photon excitation is viable, and could therefore be a preferable choice when pursuing cooling of atoms and ions with a dipole allowed transitions in VUV spectral region.

In order to employ the measured FC force to achieve FC cooling in one dimension, we split the FC beam into two beams and send them counter-propagating to the center of the trap where they are carefully overlapped. $\lambda/2$ or $\lambda/4$ waveplates are put in the beam path prior to entering the MOT chamber, depending on the beam polarization configuration to be studied: $\text{lin} \perp \text{lin}$, $\text{lin} \parallel \text{lin}$ or $\sigma^+ \sigma^-$. The measurement sequence for studying FC cooling starts by preparing a cold rubidium cloud in the MOT. At $t = 0 \text{ ms}$ the cooling beams are switched off. The weak CW repumper laser is again left on. A quadrupole magnetic field with a gradient of 13 G/cm remains on during the measurements. Since the cloud is in the center of the quadrupole field, the magnetic field is $B \approx 0$. At $t = 100 \mu\text{s}$ the FC beams are turned on. The FC beams are on for a time t_c (typically 3 ms), which we call the FC cooling time, after which the FC beams are switched off, and the cloud is left to expand freely for

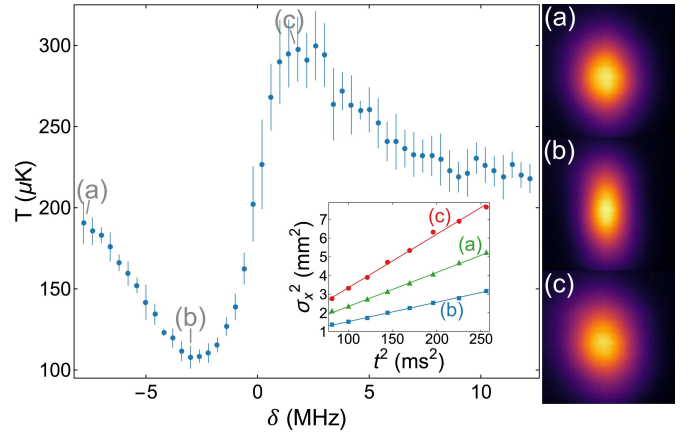


FIG. 2: (Color online) Temperature obtained by TOF spectroscopy after 1D FC cooling for $\text{lin} \perp \text{lin}$ configuration of the FC beams as a function of FC detuning. The right panel shows three TOF images taken after 8 ms expansion time for FC detuning that corresponds to the cloud's temperature that is (a), approximately equal to the initial temperature, (b), lowest obtained, and (c), highest. Corresponding TOF data for 8-16 ms expansion times are given in the inset.

several ms before it is imaged with the camera. A series of time-of-flight (TOF) images are taken in this way at different expansion times of up to 16 ms. We then determine the cloud radius (which increases with expansion time) by fitting the spatial distributions of the atoms in the cloud to a Gaussian. The obtained spatial width of the cloud as a function of the expansion time gives an accurate measure of the cloud temperature by fitting to the expression $\sigma_t^2 = \sigma_0^2 + \frac{kT}{m}t^2$, where $t = 0$ is the time when the MOT CW cooling laser is switched off. Long expansion times are used in order to reduce any systematic effects related to FC action on the cloud during the first 1 ms of expansion, as $t_{TOF}^2 \gg t_c^2$, where t_{TOF} is the TOF time. A similar experimental procedure for measuring Doppler and sub-Doppler temperatures was used in [8, 21]. We repeat the measurement protocol 7 times for a given expansion time, and subsequently average the results to obtain the temperature. Temperatures obtained by TOF measurements as a function of δ are shown in Fig. 2. $\text{lin} \perp \text{lin}$ polarization of the FC beams was used. The intensity per comb mode in the FC beams was 0.02 mW/cm^2 , initial cloud temperature $\approx 200 \mu\text{K}$, and $t_c = 3 \text{ ms}$.

The measured temperatures approach the initial cloud temperature for large δ . Fig. 2(a) shows TOF image at 8 ms for $\delta = -8 \text{ MHz}$ where the measured width along the x -axis is $2\sigma_x = 2.88 \text{ mm}$. The lowest temperature is observed for $\delta \approx -3 \text{ MHz}$, i.e. when there is a comb (n -th comb) detuned by $\approx -3 \text{ MHz}$ from the ^{87}Rb $|5S_{1/2}; F = 2\rangle \rightarrow |5P_{3/2}; F' = 3\rangle$ transition. The corresponding TOF image shown in Fig. 2(b) shows $2\sigma_x = 2.34 \text{ mm}$, and the temperature given by the slope

in the inset is $(108 \pm 7) \mu\text{K}$. The highest temperature is obtained for $\delta \approx 2 \text{ MHz}$, i.e. for a blue-detuned comb, when the force induced by the counter-propagating FC beams accelerates the atoms and causes additional heating. The corresponding TOF image shown in Fig. 2(c) shows $2\sigma_x = 3.32 \text{ mm}$. One can clearly draw analogy here between FC and CW laser cooling as a comb line red-detuned from the cooling transition is needed to obtain cooling. The changes in the cloud temperature (along the x -axis) with the FC detuning are accompanied with the increase of the temperature in the y -axis, i.e. perpendicular to the FC cooling beams, due to the heating caused by spontaneous emission. The signature of this heating along the y -axis is evident in larger σ_y in Figs. 2(b,c) than in Fig. 2(a), since more efficient excitation (and consequently more spontaneous emission) is obtained for these detunings.

We investigated FC cooling for different polarization configurations of the FC beams, $\text{lin} \perp \text{lin}$, $\text{lin} \parallel \text{lin}$ and $\sigma^+ \sigma^-$. For all three configurations we measure similar temperature dependencies on the FC detuning with comparable sub-Doppler temperatures obtained. We verify these findings by performing the same measurements with two counter-propagating CW beams (instead of FC beams), keeping all experimental parameters identical, with the two CW laser beams having a comparable intensity with the intensity of the relevant comb mode. With respect to this, we attribute the sub-Doppler temperatures observed in FC cooling to the same mechanisms that produce sub-Doppler temperatures when cooling with CW lasers, in line with the interpretation that each comb mode can be considered as a CW laser of appropriate intensity. These sub-Doppler mechanisms arise from the multilevel structure of the atomic ground state in combination with the polarization gradient of the FC field and optical pumping. For the case of the $\text{lin} \perp \text{lin}$ FC beam polarizations, we conclude that the cooling mechanism is analogous to the well known CW Sisyphus cooling [22]. Sub-Doppler cooling with CW lasers for the $\text{lin} \parallel \text{lin}$ configuration can be found in early experimental [23] and theoretical works [24] for the case of low CW laser intensities and small initial atomic velocities. In this configuration, the AC Stark shift among ground state levels differs only slightly, but the intensity of the laser field varies considerably in space due to the interference of the two counter-propagating laser beams. The cooling comes as a result of two effects: increased optical pumping time near regions of low field intensity, and a decreased momentum diffusion coefficient [24]. For weak fields, as in our experiment, the optical pumping time is two orders of magnitude larger than the ^{87}Rb excited lifetime of 26.24 ns [16], which can result in significant friction force for slow atoms [24].

It is important to note that cooling down to sub-Doppler temperatures is obtained despite the fact that when n -th comb mode is red-detuned by 3 MHz from

$^{87}\text{Rb} |5S_{1/2}; F = 2\rangle \rightarrow |5P_{3/2}; F' = 3\rangle$ transition it is simultaneously blue-detuned by $\approx 22 \text{ MHz}$ from $^{87}\text{Rb} |5S_{1/2}; F = 2\rangle \rightarrow |5P_{3/2}; F' = 1, 2\rangle$ transitions, see Fig. 1(b,c). Since similar sub-Doppler temperatures are observed in the analogous experiments performed with CW beams, we conclude that blue-detuned comb lines do not have a detrimental effect on the observed FC cooling, a fact that was not immediately clear beforehand and that can rule out additional heating coming from other blue-detuned comb lines.

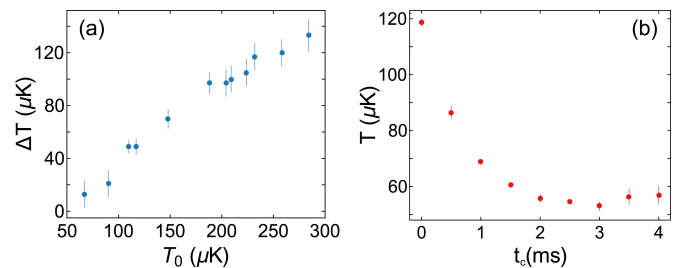


FIG. 3: (Color online) (a) The decrease in cloud temperature due to FC cooling as a function of the cloud initial temperature, and (b) the dependence of the measured sub-Doppler temperature on the FC cooling time for cloud initial temperature $T_0 = 120 \mu\text{K}$ and $\delta = -3 \text{ MHz}$.

The cloud temperature decreases from the initial value (obtained in the MOT phase) as FC cooling time is increased, as seen in Fig. 3(b), and steady state temperature (at $t_c = 3 \text{ ms}$) reaches about $55 \mu\text{K}$. This is in agreement with the measurements of the change of the cloud temperature due to FC cooling, ΔT , as a function of the cloud initial temperature, T_0 , shown in Fig. 3(a), where nearly linear dependency of ΔT on T_0 is obtained, with ΔT approaching zero at $T_0 \approx 50 \mu\text{K}$. The lowest temperature obtained in our FC cooling experiment is limited by the low intensity per comb mode, and by the existence of stray magnetic fields in the center of the experimental chamber.

In conclusion, we have studied FC cooling on a standard Rb MOT transition. By using TOF spectroscopy, we have demonstrated that sub-Doppler temperatures can be obtained in a 1D FC cooling geometry, for both linear and circular polarizations of the FC beams. Sub-Doppler temperatures as low as $55 \mu\text{K}$ have been obtained, primarily limited by the low intensity per comb mode in the FC spectrum. The analogy between FC (single comb line) and CW sub-Doppler laser cooling is verified by performing the same measurements using a CW laser of appropriate intensity. We believe that in future experiments the power per comb line can easily be increased by at least an order of magnitude. Using high-intensity FCs could therefore lead to achieving temperatures down to the recoil limit, thus opening the VUV spectral region to quantum optics experiments and their applications.

The authors acknowledge support from the Croatian Science Foundation (Project Frequency-Comb-induced OptoMechanics - IP-2014-09-7342).

-
- [1] A. D. Cronin, J. Schmiedmayer, and D. E. Pritchard, *Rev. Mod. Phys.* **81**, 1051 (2009).
- [2] B. J. Bloom, T. L. Nicholson, J. R. Williams, S. L. Campbell, M. Bishof, X. Zhang, W. Zhang, S. L. Bromley, and J. Ye, *Nature* **506**, 71 (2014).
- [3] S. Ospelkaus, K.-K. Ni, D. Wang, M. H. G. de Miranda, B. Neyenhuis, G. Quéméner, P. S. Julienne, J. L. Bohn, D. S. Jin, and J. Ye, *Science* **327**, 85317 (2010).
- [4] S. Knoop, F. Ferlaino, M. Berninger, M. Mark, H.-C. Nägerl, R. Grimm, J. P. DIncao, and B. D. Esry, *Phys. Rev. Lett.* **104**, 053201 (2010).
- [5] H. J. Metcalf, and P. van der Straten, *Laser Cooling and Trapping* (Springer Science and Business Media, 2001).
- [6] D. Kielpinski, *Phys. Rev. A* **73**, 063407 (2006).
- [7] D. Aumiler and T. Ban, *Phys. Rev. A* **85**, 063412 (2012).
- [8] A. M. Jayich, X. Long, and W. C. Campbell, *Phys. Rev. X* **6**, 041004 (2016).
- [9] E. Peters, S. A. Diddams, P. Fendel, S. Reinhardt, T. W. Hänsch, and T. Udem, *Opt. Express* **17**, 9183 (2009).
- [10] D. C. Yost, T. R. Schibli, J. Ye, J. L. Tate, J. Hostetter, M. B. Gaarde, and K. J. Schafer, *Nature Physics* **5**, 815 (2009).
- [11] B. Bernhardt, A. Ozawa, A. Vernaleken, I. Pupeza, J. Kaster, Y. Kobayashi, R. Holzwarth, E. Fill, F. Krausz, T. W. Hänsch, and T. Udem, *Opt. Lett.* **37**, 503 (2012).
- [12] J. Davila-Rodriguez, A. Ozawa, T. W. Hänsch, and T. Udem, *Phys. Rev. Lett.* **116**, 043002 (2016).
- [13] A. Cingöz, D. C. Yost, T. K. Allison, A. Ruehl, M. E. Fermann, I. Hartl, and Jun Ye, *Nature* **482**, 68 (2012).
- [14] A. Schliesser, N. Picqué, and T. W. Hänsch, *Nature Photonics* **6**, 440 (2012).
- [15] L. von der Wense, B. Seiferle, M. Laatiaoui, J. B. Neumayr, H. Maier, H. Wirth, C. Mokry, J. Runke, K. Eberhardt, C. E. Düllmann, N. G. Trautmann, and P. G. Thirolf, *Nature* **533**, 47 (2016).
- [16] D.A. Steck, Rubidium 87 D Line Data, <http://steck.us/alkalidata/rubidium87numbers.pdf>
- [17] See Supplemental Material at
- [18] N. Šantić, G. Kowzan, P. Maslowski, D. Aumiler, and T. Ban, Frequency comb stabilization without self-referencing for laser cooling (in preparation).
- [19] T. Ban, D. Aumiler, H. Skenderović, and G. Pichler, *Phys. Rev. A* **73**, 043407 (2006).
- [20] A. Marian, M. C. Stowe, J. R. Lawall, D. Felinto, and Jun Ye, *Science* **306**, 2063 (2004).
- [21] T. E. Mehlstäubler, K. Moldenhauer, M. Riedmann, N. Rehbein, J. Friebe, E. M. Rasel, and W. Ertmer, *Phys. Rev. A* **77**, 021402(R) (2008).
- [22] J. Dalibard and C. Cohen-Tannoudji, *J. Opt. Soc. Am. B* **6**, 2023 (1989).
- [23] C. Salomon, J. Dalibard, W. D. Phillips, A. Clairon, and S. Guellati, *Europhys. Lett.* **12**, 683 (1990).
- [24] V. Finkelstein, P. R. Berman, and J. Guo, *Phys. Rev. A* **45**, 1829 (1992).

Frequency comb stabilization without self-referencing

N. Šantić,¹ G. Kowzan,² D. Kovačić,¹ D. Aumiler,¹ P. Maslowski,² and T. Ban^{1, a)}

¹⁾*Institute of Physics, Bijenička c. 46, 10000 Zagreb, Croatia*

²⁾*Institute of Physics, Nicolaus Copernicus University, ul. Grudziadzka 5, Torun, Poland*

(Dated: 24 January 2018)

We develop a scheme for full stabilization of a fiber based frequency comb that does not require traditional self-referencing. The repetition frequency is locked to a stable microwave reference while the offset frequency is indirectly stabilized by referencing the frequency comb to a continuous wave laser that is stabilized by polarization spectroscopy in rubidium vapor. This makes our scheme simple to implement, especially in cold atom experiments that necessarily have continuous wave laser stabilized to a high degree. It also requires low laser power thus saving it for use in experiments, e.g. ones that explore frequency comb Doppler cooling, electromagnetically induced transparency or coherent population transfer.

I. INTRODUCTION

Since its emergence almost 20 years ago the fully stabilized frequency comb (FC) has revolutionized multiple research areas ranging from frequency metrology^{1,2} to high resolution spectroscopy^{3,4}. Recent advances⁵ have allowed metrology of optical frequencies below the single-hertz level. Aside from being a well established and invaluable tool in these areas, new avenues of research with FCs are being explored, one of these being FC Doppler cooling^{5,6}.

Laser cooling and trapping of atoms has, in its own way, contributed to research in atomic physics. The most common implementation, the magneto-optical trap (MOT), is the workhorse in many atomic physics laboratories worldwide. However, the choice of atomic species for laser cooling is limited. This is because not all atomic species have suitable transitions for laser cooling⁷. Another obstacle is the lack of intense laser sources at short wavelengths, namely in the UV. Such sources would enable laser cooling of, for instance, hydrogen and antihydrogen among other species⁸. Cooling and trapping these species would be of great value for fundamental studies, for instance tests of CPT symmetry⁹. Because continuous wave (CW) lasers are not available in the UV due to fundamental constraints¹⁰, cooling with pulses has been explored very early on in the history of laser cooling^{11–13} due to the relative ease by which higher harmonics that stretch to the UV and further can be achieved. However, short optical pulses necessarily have large bandwidth (wide spectrum), meaning that when interacting with narrow atomic resonances or narrow velocity distributions, most of the power will be wasted or misplaced and the standard Doppler cooling scheme will be impossible to implement. Instead of a continuous spectrum, the hallmark of the FC is its comb spectrum, where the power within a frequency range corresponding to the repetition rate frequency concentrates into a single, narrow peak (comb tooth). Thus, the FC offers, at the same

time, the possibility of using a pulsed source, wasting less power, and the ability to probe narrow velocity distributions opening the possibility to use the standard Doppler cooling scheme. Thus, it would be of great interest to first test this possibility on systems that are well known, such as rubidium and an Er-fiber laser FC.

The most common use of the FC today is in absolute optical frequency measurements. This stems from the fact that the FC provides a direct link from easily measurable radio frequencies to optical frequencies. The optical frequency of the n th comb mode is given by:

$$f_n = n f_{rep} + f_{ceo}, \quad (1)$$

where n is the comb mode number, f_{rep} is the repetition frequency of the laser, f_{ceo} is the carrier-to-envelope phase offset frequency. By stabilizing f_{rep} and f_{ceo} the absolute frequency of all the comb modes is defined. This is usually achieved by measuring these two frequencies, and phase locking them to stable frequency references. While measuring f_{rep} is straight forward and just requires a photodiode, measuring f_{ceo} is experimentally complex and highly power consuming, requiring the well established f-2f interferometry¹⁴ or similar interferometric techniques (2f-3f, 3f-4f or other combinations^{15–17}). However, Doppler cooling requires knowledge of the absolute position of the laser/comb tooth interacting with the atomic transition only to the same order as the width of the transition in question, that is, most important is the *relative* position with respect to the atomic transition used for cooling⁷.

In this work we demonstrate stabilization of a fiber based frequency comb to an external cavity diode laser (ECDL) which is stabilized to the cooling transition in ⁸⁷Rb, $|5S_{1/2}; F = 2\rangle \rightarrow |5P_{3/2}; F' = 3\rangle$. This enables us to determine and stabilize the detuning of a specific comb tooth relative to this transition which is needed for Doppler cooling, as discussed above. By stabilizing the relative position of a single comb tooth, f_n , in respect to the stabilized ECDL and simultaneously stabilizing f_{rep} we indirectly stabilize f_{ceo} , i.e., the whole comb, evident from eq. (1). However, the absolute stability of the comb is then determined by the stability of the ECDL. We

^{a)}Electronic mail: ticijana@ifs.hr

analyze and discuss the absolute stability of the comb later in the text.

II. STABILIZATION SETUP

The femtosecond fiber laser used to produce the comb is an erbium doped fiber laser (Toptica FemtoFiber) whose primary emission is a ≈ 130 nm (FWHM) broad spectrum centered around 1570 nm, with a repetition frequency $f_{rep} \approx 80.5$ MHz, and an average power of $P_{avg} \approx 230$ mW. This output is frequency doubled on a PPLN crystal to obtain a spectrum centered around 780 nm (FWHM = 10 nm), the wavelength of the rubidium transition of interest with an average power of $P_{avg} \approx 75$ mW. The ECDL used (Moglabs CEL002) is stabilized to the wanted rubidium line by polarization spectroscopy^{18,19}. This locking technique allows high bandwidth feedback and also avoids directly modulating the laser frequency reducing the achievable linewidth. It is important to note that cold atom experiments require the use of a stabilized laser relative to the cooling transition which means that in laboratories performing these kinds of experiments a stabilized CW laser is necessarily already set up. This makes our stabilizing scheme straightforward to implement in these setups.

We achieve the fixing of the optical frequency of a single comb mode by phase locking the frequency comb to the stabilized ECDL, see lower part of Fig. 1. A fraction of the ECDL light (≈ 10 mW) and a fraction of the FC light (≈ 1 mW) are copropagated and directed first onto a grating (Thorlabs GR13-1208) to spatially filter the unwanted comb modes to reduce background noise, and then onto a fast photodiode (Thorlabs PDA10A-EC). The signal, f_{beat} , is then fed through a series of filters (Mini Circuits BLP-30+ and BLP-50+) and amplifiers (Mini Circuits ZFL-1000LN+), shown in Fig. 1. Despite spatial filtering the beat signal contains beats with multiple comb modes, for this reason the cut-off frequency of the filters is chosen to be $f_{cut-off} < f_{rep}/2$, this way the beat with a single mode gets filtered trough. This amplified signal is then split, with one part being used for monitoring the beat frequency. The beat signal is shown in the inset of Fig. 1, we achieve a 40 dB signal-to-noise with a measured FWHM of 60 kHz (100 Hz bandwidth) sets an upper limit on the width of both the comb and the ECDL.

The other part of the filtered and amplified signal is sent to a 64-fold divider (RF bay, FAS-64). The divider serves to increase the capture range of the lock which is necessary due to limits on the feedback bandwidth characteristic to lasers based on Er-doped fibers. The output signal from the divider is fed into an analog phase detector (Mini Circuits ZRPD-1+) together with a reference signal supplied by a direct digital synthesizer board (DDS, Novatech instruments, DDS9m). The output from the phase detector is and passed through low pass filter (4 kHz cutoff) to obtain an error signal. We then use a

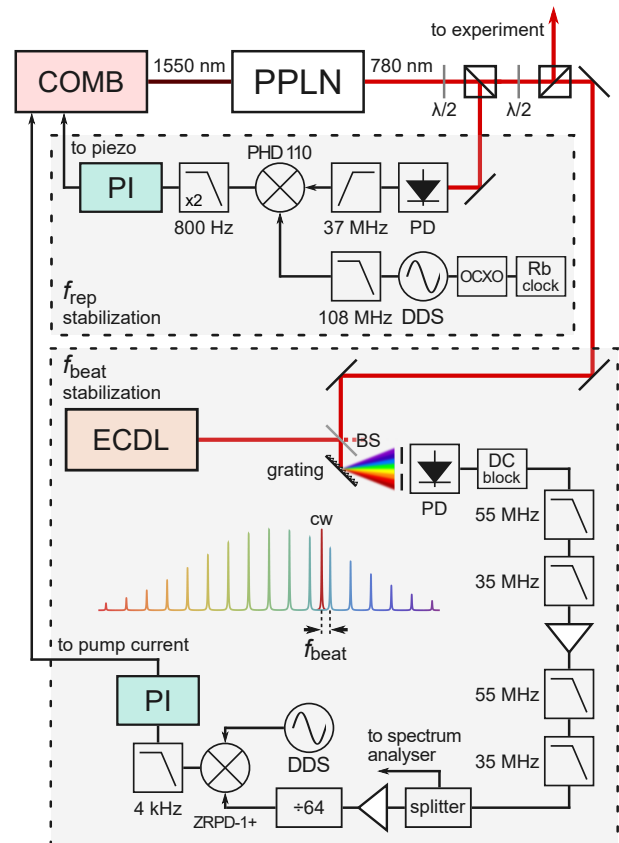


FIG. 1. Sketch of the experimental setup for fully stabilizing the comb using an ECDL. The upper and lower section of the image shows the scheme for stabilizing f_{rep} and f_{beat} , respectively. The DDS's in the upper and lower part of the figure are the same unit. The spectrum after the grating is an illustration, in reality it does not stretch to the visible part of the spectrum. The setup does not require an iris, the spatial filtering is achieved due to the photodiode active area being small. PPLN: periodically poled lithium niobate crystal, PD - photodiode, $\lambda/2$ - half-wave plate, DDS - direct digital synthesizer, OCXO - oven controlled crystal oscillator, ECDL - external cavity diode laser, BS - beam splitter.

PI controller (Newport LB1005) to generate the feedback signal which modulates the pump power in the cavity in order to keep the selected comb mode fixed relative to the ECDL frequency, at a frequency difference f_{beat} .

To stabilize the repetition frequency we mix the detected and filtered (to reduce low frequency noise, Mini Circuits BHP-50+) repetition rate with a reference signal from the same DDS generating the reference signal for the stabilization of the optical beat frequency, see upper part of Fig. 1. The error signal is generated with a modular phase detector that is installed into the laser controller (Toptica PHD 110), passed through a second order low pass filter with a 800 Hz cutoff to filter out high frequency noise, and then fed into a built-in PID controller (Toptica PID 110) which then controls the piezo which changes the length of the cavity. This enables the stabi-

lization of the repetition frequency, f_{rep} , which together with stabilizing the position of a single comb tooth as described earlier, stabilizes the whole comb.

III. STABILITY EVALUATION AND DISCUSSION

The measured repetition frequency and optical beat frequency, f_{rep} and f_{beat} , are shown in Fig. 2(a) with the corresponding Allan deviations shown in panel (b). One can see from the Allan deviations that the lock functions very well going below the mHz level at 10 s integration time. From this we can conclude that the stability of the comb is limited not by the noise introduced by the locking procedure, but rather by the stability of the ECDL reference laser, expected to be orders of magnitude lower^{19,20}.

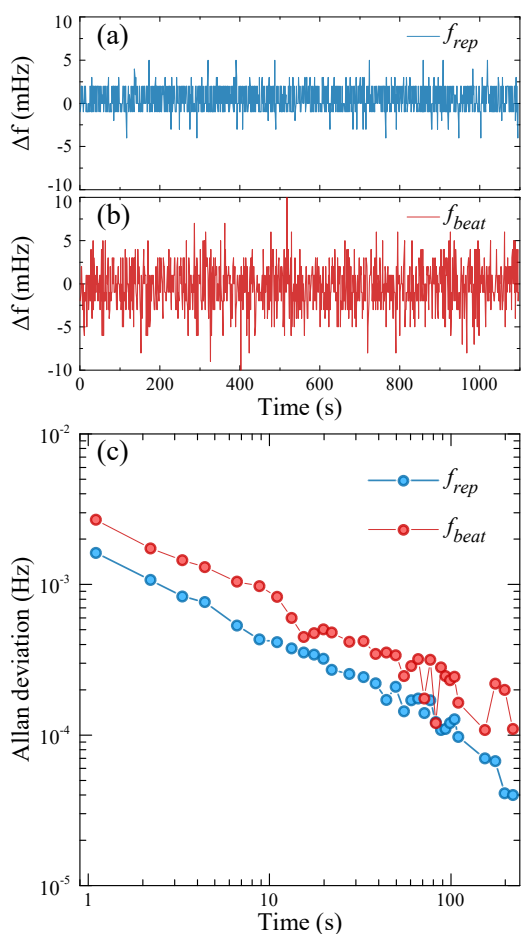


FIG. 2. Measurement of the lock performance (a) measured f_{rep} and f_{beat} frequencies while both feedback loops are enabled. (b) the corresponding Allan deviations.

The PI corners of the f_{rep} and f_{beat} loops are set to 14 Hz and 300 Hz, respectively. These values are deliberately chosen to be low, especially for the f_{rep} loop, in order to avoid transferring high frequency noise from the reference frequency onto the optical spectrum. Any noise

on the reference frequency for the loop that controls the repetition frequency transfers to the optical spectrum, multiplied by the mode number, n , evident from eq. (1). Since n is on the order of $n \approx 5 \times 10^6$ the influence on optical frequencies is considerable. For this reason it is necessary to use a frequency reference with very low phase noise. The DDS that we use to synthesize the reference frequency is itself referenced to an oven controlled crystal oscillator (OCXO, Miteq PLD-1C-10-475-15P), which is in turn phase locked to a rubidium frequency standard (Stanford Research Systems FS725) with a 10 MHz output. The OCXO has a 475 MHz output and acts here as a frequency multiplier that introduces very little phase noise. The DDS then divides this clock frequency to the wanted ≈ 80.5 MHz which is further filtered (Mini Circuits BLP-100+) to remove remainders of the clock frequency and aliasing frequencies. An alternative way would be to use the 10 MHz output of the Rb standard to reference the DDS which would then multiply this to the wanted ≈ 80.5 MHz, however, this was found to unexpectedly introduce far more phase noise. Although the resulting signal is very clean (stated phase noise of -120 dBc at 10 kHz offset) the intrinsic short term stability of the frequency comb is better. For this reason we set the PI corner of the f_{rep} loop low in order not to interfere with this intrinsic short term stability, rather only correct for long term drifts which occur mostly because of temperature variations. Since the two control loops are not orthogonal the PI corner of the f_{beat} loop is also set low so as to not transfer high frequency noise to the other loop.

As mentioned previously, the absolute stability of the FC is expected to be limited by the absolute stability of the ECDL reference laser. To evaluate this stability and to demonstrate the abilities of our locking scheme we perform a heterodyne beat of the stabilized FC with a separate ECDL laser. This laser is locked to a two-photon transition, ^{87}Rb , $|5S_{1/2}; F=2\rangle \rightarrow |5D_{5/2}; F'=4\rangle$ by a dither lock. To observe a peak to which to lock to we detect 420 nm fluorescence with a photomultiplier tube in a rubidium cell heated and to $\approx 110^\circ\text{C}$. The temperature of the cell is stabilized with a temperature controller (MPT-5000, *Wavelength Electronics*) controlling the current through the heating wire. For the purpose of this measurement, the polarization spectroscopy cell was also temperature stabilized to reduce the drift in frequency. This was done by placing the cell in a acrylic glass case and heating it to $\approx 60^\circ\text{C}$ with a Peltier module controlled with a temperature controller (MPT-2500, *Wavelength Electronics*). A laser stabilized to this transition can be used as a primary standard for length measurements due to the inherent absolute stability of the transition, reported to be on the 10^{-11} level²¹. The measured beat frequency is shown in Fig. 3(a) with the corresponding Allan deviation in Fig. 3(b).

The measured Allan deviation determines the upper limit on the absolute stability of our locking scheme which is on the order of tens of kilohertz. The measured

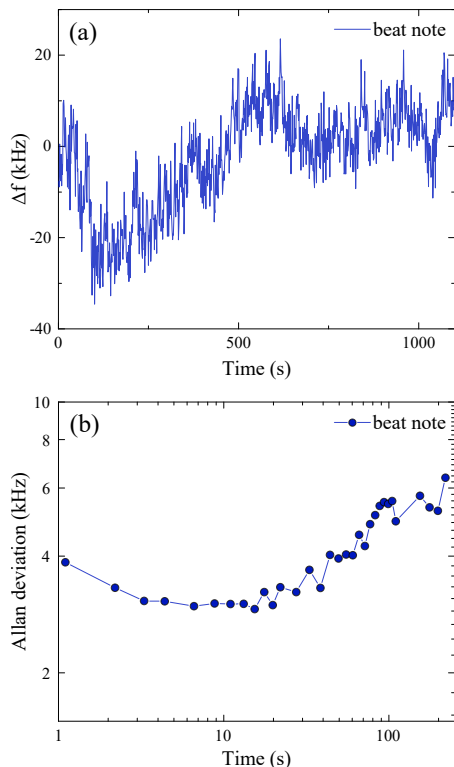


FIG. 3. Measurement of the absolute stability of our locking scheme by heterodyne beating our FC with a ECDL locked to a two-photon transition, ^{85}Rb , $|5S_{1/2}; F=2\rangle \rightarrow |5D_{5/2}; F'=4\rangle$. (a) The measured frequency drift of the beat note. (b) The corresponding Allan deviation

stability is expected from a DC locking technique such as the one used, polarization spectroscopy. The fractional stability at 10 s integration time is below $\Delta f/f \approx 10^{-11}$ which is excellent considering the simplicity of our setup, and more importantly more than satisfactory for laser cooling. Further enhancement of the absolute stability could be achieved by stabilizing the temperature of the AOM crystal that provides the light for the polarization spectroscopy. The efficiency of an AOM varies significantly with regards to temperature, hence any drift in the temperature of the crystal would change the total power in the pump and probe beams in the polarization spectroscopy setup, changing the position of the zero crossing and thus the frequency of the reference laser.

IV. CONCLUSION

We presented a scheme for fully stabilizing a Er-fiber laser frequency comb without self-referencing by referencing it to a stabilized ECDL laser. We also measured the performance of the scheme and the evaluated the attained absolute stability. The ECDL used is referenced

to a rubidium transition at 780 nm so the same scheme could be easily used to stabilize a Ti-Sapphire laser FC. The scheme is simple, cost effective and power efficient. We emphasize that our scheme two orders of magnitude less power (≈ 1 mW) than f-2f interferometry (≈ 100 - 200 mW) and achieves a absolute fractional frequency stability below $\Delta f/f \approx 10^{-11}$. Due to the availability of CW laser stabilized in this way in laboratories worldwide we expect it will be used widely in experiments exploring FC Doppler cooling or other physical phenomena involving FC-atom interaction.

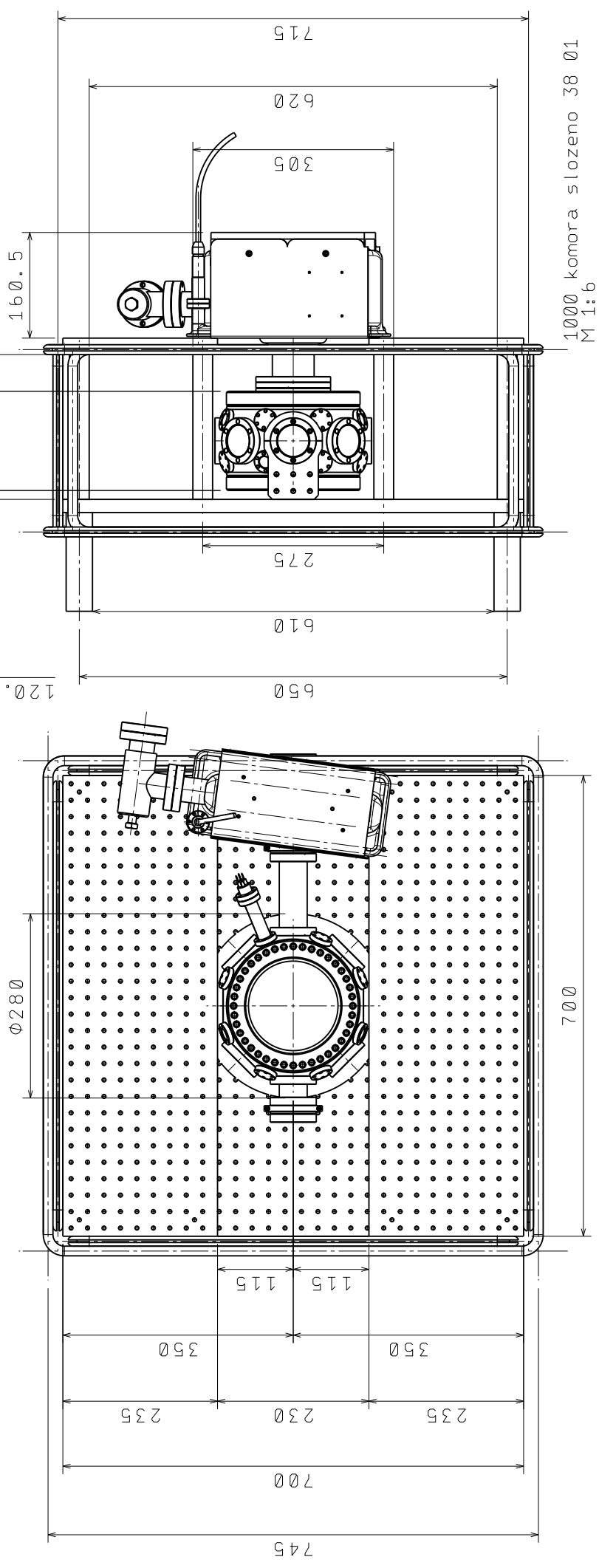
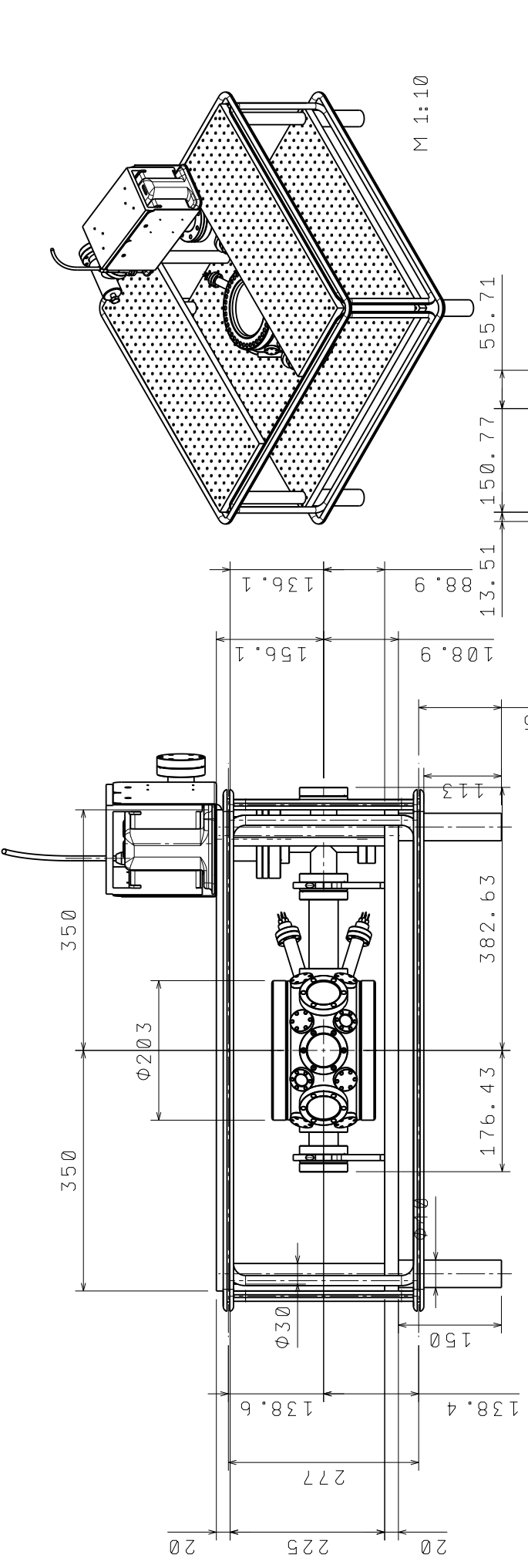
V. ACKNOWLEDGMENTS

We are grateful to M. Katić for lending of equipment. This work was funded by project Frequency-Comb-induced OptoMechanics, Hrvatska Zaklada za Znanost (HRZZ) (IP-2014-09-7342).

- ¹R. Holzwarth, M. Zimmermann, T. Udem, and T. W. Hänsch, IEEE Journal of Quantum Electronics **37**, 1493 (2001), ISSN 0018-9197.
- ²L. Hollberg, C. W. Oates, E. A. Curtis, E. N. Ivanov, S. A. Diddams, T. Udem, H. G. Robinson, J. C. Bergquist, R. J. Rafac, W. M. Itano, et al., IEEE Journal of Quantum Electronics **37**, 1502 (2001), ISSN 0018-9197.
- ³A. Marian, M. C. Stowe, J. R. Lawall, D. Felinto, and J. Ye, Science **306**, 2063 (2004), ISSN 0036-8075.
- ⁴A. Marian, M. C. Stowe, D. Felinto, and J. Ye, Phys. Rev. Lett. **95**, 023001 (2005).
- ⁵A. M. Jayich, X. Long, and W. C. Campbell, Phys. Rev. X **6**, 041004 (2016).
- ⁶J. Davila-Rodriguez, A. Ozawa, T. W. Hänsch, and T. Udem, Phys. Rev. Lett. **116**, 043002 (2016).
- ⁷H. J. Metcalf and P. van der Straten, *Laser Cooling and Trapping* (Springer-Verlag, New York, 1999).
- ⁸D. Kielpinski, Phys. Rev. A **73**, 063407 (2006).
- ⁹R. Bluhm, V. A. Kostelecký, and N. Russell, Phys. Rev. Lett. **82**, 2254 (1999).
- ¹⁰W. W. Duley, *UV Lasers: Effects and Applications in Materials Science* (Cambridge University Press, 1996), 1st ed.
- ¹¹P. Strohmeier, T. Kerseboom, E. Krüger, H. Nölle, B. Steuter, J. Schmand, and J. Andrä, Optics Communications **73**, 451 (1989), ISSN 0030-4018.
- ¹²K. Mølmer, Phys. Rev. Lett. **66**, 2301 (1991).
- ¹³M. Allegrini and E. Arimondo, Physics Letters A **172**, 271 (1993), ISSN 0375-9601.
- ¹⁴D. J. Jones, S. A. Diddams, J. K. Ranka, A. Stentz, R. S. Windeler, J. L. Hall, and S. T. Cundiff, Science **288**, 635 (2000), ISSN 0036-8075.
- ¹⁵J. Reichert, R. Holzwarth, T. Udem, and T. Hänsch, Optics Communications **172**, 59 (1999), ISSN 0030-4018.
- ¹⁶U. Morgner, R. Ell, G. Metzler, T. R. Schibli, F. X. Kartner, J. G. Fujimoto, and E. P. Ippen, in *Technical Digest. Summaries of papers presented at the Quantum Electronics and Laser Science Conference. Postconference Technical Digest (IEEE Cat. No. 01CH37172)* (2001), pp. 260–261.
- ¹⁷T. M. Ramond, S. A. Diddams, L. Hollberg, and A. Bartels, Opt. Lett. **27**, 1842 (2002).
- ¹⁸C. Wieman and T. W. Hänsch, Phys. Rev. Lett. **36**, 1170 (1976).
- ¹⁹J. S. Torrance, B. M. Sparkes, L. D. Turner, and R. E. Scholten, Opt. Express **24**, 11396 (2016).
- ²⁰M. W. Lee, M. C. Jarratt, C. Marciniak, and M. J. Biercuk, Opt. Express **22**, 7210 (2014).
- ²¹R. Felder, Metrologia **42**, 323 (2005).

Appendix C

Technical drawings



1000 komora slozeno 38 01
M 1:6

Curriculum Vitae

Neven Šantić was born in Karlovac, Croatia on 17th of December, 1986. He finished high school in 2005, the same year he enrolled in the research focused program in physics at the Faculty of Science, University of Zagreb. He earned his masters degree in June 2012 with a master thesis titled "Laser cooling" with dr. sc. Ticijana Ban as thesis advisor. The same year he started volunteering at the Cold Atom Lab at the Institute of Physics in Zagreb. In December 2013 he is employed at the Physics department of the Faculty of Science as an assistant and continues working on cold atom based research, now as a doctoral student. In October, 2016 he is employed by the Institute of Physics in Zagreb as an assistant, a position he holds at the time of writing this thesis.

List of publications

- (10) N. Šantić, G. Kowzan, D. Kovačić, D. Aumiler, P. Maslowski, and T. Ban, "Frequency comb stabilization without self-referencing," draft written
- (9) N. Šantić, A. Cipriš, I. Krešić, D. Aumiler, and T. Ban, "Sub-Doppler cooling of atoms using an optical frequency comb," submitted
- (8) N. Šantić, S. Salem, J. Garnier, A. Fusaro, A. Picozzi, and R. Kaiser, "Non-equilibrium precondensation of classical waves in two dimensions propagating through atomic vapors," *Phys. Rev. Lett.* **120**, 055301 (2018).
- (7) N. Šantić, T. Dubček, D. Aumiler, H. Buljan, and T. Ban, "Synthetic Lorentz force in an expanding cold atomic gas," *J. Opt. Soc. Am. B* **34**, 1264-1269 (2017).
- (6) N. Šantić, T. Dubček, D. Aumiler, H. Buljan, T. Ban, Experimental Demonstration of a Synthetic Lorentz Force by Using Radiation Pressure, *Scientific reports* **5**, 13485 (2015).
- (5) G. Kregar, N. Šantić, D. Aumiler, T. Ban, Radiation pressure force on cold rubidium atoms due to excitation to a non-cooling hyperfine level, *Eur. Phys. J. D* **68**, 360 (2014).
- (4) T. Dubček, N. Šantić, D. Jukić, D. Aumiler, T. Ban, H. Buljan, Synthetic Lorentz force in classical atomic gases via Doppler effect and radiation pressure, *Phys. Rev. A* **89**, 063415 (2014).
- (3) G. Kregar, N. Šantić, D. Aumiler, H. Buljan, and T. Ban, Frequency-comb-induced radiative force on cold rubidium atoms, *Phys. Rev. A*, **89**, 053421 (2014).
- (2) L. Kime, A. Fioretti, Y. Bruneau, N. Porfido, M. Viteau, G. Khalili, N. Šantić, A. Gloter, B. Rasser, P. Sudraud, P. Pillet and D. Comparat, High flux monochromatic ion and electron beams based on laser-cooled atoms, *Phys. Rev. A* **88**, 033424 (2013).
- (1) B. Šantić and N. Šantić, Potential profile of the quantum step in semiconductors and the example of GaN, *Semicond. Sci. Technol.* **27**, 085014 (2012).

Bibliography

- [1] H. J. Metcalf and P. van der Straten, *Laser Cooling and Trapping* (Springer-Verlag, New York, 1999). [Cited on pages [ii](#), [5](#), [8](#), [16](#), [20](#), [44](#), [48](#), and [67](#).]
- [2] S. Chu, C. Cohen-Tannoudji, and W. D. Phillips, *The nobel prize in physics 1997*, URL http://www.nobelprize.org/nobel_prizes/physics/laureates/1997/. [Cited on page [1](#).]
- [3] A. Aspect, E. Arimondo, R. Kaiser, N. Vansteenkiste, and C. Cohen-Tannoudji, *Phys. Rev. Lett.* **61**, 826 (1988), URL <https://link.aps.org/doi/10.1103/PhysRevLett.61.826>. [Cited on page [1](#).]
- [4] E. A. Cornell, W. Ketterle, and C. E. Wieman, *The nobel prize in physics 2001*, URL http://www.nobelprize.org/nobel_prizes/physics/laureates/2001/. [Cited on page [2](#).]
- [5] C. Chin, R. Grimm, P. Julienne, and E. Tiesinga, *Rev. Mod. Phys.* **82**, 1225 (2010), URL <https://link.aps.org/doi/10.1103/RevModPhys.82.1225>. [Cited on page [2](#).]
- [6] I. Bloch, J. Dalibard, and S. Nascimbene, *Nat Phys* **8**, 267 (2012), ISSN 1745-2473, URL <http://dx.doi.org/10.1038/nphys2259>. [Cited on pages [2](#) and [3](#).]
- [7] J. R. Abo-Shaer, C. Raman, J. M. Vogels, and W. Ketterle, *Science* **292**, 476 (2001), ISSN 0036-8075, URL <http://science.sciencemag.org/content/292/5516/476>. [Cited on page [2](#).]
- [8] N. Cooper, *Advances in Physics* **57**, 539 (2008), URL <http://dx.doi.org/10.1080/00018730802564122>. [Cited on page [2](#).]
- [9] Y.-J. Lin, R. L. Compton, K. Jimenez-Garcia, J. V. Porto, and I. B. Spielman, *Nature* **462**, 628 (2009), ISSN 0028-0836, URL <http://dx.doi.org/10.1038/nature08609>. [Cited on page [3](#).]
- [10] L. J. LeBlanc, K. Jiménez-García, R. A. Williams, M. C. Beeler, A. R. Perry, W. D. Phillips, and I. B. Spielman, *Proceedings of the National Academy of Sciences* **109**, 10811 (2012), URL <http://www.pnas.org/content/109/27/10811.abstract>. [Cited on page [3](#).]

- [11] M. Aidelsburger, M. Atala, M. Lohse, J. T. Barreiro, B. Paredes, and I. Bloch, Phys. Rev. Lett. **111**, 185301 (2013), URL <https://link.aps.org/doi/10.1103/PhysRevLett.111.185301>. [Cited on page 3.]
- [12] H. Miyake, G. A. Siviloglou, C. J. Kennedy, W. C. Burton, and W. Ketterle, Phys. Rev. Lett. **111**, 185302 (2013), URL <https://link.aps.org/doi/10.1103/PhysRevLett.111.185302>. [Cited on page 3.]
- [13] M. Aidelsburger, M. Lohse, C. Schweizer, M. Atala, J. . T. Barreiro, S. Nascimbène, N. . R. Cooper, I. Bloch, and N. Goldman, **11**, 162 EP (2014), URL <http://dx.doi.org/10.1038/nphys3171>. [Cited on page 3.]
- [14] M. W. Ray, E. Ruokokoski, S. Kandel, M. Mottonen, and D. S. Hall, Nature **505**, 657 (2014), ISSN 0028-0836, letter, URL <http://dx.doi.org/10.1038/nature12954>. [Cited on page 3.]
- [15] N. Goldman, G. Juzeliunas, P. Öhberg, and I. B. Spielman, Reports on Progress in Physics **77**, 126401 (2014), URL <http://stacks.iop.org/0034-4885/77/i=12/a=126401>. [Cited on page 3.]
- [16] J. Dalibard, F. Gerbier, G. Juzeliūnas, and P. Öhberg, Rev. Mod. Phys. **83**, 1523 (2011), URL <https://link.aps.org/doi/10.1103/RevModPhys.83.1523>. [Cited on page 3.]
- [17] R. Kaiser, *private communication*. [Cited on page 3.]
- [18] T. Walker, D. Sesko, and C. Wieman, Phys. Rev. Lett. **64**, 408 (1990), URL <https://link.aps.org/doi/10.1103/PhysRevLett.64.408>. [Cited on pages 3 and 22.]
- [19] D. W. Sesko, T. G. Walker, and C. E. Wieman, J. Opt. Soc. Am. B **8**, 946 (1991), URL <http://josab.osa.org/abstract.cfm?URI=josab-8-5-946>. [Cited on pages 3 and 22.]
- [20] L. Pruvost, I. Serre, H. T. Duong, and J. Jortner, Phys. Rev. A **61**, 053408 (2000), URL <https://link.aps.org/doi/10.1103/PhysRevA.61.053408>. [Cited on pages 4 and 63.]
- [21] J. T. Mendonça, R. Kaiser, H. Terças, and J. Loureiro, Phys. Rev. A **78**, 013408 (2008), URL <https://link.aps.org/doi/10.1103/PhysRevA.78.013408>. [Cited on page 4.]
- [22] J. T. Mendonça and R. Kaiser, Phys. Rev. Lett. **108**, 033001 (2012), URL <https://link.aps.org/doi/10.1103/PhysRevLett.108.033001>. [Cited on page 4.]
- [23] H. Terças, J. T. Mendonça, and R. Kaiser, EPL (Europhysics Letters) **89**, 53001 (2010), URL <http://stacks.iop.org/0295-5075/89/i=5/a=53001>. [Cited on page 4.]

- [24] G. Labeyrie, F. Michaud, and R. Kaiser, *Phys. Rev. Lett.* **96**, 023003 (2006), URL <https://link.aps.org/doi/10.1103/PhysRevLett.96.023003>. [Cited on page 4.]
- [25] J. D. Rodrigues, J. A. Rodrigues, O. L. Moreira, H. Terças, and J. T. Mendonça, *Phys. Rev. A* **93**, 023404 (2016), URL <https://link.aps.org/doi/10.1103/PhysRevA.93.023404>. [Cited on page 4.]
- [26] T. Dubček, N. Šantić, D. Jukić, D. Aumiler, T. Ban, and H. Buljan, *Phys. Rev. A* **89**, 063415 (2014), URL <https://link.aps.org/doi/10.1103/PhysRevA.89.063415>. [Cited on pages 4 and 44.]
- [27] N. Šantić, T. Dubček, D. Aumiler, T. Ban, and H. Buljan, *Scientific Reports* **5**, 13485 (2015), URL <https://www.nature.com/articles/srep13485>. [Cited on pages 4 and 44.]
- [28] N. Šantić, T. Dubček, D. Aumiler, H. Buljan, and T. Ban, *J. Opt. Soc. Am. B* **34**, 1264 (2017), URL <http://josab.osa.org/abstract.cfm?URI=josab-34-6-1264>. [Cited on pages 4 and 44.]
- [29] P. Strohmeier, T. Kersebom, E. Krüger, H. Nölle, B. Steuter, J. Schmand, and J. Andrä, *Optics Communications* **73**, 451 (1989), ISSN 0030-4018, URL <http://www.sciencedirect.com/science/article/pii/0030401889904604>. [Cited on page 5.]
- [30] K. Mølmer, *Phys. Rev. Lett.* **66**, 2301 (1991), URL <https://link.aps.org/doi/10.1103/PhysRevLett.66.2301>. [Cited on page 5.]
- [31] M. Allegrini and E. Arimondo, *Physics Letters A* **172**, 271 (1993), ISSN 0375-9601, URL <http://www.sciencedirect.com/science/article/pii/0375960193910206>. [Cited on page 5.]
- [32] D. Kielpinski, *Phys. Rev. A* **73**, 063407 (2006), URL <https://link.aps.org/doi/10.1103/PhysRevA.73.063407>. [Cited on page 6.]
- [33] D. Aumiler and T. Ban, *Phys. Rev. A* **85**, 063412 (2012), URL <https://link.aps.org/doi/10.1103/PhysRevA.85.063412>. [Cited on page 6.]
- [34] A. M. Jayich, X. Long, and W. C. Campbell, *Phys. Rev. X* **6**, 041004 (2016), URL <https://link.aps.org/doi/10.1103/PhysRevX.6.041004>. [Cited on pages 6, 73, 75, and 76.]
- [35] E. Peters, S. A. Diddams, P. Fendel, S. Reinhardt, T. W. Hänsch, and T. Udem, *Opt. Express* **17**, 9183 (2009), URL <http://www.opticsexpress.org/abstract.cfm?URI=oe-17-11-9183>. [Cited on page 6.]

- [36] D. C. Yost, T. R. Schibli, J. Ye, J. L. Tate, J. Hostetter, M. B. Gaarde, and K. J. Schafer, *Nat Phys* **5**, 815 (2009), ISSN 1745-2473, URL <http://dx.doi.org/10.1038/nphys1398>. [Cited on page 6.]
- [37] B. Bernhardt, A. Ozawa, A. Vernaleken, I. Pupeza, J. Kaster, Y. Kobayashi, R. Holzwarth, E. Fill, F. Krausz, T. W. Hänsch, et al., *Opt. Lett.* **37**, 503 (2012), URL <http://ol.osa.org/abstract.cfm?URI=ol-37-4-503>. [Cited on page 6.]
- [38] J. Davila-Rodriguez, A. Ozawa, T. W. Hänsch, and T. Udem, *Phys. Rev. Lett.* **116**, 043002 (2016), URL <https://link.aps.org/doi/10.1103/PhysRevLett.116.043002>. [Cited on pages 6 and 73.]
- [39] A. Cingoz, D. C. Yost, T. K. Allison, A. Ruehl, M. E. Fermann, I. Hartl, and J. Ye, *Nature* **482**, 68 (2012), ISSN 0028-0836, URL <http://dx.doi.org/10.1038/nature10711>. [Cited on page 6.]
- [40] A. Schliesser, N. Picque, and T. W. Hansch, *Nat Photon* **6**, 440 (2012), ISSN 1749-4885, URL <http://dx.doi.org/10.1038/nphoton.2012.142>. [Cited on page 6.]
- [41] H. Perrin, *Les houches lectures on laser cooling and trapping* (2012), URL http://www-lpl.univ-paris13.fr/bec/bec/Teaching/lecture1_2012.pdf. [Cited on pages 8, 20, and 22.]
- [42] A. Ashkin, *Phys. Rev. Lett.* **24**, 156 (1970), URL <https://link.aps.org/doi/10.1103/PhysRevLett.24.156>. [Cited on page 14.]
- [43] T. Hänsch and A. Schawlow, *Optics Communications* **13**, 68 (1975), ISSN 0030-4018, URL <http://www.sciencedirect.com/science/article/pii/0030401875901595>. [Cited on page 14.]
- [44] D. J. Wineland, R. E. Drullinger, and F. L. Walls, *Phys. Rev. Lett.* **40**, 1639 (1978), URL <https://link.aps.org/doi/10.1103/PhysRevLett.40.1639>. [Cited on page 14.]
- [45] S. Chu, L. Hollberg, J. E. Bjorkholm, A. Cable, and A. Ashkin, *Phys. Rev. Lett.* **55**, 48 (1985), URL <https://link.aps.org/doi/10.1103/PhysRevLett.55.48>. [Cited on pages 14 and 15.]
- [46] P. D. Lett, R. N. Watts, C. I. Westbrook, W. D. Phillips, P. L. Gould, and H. J. Metcalf, *Phys. Rev. Lett.* **61**, 169 (1988), URL <https://link.aps.org/doi/10.1103/PhysRevLett.61.169>. [Cited on page 15.]
- [47] J. Dalibard and C. Cohen-Tannoudji, *J. Opt. Soc. Am. B* **6**, 2023 (1989), URL <http://josab.osa.org/abstract.cfm?URI=josab-6-11-2023>. [Cited on pages 16 and 77.]

- [48] B. Sheehy, S.-Q. Shang, P. van der Straten, S. Hatamian, and H. Metcalf, *Phys. Rev. Lett.* **64**, 858 (1990), URL <https://link.aps.org/doi/10.1103/PhysRevLett.64.858>. [Cited on page 17.]
- [49] C. Valentin, M.-C. Gagné, J. Yu, and P. Pillet, *EPL (Europhysics Letters)* **17**, 133 (1992), URL <http://stacks.iop.org/0295-5075/17/i=2/a=009>. [Cited on pages 18 and 77.]
- [50] E. L. Raab, M. Prentiss, A. Cable, S. Chu, and D. E. Pritchard, *Phys. Rev. Lett.* **59**, 2631 (1987), URL <https://link.aps.org/doi/10.1103/PhysRevLett.59.2631>. [Cited on page 19.]
- [51] D. A. Steck, *Rubidium 87 d line data*, URL <http://steck.us/alkalidata/>. [Cited on pages 25, 40, 46, 58, 71, and 73.]
- [52] A. J. Olson, E. J. Carlson, and S. K. Mayer, *American Journal of Physics* **74**, 218 (2006), URL <http://dx.doi.org/10.1119/1.2173278>. [Cited on pages 25 and 38.]
- [53] C. J. Dedman, K. G. H. Baldwin, and M. Colla, *Review of Scientific Instruments* **72**, 4055 (2001), URL <http://dx.doi.org/10.1063/1.1408935>. [Cited on page 31.]
- [54] R. P. Encyclopedia, *External-cavity diode lasers*, URL https://www.rp-photonics.com/external_cavity_diode_lasers.html. [Cited on page 35.]
- [55] D. W. Preston, *American Journal of Physics* **64**, 1432 (1996), URL <http://dx.doi.org/10.1119/1.18457>. [Cited on page 36.]
- [56] D. Sheng, A. Pérez Galván, and L. A. Orozco, *Phys. Rev. A* **78**, 062506 (2008), URL <https://link.aps.org/doi/10.1103/PhysRevA.78.062506>. [Cited on pages 37, 46, and 59.]
- [57] C. Wieman and T. W. Hänsch, *Phys. Rev. Lett.* **36**, 1170 (1976), URL <https://link.aps.org/doi/10.1103/PhysRevLett.36.1170>. [Cited on page 38.]
- [58] C. P. Pearman, C. S. Adams, S. G. Cox, P. F. Griffin, D. A. Smith, and I. G. Hughes, *Journal of Physics B: Atomic, Molecular and Optical Physics* **35**, 5141 (2002), URL <http://stacks.iop.org/0953-4075/35/i=24/a=315>. [Cited on page 39.]
- [59] J. S. Torrance, B. M. Sparkes, L. D. Turner, and R. E. Scholten, *Opt. Express* **24**, 11396 (2016), URL <http://www.opticsexpress.org/abstract.cfm?URI=oe-24-11-11396>. [Cited on pages 39 and 69.]
- [60] J. C. B. Kangara, A. J. Hachtel, M. C. Gillette, J. T. Barkeloo, E. R. Clements, S. Bali, B. E. Unks, N. A. Proite, D. D. Yavuz, P. J. Martin, et al., *American Journal of Physics* **82**, 805 (2014), URL <https://doi.org/10.1119/1.4867376>. [Cited on page 42.]

- [61] S. H. Autler and C. H. Townes, Phys. Rev. **100**, 703 (1955), URL <https://link.aps.org/doi/10.1103/PhysRev.100.703>. [Cited on page 47.]
- [62] J. Chabé, M.-T. Rouabah, L. Bellando, T. Bienaimé, N. Piovella, R. Bachelard, and R. Kaiser, Phys. Rev. A **89**, 043833 (2014), URL <https://link.aps.org/doi/10.1103/PhysRevA.89.043833>. [Cited on pages 54 and 56.]
- [63] W. E. Lamb, Phys. Rev. **134**, A1429 (1964), URL <https://link.aps.org/doi/10.1103/PhysRev.134.A1429>. [Cited on page 65.]
- [64] L. E. Hargrove, R. L. Fork, and M. A. Pollack, Applied Physics Letters **5**, 4 (1964), URL <https://doi.org/10.1063/1.1754025>. [Cited on page 65.]
- [65] E. Ippen, C. Shank, and A. Dienes, Applied Physics Letters **21**, 348 (1972), URL <https://doi.org/10.1063/1.1654406>. [Cited on page 65.]
- [66] J. Ye and S. T. Cundiff, *Femtosecond Optical Frequency Comb: Principle, Operation and Applications* (Springer US, 2005), 1st ed. [Cited on page 65.]
- [67] D. J. Jones, S. A. Diddams, J. K. Ranka, A. Stentz, R. S. Windeler, J. L. Hall, and S. T. Cundiff, Science **288**, 635 (2000), ISSN 0036-8075, URL <http://science.sciencemag.org/content/288/5466/635>. [Cited on page 66.]
- [68] R. Holzwarth, M. Zimmermann, T. Udem, and T. W. Hansch, IEEE Journal of Quantum Electronics **37**, 1493 (2001), ISSN 0018-9197. [Cited on page 65.]
- [69] L. Hollberg, C. W. Oates, E. A. Curtis, E. N. Ivanov, S. A. Diddams, T. Udem, H. G. Robinson, J. C. Bergquist, R. J. Rafac, W. M. Itano, et al., IEEE Journal of Quantum Electronics **37**, 1502 (2001), ISSN 0018-9197. [Cited on page 65.]
- [70] S. A. Diddams, T. Udem, J. C. Bergquist, E. A. Curtis, R. E. Drullinger, L. Hollberg, W. M. Itano, W. D. Lee, C. W. Oates, K. R. Vogel, et al., Science (2001), ISSN 0036-8075, URL <http://science.sciencemag.org/content/early/2001/07/12/science.1061171>. [Cited on page 65.]
- [71] B. J. Bloom, T. L. Nicholson, J. R. Williams, S. L. Campbell, M. Bishof, X. Zhang, W. Zhang, S. L. Bromley, and J. Ye, Nature **506**, 71 (2014), ISSN 0028-0836, letter, URL <http://dx.doi.org/10.1038/nature12941>. [Cited on page 65.]
- [72] J. Reichert, R. Holzwarth, T. Udem, and T. Hänsch, Optics Communications **172**, 59 (1999), ISSN 0030-4018, URL <http://www.sciencedirect.com/science/article/pii/S0030401899004915>. [Cited on page 66.]
- [73] U. Morgner, R. Ell, G. Metzler, T. R. Schibli, F. X. Kartner, J. G. Fujimoto, and E. P. Ippen, in *Technical Digest. Summaries of papers presented at the Quantum*

- Electronics and Laser Science Conference. Postconference Technical Digest (IEEE Cat. No.01CH37172)* (2001), pp. 260–261. [Cited on page 66.]
- [74] T. M. Ramond, S. A. Diddams, L. Hollberg, and A. Bartels, *Opt. Lett.* **27**, 1842 (2002), URL <http://ol.osa.org/abstract.cfm?URI=ol-27-20-1842>. [Cited on page 66.]
- [75] K. Tamura, H. A. Haus, and E. P. Ippen, *Electronics Letters* **28**, 2226 (1992), ISSN 0013-5194. [Cited on page 67.]
- [76] M. W. Lee, M. C. Jarratt, C. Marciniak, and M. J. Biercuk, *Opt. Express* **22**, 7210 (2014), URL <http://www.opticsexpress.org/abstract.cfm?URI=oe-22-6-7210>. [Cited on page 69.]
- [77] R. Felder, *Metrologia* **42**, 323 (2005), URL <http://stacks.iop.org/0026-1394/42/i=4/a=018>. [Cited on page 71.]
- [78] A. J. Olson, E. J. Carlson, and S. K. Mayer, *American Journal of Physics* **74**, 218 (2006), URL <https://doi.org/10.1119/1.2173278>. [Cited on page 71.]
- [79] T. Ban, D. Aumiler, H. Skenderović, and G. Pichler, *Phys. Rev. A* **73**, 043407 (2006), URL <https://link.aps.org/doi/10.1103/PhysRevA.73.043407>. [Cited on page 74.]
- [80] A. Marian, M. C. Stowe, J. R. Lawall, D. Felinto, and J. Ye, *Science* **306**, 2063 (2004), ISSN 0036-8075, URL <http://science.sciencemag.org/content/306/5704/2063>. [Cited on page 75.]
- [81] T. E. Mehlstäubler, K. Moldenhauer, M. Riedmann, N. Rehbein, J. Friebe, E. M. Rasel, and W. Ertmer, *Phys. Rev. A* **77**, 021402 (2008), URL <https://link.aps.org/doi/10.1103/PhysRevA.77.021402>. [Cited on page 76.]
- [82] C. Salomon, J. Dalibard, W. D. Phillips, A. Clairon, and S. Guellati, *EPL (Europhysics Letters)* **12**, 683 (1990), URL <http://stacks.iop.org/0295-5075/12/i=8/a=003>. [Cited on page 77.]
- [83] V. Finkelstein, P. R. Berman, and J. Guo, *Phys. Rev. A* **45**, 1829 (1992), URL <https://link.aps.org/doi/10.1103/PhysRevA.45.1829>. [Cited on page 77.]
- [84] G. Labeyrie, C. Miniatura, and R. Kaiser, *Phys. Rev. A* **64**, 033402 (2001), URL <https://link.aps.org/doi/10.1103/PhysRevA.64.033402>. [Cited on page 78.]